Machine Learning Solutions for Context Information-aware Beam Management in Millimeter Wave Communications

Rezaie, Sajad

DOI (link to publication from Publisher):
10.54337/aau532690499

Publication date:
2023

Document Version
Publisher's PDF, also known as Version of record

MACHINE LEARNING SOLUTIONS FOR CONTEXT INFORMATION-AWARE BEAM MANAGEMENT IN MILLIMETER WAVE COMMUNICATIONS

BY
SAJAD REZAIE

DISSERTATION SUBMITTED 2023

AALBORG UNIVERSITY
DENMARK

Machine Learning Solutions for Context Information-aware Beam Management in Millimeter Wave Communications

Ph.D. Dissertation

Sajad Rezaie

Dissertation submitted February, 2023

Dissertation submitted:	February, 2023
PhD supervisor:	Assoc. Prof. Carles Navarro Manchón Aalborg University
Assistant PhD supervisor:	Prof. Elisabeth de Carvalho Aalborg University
PhD committee:	Associate Professor Wei Fan (chairman) Aalborg University, Denmark
	Professor Stephan ten Brink University of Stuttgart, Germany
	Professor Elza Erkip New York University, USA
PhD Series:	Technical Faculty of IT and Design, Aalborg University
Department:	Department of Electronic Systems

ISSN (online): 2446-1628
ISBN (online): 978-87-7573-737-6

Published by:
Aalborg University Press
Kroghstræde 3
DK – 9220 Aalborg Ø
Phone: +45 99407140
aauf@forlag.aau.dk
forlag.aau.dk

Printed in Denmark by Stibo Complete, 2023

Curriculum Vitae

Sajad Rezaie

Sajad Rezaie received the B.Sc. and M.Sc. degrees in Electrical Engineering from the Amirkabir University of Technology, Tehran, Iran, in 2013 and 2016, respectively. He joined the Wireless Communication Networks section at Aalborg University, Aalborg, Denmark as a Ph.D. fellow in 2019. Since August 2022, he has been with Nokia Corporation as a device research specialist in AI/ML area. His research interests include statistical signal processing for wireless communications, MIMO communications, mmWave communications, and machine learning applications in wireless communications.

Abstract

The millimeter wave (mmWave) band offers enormous bandwidth that is required for serving emerging services like virtual reality. Leveraging the angular sparsity of mmWave channels, directional beamforming is widely used to compensate for the higher path loss. A set of beams can be defined to make the beamforming task more tractable. To find the best transmitter and receiver beams for communication, an exhaustive search over all the beam pairs in the transceivers' codebooks provides good performance but at the cost of an unacceptable latency and overhead to the network. To achieve a solution that simultaneously satisfies the high-accuracy and also low-overhead requirements, extra information is needed to limit the beam search space.

Context information (CI)-aware beam management solutions have provided promising performance. We propose a location- and orientation-aware beam selection framework, which uses machine learning (ML) power for leveraging the CI. We propose several deep neural network (DNN) architectures for the ML model, which are suitable for different amounts of training samples due to including different numbers of trainable parameters. Evaluations with hand-held multi-panel devices reveal the usefulness of the terminal location and orientation for ML-enabled beam and panel selection, which provides certainty in the performance offered by the ML for more realistic configurations. In another study, the self-blockage impact on the context-aware beam selection approach is evaluated. Due to the strong relation between hand blockage effects and terminal orientation, context-aware methods can leverage the orientation information to recommend beams with the lowest possibility of blockage. Furthermore, we use the transfer learning technique to reduce the concern about the generalization and scalability aspects of context-aware ML-based solutions. In addition, this thesis proposes a novel device-agnostic beam selection framework that enables the use of a generic ML model for different device codebooks/antenna configurations

All in all, the findings of this thesis support that CI, in particular terminal position and orientation, has a great potential for more efficient mmWave beam alignment. Moreover, ML and, especially, DNNs seem to be the appropriate tool to extract the most out of the terminal position and orientation.

Resumé

Millimeterbølgebåndet (mmWave) tilbyder stor båndbredde, der er påkrævet for at levere nye tjenester såsom virtual reality. På grund af den rumlige filtrering af mmWave-kanaler, benyttes retningsbestemt stråleformning (beamforming) i vid udstrækning til at kompensere for det højere udbredelsestab. Et sæt af prædefinerede retninger, defineret i en codebook, kan gøre beamforming opgaven mere håndterbar. For at finde de bedste sender- og modtagerretninger til kommunikation, kan en udtømmende søgning over alle mulige prædefinerede retninger, defineret i transceiverens codebook, give en god ydeevne, men dog på bekostning af en uacceptabel høj latenstid og redundans i netværket. For at opnå en løsning, der samtidig opfylder kravene til høj nøjagtighed og lav redundans, er der behov for ekstra information for at begrænse søgerummet til bestemmelse af de bedste sender- og modtagerretninger.

Kontekstinformations (KI)-baseret beamforming har givet lovende resultater. Vi foreslår en placerings- og orienteringsbaseret beamforming løsning, som anvender maskinlæring (ML) til at udnytte kontekstinformationen. Vi foreslår flere dybe neurale netværksarkitekturer (DNN) til ML-modellen, som egner sig til forskellig grad af træning grundet variation i antallet af parametre der kan trænes. Evalueringer med håndholdte multi-antenne panelenheder, demonstrerer nyttevirkningen af kendskab til terminalens position og orientering for ML-baseret beamforming og panelvalg, hvilket taler for forbedring af ydeevnen med ML i mere realistiske konfigurationer. En anden undersøgelse har evalueret den signalmæssige blokering fra brugerens hånd på den kontekstbaserede beamforming. På grund af sammenhængen mellem håndblokeringseffekter og terminalorientering, kan kontekstbaserede metoder udnytte orienteringsinformationen til at anbefale retninger med lavest mulighed for blokering. Vi bruger transfer learning-teknikken til at reducere usikkerheden omkring generaliserings- og skalerbarhedsaspekterne af kontekst- og ML-baserede løsninger. Derudover foreslår denne afhandling en ny enhedsuafhængig beamforming metode, der muliggør brugen af en generisk ML-model til forskellige codebooks/antenne-konfigurationer.

Samlet set understøtter resultaterne i denne afhandling, at kontekstinformation, her især terminal-position og orientering, har et stort potentiale for mere effektiv mmWave beamforming. Desuden ser ML, og især DNN, ud til at være værktøjet til at få mest muligt ud af terminalens position og orientering.

Contents

Acknowledgements

First and foremost, I would like to show my appreciation and gratitude to my research supervisors, Assoc. Prof. Carles Navarro Manchón and Prof. Elisabeth de Carvalho. Without your guidance, suggestions, and support at every step throughout this journey, this thesis would have never been completed. Throughout this process, I have learned important lessons about problem definition, critical thinking, and learning.

I would like to thank Abolfazl Amiri for joining the supervision meetings and sharing his constructive comments and suggestions. I am also grateful to all the members of the Wireless Communication Networks section, for their help and support.

Special thanks go to Assist. Prof. Ahmed Alkhateeb at Arizona State University, USA for dedicating your time to our virtual collaboration and sharing great comments and suggestions on our articles. I would also like to thank João Morais for offering help and support in conducting research and publishing our findings.

I would like to extend my sincere thanks to Assoc. Prof. Wei Fan, Prof. Stephan ten Brink, and Prof. Elza Erkip for agreeing to be a part of the assessment committee and for dedicating their time to assess this dissertation.

I am also grateful to my family, especially my mom and dad, for their endless love and encouragement. Thank you for believing in me. I would also like to thank my remarkable friends for being the most supportive friends anyone could ask for.

I owe many thanks to my life partner, Anahita, to whom I dedicate this thesis, for encouraging me to pursue this PhD in the first place. At every step of my journey, your boundless love and support were invaluable, and your deep faith in my capabilities was appreciated.

Sajad Rezaie
Aalborg University, February 28, 2023

Part I

Introductory Chapters

Chapter 1

Introduction and Motivation

Over the last few decades, communication systems have changed humans' lives radically. Nowadays, it is hard to find applications that do not rely on communication networks and connectivity to the internet. Communication systems have always been designed to answer the current and future demands of various applications [6]. Virtual reality (VR) and augmented reality (AR), as two principal immersive technologies that bring imagination to people's lives, are at the center of market growth. VR has changed the gaming experience, efficient training of workers in industries, and safety training of firefighters and soldiers in dangerous situations [19, 25, 49]. Metaverse beyond a shadow of a doubt will continue to grow and spread to the consumer and global business markets. To facilitate a high-fidelity metaverse experience, the next generation of communication networks needs to provide reliable connections with higher data rates [27, 31, 44].

1 Beam Management in Millimeter Wave Communications

The demanded higher network capacity can only be catered for by allocating a large channel bandwidth. However, sub-6 GHz bands have already been occupied by several wireless technologies like WiFi, Bluetooth, and cellular communications 2nd generation (2G) to 5th generation (5G). It is inevitable to use other bands like millimeter wave (mmWave) bands that offer a continuous enormous unallocated bandwidth [8, 20]. However, higher propagation and penetration losses and lack of diffraction in mmWave frequencies make mmWave links susceptible to connection loss. Thus, it is necessary to design mmWave communication systems that are robust to blockage [26].

On the other hand, antenna size and inter-element separation in an an-

tenna array are proportional to the wavelength of the radio waves. Therefore, the smaller wavelength of mmWave frequencies offers the possibility of considering more antenna elements at transceivers. Thus, the higher propagation and penetration losses in mmWave bands compared to sub-6 GHz bands can be compensated using multiple-input multiple-output (MIMO) beamforming [14]. The array gain resulting from beamforming grants an adequate link budget to deploy a high throughput and reliable mmWave communication link. Even though directional beamforming compensates for the high path loss at mmWave frequencies, another challenge arises due to the difficulty of aligning the beam over the directions of the line-of-sight (LOS) or strong no-line-of-sight (NLOS) paths. As the number of antenna elements at transceivers grows, and narrower beams are used to reach higher beamforming gain, the problem of aligning the beams becomes more complex [13].

Fully digital beamforming architecture enables transceivers to transmit or sense multiple beams simultaneously. However, this architecture needs one radio frequency (RF)-chain for each antenna element, which causes high cost, power consumption, and implementation difficulties in practice [13, 21]. On the other hand, analog beamforming architecture uses analog phase shifters to align the beam towards different directions. Although only one beam can be configured at a time by analog beamforming, this architecture relies only on one RF-chain which makes it attractive for many applications. Hybrid analog-digital architecture is a trade-off between analog and digital implementations that makes simultaneous transmission or reception over several beams possible using several RF-chains [21, 42].

To make the beam alignment problem and the RF implementation more tractable, codebook-based beamforming is introduced. In this approach, a finite set of beamformer configurations is designed to provide sufficient array gain over different directions. Thus, the beam alignment problem can be cast as a selection problem from the codebook beams [47]. Although an exhaustive search over all the transceivers' beams finds the best beam pair for communication, it causes unacceptable overhead and latency to the wireless network [10, 13]. As an alternative, hierarchical beam search (HBS) uses a multi-stage search to reduce the beam alignment overhead. Initially, the search is operated over wide beams and narrows down towards the narrow beams pointing to the dominant path. However, the HBS method suffers from a low Signal-to-Noise Ratio (SNR) at the first stages with wide transmission and reception beams [48]. It is worth mentioning that a mistake in the first stages leads to a considerably different communication direction, i.e., the narrow beams probably point towards one of the NLOS paths [10, 13].

compressive sensing (CS)-based beam alignment is considered another avenue for reducing the overhead of mmWave beam selection. The angle-domain sparsity in mmWave communication is used for estimating the angle-of-departure (AOD) or angle-of-arrival (AOA) of the dominant path. The

main challenge of a CS-based beam alignment method is the recovery of information in different AODs/AOAs of a multi-path environment with a small number of beam measurements [2].

1.1 Beyond 5G Millimeter Wave Beam Alignment

Due to the growing demand for high-quality mmWave links, it is most likely that base stations and user terminals will include a large number of antenna elements. Consequently, transceivers support a large number of narrow beams, resulting in higher beamforming gains at the transceivers and better link quality. However, directional beams become narrower in the angular domain, which makes the link quality more vulnerable to blockage and beam misalignment. In addition, beam codebook size also scales with the number of antenna elements, making mmWave beam alignment more intractable to deal with. These expectations and requirements imply the need to consider either a larger number of beam measurements for beam selection, or much more "intelligent" beam management algorithms.

Beyond 5G systems need to use advanced technologies to overcome the upcoming challenges. context information (CI) like the user terminal's position and orientation, camera images, radio detection and ranging (RADAR) and light detection and ranging (LIDAR) signals, etc. can alleviate the need for a larger amount of beam measurements by providing other types of relevant information. Artificial intelligence (AI) and machine learning (ML) have caused a paradigm shift in image processing and natural language processing. Thus, ML is the right tool to combine CI and beam measurements in an "intelligent" manner. To address the complexities of mmWave beam management, ML-based solutions are proposed to optimize the beam alignment procedure using site-specific measurement data, especially in the absence of a need for a model of the channel or propagation properties of the environment.

1.2 Context Information Acquisition

Although context information can play a key role in beyond 5G systems, acquiring this information can be challenging. There is a common need for extra resources and sensors to acquire different types of CI, like camera images, LIDAR, RADAR, etc. As user location, user orientation, and out-of-band channel information have been used in the performance evaluations in this thesis, the possible ways of acquiring such information are explained here.

Ultra-wideband (UWB) positioning systems, global navigation satellite system (GNSS) signals, and inertial sensors on the device can provide an

estimation of the device position. Moreover, in 5G-advanced and 6th generation (6G) research and standardization, a joint communication, sensing and localization paradigm has been investigated that will enable accurate estimation of the user location [9, 35, 46]. Moreover, such information may be required for other applications, which yields the opportunity to exploit the information in beam management procedures. For example, reliable and safe autonomous mobile robot systems rely on accurate positioning in industrial environments, so measured robot positioning information can be reused in mmWave beam management.

Furthermore, inertial sensors like three dimensional (3D) accelerometers and 3D gyroscopes can provide device orientation information. These widely used and low-cost sensors deliver real-time orientation information in yaw, pitch, and roll. In addition, out-of-band channel information can be acquired by using dual communication modules on devices, one for mmWave communication and one for communication at another band, like sub-6 GHz bands. Several channel estimation techniques can be used to estimate the channel state information (CSI) between the transceivers in the sub-6 GHz band [5, 16].

All in all, CI can help to improve beam management efficiency, but it does not come for free. It is worth pointing out that accruing accurate CI is challenging, so inaccuracy in such information on the beam management efficiency needs to be evaluated. In addition, there is a valid concern that such information may harm user privacy.

2 Structure of the Thesis

With the above challenges and opportunities in mind, this thesis explores the capabilities of context information for mmWave beam alignment in the next generation of wireless and cellular networks. In this thesis, the focus is on the role of machine learning in leveraging context information for this task.

2.1 Organization and Notations

The rest of the thesis is organized as follows. The Chapter 2 presents the principal problem, the main challenges, and the research objectives, followed by the key research questions of the studies in this thesis. In Chapter 3, an overview of the system and channel models that are considered in the contributions made in the thesis are briefly described. Then, the beam selection procedure and the required signaling between the network nodes are explained, followed by an overview and background on the state-of-art in this area. Lastly, this chapter presents the contributions of this thesis from four perspectives: *ML Model Architecture*, *Performance*, *Robustness*, and *Gener-*

alization and Scalability. Chapter 4 completes the introductory part by summarizing the main takeaways from the studies of this thesis in the format of answering the raised research questions in Chapter 2. In the end, Part II provides a collection of the publications that compose this thesis.

In this thesis, the fields of real and complex numbers are denoted, respectively, as $\mathbb{R}$ and $\mathbb{C}$. A set is defined as $\mathcal{A}$ with the cardinality of $|\mathcal{A}|$. We use a, $\boldsymbol{a}$, and $\boldsymbol{A}$ respectively for a scalar, a vector, and a matrix. Also, a_i and $A_{i,j}$ are used for the ith entry of the vector $\boldsymbol{a}$ and the entry in the ith row and jth column of the matrix $\boldsymbol{A}$, respectively. In addition, $(\cdot)^T$ and $(\cdot)^H$ represent, respectively, the transposition and complex transposition of vectors and matrices. $\arg\max_{i,j} A_{i,j}$ results in a tuple with the row and column indices of the maximum entry of matrix $\boldsymbol{A}$. Also, $\arg\operatorname{sort}_{i,j} A_{i,j}$ results in a list of tuples including the row and column indices of the sorted entries of matrix $\boldsymbol{A}$ in descending order. Moreover, $\mathcal{CN}(0, \sigma_n^2)$ denotes a zero-mean complex Gaussian random variable with variance σ_n^2. Lastly, $\otimes$ denotes the Kronecker product.

Chapter 2

Problem Statement

Following the broad background introduced in the previous chapter, we are now in a position to state the principal problem that this thesis aims to address.

Ultra-high data-rate mmWave communication links are required to serve emerging applications. To offer the best user experience, these applications demand a high reliability and low latency connection. The current beam management technologies using in-band measurements cannot fulfill the requirement. Therefore, these ambitious goals require a novel approach to make mmWave beam alignment reliable, efficient in beam sensing, and robust to blockage.

Naturally, questions may arise about the performance of the current technologies and why they cannot fulfill the forthcoming requirements. Looking deeper into the existing 5G beam management, we find a flexible procedure for beam training. The transceivers may use an exhaustive search over all the beam pairs to find the best beam pair for communication. Although the exhaustive search approach provides the best accuracy and reliability, it burdens high latency and overhead to the network, particularly for a large number of beam pair combinations. In addition, the beam measurements may be outdated at the time of beam selection due to the channel coherence time, user device rotation and mobility, etc. Furthermore, the transceivers may use a hierarchical beam sensing scheme, where the beam search space is reduced by sensing with wide beams at the initial stages of the hierarchical search. Although the hierarchical search imposes moderately low latency and overhead to the network, it suffers from low SNR and subsequently, a high probability of error in the first search stages, particularly for cell edge users [13, 15, 24].

However, the fundamental challenge arises when we are interested in one solution fulfilling all the requirements simultaneously. This challenge is mainly due to the inherent trade-offs between reliability and latency of

selecting the most profitable option among a set. An identified solution approach to this trade-off is to provide more information on the beam selection problem, which helps to reduce the beam search space [13].

Context information can play an important role in reducing the search space in finding the optimal communication beam pair. Such knowledge can add extra value to the existing beam management procedures by pruning irrelevant beams out of the search space for a specific user or environment condition [12, 13].

Furthermore, the history of beam alignment in an environment can be used to relax the problem for future users. In addition, the collected historical data hold information about blockers in the surroundings that can be exploited to propose a reliable and robust beam alignment solution [23, 45]. As this information is site-specific, it needs data collection in the deployed environment and data-driven algorithms for processing. This thesis is focused on currently trending machine learning algorithms as the most promising approach for data-driven discovery of dynamics. Accordingly, the main research objective of the thesis is to propose ML-based methods to exploit CI in mmWave networks that can result in accurate and fast beam management frameworks.

1 Research Questions

After stating the research problem, grand challenges, and research objectives in the preceding section, it is time to formulate the principal research questions of this thesis.

I Can the latency and accuracy of beam management operations be significantly improved by using of CI? And, in that case, which types of CI are the most promising/advantageous?

II Are ML methods suitable to formulate CI-aware beam management solutions? And to which extent can they outperform traditional probabilistic methods and context-unaware solutions?

III How sensitive are potential ML-enabled beam alignment methods to the size of historical datasets? How can we reduce this sensitivity?

IV Can CI still be helpful in a multi-panel antenna placement with more realistic antenna radiation patterns?

V Is it feasible to come up with a generic ML model that is able to serve devices with different beam codebooks?

2 Methodology

Several tools have been used in the development of the articles forming this thesis. These tools can be generally classified into ray-tracing and simulation programming categories. A simple two dimensional (2D) ray tracing software has been developed in Python to conduct initial evaluations. In addition, Altair Feko-Winprop software [1] as a professional 3D ray-tracing tool, and DeepMIMO datasets [4] based on the accurate Remcom 3D ray-tracing have been used to simulate 3D scenarios with more details and objects in the environment. Besides, constructing the channel responses based on the ray tracing results, simulation of beamforming with the beam codebooks, and performance evaluation have been conducted in Python and MATLAB. Most of the proposed ML models are trained in Python with Keras and TensorFlow backend.

In the experiments of individual contributions, modeling of the systems' dynamics relied mainly on the Monte-Carlo approach for simulations. Particularly, in the scenario definition phase, several sources of randomness have been considered including the position and density of mobile scatters in an environment, a statistical channel blockage model, and the addition of white Gaussian noise to the received signals.

Since conducting the simulations involved several difficulties, the author of this thesis would like to take this opportunity to raise awareness about the major technical challenges. Although ray-tracing tools provide accurate information about the channel, they suffer from too much determinism. By repeating an experiment while the environment is fixed, we measure exactly the same received signal for a specific position. This is due to the lack of randomness in the ray-tracing approach, which emphasizes the need for mobile objects in the environment or applying a form of statistical blockage model to provide some randomness in the channel responses. Another challenge was to consider a multi-panel device with arbitrary position and orientation. This challenge was addressed by conducting ray-tracing simulations for each device panel, while the other factors in the environment were kept fixed.

In all the contributions presented in Part II, service-related key performance indicators (KPIs) were defined as a set of metrics to reflect the level of confidence, latency, and operational performance of the proposed beam alignment solutions. Furthermore, relevant benchmark techniques have been used for comparison with the proposed methods and frameworks.

2.1 Scope of the Thesis

It is time to clearly define the scope and assumptions of this thesis. We consider that the required context information for the beam management procedure is obtained by some of the means described in Chapter 1. Thus, the

evaluation of the cost incurred in acquiring such information and the potential privacy concerns are out of scope of this study. Also, in all the contributions made in this thesis, we consider a single-user MIMO mmWave system where one access point serves the user. In all the papers except paper F, we assume the context information is invariant during the beam sensing phase. In addition, analog or hybrid digital-analog structures have been used for creating user beam codebooks, where each device panel is connected to one RF-chain. We leave the fully digital and the fully-connected hybrid analog-digital schemes, where several RF-chains are connected to each device panel, out of the scope of this research. As assumed in many similar state-of-art investigations, discrete Fourier transform (DFT)-based codebooks were considered in the contributions of the thesis, and designing a codebook for each specific configuration and condition is out of scope of this thesis. While the effect of thermal noise is of course included in the mmWave channel, e.g. when modeling beam measurements, the exchange of control information between the involved transceivers is ideally assumed to be error-free.

Chapter 3

Millimeter Wave Beam Selection using Machine Learning

This chapter presents the main contributions made in this thesis, the opportunities offered by machine learning to respond to the expected demands of future communication systems, and the challenges on the way towards machine learning in mmWave beam alignment. First, a general system model is introduced to make it easy to follow the subsequent discussions in this chapter. Then, a brief overview of the mmWave beam selection procedure is provided. In the end, different aspects of the ML-based beam selection approach are discussed and analyzed.

1 System Model

Consider a downlink mmWave link with a fixed access point (AP) and a moving user terminal (UT). Figure 3.1 shows the vanilla version of the considered system model, where the objects in the environment may reflect or block some of the transmitted paths. While the AP is made of single antenna panel, the UT is composed of one or multiple antenna panels. Each AP or UT panel is equipped with a uniform linear array (ULA) or a uniform planar array (UPA). The received signal at the pth UT panel, $y^{(p)}$, may be written as

$$y^{(p)} = \sqrt{P_{\text{AP}}}\boldsymbol{v}^{(p)^H}\boldsymbol{H}^{(p)}\boldsymbol{u}s + \boldsymbol{v}^{(p)^H}\boldsymbol{n}^{(p)} \tag{3.1}$$

where s, P_{AP}, and $\boldsymbol{H}^{(p)}$ denote, respectively, the transmitted symbol with unit-power, the transmission power at the AP, and the channel matrix be-

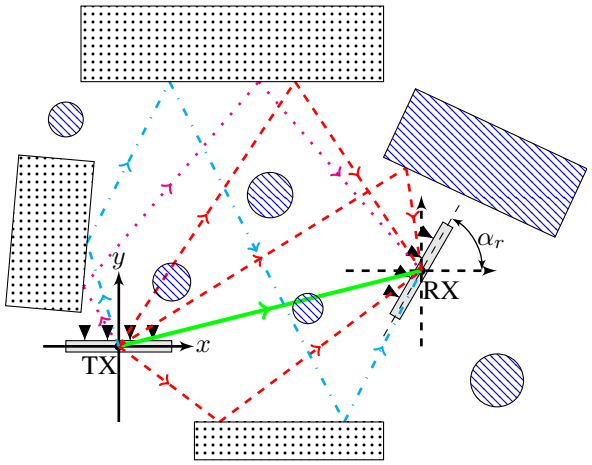

Fig. 3.1: An example of the considered mmWave system model consisting of several static and mobile objects that may impact the communication paths [37].

tween the AP and the pth UT panel. $\boldsymbol{u}$ and $\boldsymbol{v}^{(p)}$ are the beamforming vectors at the AP and pth UT panel, respectively. Also, $\boldsymbol{n}^{(p)}$ denotes a complex Gaussian noise vector with i.i.d $\mathcal{CN}(0, \sigma_n^2)$ components representing the thermal noise contribution.

A global coordinate system (GCS) can be considered for the environment, and the AP and UT placement, i.e., like their position and orientation, are defined in the GCS. For the sake of simplicity in analysis and modeling the transmission process, a local coordinate system (LCS) is considered for each network node, so that incidence angles of multipath components and beam steering directions can be defined with respect to the AP and UT LCSs.

Constructing the channel matrix between the AP and UT panels needs the results from the ray-tracing tools for all the panels. These results include AOD, AOA, and path gains for all the paths between the AP and UT panels. In case of considering non-isotropic antenna elements, the antenna radiation pattern shapes the channel matrix.

The studies in this thesis consider a sparse multipath narrow-band channel between the AP and each UT panel, $\boldsymbol{H} \in \mathbb{C}^{N_{\text{UT}}^{(p)} \times N_{\text{AP}}}$, where $N_{\text{UT}}^{(p)}$ and N_{AP} respectively denote the number of antenna elements in the UT panel and the AP. The contributions of L paths that make up the channel can be expressed as

$$\boldsymbol{H} = \sum_{l=1}^{L} \sqrt{\rho_l}\, e^{j\vartheta_l}\, \boldsymbol{a}_{\text{UT}}(\phi_l, \theta_l)\, \boldsymbol{a}_{\text{AP}}^{H}(\psi_l, \omega_l) \tag{3.2}$$

where ρ_l and ϑ_l denote the power and phase of the lth received path, respectively. In addition, $\phi_l^{(p)}$ and $\theta_l^{(p)}$ denote the azimuth and elevation AOD of

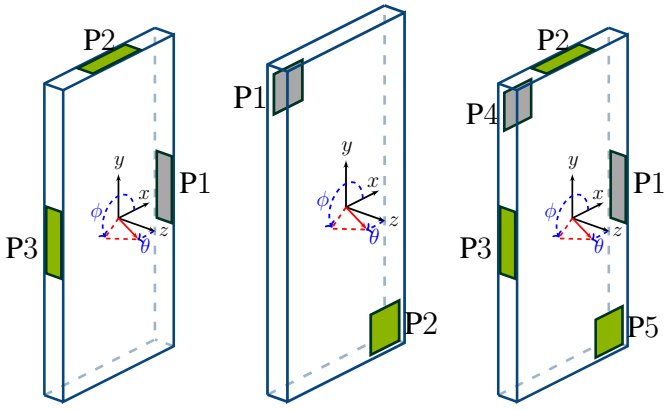

(a) Edge design **(b)** Face design **(c)** Edge-face design

Fig. 3.2: The three considered antenna placement designs in the contributions (a) edge (E) placement design including 3 ULAs placed on the device's edges (b) face (F) placement design including 2 UPAs placed on the device's face and back (c) edge-face (EF) placement design including 5 panels [38]. The designs are inspired from [33]

the lth path in the AP LCS. Likewise, $\psi_l^{(p)}$ and $\omega_l^{(p)}$ can be defined for the azimuth and elevation AOA of the lth path in the UT LCS. Also, the antenna steering vector of the UT panel and the AP are represented as $\boldsymbol{a}_{\mathrm{UT}}$ and $\boldsymbol{a}_{\mathrm{AP}}$.

In all the contributions in this thesis, analog phased antenna arrays are considered for the AP and UT, where the signal phase of each array element can be regulated. Analog phase shifters, as electronically controlled passive devices, are the key elements in the realization of analog phased arrays. To make the simulations more realistic, multi-panel devices are considered in some of the contributions. Fig. 3.2 shows the three considered antenna placement designs for the multi-panel devices. In case of presence of multiple panels at a node, for the sake of simplicity, multi-panel beamforming is not considered in this thesis. Thus, a single-panel AP codebook is made of N_{AP} beamforming vectors $\boldsymbol{\mathcal{U}} = \{\boldsymbol{u}_1, \ldots, \boldsymbol{u}_{N_{\mathrm{AP}}}\}$. Also, the pth UT panel codebook is a set of $N_{\mathrm{UT}}^{(p)}$ beams, i.e., $\boldsymbol{\mathcal{V}}^p = \{\boldsymbol{v}_1^p, \ldots, \boldsymbol{v}_{N_{\mathrm{UT}}^{(p)}}^p\}$. The UT beam codebook, $\boldsymbol{\mathcal{V}} = \{\boldsymbol{v}_1, \ldots, \boldsymbol{v}_{N_{\mathrm{UT}}}\}$, can be formed by unioning all the UT panel codebooks with N_{UT} combiners. A set $\mathcal{B}$ of beam pairs can also be defined by including the indices of all possible combinations of AP beamformers and UT combiners.

2 Millimeter Wave Beam Selection Procedure

Employing the beamforming vectors $\boldsymbol{u}_i$ and $\boldsymbol{v}_j$, respectively, at the AP and UT results in the received signal strength (RSS) as

$$R_{i,j} = \left| \sqrt{P_{\text{AP}}} \boldsymbol{v}_j^H \boldsymbol{H}^{(p_j)} \boldsymbol{u}_i s + \boldsymbol{v}_j^H \boldsymbol{n} \right|^2 \tag{3.3}$$

where p_j is the panel index corresponding to the beamforming vector $\boldsymbol{v}_j$. The beam alignment process aims to find the beam pair that maximizes the RSS, i.e.,

$$i^\star, j^\star = \underset{(i,j)\in\mathcal{B}}{\arg\max}\, E[R_{i,j}] \tag{3.4}$$

where $E[R_{i,j}]$ denotes the expectation of $R_{i,j}$ taken with respect to the noise vector $\boldsymbol{n}$.

In the exhaustive beam search method, all the combinations of the AP beamformers and the UT combiners in set $\mathcal{B}$ are sensed in the environment to identify the optimal beam pair for communication. After sensing all the beam pairs, the UT feeds back the index of the optimal beam pair to the AP. The optimal communication beam pair naturally depends on the environment geometry, however, it also depends on the AP and UT conditions like their locations and orientations. These dependencies make the beam alignment process even more challenging. Although an exhaustive search may find the optimal or appropriate beam pair, sensing all the beam pairs in set $\mathcal{B}$ delivers undesirable latency and overhead. Since the latency increases with the number of beams used at the transceivers, exhaustive search becomes infeasible with increasing number of antennas and increasingly narrower beams, as expected in beyond 5G systems.

Hierarchical beam search (HBS) uses a coarse-to-fine strategy, which reduces the overhead of the beam alignment process significantly. In the first stage of the search, a set of wide beams is considered to carry UT a coarse beam selection. Towards the final stage, the beam width of the candidate beams gradually decreases. The best beam index of a search stage is passed to the next stage, which is necessary for specifying the beam candidates for sensing. Thus, it leads to the need for several feedback messages from the UT to the AP. Although sensing with wider beams helps to discard a significant portion of the search space, decision-making in the first stages are susceptible to error, particularly in a rich multi-path environment or a low SNR. Also, a mistake in the first stages leads to a different search path than the optimal search path, which results in pointing toward the non-strongest path at the final search stage.

In case of availability of CI at the network nodes, the information can be used to reduce the beam search space. A probabilistic or ML-based recommender processes the CI and proposes a list of candidate beam pairs for

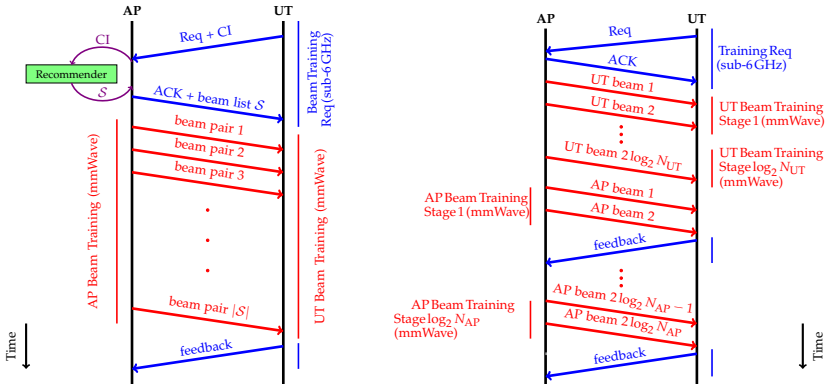

(a) CI-aware beam selection **(b)** Hierarchical beam search

Fig. 3.3: The considered mmWave beam sensing procedures (a) context-aware beam selection, (b) hierarchical beam search [36].

sensing, $\mathcal{S} \subset \mathcal{B}$. The cardinality of the candidate beam list determines the latency and overhead of the beam selection procedure and thus generally $|\mathcal{S}| \ll |\mathcal{B}|$. On the other hand, one would expect that a larger candidate set increases the probability of including the optimal communication beam pair, $(i^\star, j^\star)$, in set $\mathcal{S}$. The recommender exploits the CI and potential historical beamforming information in the environment to propose a beam candidate list which minimizes the misalignment probability, i.e.,

$$\begin{aligned} \min_{\mathcal{S}} \quad & \mathbb{P}\left[\max_{(t,w)\in\mathcal{S}} R_{t,w} < \max_{(i,j)\in\mathcal{B}} R_{i,j}\right], \\ \text{s.t.} \quad & |\mathcal{S}| = C \end{aligned} \tag{3.5}$$

where C is a pre-determined constant that indicates the number of beam pairs in the proposed set $\mathcal{S}$. The recommended beam pairs need to be shared with the other network node, then those beam pairs are sensed in the environment. The UT selects the beam pair with highest RSS and shares its index with the AP. Figure 3.3 shows the beam selection procedure including the mmWave sensing and sub-6 GHz signaling for the CI-aware beam selection and HBS methods.

2.1 Dataset structure and construction

In the CI-aware beam selection approach, the recommender may utilize historical beamforming information in the deployed environment. In this case, it is required to collect samples with different realizations of the environment. Representing the collected dataset as $\mathbb{D}^{\Xi} = \{(\boldsymbol{CI}_m, \mathcal{T}_m)\}, m = 1, \cdots, N^{\Xi}$ with

N^{Ξ} samples, the mth dataset sample includes the measured CI of the corresponding realization, $\boldsymbol{CI}_m$. Also, each sample comprises information about the best communication beams, which can be found through an exhaustive search in the data collection phase. Thus, the beam pairs providing the highest M RSSs are identified, i.e.,

$$\boldsymbol{r} = \underset{i,j}{\arg\,\mathrm{sort}}\,(R_{i,j}), \tag{3.6a}$$

$$\mathcal{T} = \{r_k | k = 1, \ldots, M\}, \tag{3.6b}$$

where $\mathcal{T}$ contains the indices of the best pairs. In case of $M = 1$, only the optimal beamforming vectors $(i^\star, j^\star)$ are recorded for each sample.

3 Machine Learning in Millimeter Wave Beam Selection: Challenges and Opportunities

First, the applications of ML in mmWave beam alignment is briefly explained. ML has played a key role in the development of CI-unaware and CI-aware beam alignment methods. Note that many of the relevant SoA studies were published concurrently with my PhD project.

3.1 Background

ML has been explored to learn the AOD or AOA of the dominant path based on compressed sensing mechanisms. The learned AOD/AOA can be further processed to predict communication beams. On the other hand, the AOD/AOD and power of the dominant path for different users can be estimated using traditional methods, then an ML-based multi-user beam selection processes these estimates and predicts beams for all the users [7, 41]. Although these methods achieve remarkable results in estimating AOA/AOD in a single-path channel, they are susceptible to significant performance degradation in multipath propagation environments. Also, researchers have explored the capabilities of ML models in inferring AOA by exploiting the unique patterns in the in-phase-quadrature representation of the waveform of each beam [32]. Reinforcement learning (RL) [43], another machine learning training approach, has been applied to the mmWave beam alignment problem to overcome the need for ground truth in the supervised learning approach. In a specific environment, an RL model has the capability to learn the optimal beam for communication from the historical beam alignment data, which consequently reduces the beam training overhead [39]. However, an RL model needs a considerable number of interactions with the environment to learn the optimal policy [52].

Beam selection using CI has also been considered as another avenue that may improve the accuracy and latency of beam management. Several methods are proposed to use user location, device orientation, or radar information as CI in beam prediction algorithms. Authors in [45] introduced an inverse-fingerprinting (IFP) approach that proposes a beam candidate list considering the history of beam alignment at the neighborhood of the device location. In addition, RADAR signals can be used to estimate AOAs and AODs, and subsequently configure the beams [17].

Because of the high complexity of exploiting CI in beam alignment, particularly in NLOS scenarios with mobile scatters, ML has been widely used to extract useful information for beam alignment. ML models learn how to map the available CI to the optimal communication beam from training data. For example, several ML-enabled methods have been proposed for vehicle-to-everything (V2X) mmWave beam alignment using LIDAR signals, camera images, and out-of-band channel information [5, 11, 51].

Considering more antenna elements and beams at devices makes device rotation a grand challenge for beam alignment beyond 5G systems. In some scenarios like gaming, the device orientation can change very fast, which can cause beam and consequently connection loss [18, 22, 50]. Due to the codebook design and hardware imperfections, the device beams usually have unequal beam widths, which makes device beam alignment more susceptible to failure because of device rotation [28]. However, the mentioned ML-based methods are mostly proposed for the V2X application, where the antenna array orientation is usually inferable from the vehicle position. Therefore, several methods have been proposed to consider user terminal orientation in the beam management procedure. As the measurements by the device are affected by the terminal rotation, the methods take this effect into account in the beam management procedure [3, 30].

Due to the smaller wavelength and higher penetration loss in mmWave bands compared to sub-6 GHz bands, there is more space and need for several panels at mmWave-enabled devices. Beyond 5G systems needs to provide beam management solutions that consider the limitations and opportunities of multi-panel antenna placement design in the beam sensing designs [24, 40]. To mitigate the effects of hand and body blockage on mmWave beamforming, future technologies need to adapt not only the beam management procedures but also the beam codebook design to the properties of mmWave communications [29, 34].

3.2 Summary of Contributions

This section presents the thesis's main contributions and proposals about the application of ML in mmWave beam selection. Within this PhD research, the following scientific papers on the topic ML-enabled mmWave beam selection

have been produced:

- **Paper A**: Sajad Rezaie, Carles Navarro Manchón, and Elisabeth De Carvalho, "Location- and Orientation-Aided Millimeter Wave Beam Selection Using Deep Learning," *ICC 2020 - 2020 IEEE International Conference on Communications (ICC)*, 2020, pp. 1–6.(published)
- **Paper B**: Sajad Rezaie, Abolfazl Amiri, Elisabeth de Carvalho, and Carles Navarro Manchón, "Deep Transfer Learning for Location-aware Millimeter Wave Beam Selection," in *IEEE Communications Letters*, vol. 25, no. 9, pp. 2963–2967, Sept. 2021.(published)
- **Paper C**: Sajad Rezaie, Elisabeth de Carvalho, and Carles Navarro Manchón, "A Deep Learning Approach to Location- and Orientation-aided 3D Beam Selection for mmWave Communications," in *IEEE Transactions on Wireless Communications*, vol. 21, no. 12, pp. 11110–11124, Dec. 2022.(published)
- **Paper D**: Sajad Rezaie, João Morais, Elisabeth de Carvalho, Ahmed Alkhateeb, and Carles Navarro Manchón, "Location- and Orientation-aware Millimeter Wave Beam Selection for Multi-Panel Antenna Devices," 2022 IEEE Global Communications Conference (GLOBECOM), 2022, pp. 597–602. (Published)
- **Paper E**: Sajad Rezaie, João Morais, Ahmed Alkhateeb, and Carles Navarro Manchón, "Device-Agnostic Millimeter Wave Beam Selection using Machine Learning," *IEEE Transactions on Wireless Communications*, Nov. 2022. (submitted)
- **Paper F**: Filipa Fernandes, Sajad Rezaie, Christian Rom, Johannes Harrebek, and Carles Navarro Manchón, "Machine Learning-based Millimeter Wave Beam Management for Dynamic Terminal Orientation," 2023 IEEE 97th Vehicular Technology Conference: (VTC2023-Spring), 2023. (submitted)
- **Paper G**: Sajad Rezaie, João Morais, Ahmed Alkhateeb, and Carles Navarro Manchón, "Context-aware Machine Learning-based Beam Selection with Multi-Panel Devices in the Presence of Self-Blockage," *IEEE Transactions on Machine Learning in Communications and Networking*, 2023. (submitted)

These papers have discussed the following areas: (a) ML model **architecture** and how the context-aware beam selection task can be formulated as a classification problem, (b) **performance** of the proposed context-aware ML-enabled solutions in different scenarios/conditions, (c) **robustness** of the context-aware solutions to mismatch in the training and test conditions and also

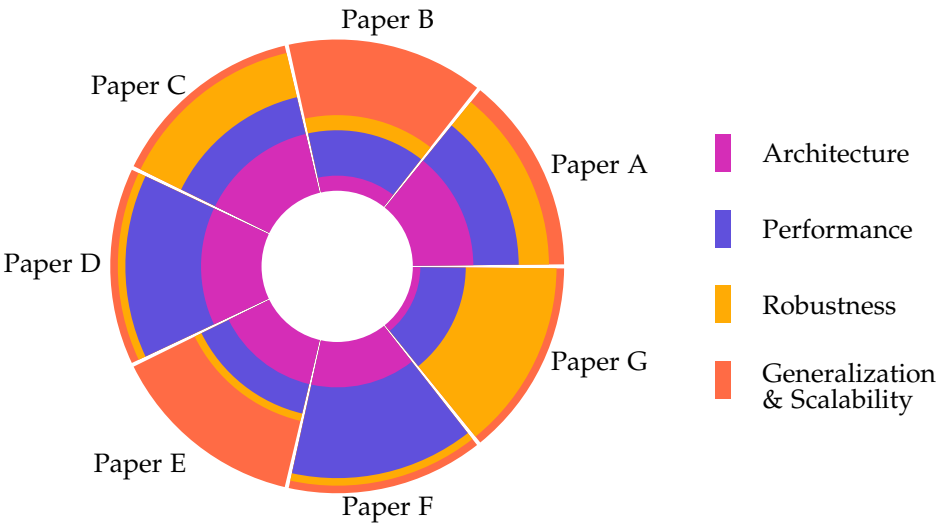

Fig. 3.4: Outline of the contributions made in this thesis.

inaccuracy in the CI, and (d) **generalization and scalability** of ML-based beam selection solutions with respect to different scenarios and configurations. Figure 3.4 depicts the main contribution areas of the papers, where the thickness of each of the sectors is roughly proportional to how much of the contribution in the corresponding paper belongs to the specific area. In the following, the notable aspects and challenges of the ML-based approach are discussed.

3.3 ML Model Architecture

Deep neural networks (DNNs) have shown excellent performance in many areas such as computer vision and natural language processing (NLP). Therefore, we have also considered DNNs as the core of the proposed ML-based beam selection frameworks. As the selection process is aligned with the classification scheme of DNNs, the considered DNN models are trained as classifiers. Thus, the objective of the DNN models are to classify the fed CI correctly to the right class corresponding to the optimal beam pair. In this thesis, various ML model architectures are introduced, where the architectures are tailored to the specific properties of different antenna placement configurations and use case properties.

Paper A proposes a feedforward neural network (FNN) structure that exploits the device orientation and location for mmWave beam pair selection. As this structure directly maps the 2D location and orientation information to the transceivers beam pairs, it is named as *single-task (ST)* structure. In

paper C, this structure extended to location- and orientation-aware 3D beamforming architecture which proposes beam pairs for transceivers with UPAs.

Paper C also introduces the *multi-task (MT)* architecture, where the DNN predicts two separate sets of outputs, which represent the optimality probability of the AP and UT beams. The MT DNN is followed by an outer product block that provides the optimality probabilities for the beam pairs. It is worth pointing out that the outer product block does not include any trainable parameters. Although the simplifying assumption in the outer product unit leads to performance loss and degradation, it significantly reduces the number of trainable parameters compared to the ST DNN architecture. The fewer trainable parameters in the MT DNN results in performance enhancement than the ST DNN architecture in training datasets of limited size. To scale down, even more, the number of trainable variables, the separation idea can be extended to separate beamforming in the horizontal (azimuth) and vertical (elevation) directions at the AP and UT. Thus, the extended multi-task (EMT) architecture, as an extended version of MT DNN, works well on tiny training datasets.

Paper D introduces multi-network beam selection (MN-BS) architecture that considers sequential optimality beam prediction for the AP and UT. The first network aims to select the optimal transmission beam for the AP, and the second network predicts the optimality probability for the UT beams conditional to the selected AP beam by the first network. This architecture may result in fewer trainable parameters compared to the ST structure, while, at the same time, overcoming the simplifying assumption of separability of transmit and receive beamforming used in the MT structures. Moreover, Paper D proposes multi-network panel selection (MN-PS) architecture, which is specialized for multi-panel UTs. The main difference between the MN-PS and MN-BS architectures is the role of the second network, where the MN-PS second network aims to select UT panels instead of UT beams.

Even though all the proposed architectures enable the ML-beam selection framework, they all suffer from dependency on the UT hardware and beam codebook. Therefore, Paper E proposes a device-agnostic beam selection framework, which includes a generic network and a post-processing unit. The generic network predicts the optimal AP beam - UT direction to set up a link between the network nodes. A discretized direction space is considered to limit the number of neurons as the output of the generic network. The non-trainable post-processing unit maps the AP beams - UT directions to the AP - UT beam pairs. This mapping needs information about the beam with the highest array gain at the discretized directions. For an unseen UT device, the device-agnostic framework provides almost the same performance as the device-specific architectures trained specifically for the UT device.

3.4 Performance

Paper A shows the performance of an ML-based beam selection framework with the ST structure. The results confirm that the proposed ML-based framework outperforms the generalized inverse-fingerprinting (GIFP) method as a data-driven lookup table approach. An experiment on various mobile object densities reveals the capabilities of the proposed beam selection framework in recommending beams over the direction of the LOS or strong NLOS paths in scenarios with high blockage probability. However, the performance gain of the ML-based approach over the GIFP method reduces with the decrease in training dataset size.

Thanks to the MT and EMT architectures, paper C presents that the ML-based beam selection significantly outperforms the GIFP method even at tiny training datasets. Moreover, the proposed framework not only outperforms the HBS method but also reduces the beam alignment overhead and latency several times. Another experiment was conducted to assess the benefits of marking M best beam pairs during the training process on different ML structures. The experiment result shows more performance gain in using the multi-label technique for the ST architecture than the MT and EMT ones. Due to the simplifying assumption in providing the beam pair optimality probabilities from the MT and EMT networks, there is a performance loss compared to the ST architecture with large enough training datasets.

The numerical evaluations in Paper D show no performance loss with the MN-BS architecture than the ST structure with large training datasets. Also, the former architecture provides performance gain compared to the latter architecture. Moreover, using more than one RF-chain at the device does not help the well-trained ML models with large training datasets. The MN-PS architecture also provides acceptable performance in limited training dataset sizes.

Paper F shows the results for mmWave beam selection in scenarios with time-varying terminal orientation during the beam sensing procedure. A ST DNN architecture is considered in this study, which processes the reference signal received power (RSRP) values measured with different UT orientations than the UT orientation at the prediction time. It is important to note that the UT orientation is not fed to the ML-based framework. With 3rd generation partnership project (3GPP) compliant channel models and simulator, the proposed framework provides performance gain over the traditional beam selection method, which does not take the UT rotation into account in the beam selection process. Although the proposed ML-based framework provides significant gains at various user speeds in the free space and urban Micro (UMi) LOS scenarios, the framework's effectiveness deteriorates in the considered UMi NLOS environment.

Paper G evaluates the self-blockage impact on the mmWave link perfor-

mance with ideal beamforming and on the practical beam alignment methods using DNN and GIFP. Evaluations with different types of user-induced blockage models show that the location- and orientation-aware ML-based solutions can provide excellent performance in the presence of self-blockage.

3.5 Robustness

It is important to evaluate the performance of beam selection methods when the deployment scenario/configuration is different from the designed scenario/configuration. Paper A represents the results of ST DNN-based and GIFP frameworks when there is a mismatch in the train and test density of mobile scatters. Thanks to the large degree of randomness in UT location and orientation in training datasets, both the ML-based and GIFP methods show high robustness to the density of mobile objects and, consequently, blockage probability.

Paper C evaluates the robustness of the CI-based beam selection methods to inaccuracies in location and orientation information. Different ML architectures indicate higher robustness than the GIFP method to noisy CI. Moreover, the ST architecture provides the least sensitivity to inaccuracies in UT location and orientation information. This robustness seems to be rooted in better training of the ST architecture in dealing with uncertainties in the CI.

Paper G presents the results of the self-blockage impact on the context-aware beam selection solutions with deterministic and probabilistic hand grip schemes. The most interesting takeaway from the evidence shown in the paper is that the ML recommender can, with sufficient data, infer the patterns of blockage that are most prominent in different terminal orientations and can then adapt its recommended list of beam pairs to mitigate the blockage effects. This can be noticed when inspecting the distribution of the amount of different panels that are measured for a given recommendation: while in conditions without blockage, the recommender tends to focus its beam recommendations in just one or two panels, under blockage conditions the recommended list includes beams typically distributed over almost all panels. Such diversification leads then to a list of recommended beam pairs that is robust against user-induced blockage, at the expense of only a minor degradation in the performance of the beam alignment procedure.

3.6 Generalization and Scalability

ML-enabled beam selection approach offers novel opportunities for reducing the beam alignment overhead and latency while providing high beam alignment accuracy in using the optimal communication beam pair. However, ML models need large datasets to be trained to achieve high accuracy. The dataset

requirement results in high deployment time and cost, which makes the ML-based approach less attractive. To reduce the data collection burden, Paper B recommends using the transfer learning (TL) technique in CI-based beam selection. The TL idea is to reuse part of the learned knowledge by a trained DNN for a specific scenario/configuration in the training process of another DNN for a different scenario/configuration. The numerical results presented in Paper B show that reusing the trained weights of a trained DNN in the source environment can significantly reduce the required fine-tuning dataset for training a DNN in the target environment. In addition, transferring the weights of the trained model A for antenna configuration A to model B for another antenna configuration provides performance gain compared to the case when model B is trained from scratch. Moreover, freezing some layers of the DNN after weight transfer reduces the number of trainable parameters, which leads to performance improvement with tiny fine-tuning datasets at target scenarios/configurations.

Although the TL technique reduces the dataset requirements, a fine-tuning dataset still needs to be collected. The device-agnostic beam selection framework in Paper E solves the problem for serving different UTs. Thus, the generic network of this framework can serve various UTs even with unseen antenna configuration in the training dataset. In addition, the device-agnostic framework can be trained with a dataset measured by UTs with different antenna configurations/codebooks, which substantially reduces the data collection burden. Since we are talking about generalizations, it is worth highlighting the fact that the proposed device-agnostic framework has been tested with different types of CI: location/orientation, and out-of-band (sub-6 GHz) channel measurements.

Chapter 4

Conclusions and Remarks

This chapter includes a synopsis of the contributions made in this thesis and how they provide solutions for the main problem and answer the research questions raised in Chapter 2. Thereafter, an overview and perspectives for future research directions are outlined. For the reader's convenience, the research questions are re-stated here.

I Can the latency and accuracy of beam management operations be significantly improved by using of CI? And, in that case, which types of CI are the most promising/advantageous?

II Are ML methods suitable to formulate CI-aware beam management solutions? And to which extent can they outperform traditional probabilistic methods and context-unaware solutions?

III How sensitive are potential ML-enabled beam alignment methods to the size of historical datasets? How can we reduce this sensitivity?

IV Can CI still be helpful in a multi-panel antenna placement with more realistic antenna radiation patterns?

V Is it feasible to come up with a generic ML model that is able to serve devices with different beam codebooks?

1 Conclusions

The contributions presented in this thesis shed light on the capabilities of ML in CI-aware beam management in deploying a fast and reliable mmWave communication link between transceivers with large antenna arrays. Also, the potential benefits and challenges of ML-based approach are discussed.

Although, in most of the contributions, UT location and orientation were considered as the CI, the conclusions and challenges of using ML in the framework of beam management are potentially generalizable to other types of CI. As an example, Paper E shows that the proposed method and conclusions are extendable to the beam selection problem with Sub-6 GHz channel response as the CI.

In response to the first research question, our studies showed a significant gain in using CI in the mmWave beam management problem. The extra information results in fast and reliable initial access in mmWave networks. Although the vehicle's position is the most common CI for beam alignment in V2X applications, our findings reveal that the device location and orientation are two beneficial sources of CI for phased-array based hand-held or wearable devices. In all the contributions in this thesis, it is shown that the device rotation may change the optimal beam pair for beam management. Therefore, the device orientation is a valuable source of information for mmWave beam management. Moreover, Paper E showed that the sub-6 GHz channel response with a single antenna element in the sub-6 GHz band includes information about the environment that can be used in UT beamforming at the mmWave band.

Answering the second research question, the beam pair selection is a classification problem, where the optimal beam pair determines the label of the classification task. As classification problem has a long-established legacy in AI and ML, the beam selection problem can be fully supported by ML. The ML-based methods provided a limited performance loss with respect to the perfect alignment while keeping the latency and overhead very low by sensing only a few beam pairs compared to sensing hundreds/thousands of beam pairs in an exhaustive manner. In addition, the ML-based context-aware methods significantly outperform the hierarchical beam search in terms of overhead and accuracy. Moreover, the proposed ML-enabled CI-aware frameworks have shown superior performance than probabilistic CI-aware algorithms in a variety of scenarios/configurations in all the contributions.

In response to the third research question, as a rule of thumb, the required dataset size for training well an ML model depends on the number of trainable parameters in the model. In addition, for most of the considered ML models in this thesis, the number of parameters is mostly dominated by the number of beams in the AP and UT codebooks. As a consequence, the required dataset size also depends on the size of the codebook, or equivalently, on the directivity of the beams and the antenna array sizes. Hence, the price to pay for more directive codebooks with a large number of beams is to collect more samples to train the models. Moreover, our findings in Paper C and Paper D show that the properties of the beam selection problem can be considered in the architecture of ML models to reduce the number of trainable parameters. For example, Tx and Rx beam selection can be done as separate

tasks or sequentially, which results in reducing the number of trainable parameters. From another point of view, Paper B shows Transfer Learning can reduce the required training dataset size by transferring the learned knowledge from a scenario/configuration to another scenario/configuration.

The fourth research question, which concerns realistic configurations, has been addressed in Papers D and G. Although replacing a single-panel including isotropic antenna array with multi-panel devices including patch antenna arrays introduces more complexity to the beam selection problem, the proposed ML frameworks were able to extract CI and map them to the Tx-Rx beam pair selection task. In addition, ML-based methods have shown robustness to self-blockage caused by the user's hand and body. The results show that the ML models were able to adapt to severe self-blockage conditions, where deterministic or probabilistic schemes are considered for panel blockage.

The fifth research question discusses the scalability of ML-based context-aware beam management solutions. Due to antenna placement designs, codebook designs, and hardware imperfections, it is most likely to have various codebooks among different devices. As the device-specific beam selection approach suffers from the need for data collection, training an ML model, and model management for each device at base stations, it makes the ML-based approach less desirable. Therefore, paper E proposed a device-agnostic framework that is able to serve different devices with different beam codebooks. The proposed framework is able to serve unseen devices/codebooks in the training dataset without any fine-tuning dataset. A device needs only to share limited information about its codebook, and the proposed framework adapts the beam proposal based on the received information. The proposed device-agnostic framework paves the road for further research in scalable ML-enabled solutions in wireless communication applications.

2 Future Works

Research is a road with no end, and there is no exception here. Although solid contributions and scientific outcomes are presented in this thesis, the research outcomes open doors to new challenges, areas of research, and innovations. Here, I would like to propose potential future works in the area of context-aware beam alignment, starting with more realistic proposals and continuing toward more visionary prospects.

As the considered beam sensing procedure in the contributions of this thesis is designed for a single-AP single-UT scenario, the generalization of the sensing procedure for a multi-AP multi-UT scenario requires investigation. These changes make the proposed context-aware beam management solutions more attractive to industrial parties. Also, investigating the details

of beam reporting, beam maintenance, beam recovery, and beam tracking for context-aware solutions is a big move toward the practicality of this approach.

There are obvious strong motivations to reduce the computational complexity of an ML-enabled solution, which makes the solution more interesting. Future research may investigate the solutions with light ML models. In addition, this investigation needs to take into account the other factors like cost and energy of context information acquisition step, potentially saved energy by using an ML-enabled method for providing the same service as a context-unaware solution (e.g., hierarchical beam search).

Although multi-panel beamforming increases the complexity of beamforming exponentially, it may provide significant performance gain over commonly used single-panel beamforming. Also, the hand blockage impact on the multi-panel devices with the capability of multi-panel beamforming is another question.

The focus of the contributions in this thesis was on supervised learning solutions. However, this type of solution requires labeled samples, which may be the main bottleneck in deploying this solution in a new environment. Therefore, there is an extreme wish for solutions based on semi-supervised learning or unsupervised learning approaches, that reduces the dependency on labeled training samples. Also, pre-training a supervised learning ML model based on the collected samples from a digital twin of the environment may help to decrease the dependency on labeled datasets.

Although we considered acquiring CI from other systems / out-of-band measurements in this thesis, the network itself would have the capability to acquire relevant CI with integrated sensing and communications, which is expected to be introduced in 6G. An interesting question is how to weigh the two parts: how much emphasis should be put into sensing, and how much into utilizing the sensing information to improve communication performance? Can we extract relevant CI from the signals we send for communications?

A visionary topic in context-aware beam management is considering meta-learning, where the ML model instead of learning site-specific beam management, learns the beam management task. The learned meta-model potentially can adapt to the deployed scenario with few training samples, which is also called few-shot learning. The meta-learning approach may solve a grand challenge about the generalization of ML-enabled solutions to different scenarios.

References

[1] "Altair Feko WinProp," [online] Available: https://www.altair.com/feko.

[2] A. Abdelreheem, E. M. Mohamed, and H. Esmaiel, "Millimeter wave location-based beamforming using compressive sensing," in *2016 28th International Conference on Microelectronics (ICM)*, Dec. 2016, pp. 213–216.

[3] A. Ali, J. Mo, B. L. Ng, V. Va, and J. C. Zhang, "Orientation-Assisted Beam Management for Beyond 5G Systems," *IEEE Access*, vol. 9, pp. 51 832–51 846, 2021.

[4] A. Alkhateeb, "DeepMIMO: A Generic Deep Learning Dataset for Millimeter Wave and Massive MIMO Applications," *arXiv:1902.06435 [cs, eess, math]*, Feb. 2019, arXiv: 1902.06435. [Online]. Available: http://arxiv.org/abs/1902.06435

[5] M. Alrabeiah and A. Alkhateeb, "Deep Learning for mmWave Beam and Blockage Prediction Using Sub-6 GHz Channels," *IEEE Trans. Commun.*, vol. 68, no. 9, pp. 5504–5518, Sep. 2020.

[6] C. D. Alwis, A. Kalla, Q.-V. Pham, P. Kumar, K. Dev, W.-J. Hwang, and M. Liyanage, "Survey on 6G Frontiers: Trends, Applications, Requirements, Technologies and Future Research," *IEEE Open Journal of the Communications Society*, vol. 2, pp. 836–886, 2021, conference Name: IEEE Open Journal of the Communications Society.

[7] C. Antón-Haro and X. Mestre, "Learning and Data-Driven Beam Selection for mmWave Communications: An Angle of Arrival-Based Approach," *IEEE Access*, vol. 7, pp. 20 404–20 415, 2019.

[8] Q. Bi, "Ten Trends in the Cellular Industry and an Outlook on 6G," *IEEE Communications Magazine*, vol. 57, no. 12, pp. 31–36, Dec. 2019, conference Name: IEEE Communications Magazine.

[9] C. De Lima, D. Belot, R. Berkvens, A. Bourdoux, D. Dardari, M. Guillaud, M. Isomursu, E.-S. Lohan, Y. Miao, A. N. Barreto, M. R. K. Aziz, J. Saloranta, T. Sanguanpuak, H. Sarieddeen, G. Seco-Granados, J. Suutala, T. Svensson, M. Valkama, B. Van Liempd, and H. Wymeersch, "Convergent Communication, Sensing and Localization in 6G Systems: An Overview of Technologies, Opportunities and Challenges," *IEEE Access*, vol. 9, pp. 26 902–26 925, 2021.

[10] V. Desai, L. Krzymien, P. Sartori, W. Xiao, A. Soong, and A. Alkhateeb, "Initial beamforming for mmWave communications," in *2014 48th Asilomar Conference on Signals, Systems and Computers*. Pacific Grove, CA, USA: IEEE, Nov. 2014, pp. 1926–1930. [Online]. Available: http://ieeexplore.ieee.org/document/7094805/

[11] M. Dias, A. Klautau, N. González-Prelcic, and R. W. Heath, "Position and LIDAR-Aided mmWave Beam Selection using Deep Learning," in *Proc. IEEE Int. Workshop Signal Process. Adv. Wireless Commun. (SPAWC)*, Jul. 2019, pp. 1–5.

[12] I. Filippini, V. Sciancalepore, F. Devoti, and A. Capone, "Fast Cell Discovery in mm-Wave 5G Networks with Context Information," *IEEE Transactions on Mobile Computing*, vol. 17, no. 7, pp. 1538–1552, Jul. 2018.

[13] M. Giordani, M. Mezzavilla, and M. Zorzi, "Initial Access in 5G mmWave Cellular Networks," *IEEE Commun. Mag.*, vol. 54, no. 11, pp. 40–47, Nov. 2016.

[14] M. Giordani, M. Polese, M. Mezzavilla, S. Rangan, and M. Zorzi, "Toward 6G Networks: Use Cases and Technologies," *IEEE Commun. Mag.*, vol. 58, no. 3, pp. 55–61, Mar. 2020.

[15] M. Giordani, M. Polese, A. Roy, D. Castor, and M. Zorzi, "Standalone and Non-Standalone Beam Management for 3GPP NR at mmWaves," *arXiv:1805.04268 [cs]*, May 2018, arXiv: 1805.04268. [Online]. Available: http://arxiv.org/abs/1805.04268

[16] N. Gonzalez-Prelcic, A. Ali, V. Va, and R. W. Heath, "Millimeter-Wave Communication with Out-of-Band Information," *IEEE Commun. Mag.*, vol. 55, no. 12, pp. 140–146, Dec. 2017.

[17] N. González-Prelcic, R. Méndez-Rial, and R. W. Heath, "Radar aided beam alignment in MmWave V2I communications supporting antenna diversity," in *2016 Information Theory and Applications Workshop (ITA)*, Jan. 2016, pp. 1–7.

[18] Y. Heng, J. G. Andrews, J. Mo, V. Va, A. Ali, B. L. Ng, and J. C. Zhang, "Six Key Challenges for Beam Management in 5.5G and 6G Systems," *IEEE Commun. Mag.*, vol. 59, no. 7, pp. 74–79, Jul. 2021.

[19] M. Hu, X. Luo, J. Chen, Y. C. Lee, Y. Zhou, and D. Wu, "Virtual reality: A survey of enabling technologies and its applications in IoT," *Journal of Network and Computer Applications*, vol. 178, p. 102970, Mar. 2021. [Online]. Available: https://www.sciencedirect.com/science/article/pii/S1084804520304215

[20] W. Jiang, B. Han, M. A. Habibi, and H. D. Schotten, "The Road Towards 6G: A Comprehensive Survey," *IEEE Open Journal of the Communications Society*, vol. 2, pp. 334–366, 2021, conference Name: IEEE Open Journal of the Communications Society.

[21] W. Jiang and H. D. Schotten, "Initial Access for Millimeter-Wave and Terahertz Communications with Hybrid Beamforming," in *ICC 2022 - IEEE International Conference on Communications*, May 2022, pp. 3960–3965, iSSN: 1938-1883.

[22] V. Kelkkanen, M. Fiedler, and D. Lindero, "Bitrate Requirements of Non-Panoramic VR Remote Rendering," in *Proceedings of the 28th ACM International Conference on Multimedia*. Seattle WA USA: ACM, Oct. 2020, pp. 3624–3631. [Online]. Available: https://dl.acm.org/doi/10.1145/3394171.3413681

[23] T. Li, Y. Xu, H. Tong, and K. Pang, "Low-Band Information and Historical Data Aided Non-Uniform Millimeter Wave Beam Selection Algorithm in 5G-R High-Speed Railway Communication Scene," *IEEE Transactions on Vehicular Technology*, vol. 71, no. 3, pp. 2809–2823, Mar. 2022, conference Name: IEEE Transactions on Vehicular Technology.

[24] Y.-N. R. Li, B. Gao, X. Zhang, and K. Huang, "Beam Management in Millimeter-Wave Communications for 5G and Beyond," *IEEE Access*, vol. 8, pp. 13 282–13 293, 2020.

[25] H. Lin, S. Wan, W. Gan, J. Chen, and H.-C. Chao, "Metaverse in Education: Vision, Opportunities, and Challenges," Nov. 2022, arXiv:2211.14951 [cs]. [Online]. Available: http://arxiv.org/abs/2211.14951

[26] C. Liu, M. Li, S. V. Hanly, P. Whiting, and I. B. Collings, "Millimeter-Wave Small Cells: Base Station Discovery, Beam Alignment, and System Design Challenges," *IEEE Wirel. Commun.*, vol. 25, no. 4, pp. 40–46, Aug. 2018.

[27] P. K. R. Maddikunta, Q.-V. Pham, P. B, N. Deepa, K. Dev, T. R. Gadekallu, R. Ruby, and M. Liyanage, "Industry 5.0: A survey on enabling technologies and potential applications," *Journal of Industrial Information Integration*, vol. 26, p. 100257, Mar. 2022. [Online]. Available: https://www.sciencedirect.com/science/article/pii/S2452414X21000558

[28] F. Maschietti, D. Gesbert, P. d. Kerret, and H. Wymeersch, "Robust Location-Aided Beam Alignment in Millimeter Wave Massive MIMO," in *GLOBECOM 2017 - 2017 IEEE Global Communications Conference*, Dec. 2017, pp. 1–6.

[29] J. Mo, B. L. Ng, S. Chang, P. Huang, M. N. Kulkarni, A. Alammouri, J. C. Zhang, J. Lee, and W.-J. Choi, "Beam Codebook Design for 5G mmWave Terminals," *IEEE Access*, vol. 7, pp. 98 387–98 404, 2019.

[30] K. N. Nguyen, A. Ali, J. Mo, B. L. Ng, V. Va, and J. C. Zhang, "Beam Management with Orientation and RSRP using Deep Learning for Beyond 5G Systems," in *2022 IEEE International Conference on Communications Workshops (ICC Workshops)*, May 2022, pp. 133–138, iSSN: 2694-2941.

[31] H. Peng, P.-C. Chen, P.-H. Chen, Y.-S. Yang, C.-C. Hsia, and L.-C. Wang, "6G toward Metaverse: Technologies, Applications, and Challenges," in *2022 IEEE VTS Asia Pacific Wireless Communications Symposium (APWCS)*, Aug. 2022, pp. 6–10.

[32] M. Polese, F. Restuccia, and T. Melodia, "DeepBeam: Deep Waveform Learning for Coordination-Free Beam Management in mmWave Networks," in *Proc. ACM MobiHoc '21*, Jul. 2021, pp. 61–70.

[33] V. Raghavan, M.-L. Chi, M. A. Tassoudji, O. H. Koymen, and J. Li, "Antenna Placement and Performance Tradeoffs With Hand Blockage in Millimeter Wave Systems," *IEEE Trans. Commun.*, vol. 67, no. 4, pp. 3082–3096, Apr. 2019.

[34] V. Raghavan, R. A. Motos, M. A. Tassoudji, Y.-C. Ou, O. H. Koymen, and J. Li, "Mitigating Hand Blockage with Non-Directional Beamforming Codebooks," *arXiv:2104.06472 [cs, math]*, Apr. 2021. [Online]. Available: http://arxiv.org/abs/2104.06472

[35] T. S. Rappaport, Y. Xing, O. Kanhere, S. Ju, A. Madanayake, S. Mandal, A. Alkhateeb, and G. C. Trichopoulos, "Wireless Communications and Applications Above 100 GHz: Opportunities and Challenges for 6G and Beyond," *IEEE Access*, vol. 7, pp. 78 729–78 757, 2019, conference Name: IEEE Access.

[36] S. Rezaie, E. De Carvalho, and C. N. Manchón, "A Deep Learning Approach to Location- and Orientation-aided 3D Beam Selection for mmWave Communications," *IEEE Trans. Wireless Commun.*, vol. 21, no. 12, pp. 11 110–11 124, 2022.

[37] S. Rezaie, C. N. Manchón, and E. de Carvalho, "Location- and Orientation-Aided Millimeter Wave Beam Selection Using Deep Learning," in *Proc. IEEE Int. Conf. Commun.*, Jun. 2020, pp. 1–6.

[38] S. Rezaie, J. Morais, A. Alkhateeb, and C. N. Manchón, "Device-Agnostic Millimeter Wave Beam Selection using Machine Learning," Nov. 2022, arXiv:2211.12125 [eess]. [Online]. Available: http://arxiv.org/abs/2211.12125

[39] L.-H. Shen, T.-W. Chang, K.-T. Feng, and P.-T. Huang, "Design and Implementation for Deep Learning Based Adjustable Beamforming Training for Millimeter Wave Communication Systems," *IEEE Transactions on Vehicular Technology*, vol. 70, no. 3, pp. 2413–2427, Mar. 2021.

[40] W.-T. Shih, C.-K. Wen, S. Jin, and S.-H. Tsai, "Fast Antenna and Beam Switching Method for mmWave Handsets with Multiple Subarrays," in *ICC 2020 - 2020 IEEE International Conference on Communications (ICC)*, Jun. 2020, pp. 1–6.

[41] F. Sohrabi, Z. Chen, and W. Yu, "Deep Active Learning Approach to Adaptive Beamforming for mmWave Initial Alignment," *IEEE Journal on Selected Areas in Communications*, vol. 39, no. 8, pp. 2347–2360, Aug. 2021.

[42] X. Song, T. Kuhne, and G. Caire, "Fully-/Partially-Connected Hybrid Beamforming Architectures for mmWave MU-MIMO," *IEEE Trans. Wireless Commun.*, vol. 19, no. 3, pp. 1754–1769, Mar. 2020.

[43] R. S. Sutton and A. G. Barto, *Reinforcement Learning, second edition: An Introduction*. MIT Press, Nov. 2018, google-Books-ID: sWV0DwAAQBAJ.

[44] F. Tang, X. Chen, M. Zhao, and N. Kato, "The Roadmap of Communication and Networking in 6G for the Metaverse," *IEEE Wireless Communications*, pp. 1–15, 2022, conference Name: IEEE Wireless Communications.

[45] V. Va, J. Choi, T. Shimizu, G. Bansal, and R. W. Heath, "Inverse Multipath Fingerprinting for Millimeter Wave V2I Beam Alignment," *IEEE Trans. Veh. Technol.*, vol. 67, no. 5, pp. 4042–4058, May 2018.

[46] H. Viswanathan and P. E. Mogensen, "Communications in the 6G Era," *IEEE Access*, vol. 8, pp. 57 063–57 074, 2020, conference Name: IEEE Access.

[47] J. Wang, Z. Lan, C.-w. Pyo, T. Baykas, C.-s. Sum, M. Rahman, J. Gao, R. Funada, F. Kojima, H. Harada, and S. Kato, "Beam codebook based beamforming protocol for multi-Gbps millimeter-wave WPAN systems," *IEEE Journal on Selected Areas in Communications*, vol. 27, no. 8, pp. 1390–1399, Oct. 2009, conference Name: IEEE Journal on Selected Areas in Communications.

[48] Z. Xiao, T. He, P. Xia, and X. Xia, "Hierarchical Codebook Design for Beamforming Training in Millimeter-Wave Communication," *IEEE Trans. Wireless Commun.*, vol. 15, no. 5, pp. 3380–3392, May 2016.

[49] B. Xie, H. Liu, R. Alghofaili, Y. Zhang, Y. Jiang, F. D. Lobo, C. Li, W. Li, H. Huang, M. Akdere, C. Mousas, and L.-F. Yu, "A Review on Virtual Reality Skill Training Applications," *Frontiers in Virtual Reality*, vol. 2, 2021. [Online]. Available: https://www.frontiersin.org/articles/10.3389/frvir.2021.645153

[50] M. Xu, D. Niyato, J. Kang, Z. Xiong, C. Miao, and D. I. Kim, "Wireless Edge-Empowered Metaverse: A Learning-Based Incentive Mechanism for Virtual Reality," in *ICC 2022 - IEEE International Conference on Communications*, May 2022, pp. 5220–5225, iSSN: 1938-1883.

[51] W. Xu, F. Gao, S. Jin, and A. Alkhateeb, "3D Scene-Based Beam Selection for mmWave Communications," *IEEE Wireless Commun. Lett.*, vol. 9, no. 11, pp. 1850–1854, Nov. 2020.

[52] Z. Zhu, K. Lin, and J. Zhou, "Transfer Learning in Deep Reinforcement Learning: A Survey," *arXiv:2009.07888 [cs, stat]*, Mar. 2021. [Online]. Available: http://arxiv.org/abs/2009.07888

Part II

Papers

Paper A

Location- and Orientation-Aided Millimeter Wave Beam Selection Using Deep Learning

Sajad Rezaie, Carles Navarro Manchón, Elisabeth de Carvalho

The paper has been published in the
IEEE International Conference on Communications (ICC), pp. 1–6, Jun. 2020.

The layout has been revised.

Abstract

Location-aided beam alignment methods exploit the user location and prior knowledge of the propagation environment to identify the beam directions that are more likely to maximize the beamforming gain, allowing for a reduction of the beam training overhead. They have been especially popular for vehicle to everything (V2X) applications where the receive array orientation is approximately constant for each considered location, but are not directly applicable to pedestrian applications with arbitrary orientation of the user handset. This paper proposes a deep neural network based beam selection method that leverages position and orientation of the receiver to recommend a shortlist of the best beam pairs, thus significantly reducing the alignment overhead. Moreover, we use multi-labeled classification to not only capture the beam pair with highest received strength but also enrich the neural network with information of alternative beam pairs with high received signal strength, providing robustness against blockage. Simulation results show the better performance of the proposed method compared to a generalization of the inverse fingerprinting algorithm in terms of the misalignment and outage probabilities.

1 Introduction

Beyond 5G systems will serve the recent emerging services such as high-definition multimedia applications as well as both virtual and augmented reality where ultra high throughput is required. Such high throughput can be obtained by accessing the millimeter wave (mmWave) band, which offers enormous and continuous unallocated bandwidth [1–3]. MmWave communication can moreover be easily used in small cells due to higher propagation and penetration loss at mmWave frequencies; nonetheless, high penetration losses causes common blockage, which makes it difficult to establish a reliable mmWave link. Directional beamforming using multiple-input multiple-output (MIMO) antenna arrays with large number of elements is frequently employed to obtain a sufficient link budget, thanks to the array gain. To do this successfully, transmitter and receiver need to align their transmissions over the direction of the line-of-sight (LOS) channel component, or a strong non-line-of-sight (NLOS) path when the LOS is blocked. As a result, configuring antenna arrays at transmitter and/or receiver is challenging in highly dynamic propagation environments [2].

Commonly, codebook-based analog beamforming with a set of predefined beams has been proposed to reduce the complexity of the arrays configuration and alignment process. Typically, the set of predefined beams in the codebook is realized via analog beamforming or a combination of digital and analog processing. Although an exhaustive search procedure over all beam pairs in the codebooks yields the optimal beam pairs in high signal-

to-noise ratio (SNR) conditions, it requires unacceptably high latency and overhead. On the other hand, hierarchical search algorithms have lower overhead but there is no guarantee to cover cell edges [4]. Context information (CI)-based beam alignment methods were proposed to leverage contextual information such as user location to overcome these challenges. The authors of [3] proposed a data-driven beam alignment method for mmWave vehicle to infrastructure (V2I) communication which utilizes multipath fingerprints and position information to extend CI-based beam alignment in the case of NLOS links. To reduce effects of imperfect position information at both ends, one approach based on Bayesian decision theory has been proposed in [5]. In [10], the authors propose a beam selection scheme that, in addition, estimates the position and orientation of receiver in each step of beam alignment procedure, showing that the position/orientation estimation and the beam alignment procedures benefit from each other.

As another strategy, machine learning based beam alignment methods have been proposed to use the high capacity of kernel based models and neural networks (NN) in learning the non-linearities present in the function mapping the best beam pair with highest received power and receiver location [6, 7]. Due to the opportunity of using additional information in vehicular scenarios, RADAR and LIDAR based beam alignments were proposed to capture more information about obstacles in environment [8, 9]. However, the mentioned machine learning methods deal with V2X applications in which the receiver array orientation can be directly inferred from the vehicle position. As such, they cannot be applied to indoor scenarios with pedestrian users where receivers can take any arbitrary orientation. Note that directional beam codebooks are typically made of beams with different beamwidths and, therefore, the transformation that a receiver rotation imposes on the received signal strength of each possible beam pair cannot be deterministically predicted, even when the rotation angle is perfectly known.

In this paper, we propose a new data-driven beam selection method for mmWave communications that leverages both orientation and location information of users. We consider an indoor scenario in which, contrary to the vehicular applications, the receivers can take any arbitrary orientation and position. In addition, the environment includes static and mobile scattering objects, which reflect and block the multipath components complicating the beam selection task. Since deep learning is able to capture the structure of the environment, we propose a deep neural network structure for classification that takes as input the position and orientation of the receiver, and outputs probabilities of being the best for each beam-pairs. The overhead of beam selection procedure is reduced significantly by sensing only beam pairs with high probabilities.

As another contribution, we apply multi-label classification to enhance the procedure of learning the environment's structure by training the model

in the direction of not only the most powerful path but also alternative paths with high power. This endows the proposed model with robustness against mismatches in the training data. Furthermore, in order to compare the proposed method with a data driven based algorithm, we generalize the inverse fingerprinting method proposed by [3] to work with varying receiver orientation. Our numerical results show that the proposed framework offers a performance close to that of perfect beam alignment and significantly superior to that of the generalized inverse fingerprinting (GIFP) method trained with identical data.

2 System Model

We consider a 2D indoor downlink scenario where one transmitter and one receiver with N_t and N_r antennas, respectively, want to establish a mmWave communication link.

2.1 Channel Model

Due to the importance of location information for fast beam alignment in mmWave communication, we use a 2-dimensional (2D) geometric based channel model proposed by [11]. In this model, objects in the environment such as building, equipment, and humans are mapped to 2D rectangular or circular objects. In each realization, we define mobile scatterers with varying position and orientation, in contrast to static scatterers with fixed position and orientation, to simulate mobile blockers. For simplicity, we place the transmitter at position $\boldsymbol{p}_t = (0, 0)$ with fixed angle of antenna arrays α_t, with respect to the x-axis. As depicted in Fig. A.1, the receiver can take any position $\boldsymbol{p}_r = (x_r, y_r) \in \mathbb{R}^2$ with random orientation $\alpha_r \in [0, 2\pi)$ where there is no overlap with other static or mobile objects.

In addition to the LOS path between transmitter and receiver, we consider first, second, and third order reflection of static and/or mobile rectangular objects using image theory [11, 12]. We apply a narrow band channel model to the contribution of one LOS and L NLOS paths,

$$\boldsymbol{H} = \sum_{l=0}^{L} \sqrt{N_t N_r}\, \beta_l\, c_l\, \boldsymbol{a}_r(\theta_{r,l})\, \boldsymbol{a}_t^H(\theta_{t,l}), \tag{A.1}$$

in which $\boldsymbol{H}$ and $c_l \in [0, 1]$ denotes the $N_R \times N_T$ channel matrix and transfer coefficient of l-th path due to penetration loss by blockers[1], respectively. $\beta_l \in$

[1]To consider effects of blockers on l-th path, we consider a simple model as $c_l = \eta^{n_l}$, where η and n_l denote the transmission coefficient of objects and the number of objects which have intersection with the l-th path, respectively.

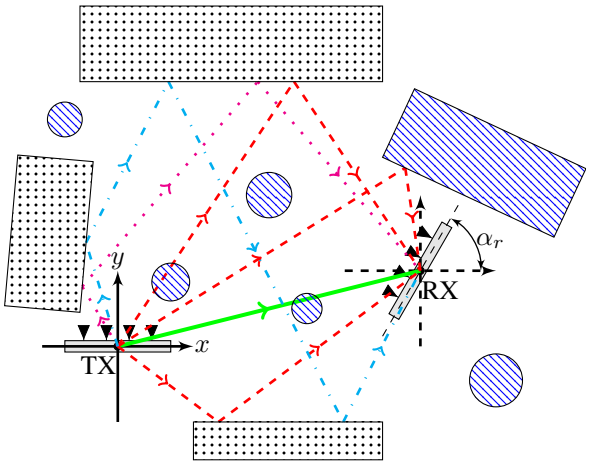

Fig. A.1: A top view of the outoor ray-tracing scenario.

$\mathcal{CN}(0, \sigma_l^2)$ is the complex fading gain of l-th path with variance $\sigma_l^2 \propto d_l^{-\gamma}$, where d_l and γ are the distance that l-th path traverses to the receiver and path loss exponent, respectively. Also, $\theta_{r,l}$, $\theta_{t,l}$, $\boldsymbol{a}_r(\theta_{r,l})$ and $\boldsymbol{a}_t(\theta_{t,l})$ are the angle of arrival (AoA) and angle of departure (AoD) with respect of the array axis, the antenna array response of receiver and transmitter, respectively. We consider uniform linear arrays (ULA) of ideal isotropic antenna elements with $\lambda/2$ antenna spacing, yielding the array responses

$$\boldsymbol{a}_r(\theta_{r,l}) = \frac{1}{\sqrt{N_r}}[1, e^{-j\pi cos(\theta_{r,l})}, \ldots, e^{-j\pi(N_r-1)cos(\theta_{r,l})}]^T, \tag{A.2}$$

$$\boldsymbol{a}_t(\theta_{t,l}) = \frac{1}{\sqrt{N_t}}[1, e^{-j\pi cos(\theta_{t,l})}, \ldots, e^{-j\pi(N_t-1)cos(\theta_{t,l})}]^T. \tag{A.3}$$

2.2 Beam Codebook

In analog beamforming, the beamforming operations are performed in the analog domain by connecting each antenna to one analog phase shifter. We assume a codebook-based analog beamforming architecture to beamform signals with a single RF chain at transmitter and receiver. We denote by $\mathcal{F} = \{\boldsymbol{f}_1, \ldots, \boldsymbol{f}_{N_t}\}$ and $\mathcal{W} = \{\boldsymbol{w}_1, \ldots, \boldsymbol{w}_{N_r}\}$ the codebooks used for analog beamforming at the transmitter and analog combining at the receiver, each of them with N_t and N_r beams, respectively. We use the common Discrete Fourier transform (DFT)-based codebooks [5, 13] with precoders and com-

biners reading

$$\boldsymbol{f}_p = \frac{1}{\sqrt{N_t}}[1, e^{-j\pi\frac{2p-1-N_t}{N_t}}, \ldots, e^{-j\pi(N_t-1)\frac{2p-1-N_t}{N_t}}]^T, \tag{A.4}$$

$$\boldsymbol{w}_q = \frac{1}{\sqrt{N_r}}[1, e^{-j\pi\frac{2q-1-N_r}{N_r}}, \ldots, e^{-j\pi(N_r-1)\frac{2q-1-N_r}{N_r}}]^T, \tag{A.5}$$

where $p \in \{1, \ldots, N_t\}$ and $q \in \{1, \ldots, N_r\}$.

On each time slot, according to the precoder $\boldsymbol{f}_p \in \mathcal{F}$ and combiner $\boldsymbol{w}_q \in \mathcal{W}$, the received signal power $\mathbf{R} \in \mathbb{R}^{N_t \times N_r}$ can be written as

$$\mathbf{R}[p, q] = \left\| \sqrt{P_t}\boldsymbol{w}_q^H \boldsymbol{H} \boldsymbol{f}_p s + \boldsymbol{w}_q^H \boldsymbol{n} \right\|^2 \tag{A.6}$$

in which P_t, $s \in \mathbb{C}$, and $\boldsymbol{n} \in \mathbb{C}^{N_r}$ denote the transmission power, the known training symbol with normalized power, and a zero mean complex Gaussian noise vector with variance σ_n^2.

3 Data-Driven Beam Selection

Besides prior knowledge of the propagation environment, position and orientation of RX ($\boldsymbol{p}_r$ and α_r) can be used to reduce the overhead of the beam alignment procedure. The prior knowledge of the environment is acquired from measurements in a training phase, which are collected in the target environment. Each sample of the training data corresponds to a realization of the environment where the receiver and mobile objects take an arbitrary location and orientation. The training data includes position and orientation of receiver in addition to the measured received signal strength for all combinations of $\mathcal{F}$ and $\mathcal{W}$. Thus for a given realization of the environment, according to the prior knowledge and the location and orientation of the receiver, data-driven methods recommend a shortlist of beam pairs to limit the search space of finding the best beam pair with the highest received strength.

As mentioned in Section 1, probabilistic and machine learning based beam selections are two common types of data-driven procedures to exploit the prior information of the environment for a given receiver location. To give a comparison between these two approaches, we use the inverse fingerprinting (IFP) beam selection method [3] as a baseline of comparison with the proposed machine learning based approach. However, the IFP method considers only the location of vehicles, not taking into account the arbitrary orientation of the receiver array. Moreover, knowledge of the beam direction recommended by the IFP method at angle α_{r_1} does not determine the corresponding unique beam direction at angle α_{r_2}, due to the beam patterns having unequal beamwidths in the DFT-based codebook. Therefore, we extend the IFP method to be able to select beam pairs in varying receiver angles.

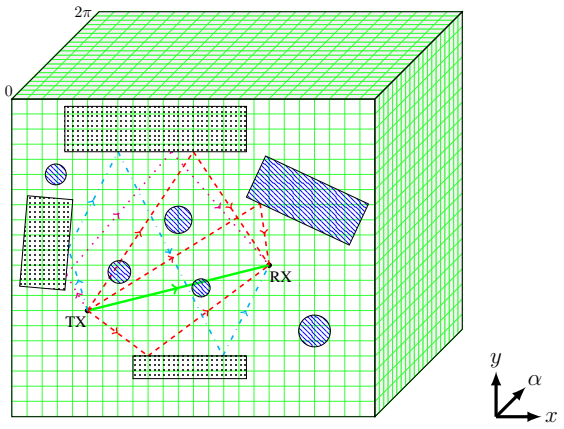

Fig. A.2: Bin definition in Generalized Inverse Fingerprinting beam alignment. The third dimension is used only to show impacts of orientation in bin definition procedure.

3.1 Generalized Inverse fingerprinting Method

To consider the orientation of receivers in the IFP method, bin definition is extended to discretize both the spatial and angular domains. As depicted in Fig. A.2, the corresponding bin of each observation is determined using position and angle of the receiver ($\boldsymbol{p}_r$ and α_r). We could define the k-th bin as:

$$\mathcal{B}_k = [x_k, x_k + \Delta_s) \times [y_k, y_k + \Delta_s) \times [\alpha_k, \alpha_k + \Delta_a), \tag{A.7}$$

where Δ_s and Δ_a denotes spatial bin size (SBS) and angular bin size (ABS), respectively. Also, by setting $\Delta_a = 2\pi$ we recover the classical IFP bin definition.

Similar to the IFP method, a set of N_b candidate beam pairs of the k-th bin, denoted by $\mathcal{S}_k$, is selected to minimize the probability of not containing the beam pair with the highest received power in it. We define this probability as the misalignment probability, and it can be expressed as

$$P_m(\mathcal{S}_k) = \mathbb{P}\left[\max_{(i,j)\in\mathcal{S}_k} \mathbf{R}[i,j] < \max_{(p,q)\in\mathcal{B}} \mathbf{R}[p,q]\right], \tag{A.8}$$

where $\mathcal{B}$ denotes the set of all possible beam pair combinations. In [3], it is proved that $\mathcal{S}_k$ is equivalent to top N_b ranked beam pairs according to their frequency of being best in the training observations associated with the kth bin. Due to the increased number of bins in GIFP compared to conventional IFP, more training data is needed to reach the same number of training samples per bin.

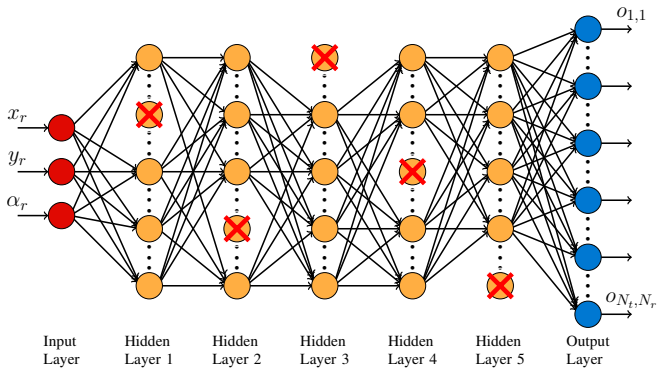

Fig. A.3: Deep neural network architecture of the proposed beam alignment method using context information.

3.2 Proposed Deep-Learning Based Method

The presence in the environment of static and mobile scatterers, which can block or reflect the multipath components with highest power, implies that beam selection using context information is a highly nonlinear classification problem. While support vector machine (SVM) and shallow neural network have the ability to classify linear and slightly nonlinear problems by hyperplane separators, a deep neural network is able to learn highly complex nonlinear functions by adding hidden layers. We hence select a deep neural network model for classification as explained in the following. As depicted in Fig. A.3, we consider a deep neural network with 3 inputs, corresponding to the receiver's location (x_r, y_r) and its orientation α_r. The network is made 5 fully-connected hidden layers so that it has enough depth to learn the non-linearities present in a highly crowded environment. To enable the capacity of the neural network to learn non-linearities, we use tanh and Softmax functions as the activation functions in the hidden layers and the output layer, respectively. Each of the hidden layers contains N_{hid} neurons, while the output layer is made of $N_t N_r$ outputs, one for each possible beam pair. This results in a total of $4N_{\text{hid}} + 4N_{\text{hid}}(N_{\text{hid}} + 1) + (N_{\text{hid}} + 1)N_t N_r$ trainable parameters.

We configure the neural network to learn the index of the best beam pair by labeling the outputs $\mathcal{O} = \{o_{i,j} | i = 1, \ldots, N_t; j = 1, \ldots, N_r\}$ of the training data as

$$o_{i,j} = \begin{cases} 1, & \text{if } (i,j) = \arg\max_{m,n} \mathbf{R}[m,n], \\ 0, & \text{otherwise.} \end{cases} \tag{A.9}$$

This implies that $\mathcal{O}$ has only one nonzero member $o_{m,n}$, where m and n are the indices of TX and RX beam of the best beam pair, respectively.

Overfitting occurs when a neural network is trained on a small or not large enough dataset and degrades the performance of the neural network on test data. To overcome this problem, we use dropout as a regularization mechanism. Dropout attempts to combine different structures of neural networks to prevent memorizing the training data [14]. In this technique, as depicted in Fig. A.3, some nodes of a specific layer are dropped out randomly in each batch of training data. We set a dropout ratio $p = 0.1$ to give up 10% of nodes in each hidden layer randomly. The dropped out nodes are illustrated by red cross marks in Fig. A.3.

In test mode, the inputs of the neural network are fed with the position and angle of the receiver. Since the activation function of the output layer is Softmax, the neural network generates the probability of being best for all beam pairs. The candidate list of beam pairs can be chosen by truncating the N_b first indices of the outputs sorted in descending order, i.e.,

$$\begin{aligned} \boldsymbol{g} &= \underset{i,j}{\arg\operatorname{sort}}\,(o_{i,j}), \\ \mathcal{S} &= \{\boldsymbol{g}(k)|k = 1, \ldots, N_b\}. \end{aligned} \tag{A.10}$$

Multi-label classification: Both inverse fingerprinting and single-labeled classifier beam alignment methods focus on the path with highest power and, consequently, these methods need large training datasets to yield acceptable accuracy especially in highly crowded scenarios. To overcome this problem, we propose to use multi-label classification to capture not only the best beam pair but also the remaining high power beam pairs in the training data. By adding this data to our training labels, the neural network can learn other paths between transmitter and receiver. The output label during the training phase of the M-labeled classification should be revised as:

$$\begin{aligned} \boldsymbol{r} &= \underset{i,j}{\arg\operatorname{sort}}\,(\mathbf{R}[i,j]), \\ \mathcal{T} &= \{\boldsymbol{r}(k)|k = 1, \ldots, M\}, \\ o_{i,j} &= \begin{cases} 1, & \text{if } (i,j) \in \mathcal{T}, \\ 0, & \text{otherwise}, \end{cases} \end{aligned} \tag{A.11}$$

where the kth element of $\boldsymbol{r}$ contains the indices of the kth highest value in $\mathbf{R}$, and $\mathcal{T}$ contains the first M elements of $\boldsymbol{r}$. Thus, M outputs are labelled with a 1 in $\mathcal{O}$, which correspond to the top-M beam pairs with the highest received power.

4 Simulation Results and Discussions

This section presents simulation results of the proposed deep learning based beam alignment method and compares it with the generalized inverse finger-

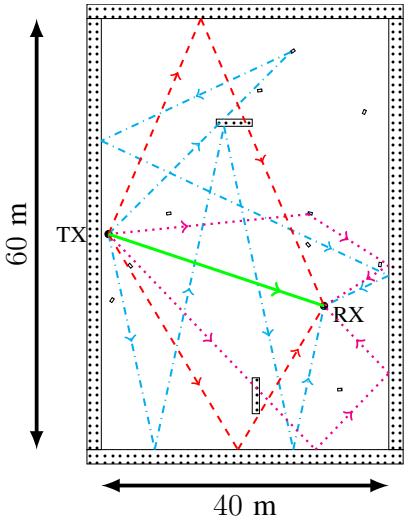

Fig. A.4: An Indoor mmWave system model with 6 static and 10 mobile objects. In addition to LOS, to have better representation, only 6 NLOS paths are drawn among all 24 reflected paths.

printing as the baseline method. To make a fair comparison between these methods, we calculate performance metrics by feeding both of them with same training and test data. We consider 6 static objects, including four walls and two fixed obstacles, in addition to varying the number of mobile objects to model an indoor environment. The parameters used for channel modeling are $N_t = 64$, $N_r = 64$, $\gamma = 2$, $P_t = 24$ dBm, and $\sigma_n^2 = -84$ dBm. Also, the reflection coefficient and the transmission coefficient of all objects are $\Gamma = 0.4$ and $\eta = 0.05$, respectively. Fig. A.4 depicts the indoor scenario where a transmitter, which is placed at a distance of 1 m from the left wall, communicates with a receiver placed randomly in the room.

4.1 Generation of Training and Test Datasets

In each realization of the environment, mobile objects are newly drawn inside of the room according to a two-dimensional homogeneous Poisson point process with mean number of points λ, while static objects preserve always the same position and orientation over all environment realizations. The mobile objects' size is chosen in order to model the effect of pedestrians with dimension 0.35m $\times$ 0.6m. A receiver is placed randomly inside of the room where there is no overlap with the static and mobile objects. In this scenario, some or all paths may be blocked due to the two fixed obstacles inside the room with dimension 5m $\times$ 1m and other mobile objects.

Based on image theory, the probability of having a reflected path reach-

ing the receiver from a given object is proportional to the object's dimensions. Moreover, higher order reflected paths reach the receiver after more than one reflection with the objects [11]. Since, in the considered indoor scenario, mobile objects are much smaller than static ones, the probability of a having a reflected path from more than one mobile objects reaching the receiver is close to zero, in addition to those path having much smaller signal energy than lower-order ones. Therefore, we disregard paths with reflections from more than one mobile objects to reduce the computation time of the ray tracing procedure. The received signal power in each beam pair is saved in a dataset, which we randomly split into two groups: 80% of data is dedicated for training and the remaining part for evaluating performance of the beam alignment methods.

4.2 Numerical Evaluation

According to the $N_t N_r = 4096$ neurons in the last layer of neural network and using $N_{\text{hid}} = 128$ neurons in each hidden layer, there are 594944 trainable weights in the network. Since the number of neurons in the output layer is 32 times larger than N_{hid}, more than 88% of the trainable weights are located in the last dense layer. We use Adam optimizer and train the deep neural network with 50 epochs with minibatch size progressively increasing from 32 to 8192 examples. Fig. A.5 shows the misalignment probability of the proposed method, according to (A.8), in comparison with the GIFP method with different spatial and angular bin sizes by processing two datasets A and B with $10,000$ and $100,000$ samples, respectively. The performance of GIFP method is very dependent to the values of SBS and ABS. Basically, there is a tradeoff on the selection of the bin sizes, whose optimal setting depends on the dataset size. On the one hand, larger bin sizes allow more data samples per bin, which results in obtaining better statistics for construction of the list of beam candidates. On the other hand, though, larger bins result in lower spatial resolution and the bundling together of positions for which the optimal beam pairs are significantly different. Anyway, the deep learning based method always outperforms the GIFP method with various values of SBS and ABS. Using multi-label classification decreases the misalignment probability of the proposed method with respect to the single-labeled one. Since the multi-labeling technique can be seen as a data augmentation strategy, it has a stronger impact on the results of dataset A which includes fewer samples.

To evaluate the robustness of the multi-labeled deep learning based beam alignment in indoor mmWave communications, we use the outage probability and achievable spectral efficiency in the same scenario. The outage probability of a link is defined as the probability that the signal to noise ratio (SNR) corresponding to a given pair of the precoder and combiner is smaller than a required threshold level SNR_{TH}. The SNR corresponding to the beam

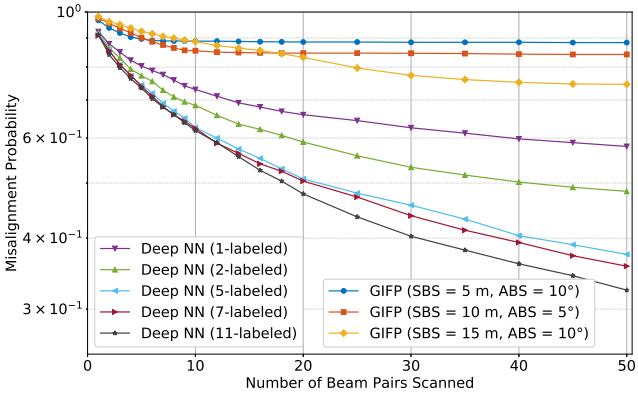

(a) Dataset A with $10,000$ samples

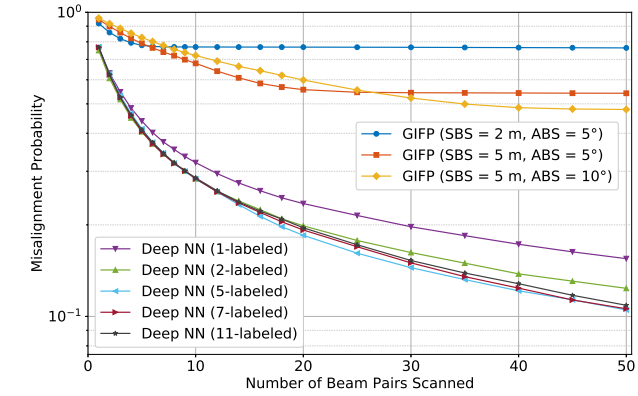

(b) Dataset B with $100,000$ samples

Fig. A.5: Misalignment probability of deep learning based beam alignment and GIFP method with different spatial and angular bin sizes when $\lambda = 10$.

pair (p, q) is defined as

$$\mathrm{SNR}_{p,q} = \frac{\left\| \sqrt{P_t} \boldsymbol{w}_q^H \boldsymbol{H} \boldsymbol{f}_p \boldsymbol{s} \right\|^2}{\sigma_n^2}. \tag{A.12}$$

In the following simulation, we set $\mathrm{SNR}_{\mathrm{TH}} = 20\mathrm{dB}$. In addition, the achievable spectral efficiency of beam pair (p, q) can be calculated as

$$\mathrm{SE}_{p,q} = \log_2(1 + \mathrm{SNR}_{p,q}). \tag{A.13}$$

As Fig. A.6 demonstrates, deep neural network based beam selection has lower outage probability than GIFP method with the same number of recommended beam pairs. Moreover, by increasing the number of labels at the multi-label classification, the loss of the deep learning method with respect to the perfect beam alignment is reduced.

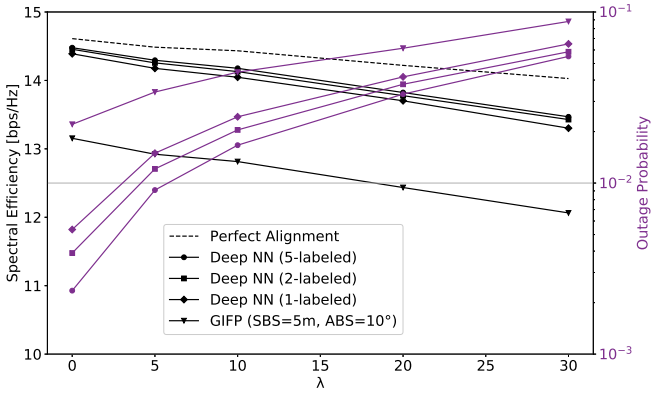

Fig. A.6: Spectral efficiency (black) and outage probability (purple) with $N_b = 40$.

A usual concern when using data-based approaches is the robustness of a model trained in a certain environment when evaluated in an environment with mismatched characteristics. In vehicular to infrastructure mmWave networks performance of beam alignment dropped significantly with a mismatch in the number of mobile vehicles in training and test samples [3]. In order to evaluate the effects of this mismatch on our proposed solution and scenario, Fig.A.7 shows the misalignment probability of GIFP and deep NN methods when trained on an environment with mean number of mobile objects λ_{train} and evaluated in an environment with mean number of mobile objects λ_{test}. The results show that both the GIFP and Deep NN methods are fairly robust to this mismatch in our problem, contrary to the findings in [3]. We attribute this difference to larger degree of randomness in location and orientation in our setup, compared to the very structured distribution of mobile reflectors in vehicular applications.

5 Conclusion

Location information has valuable potential to reduce the overhead of initial access in indoor mmWave networks. In this paper, we proposed a beam alignment procedure by exploiting both position and orientation information of the receiver using machine learning. A Deep neural network is trained to capture the most important beam directions for each receiver location in the training dataset and predicts the most powerful paths for unseen receiver positions and orientations.

We generalized the inverse fingerprinting beam alignment method to include orientation information as additional input in its procedure. We used this probabilistic method as baseline to be able compare our results

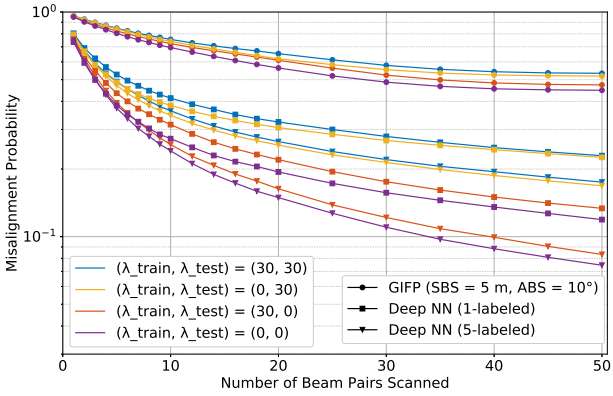

Fig. A.7: Misalignment probability with mismatch in the number of mobile objects in train and test data.

with a well known, simple and data driven based algorithm. According to the numerical evaluations and comparisons, we observe that the proposed beam alignment approach outperforms the generalized inverse fingerprinting method. It is also shown that the proposed methods are robust to different configurations of mobile objects in the training and test data especially using multi-label classification by capturing more paths in each training sample. Overall, our results stand as proof of the superiority of deep neural networks as location-based beam selection method compared to other data-based approaches such as inverse fingerprinting.

References

[1] M. Giordani, M. Polese, M. Mezzavilla, S. Rangan, and M. Zorzi, "Towards 6G networks: Use cases and technologies," *arXiv*:1903.12216 [cs.NI], Mar. 2019. [Online]. Available: https://arxiv.org/abs/1903.12216.

[2] C. Liu and M. Li and S. V. Hanly and P. Whiting and I. B. Collings, "Millimeter-Wave small cells: Base station discovery, beam alignment, and system design challenges," *IEEE Wirel. Commun.*, vol. 25, no. 4, pp. 40–46, Aug. 2018.

[3] V. Va and J. Choi and T. Shimizu and G. Bansal and R. W. Heath, "Inverse multipath fingerprinting for millimeter wave V2I beam alignment," *IEEE Trans. Veh. Technol.*, vol. 67, pp. 4042–4058, May 2018.

[4] M. Giordani and M. Mezzavilla and M. Zorzi, "Initial access in 5G mmwave cellular networks," *IEEE Commun. Mag.*, vol. 54, no. 11, pp. 40–47, Nov. 2016.

[5] F. Maschietti and D. Gesbert and P. de Kerret and H. Wymeersch, "Robust location-aided beam alignment in millimeter wave massive MlMO," in *Proc. IEEE GLOBECOM*, Dec. 2017, pp. 1–6.

[6] V. Va and T. Shimizu and G. Bansal and R. W. Heath, "Position-aided millimeter wave V2I beam alignment: A learning-to-rank approach," in *Proc. IEEE 28th Annu. Int. Symp. Pers. Indoor Mobile Radio Commun.*, Oct. 2017, pp. 1–5.

[7] Y. Wang and A. Klautau and M. Ribero and A. C. K. Soong and R. W. Heath, "MmWave vehicular beam selection with situational awareness using machine learning," *IEEE Access*, vol. 7, pp. 87479–87493, Jun. 2019.

[8] N. González-Prelcic and R. Méndez-Rial and R. W. Heath, "Radar aided beam alignment in mmwave v2i communications supporting antenna diversity," in *Information Theory and Applications Workshop (ITA)*, Jan. 2016, pp. 1–7.

[9] M. Dias and A. Klautau and N. González-Prelcic and R. W. Heath, "Position and LIDAR-aided mmWave beam selection using deep learning," in *2019 IEEE 20th International Workshop on Signal Processing Advances in Wireless Communications(SPAWC)*, Jul. 2019, pp. 1–5.

[10] G. E. Garcia and G. Seco-Granados and E. Karipidis and H. Wymeersch, "Transmitter beam selection in millimeter-wave MIMO with in-band position-aiding," *IEEE Trans. Wireless Commun.*, vol. 17, no. 9, pp. 6082–6092, Sep. 2018.

[11] R. T. Rakesh, G. Das, and D. Sen, "An analytical model for millimeter wave outdoor directional non-line-of-sight channels," in *Proc. IEEE Int. Conf. Commun.*, May 2017, pp. 1–6.

[12] 3GPP, "Study on channel model for frequencies from 0.5 to 100 GHz," *3rd Gener. Partnership Project, Tech. Rep.* 38.901 V14.3.0, Dec. 2017.

[13] A. Ali and R. W. Heath, "Compressed beam-selection in millimeterwave systems with out-of-band partial support information," in *Proc. IEEE Int. Conf. Acoust., Speech Signal Process. (ICASSP)*, Mar. 2017, pp. 3499–3503.

[14] N. Srivastava, G. Hinton, A. Krizhevsky, I. Sutskever, and Ruslan Salakhutdinov, "Dropout: A simple way to prevent neural networks from overfitting," *J. Mach. Learn. Res.*, vol. 15, no. 1, pp. 1929–1958, Jan, 2014.

Paper B

Deep Transfer Learning for Location-aware Millimeter Wave Beam Selection

Sajad Rezaie, Abolfazl Amiri, Elisabeth de Carvalho, Carles Navarro Manchón

The paper has been published in the
IEEE Communications letters, vol. 25, no. 9, pp. 2963-2967, Sep. 2021.

The layout has been revised.

Abstract

The main bottleneck for using deep neural networks in location-aided millimeter wave beam alignment procedures is the need for large datasets to tune their large set of trainable parameters. This paper proposes to use the transfer learning technique in order to reduce the dataset size requirements in deep-learning based beam selection. Information transfer can be done from one environment to another, or from one antenna configuration to another, which we refer to as domain and task adaptation, respectively. Numerical evaluations show a significant gain in using transfer learning in both domain and task adaptation scenarios, especially with limited datasets.

Index Terms— millimeter wave, initial access, beam alignment, location-aided, orientation-aided, deep learning

1 Introduction

While the use of highly directional transmission in mmWave communications allows for high antenna gains, it introduces the challenge of aligning beams with the direction of the line of sight (LOS) or strong non LOS (NLOS) paths. To simplify the beam alignment procedure and also the radio frequency (RF) implementation, codebook-based analog beamforming has been proposed [1]. A simple approach is to exhaustively search over all combinations of the precoder and combiner configurations; however, this procedure suffers from high overhead and latency. As an alternative to the exhaustive search, hierarchical search methods have been proposed to reduce the latency by searching directions with different beam widths [1]. They suffer, however, from a degraded accuracy when dealing with low signal-to-noise ratio (SNR) at large beam widths. Context information-based (CI-based) beam alignment methods have been proposed to exploit contextual information such as user position and speed to address these challenges. CI can be obtained by either sensors on transceivers or out-band measurements which may cause additional overheads [2]. Making use of the context information of the user and environment, probabilistic data-driven methods propose a short list of candidate beams by leveraging the information in the training data [3].

Furthermore, machine learning techniques, especially reinforcement learning (RL) and neural networks (NNs), have been used to provide more accurate beam alignment using their high capability in non-linear problems [4, 5]. Although RL is a well-behaved solution for sequential decision-making problems, it needs constant interaction with the environment to find the optimal policy [6]. NNs can predict LOS blockage and yield accurate beam alignment, significantly outperforming look-up table type of algorithms such as inverse fingerprinting [7]. NN-based approaches, however, need a large training dataset to optimize all the trainable parameters in their networks. The

training datasets are specific to each deployment site and its propagation environment, as well as to the antenna array configurations used by BS and user [7, 8]. Due to the time and cost associated with measurement collection, the construction of these large training datasets constitutes the main obstacle to the use of neural networks in practice. As a solution to this problem, the transfer learning (TL) technique can be used to transfer parts of information in a network previously trained with a large dataset to another network for which only a small training dataset is available. The information can be transferred from an environment to another environment or from an antenna configuration to a different one, which are known in the research community as domain and task adaptation, respectively [9, 10].

In this paper, we propose a TL framework for location-based beam selection that optimizes the neural networks' parameters using small datasets. The proposed procedure can transfer useful information from a network trained with large datasets. We show the benefits of using TL techniques when it is not feasible to measure many samples at each environment and for each possible configuration. To benchmark the proposed method, we considered the two hierarchical beam-search (HBS) methods proposed by [1] and the deep learning (DL)-based beam alignment without TL in [7] as baselines. The numerical results, which are obtained based on ray-traced channel responses, show that the proposed method can reduce the performance gap of training with large and small datasets, and it also outperforms the baselines. Significant performance improvement is observed when applying TL in both cases: from an environment to another environment and from an antenna configuration to a different one.

2 System Model

We consider a 3-dimensional (3D) indoor downlink scenario consisting of a transmitter (TX) and a receiver (RX) equipped with uniform linear arrays (ULA) and operating in the mmWave frequency band. We assume that TX and RX ULAs are placed horizontally and are made respectively of N_t and N_r elements, with the elements separated by half a wavelength.

2.1 Channel Model

Without loss of generality, the transmitter is located at the origin of the coordinate system, $\boldsymbol{p}_t = (0, 0, 0)$, with fixed angle α_t, relative to the x-axis. The receiver is placed randomly inside the defined area at position $\boldsymbol{p}_r = (x_r, y_r, z_r)$ with a random orientation $\alpha_r \in [0, 2\pi)$. We only consider changes of the RX's ULA orientation in the azimuth plane.

The channel matrix between the transmitter and the receiver with one LOS and L non-line-of-sight (NLOS) paths, is modeled as

$$\boldsymbol{H} = \sum_{l=0}^{L} \sqrt{\rho_l}\, e^{j\vartheta_l}\, \boldsymbol{a}_r(\phi_{r,l}, \theta_{r,l})\, \boldsymbol{a}_t^H(\phi_{t,l}, \theta_{t,l}), \tag{B.1}$$

where $\boldsymbol{H} \in \mathbb{C}^{N_r \times N_t}$, ρ_l and ϑ_l are the receive power and the phase of the l-th path, respectively. Furthermore, $\phi_{r,l}$ and $\theta_{r,l}$ denote the azimuth and elevation angle of the AoA with respect to the receiver array axis. The antenna array response of the receiver, $\boldsymbol{a}_r$, is

$$\boldsymbol{a}_r(\phi_{r,l}, \theta_{r,l}) = \frac{1}{\sqrt{N_r}}[1, e^{j\pi sin(\theta_{r,l})\, cos(\phi_{r,l})}, \dots \\ , e^{j\pi(N_r-1)\, sin(\theta_{r,l})\, cos(\phi_{r,l})}]^T.$$

The antenna array response of the transmitter, $\boldsymbol{a}_t$, is analogously defined using the azimuth and elevation AoDs, $\phi_{t,l}$ and $\theta_{t,l}$, which are measured relative to the TX array axis.

2.2 Beam Codebook

Analog phase shifters have the ability to form beams by applying phase shifts to the signal of each antenna element. For simplicity, we employ discrete Fourier transform (DFT)-based codebooks with predefined precoders and combiners that steer the arrays in the azimuth direction. We define the precoders and combiners as

$$\begin{aligned} \boldsymbol{u}_p &= \boldsymbol{a}_t(\phi_p, \pi/2), \quad p \in \{1, \dots, N_t\}, \\ \boldsymbol{v}_q &= \boldsymbol{a}_r^H(\phi_q, \pi/2), \quad q \in \{1, \dots, N_r\}. \end{aligned}$$

where ϕ_p and $\phi_q \in [0, \pi)$ are $\arccos((2p - 1 - N_t)/N_t)$, and $\arccos((2q - 1 - N_r)/N_r)$, respectively.

The sets $\mathcal{U} = \{\boldsymbol{u}_1, \dots, \boldsymbol{u}_{N_t}\}$ and $\mathcal{V} = \{\boldsymbol{v}_1, \dots, \boldsymbol{v}_{N_r}\}$ denote the codebooks of all possible analog beamformers at the transmitter and the receiver, respectively. By applying the precoder $\boldsymbol{u}_p$ and combiner $\boldsymbol{v}_q$, the received signal strength (RSS) at the receiver may be expressed as

$$\mathbf{R}[p, q] = \left\| \sqrt{P_t} \boldsymbol{v}_q^H \boldsymbol{H} \boldsymbol{u}_p s + \boldsymbol{v}_q^H \boldsymbol{n} \right\|^2 \tag{B.2}$$

where P_t and $s \in \mathbb{C}$ are the transmission power and the known, unit power training symbol, respectively. Also, $\boldsymbol{n} \in \mathbb{C}^{N_r}$ denotes zero mean complex Gaussian noise variance σ_n^2.

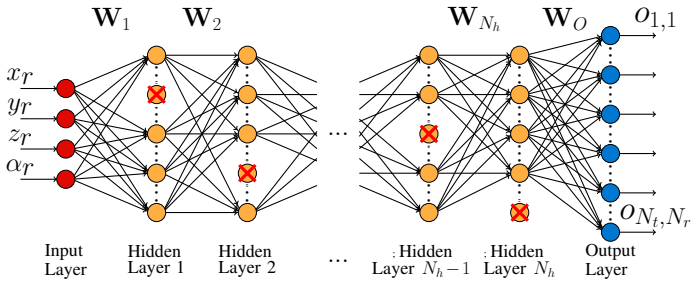

Fig. B.1: Deep neural network architecture of the beam alignment method using receiver coordinates and orientation as context information.

3 Transfer Learning for Beam Selection

Exploiting propagation environment information together with the position and orientation information helps to make the beam alignment procedure more robust against blockage, along with reducing the latency of the procedure. This prior knowledge is extractable from measurements in the same environment in a training phase. However, the mapping from context information of the receiver, accounting for the geometry of the environment, to the best beam alignment is a highly non-linear function. Due to the high capacity of neural networks to learn non-linear functions, deep neural networks (DNNs) are suitable for our problem. While DNN needs a large dataset to tune its parameters, capturing many samples at each environment is not feasible. TL is a technique that transfers the knowledge learned in a situation, usually with a large dataset, to improve the performance of learner in a new situation, usually with a smaller dataset.

3.1 Network Architecture

Fig. B.1 shows a proposal structure of a feedforward, fully-connected, deep neural network that predicts probabilities of each beam pair resulting in the largest RSS according to the coordinates and orientation of the receiver. This network design is inspired by the structure in [7], where each output corresponds to a unique beam pair. Thus, there are $N_t N_r$ outputs in the proposed network. Also, *tanh* and $softmax$ functions, respectively, are used as the non-linear activation functions of the hidden and output layers. The outputs of the deep neural network, $\mathbf{O}$, are the nonlinear functions of the input vector $\mathbf{x}$ as

$$\mathbf{O} = f^{(O)}_{\mathbf{W}_O} \circ f^{(N_h)}_{\mathbf{W}_{N_h}} \circ \ldots f^{(1)}_{\mathbf{W}_1}(\mathbf{x}) \tag{B.3}$$

where $h \circ g(x) = h(g(x))$. $f^{(i)}_{\mathbf{W}_i}$, $i = 1, \cdots, N_h$ and $f^{(O)}_{\mathbf{W}_O}$ denote the nonlinear transformation function of the N_h hidden layers and output layer, respectively. In addition, $\mathbf{W}_i$, $i = 1, \cdots, N_h$ denotes the matrix of all the trainable weights at the i-th hidden layer, and $\mathbf{W}_O$ includes all the trainable weights at the output layer of the network. Consider the set $\mathcal{W} = \{\mathbf{W}_1, \ldots, \mathbf{W}_{N_h}, \mathbf{W}_O\}$ which includes all the trainable parameters of the network. The number of trainable parameters depends on the number of neurons in each layer and also the number of considered hidden layers in the structure. According to the previous research, there are hundreds of thousands trainable weights in a fully connected neural network with enough capacity for mapping context information to beam pairs [4, 5, 7]. However, training a large number of parameters requires a large dataset, between $10,000$ to $100,000$ samples from the environment with a given antenna configuration at the transceivers [4, 7], which is a time- and cost-consuming operation.

To generate the training dataset of environment Ξ with M^{Ξ} user points, we calculate each beam pair's RSS using (B.2) for each user position and orientation in the user grid. The dataset $\mathbb{D}^{\Xi} = \{(\mathbf{x}^m, L^m)\}, m = 1, \cdots, M^{\Xi}$, is composed of M^{Ξ} pairs, where $\mathbf{x}^m$ and L^m, respectively, are the vector of the NN's input ($[x_r, y_r, z_r, \alpha_r]$) and the index of beam pair with the highest RSSs for m-th user. As L^m is the post-processed version of the received signals for all beam pairs, it implicitly contains the information about geometry and size of the environment. As an example, when the LOS is blocked, other strong paths determine the beam pair with the highest RSSs. So, the NN can learn, for a given location and orientation, which beam pairs have higher probability to be the best choice for transmission [7].

3.2 Transfer Learning

Transfer learning can be applied across domains and tasks, where the goal is to transfer knowledge between different environments or different tasks, respectively [9].

Domain Adaptation

Assume we have a large dataset of measurements in an environment, which we refer to as source domain, with N_t and N_r antenna elements at the TX and RX, respectively. Also, consider a network NET^S with ${N_h}^S$ and n^S hidden layers and neurons at each hidden layer, respectively, predicting the best beam pair accurately. Due to the availability of a large dataset, $\mathbb{D}^S$, the weights of the network NET^S can be initialized with random values and be trained by a standard backpropagation algorithm. On the other hand in a second environment, which we refer to as destination domain, only a limited-size dataset, $\mathbb{D}^D$, with the same antenna configuration as the source domain is available. If

we consider another network NET^D with the same number of layers and neurons as NET^S, there is a chance to reuse $\mathcal{W}^S$, the trained weights of network NET^S. The information learned from the source domain can be transferred to the destination by using $\mathcal{W}^S$ as the initial values of the trainable weights for NET^D. By way of explanation, NET^D leverages $\{\mathcal{W}^S, \mathbb{D}^D\}$ to optimize its nonlinear transformation functions.

Although the weights $\mathcal{W}^S$ do not contain information about the propagation environment in the destination domain, they are enough for the network to predict the beam pair corresponding to the LOS, which is a non-linear function. By transferring the trained weights $\mathcal{W}^S$ to NET^D, having to re-learn such mapping in the destination domain is avoided. The Network NET^D can tune its parameters to consider the NLOS cases in the destination environment with few measurements. As the input and output spaces are the same for both NET^S and NET^D, the TL is inductive and homogeneous [9].

Task Adaptation

Collecting many measurements of the environment with all possible antenna configurations for TX and RX is clearly infeasible. Using TL, the knowledge about a given propagation environment that is present in a dataset obtained with a specific antenna configuration can be partly reused in other antenna setups. The hypothesis is that, by using this technique, only a small training dataset with the new antenna configuration is required to obtain acceptable performance. We denote with NET^B and NET^T the beam selection networks at the same environment with the base and target antenna configurations of transceivers $\{N_t^B; N_r^B\}$ and $\{N_t^T; N_r^T\}$, respectively. Both networks have exactly the same structure and number of neurons except for their output layers, whose dimensions follow their specific antenna configurations: $N_t^B N_r^B$ neurons in NET^B and $N_t^T N_r^T$ in NET^T.

Assume the network NET^B is accurately trained due to the large training dataset $\mathbb{D}^B$, and it reliably provides the best beam pair at the base configuration. Since both networks use samples from the same environment and the first layers of a deep neural network can be seen as a feature extraction module [12], the weights corresponding to the initial layers of NET^B can be used as initialization of the corresponding weights at NET^T. Thus, the learned mapping from position and orientation of RX to appropriate directions can be transferred. Since the structure of both networks is the same for their input and hidden layers, we use the trained weights for the base antenna configuration $\mathbf{W}_1^B, \mathbf{W}_2^B, \ldots \mathbf{W}_{N_h}^B$ as initial values for the weights $\mathbf{W}_1^T, \mathbf{W}_2^T, \ldots \mathbf{W}_{N_h}^T$ in the target configuration network NET^T. As the output layers have different dimensions in both networks, we use random initialization of the weights $\mathbf{W}_O^B$ at the output layer of NET^T. Weights of NET^T are then fine-tuned with a dataset obtained with the target antenna configuration. Contrary to do-

main adaptation, the learned mapping between coordinate and beam indices in LOS and NLOS situations is transferred partially to NET^T. As the output spaces in NET^B and NET^T are different, the TL is categorized as inductive and heterogeneous [9].

Freezing Trainable Parameters

The hidden layers of the network can be seen as the part learning the most common directions for each input $\mathbf{x}$, while the output layer maps these directions to the right beamforming codewords. With this interpretation, as in the domain adaptation the codebook is the same, we have the option to freeze the output layer after loading $\mathbf{W}_O^S$. In the task adaptation case the environment is the same, so the weights of the hidden layers can be frozen after loading $\mathbf{W}_1^B, \mathbf{W}_2^B, \dots \mathbf{W}_{N_l}^B$, with only the last layer being fine-tuned. Freezing these layers decreases the number of trainable parameters in the network, which improves performance especially when few samples are available for training.

4 Simulation Results and Discussions

We present numerical evaluations to compare the proposed TL based beam selection with two baselines: the DL-based method without TL [7] and hierarchical beam-search [1]. We consider a 3D scenario with three different environments, an anechoic chamber (AC), a conference room (CR), and a living room (LR), which are shown in Fig. B.2. The AC represents an environment without any scatterers, where only the LOS path is present in the wireless channel. The CR and LR are described in detail by IEEE 802.11ad task group [11], and their datasets are generated with half of the instances in LOS conditions and the other half in NLOS conditions. The main information about the indoor environments is summarized in Table B.1. The different indoor environments are used to assess the TL idea in the domain adaptation case.

We use the accurate ray-tracing tool, Altair Feko-Winprop software [13] to generate channel responses. The ray tracing tool provides all the necessary information such as the angle of departure (AoD), angle of arrival (AoA), path gains, etc. for all paths to construct accurately the channel response between the TX and RX using (B.1). In the ray-tracing tool, empirical losses for transmission, reflection and diffraction are considered. We use the 25 strongest paths at each receiver location to construct the channel response.

The parameters $P_t = 0\,\text{dBm}$ and $\sigma_n^2 = -84\,\text{dBm}$ are used in the dataset generation step. After generating the datasets by calculating the RSS for each beam pair at each user position, 80% of each dataset is used to train a net-

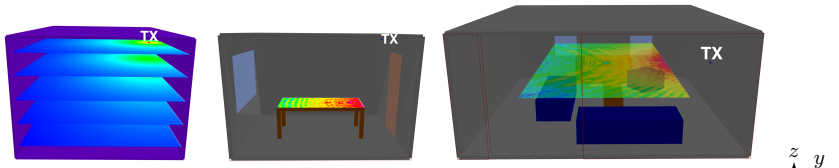

(a) AC **(b)** CR **(c)** LR

Fig. B.2: Three standard indoor environments where the rooms have different dimensions and static objects. The LOS power is illustrated for the user grids of the environments.

Table B.1: Geometrical information of the indoor environments

	Dimension (m)	AP's pos. (m)	User grid (m)	Dataset size
AC	$4 \times 5 \times 3$	$(3.5, 2.5, 2.5)$	$[0-3.5] \times [0-5] \times [0.5-2.5]$	90,000
CR	$4 \times 3 \times 3$	$(4, 1.5, 2.9)$	$[1-3.5] \times [1-2] \times [1]$	6,250
LR	$7 \times 7 \times 3$	$(7, 3.5, 1.5)$	$[1.5-5.5] \times [0-7] \times [1.5]$	70,000

work and the rest for the evaluation process. Thus, there are $72,000$, $5,000$, and $56,000$ samples for training in the AC, CR, and LR, respectively. On the structure of all neural networks, we consider 5 hidden layers with 128 neurons at each layer and 10% dropout for all hidden layers to prevent overfitting. Adam optimizer with 50 epochs is used to train the neural network, with a minibatch size gradually increasing from 32 to 8192 samples [7]. Also, the labels are converted to one-hot vectors which are used in the calculation of the cross entropy as loss function. To replicate the simulation results, the code and datasets are available in `https://github.com/SajadRezaie/DeepTLBeamSelection`. In the evaluations, we consider three training-based approaches:

1. **DNN**: The DNN method with random weight initialization and trained on the destination/target datasets,

2. **DNN-TL**: The DNN method in which source weights are used as initialization, and all layers are fine tuned with the destination/target dataset,

3. **DNN-TL-FR**: The DNN method in which source weights are used as initialization, and some layers (the output layer and hidden layers, respectively, in domain and task adaptation) are frozen and the rest are fined tuned witht the destination/target dataset.

To assess the effects of the TL technique in the domain adaptation scenario, we consider 64 and 16 antenna elements, respectively, at the TX and RX of the 3 environments. We train the network NET^S in the AC as source domain, with a large training dataset $\mathbb{D}^S$ including $72,000$ realizations. For fine-tuning of the network NET^D at the destination domain CR or LR, we

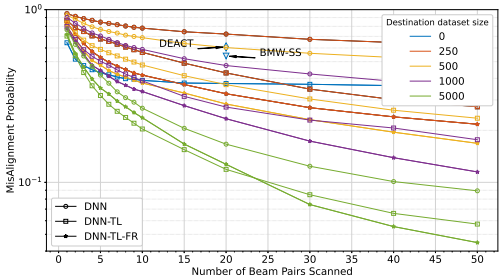

(a) Destination domain: the CR

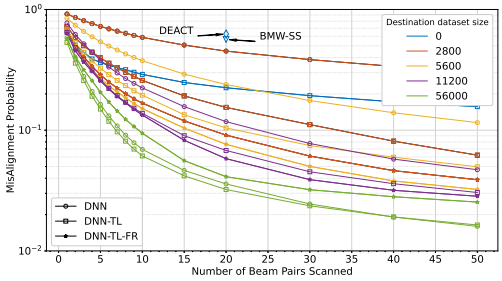

(b) Destination domain: the LR

Fig. B.3: Misalignment probability of DL-based beam alignment with and without using TL for domain adaptation. The full destination training dataset includes $5,000$ and $56,000$ samples at the CR and LR, respectively.

use a subset of the training dataset to evaluate the impacts of the destination dataset size on the TL performance.

Fig. B.3 shows the misalignment probability, i.e. the probability of missing the best beam pair in a candidate list with limited size N_b, of different beam selection methods by processing only a portion of the destination dataset at the CR or LR. We consider both of the CR or LR as a destination domain to evaluate the effects of different propagation properties and different dataset sizes at the TL process. The plots with 0 samples depict the case where no samples captured at the destination environment are used, and there is no fine-tuning in the TL method. We also show the beam selection method's performance using the full datasets to have a lower bound for comparison. Besides, the performance of two hierarchical beam-search methods (DEACT and BMW-SS) from [1] is shown, where the number of beam pair scans needed by these methods is fixed and fully determined by the antenna array configurations (20 in this case).

As illustrated in Fig. B.3, when training with a very limited dataset (5% of the training dataset) a significant improvement in the beam alignment is achievable using the TL technique. Furthermore, by freezing the output layer with 132096 parameters, the number of trainable parameters decreases from

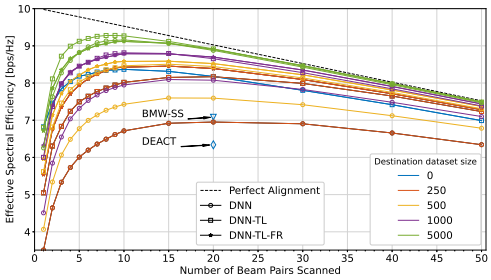

Fig. B.4: Spectral efficiency of different beam alignment at the CR, with the option of transferring learned knowledge from the AC.

198784 to 66688. Freezing around 66% of the weights helped the network to work better especially with very few training samples in the destination domain. As shown in Fig. B.3, the proposed beam selection method using the TL technique outperforms both the DEACT and BMW-SS methods. The results show transferring only the LOS information from the source domain AC can be very useful.

Fig. B.4 shows the achievable spectral efficiency using hierarchical and DL-based beamforming. By assuming a fixed channel coherence time, the proportion of channel resources used for beam alignment for each coherence time period is subtracted from the system's achievable rate. Hence, the effective spectral efficiency can be defined as

$$\mathrm{SE}_{\mathrm{eff}} = \frac{T_{fr} - N_b T_s}{T_{fr}} \log_2(1 + \mathrm{SNR}_{p,q}), \tag{B.4}$$

where T_s and T_{fr} denote the time required to scan a beam pair in beam alignment process and the time duration of one frame with fixed channel response, respectively [14]. Also, $\mathrm{SNR}_{p,q}$ is the SNR corresponding to the selected beam pair (p, q) after the beam alignment phase, and is defined as

$$\mathrm{SNR}_{p,q} = \frac{\left\| \sqrt{P_t} \boldsymbol{v}_q^H \boldsymbol{H} \boldsymbol{u}_p s \right\|^2}{\sigma_n^2}. \tag{B.5}$$

In the simulations, we consider $T_{fr} = 20$ms and $T_s = 0.1$ms [14]. Contrary to HBS, in which the number of scanned beam pairs is fixed, N_b can be tuned in the DL methods by adjusting the candidate beam list size. By using TL and freezing the output layer, DL-based beamforming provides the same spectral efficiency as HBS methods with only 3 scanned beams, hence reducing the alignment latency by 85%.

The capability of TL in the task adaptation problem is shown in Fig. B.5, where the tasks are beam alignment with different antenna configurations

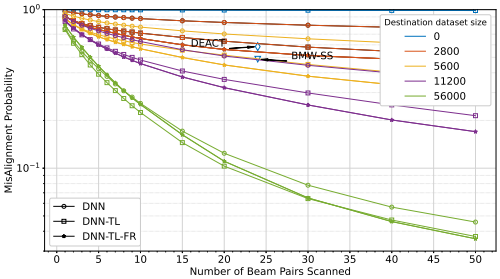

Fig. B.5: The different beam alignment performance at the LR with antenna configuration of transceivers $\{64;64\}$, where the learned knowledge from the same environment with $\{64;16\}$ antenna elements can be transferred.

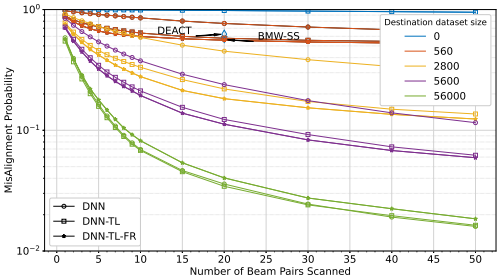

Fig. B.6: Misalignment probability of the beam alignment methods at the LR with antenna configuration of transceivers $\{64;16\}$, with weights being transferred from the same environment with configuration $\{64;64\}$.

in a same environment. At the LR, a large dataset is captured with TX and RX having 64 and 16 antenna elements, respectively. In the same environment, we collect a small dataset with antenna configuration of transceivers $\{64;64\}$. In line with our expectation, increasing the dataset size lowers the misalignment probability, and using TL proves to be more useful with more limited datasets. In addition, Fig. B.6 shows the performance of different beam alignment methods in the reverse case, where the target task is alignment of transceivers with $\{64;16\}$ antenna elements, and we can transfer the trained weights with $\{64;64\}$ antenna elements. Since beam alignment with antenna configuration $\{64;16\}$ is easier than $\{64;64\}$, smaller target dataset sizes are needed to obtain acceptable performance. As illustrated in Fig. B.6, freezing the hidden layers helps to have better performance, but not as much as the domain adaptation case. The reason is that here we freeze only around 34% of the parameters. These improvements prove the potential of using the TL technique across neural networks of different dimensions, even when the output layer is initialized with random weights.

5 Conclusion

The findings of this paper have shown that transfer learning techniques, in particular parameter reuse, can be leveraged to significantly reduce the training data requirements for deep neural networks performing location- and orientation-based beam alignment. Trained neural network weights can be effectively reused in other propagation environments or antenna configurations by fine tuning them with small datasets in the destination environment or the target antenna setup. Future research will focus on exploring more sophisticated transfer learning techniques, and extending the deep learning paradigm to location-aware beam tracking.

References

[1] Z. Xiao, T. He, P. Xia and X. Xia, "Hierarchical Codebook Design for Beamforming Training in Millimeter-Wave Communication," *IEEE Trans. Wireless Commun.*, vol. 15, no. 5, pp. 3380–3392, May 2016.

[2] M. Kok, J. D. Hol and T. B. Schön, "Using Inertial Sensors for Position and Orientation Estimation", *Found. Trends Signal Process.*, vol. 11, nos. 1-2, pp. 1–153, 2017.

[3] V. Va, J. Choi, T. Shimizu, G. Bansal and R. W. Heath, "Inverse multipath fingerprinting for millimeter wave V2I beam alignment," *IEEE Trans. Veh. Technol.*, vol. 67, pp. 4042–4058, May 2018.

[4] M. Alrabeiah and A. Alkhateeb, "Deep Learning for mmWave Beam and Blockage Prediction Using Sub-6GHz Channels," *IEEE Trans. Commun.*, vol. 68, no. 9, pp. 5504–5518, Sep. 2020.

[5] W. Xu, F. Gao, S. Jin and A. Alkhateeb, "3D Scene Based Beam Selection for mmWave Communications," *IEEE Commun. Lett.*, 2020.

[6] Z. Zhu and K. Lin, and J. Zhou, "Transfer Learning in Deep Reinforcement Learning: A Survey," *arXiv*:2009.07888, Sep. 2020, [Online] Available: https://arxiv.org/abs/2009.07888.

[7] S. Rezaie, C. N. Manchón, and E. D. Carvalho, "Location- and Orientation-Aided Millimeter Wave Beam Selection Using Deep Learning," in *Proc. IEEE Int. Conf. Commun.*, Jun. 2020, pp. 1–6.

[8] C. Lin, W. Kao, S. Zhan and T. Lee, "BsNet: A Deep Learning-Based Beam Selection Method for mmWave Communications," in *Proc. IEEE 90th Veh. Technol. Conf.*, Sep. 2019, pp. 1–6.

[9] F. Zhuang et al. “A Comprehensive Survey on Transfer Learning,” in *Proc. of the IEEE*, vol. 109, no. 1, pp. 43–76, Jan. 2021.

[10] W. Alves, I. Correa, N. González-Prelcic and A. Klautau, “Deep Transfer Learning for Site-Specific Channel Estimation in Low-Resolution mmWave MIMO,” *IEEE Wireless Commun. Lett.*, Mar. 2021.

[11] A. Maltsev et al., “Channel models for 60 GHz WLAN systems,” *IEEE Document*, 802.11-09-0334r6, Jan. 2010.

[12] Y. Bengio, A. Courville and P. Vincent, “Representation Learning: A Review and New Perspectives,” *IEEE Trans. Pattern Anal. Mach. Intell.*, vol. 35, no. 8, pp. 1798–1828, Mar. 2013.

[13] Altair Feko Winprop, https://www.altair.com/feko-applications.

[14] M. Hussain and N. Michelusi, “Second-Best Beam-Alignment via Bayesian Multi-Armed Bandits,” in *Proc. IEEE GLOBECOM*, Dec. 2019, pp. 1–6.

Paper C

A Deep Learning Approach to Location- and Orientation-aided 3D Beam Selection for mmWave Communications

Sajad Rezaie, Elisabeth de Carvalho, Carles Navarro Manchón

The paper has been published in the
IEEE Transactions on Wireless Communications, vol. 21, no. 12, pp. 11110-11124, Dec. 2022.

The layout has been revised.

Abstract

Position-aided beam selection methods have been shown to be an effective approach to achieve high beamforming gain while limiting the overhead and latency of initial access in millimeter wave (mmWave) communications. Most research in the area, however, has focused on vehicular applications, where the orientation of the user terminal (UT) is mostly fixed at each position of the environment. This paper proposes a location- and orientation-based beam selection method to enable context information (CI)-based beam alignment in applications where the UT can take arbitrary orientation at each location. We propose three different network structures, with different amounts of trainable parameters that can be used with different training dataset sizes. A professional 3-dimensional ray tracing tool is used to generate datasets for an IEEE standard indoor scenario. Numerical results show the proposed networks outperform a CI-aided benchmark such as the generalized inverse fingerprinting (GIFP) method as well as hierarchical beam search as a non-CI-based approach. Moreover, compared to the GIFP method, the proposed deep learning-based beam selection shows higher robustness to different line-of-sight blockage probability in the training and test datasets and lower sensitivity to inaccuracies in the position and orientation information.

Index Terms— millimeter wave, beam alignment, deep learning, transfer learning, domain adaptation, task adaptation

1 Introduction

Emergent services such as virtual and augmented reality or high definition multimedia applications are gaining increasing popularity and will be commonplace in beyond 5G systems. Their large data-rate demands can only be satisfied using large portions of available bandwidth, which millimeter wave (mmWave) bands currently offer [1]. Although higher propagation and penetration losses in mmWave bands make mmWave communication a good choice for establishing a network in small cells, those properties, besides the lack of diffraction in mmWave frequencies, make it difficult to establish reliable mmWave links [2]. Multiple-input multiple-output beamforming is an inseparable part of mmWave communication, as it allows for compensating for the higher path loss compared to sub-6 GHz communications. To establish a high-quality directional link, transceivers need to transmit and receive over the direction of the line-of-sight (LOS) path or a powerful non-line-of-sight (NLOS) path in case the LOS is blocked. Thus the selection of appropriate beamforming and combining solutions at mmWave transceivers' antenna arrays is a crucial and challenging task [3].

Codebook-based beamforming is an attractive solution to reduce the complexity of the beam selection problem as well as the radio-frequency (RF)

implementation of beamformers. It considers predefined directional beam configuration sets for precoder and combiner at access point (AP) and user terminal (UT), respectively [4]. Analog or hybrid beamforming is usually employed to construct the beams in the codebook. Although the optimal precoder and combiner configurations can be determined by exhaustively searching over all possible combinations of beamformers at the AP and UT, this results in undesirably high overhead and latency. Hierarchical beam search (HBS) is an alternative approach that reduces the search space of the beam alignment (BA) procedure by progressively sensing the environment with narrower beam widths based on the counterpart's feedback [4, 5]. However, HBS methods suffer a degradation in accuracy due to low antenna gain and insufficient spatial resolution when using large beam widths, which lead to wrong decisions in the search procedure. To address these downsides, machine learning (ML)-based methods can be used to obtain solutions that are optimized using measurement data obtained at specific deployments without the need for a model of the channel or the propagation scenario. The authors of [6] propose an ML-based framework that designs adaptive compressed sensing beamformers, which helps estimate the posterior distribution of the angle of arrival (AoA) of the dominant path. Estimates of the AoA and power of the dominant path of users are fed to support vector classifiers and neural networks to perform beam selection in a mmWave communication link in [7]. However, these methods are designed to perform initial BA in a mmWave environment assuming a single-path channel and are therefore susceptible to performance degradation in multipath conditions. As a new approach to estimates the AoA, a deep-learning based framework is proposed in [8] that uses the unique patterns in the in-phase-quadrature representation of each beam.

Another avenue to achieve high beamforming accuracy while limiting the overhead and latency of BA is to exploit context information (CI) about the users and/or environment. In CI-based methods, different types of sensors on transceivers or out-band channel measurements are used to acquire CI, at the cost of power and device complexity [9]. As an example of such methods, the inverse fingerprinting (IFP) method in [10] recommends a candidate beam list based on the location of the user and the history of optimal beam pairs in the training examples. Furthermore, ML-based methods have been widely used to exploit context information and achieve higher accuracy owing to their unparalleled capability in dealing with non-linear problems. Reinforcement learning (RL) and deep neural networks (DNNs) are the two areas of machine learning most frequently employed in mmWave BA [11–13]. For instance, an RL-based method that uses historical beam management data in a specific environment to reduce the beam training overhead is presented in [14]. However, a large number of interactions with the environment are needed before a RL agent is able to learn the optimal policy [15]. A neural

network (NN)-based method is proposed in [16] that uses sub-6 GHz channel measurements as input and exploits the spatial correlation between the sub-6 GHz and mmWave links to predict the best beam for data transmission in the mmWave band. For vehicular-to-everything (V2X) application, RADAR signals from joint sensing and communication functionalities at road side units are used for the beamforming of vehicular links in [17]. Also, the authors of [18] propose an ML-based structure that fuses LIDAR data and the position of vehicles to propose a more accurate beam selection method by exploiting knowledge about the obstacles in the environment. As another way of detecting static and mobile obstacles and predicting future link blockage, images from cameras placed in the environment are processed using computer vision and deep learning techniques in [13, 19, 20].

Although NN-based BA methods achieve the best performance in beam initialization, beam tracking, and blockage prediction, they require large amounts of training data at each deployment site and for each array configuration [16]. As a solution, the transfer learning technique is used in [21] to reuse the knowledge learned by the NN from a previous environment and array configuration in a new setup. Moreover, one of the key challenges for beam management in beyond 5G systems is device rotation [22]. It becomes more critical as beams in directional codebooks usually have unequal beamwidths and, therefore, the effects of rotation on the received signal strength (RSS) at each beam cannot be fully predicted by the beams' RSS before rotation. In addition, the mentioned machine learning approaches are mainly focused on the V2X application, where the orientation of the UT array can typically be inferred from the vehicle position. The authors of [23] proposed a beam management method using particle filters that exploits the knowledge of changes in the orientation of the user device to track the best beam at the user side. However, this method is limited to beam tracking only at the UT, and it is assumed that the BS has genie-aided knowledge of the best transmit beam.

1.1 Contributions

To address the above-mentioned gaps, we consider the initial BA problem for mmWave communication where the UT can take an arbitrary orientation and position. This study focuses on indoor environments and handset terminals, contrary to many of the works focusing on outdoor V2X communications. We propose a deep learning-based initial BA framework that considers the handset's position and rotation. The proposed solution yields a list of recommended beam pairs that should, later, be sensed by AP and UT. This approach results in a drastic reduction of the overhead compared to exhaustive search and a significantly improved accuracy compared to HBS. The beam recommendation solution operates using only the position and orientation

information of the UT handset as an input. A first version of the method was presented in [24] where an ML-based beam selection method can handle the handset's position and rotation in a 2-dimensional environment. Compared to it, this paper has the following contributions:

1. We generated datasets using Altair Feko-Winprop software [25] as a professional ray-tracing tool. Since UTs can take any arbitrary rotation in a 3-dimensional (3D) environment, it significantly increases the problem's non-linearity. In addition, instead of a uniform linear array (ULA), we use a uniform planar array (UPA) at both sides of the communication links to investigate the effects of rotations in 3D space on the BA of horizontal and vertical beamforming.

2. We present three different neural networks: single task (ST), multi-task (MT), and extended multi-task (EMT) structures to make accurate beam recommendations with different training dataset sizes. In the MT structure, we solve the problem of the AP and UT beamforming as separate tasks. We extend this idea to also separate vertical and horizontal beamforming in the EMT structure. The MT and EMT structures have significantly fewer trainable parameters than the ST one, resulting in faster performance in the training and running mode at the expense of a slight accuracy loss.

3. To enhance the performance of the deep learning-based method, we use the multi-labeling technique to train the NNs. This technique helps the network learn more about the environment and the possible NLOS paths at each location. The effects of the multi-labeling technique on all the three structures DNN-ST, DNN-MT, and DNN-EMT are investigated.

4. We evaluate the sensitivity of the data-driven-based methods to estimation errors in the location and orientation information by training and evaluating the proposed algorithms with inaccurate CI. In another experiment, we assess the robustness of the proposed deep learning-based methods against mismatch between the channel conditions present in the training and test datasets.

5. Our proposed method's performance is compared against several benchmarks. Besides ideal BA, we generalize the inverse fingerprinting method in [10] to deal also with arbitrary orientation of user handset. In order to compare with a non-CI based method, we extend the deactivation (DEACT) method in [4] to perform 3D HBS using UPAs. The proposed deep learning-based beam selection methods significantly outperform the generalized inverse fingerprinting (GIFP) and DEACT methods in terms of accuracy and latency of initial access BA.

1.2 Organization and Notations

First, the system model, channel model, and codebook definition are described in Section 2. The general description of the beam alignment problem and two possible approaches for dealing with the problem are given in Section 3. In Section 4, we present the three proposed structures for the DNN. The simulation setup and numerical results are presented in Section 5. Conclusions are drawn in Section 6.

In this paper, $\mathbb{R}$ and $\mathbb{C}$ respectively denote the fields of real and complex numbers. $\mathcal{A}$ denotes a finite set, with $|\mathcal{A}|$ being its cardinality. Also, a, $\boldsymbol{a}$, and $\boldsymbol{A}$ denote a scalar, a vector, and a matrix, respectively, with a_i being the ith entry of the column vector $\boldsymbol{a}$, and $A_{i,j}$ is the entry in the ith row and jth column of the matrix $\boldsymbol{A}$. Transposition and complex transposition of vectors and matrices are respectively represented as $(\cdot)^T$ and $(\cdot)^H$, and $\otimes$ is the Kronecker product. In addition, $\arg\max_{i,j} A_{i,j}$ is the index of the maximum entry of matrix $\boldsymbol{A}$ as a tuple, and $\arg\operatorname{sort}_{i,j} A_{i,j}$ denote the list of indices (as tuples) of entries of matrix $\boldsymbol{A}$ sorted in descending order.

2 System Model

We consider a downlink communication system consisting of a fixed AP and a mobile UT operating in the mmWave frequency band. Both AP and UT are equipped with UPAs and are placed in a 3D propagation scenario. The received signal at the UT may be written as

$$\boldsymbol{y} = \sqrt{P_{\mathrm{AP}}}\boldsymbol{v}^H \boldsymbol{H}\boldsymbol{u}s + \boldsymbol{v}^H\boldsymbol{n} \tag{C.1}$$

where $\boldsymbol{u}$ and $\boldsymbol{v}$ denote the precoder and combiner at AP and UT, respectively. Also, P_{AP}, $s \in \mathbb{C}$, and $\boldsymbol{n} \in \mathbb{C}^{N_{\mathrm{UT}}}$, respectively, are the transmission power, the transmitted symbol with unit power, and a complex Gaussian noise vector with zero mean and variance σ_n^2.

We assume that AP and UT UPAs are made respectively of $\{N_{\mathrm{AP_H}}, N_{\mathrm{AP_V}}\}$ and $\{N_{\mathrm{UT_H}}, N_{\mathrm{UT_V}}\}$ elements in horizontal and vertical dimensions, with the elements spaced half a wavelength apart in both dimensions. The total number of antenna elements at AP and UT is $N_{\mathrm{AP}} = N_{\mathrm{AP_H}} N_{\mathrm{AP_V}}$ and $N_{\mathrm{UT}} = N_{\mathrm{UT_H}} N_{\mathrm{UT_V}}$, respectively. We consider a global coordinate system (GCS) for the environment, and the positions and orientations of AP and UT are defined in the GCS. In addition, both AP and UT have their own local coordinate systems (LCS), shown in Fig. C.1. The LCS is selected such that the UPA is oriented parallel to the xz plane. We assume the AP is placed at fixed position $\boldsymbol{p}_{\mathrm{AP}} = (x_{\mathrm{AP}}, y_{\mathrm{AP}}, z_{\mathrm{AP}}) \in \mathbb{R}^3$ with fixed angles of

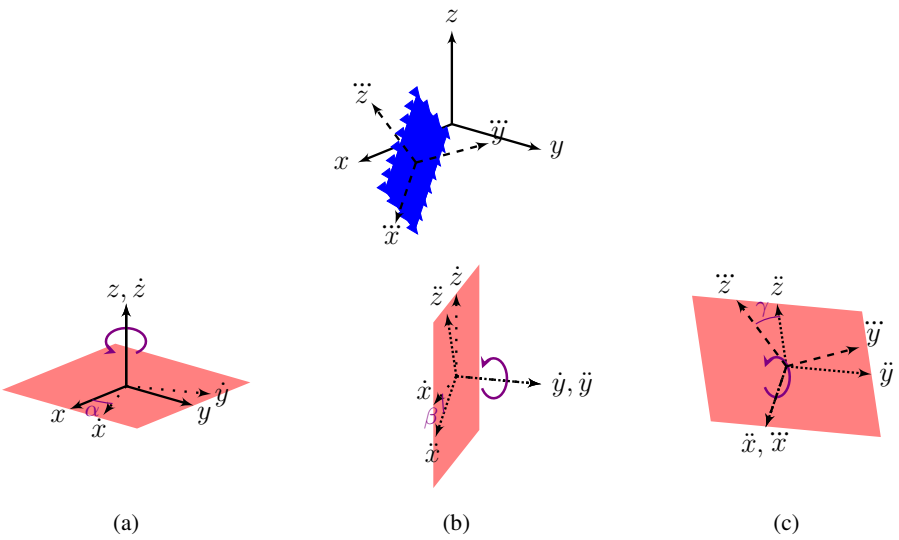

Fig. C.1: By rotating around the x, y, and z axes, a transition from the global coordinate system $(x\,y\,z)$ to any arbitrary local coordinate system $(\dddot{x}\ \dddot{y}\ \dddot{z})$ is possible. The red rectangles show the rotation planes at three rotation steps. The coordinate systems $(\dot{x}\,\dot{y}\,\dot{z})$ and $(\ddot{x}\,\ddot{y}\,\ddot{z})$ show the rotated versions of $(x\,y\,z)$ after the first and second rotation around z and $\dot{y}$ axes, respectively.

antenna arrays $\boldsymbol{\psi}_{\mathrm{AP}} = (\alpha_{\mathrm{AP}}, \beta_{\mathrm{AP}}, \gamma_{\mathrm{AP}})$ rotated around z, y, and x axes, respectively. Also, the UT can be placed randomly in the environment at position $\boldsymbol{p}_{\mathrm{UT}} = (x_{\mathrm{UT}}, y_{\mathrm{UT}}, z_{\mathrm{UT}}) \in \mathbb{R}^3$ with orientation $\boldsymbol{\psi}_{\mathrm{UT}} = (\alpha_{\mathrm{UT}}, \beta_{\mathrm{UT}}, \gamma_{\mathrm{UT}})$ where the orientation angles are uniformly random in the ranges $\alpha_{\mathrm{UT}} \in [-\pi, \pi)$, $\beta_{\mathrm{UT}} \in [-\pi/4, \pi/4)$, and $\gamma_{\mathrm{UT}} \in [-\pi/4, \pi/4)$. The relation between the GCS, LCS and the orientation angles is illustrated in Fig. C.1. This study assumes that all the devices share the same reference system for estimating the device orientation.

2.1 Channel Model

We use Altair WinProp$^{\mathrm{TM}}$ software package [25] to generate channel responses at each UT point in the environment based on the ray-tracing technique. The outputs of the ray-tracing tool such as the angle of departure (AoD), AoA, path gains, etc. for all paths between the AP and each user point are reported as results of the ray-tracing tool. We collect channel responses of UT points at each scene of the environment. The dataset generation steps and assumptions are explained in detail in Section 4.1.

By applying a narrow band channel model on the contributions of one LOS and L NLOS paths, the channel matrix $\boldsymbol{H} \in \mathbb{C}^{N_{\mathrm{UT}} \times N_{\mathrm{AP}}}$ between the AP

and UT is modeled as

$$\boldsymbol{H} = \sum_{l=0}^{L} \sqrt{\rho_l}\, e^{j\vartheta_l}\, \boldsymbol{a}_{\mathrm{UT}}(\phi_l^A, \theta_l^A)\, \boldsymbol{a}_{\mathrm{AP}}^H(\phi_l^D, \theta_l^D) \tag{C.2}$$

where ρ_l and ϑ_l are the receive power and the phase of the lth path, respectively. Also, ϕ_l^A and θ_l^A denote the azimuth and elevation AoAs with respect to the UT array plane. Likewise, ϕ_l^D and θ_l^D are the azimuth and elevation AoDs with reference to the AP array plane. The antenna array response of the UT and AP, respectively $\boldsymbol{a}_{\mathrm{UT}} \in \mathbb{C}^{N_{\mathrm{UT}} \times 1}$ and $\boldsymbol{a}_{\mathrm{AP}} \in \mathbb{C}^{N_{\mathrm{AP}} \times 1}$, can be written as

$$\boldsymbol{a}_{\mathrm{UT}}(\phi_l^A, \theta_l^A) = \frac{1}{\sqrt{N_{\mathrm{UT}}}} \boldsymbol{a}_{\mathrm{E}}(N_{\mathrm{UT_V}}, \theta_l^A) \otimes \boldsymbol{a}_{\mathrm{A}}(N_{\mathrm{UT_H}}, \phi_l^A, \theta_l^A), \tag{C.3}$$

$$\boldsymbol{a}_{\mathrm{AP}}(\phi_l^D, \theta_l^D) = \frac{1}{\sqrt{N_{\mathrm{AP}}}} \boldsymbol{a}_{\mathrm{E}}(N_{\mathrm{AP_V}}, \theta_l^D) \otimes \boldsymbol{a}_{\mathrm{A}}(N_{\mathrm{AP_H}}, \phi_l^D, \theta_l^D) \tag{C.4}$$

where $\boldsymbol{a}_{\mathrm{A}} \in \mathbb{C}^{N \times 1}$ and $\boldsymbol{a}_{\mathrm{E}} \in \mathbb{C}^{N \times 1}$ are

$$\boldsymbol{a}_{\mathrm{A}}(N, \phi, \theta) = [1, e^{j\pi sin(\theta)\, cos(\phi)}, \ldots, e^{j\pi(N-1)\, sin(\theta)\, cos(\phi)}]^T, \tag{C.5}$$

$$\boldsymbol{a}_{\mathrm{E}}(N, \theta) = [1, e^{j\pi cos(\theta)}, \ldots, e^{j\pi(N-1)\, cos(\theta)}]^T. \tag{C.6}$$

2.2 Beam Codebook

We consider analog phased antenna array at both AP and UT. Analog electrically controlled phase shifters are passive devices that can control the signal phase at each array element. We use discrete Fourier transform (DFT)-based codebook to simplify the beamforming procedure where there is one RF chain at each transceiver side. The analog precoder at the AP and the analog combiner at the UT are defined as

$$\boldsymbol{u}_{p,q} = \boldsymbol{a}_{\mathrm{AP}}(\phi_p^D, \theta_q^D), \quad p \in \{1, \ldots, N_{\mathrm{AP_H}}\}, \quad q \in \{1, \ldots, N_{\mathrm{AP_V}}\}, \tag{C.7}$$

$$\boldsymbol{v}_{m,n} = \boldsymbol{a}_{\mathrm{UT}}(\phi_m^A, \theta_n^A), \quad m \in \{1, \ldots, N_{\mathrm{UT_H}}\}, \quad n \in \{1, \ldots, N_{\mathrm{UT_V}}\}. \tag{C.8}$$

where ϕ_p^D, θ_q^D, ϕ_m^A and θ_n^A are

$$\phi_p^D = \arccos \frac{2p - 1 - N_{\mathrm{AP_H}}}{N_{\mathrm{AP_H}}}, \;\; \theta_q^D = \arccos \frac{2q - 1 - N_{\mathrm{AP_V}}}{N_{\mathrm{AP_V}}}, \tag{C.9}$$

$$\phi_m^A = \arccos \frac{2m - 1 - N_{\mathrm{UT_H}}}{N_{\mathrm{UT_H}}}, \;\; \theta_n^A = \arccos \frac{2n - 1 - N_{\mathrm{UT_V}}}{N_{\mathrm{UT_V}}}. \tag{C.10}$$

By mapping all tuples (p, q) and (m, n) into the sets of integers $\{1, 2, \ldots, N_{\mathrm{AP}}\}$ and $\{1, 2, \ldots, N_{\mathrm{UT}}\}$, the sets $\mathcal{U} = \{\boldsymbol{u}_1, \ldots, \boldsymbol{u}_{N_{\mathrm{AP}}}\}$ and $\mathcal{V} = \{\boldsymbol{v}_1, \ldots, \boldsymbol{v}_{N_{\mathrm{UT}}}\}$ indicate all available analog precoders and combiners at the AP and the UT, respectively. By employing the precoder $\boldsymbol{u}_i$ and combiner $\boldsymbol{v}_j$ at the transceivers,

the (i, j)th entry of the RSS matrix, $\boldsymbol{R} \in \mathbb{R}^{N_{\mathrm{AP}} \times N_{\mathrm{UT}}}$, can be set as

$$R_{i,j} = \left\| \sqrt{P_{\mathrm{AP}}} \boldsymbol{v}_j^H \boldsymbol{H} \boldsymbol{u}_i s + \boldsymbol{v}_j^H \boldsymbol{n} \right\|^2. \tag{C.11}$$

In the BA phase, $s \in \mathbb{C}$ is a pilot symbol with unit power.

3 Beam Alignment Procedures

3.1 Context-Aware Beam Selection

The position and orientation of the UT can be used to predict the LOS direction. Although knowledge of the LOS direction is valuable, it is insufficient due to the frequent blockage occurrence in mmWave communications. Besides, the direction and strength of NLOS paths are environment-dependent. Information about the properties of the propagation environment can be obtained from extensive measurements obtained in the specific environment. It is important to note that obtaining the location and orientation information of the device comes at a price, and it may imply additional overhead or implementation cost to the system. However, we expect that the introduction of joint communication, sensing, and localization in upcoming beyond 5G systems will facilitate position- and orientation-aided BA [26]. In Section 4, we discuss two data-driven methods that use position and orientation information to recommend a list of beam pair candidates.

Consider $\mathcal{B}$ as a set of all possible combinations of precoders and combiners in the transceivers. In the exhaustive search approach, the environment is sensed with all members of $\mathcal{B}$, but this yields unacceptably high overhead [3]. Context information from the environment and the transceivers can boost the sensing phase of BA. In particular, context information such as geometrical properties of environment, position and orientation information of transceivers, etc. can be used to reduce the space of sensed precoders and combiners. Thus, in this approach, a candidate list $\mathcal{S}$ including a few beam pair indices is proposed based on the context information, where $|\mathcal{S}| \ll |\mathcal{B}|$. The probability of including the optimal beam-pair increases with the cardinality of $\mathcal{S}$, at the expense of increased latency in the beam-alignment process.

Fig. C.2a shows the beam selection process including the beam-training request and feedback in sub-6 GHz communication links. First, a beam-training request is sent from the UT, including the location and orientation information of the UT array. The AP uses the provided information to recommend a candidate beam list $\mathcal{S}$. Subsequently, the AP shares the beam list $\mathcal{S}$ with the UT. Then, as the AP and UT know their beamformer at each time interval, they start to sense all the beam pairs in $\mathcal{S}$. Then, the UT feeds back

the index of the beam pair which yielded the largest RSS. Note that in this work we assume that all control information exchanged over the sub-6 GHz link is conveyed error-free.

3.2 Hierarchical Beam Search

In contrast to the context-aware beam selection approach, the hierarchical beam search method does not need extra information about the environment or transceivers. In HBS, the AP and UT sense the environment with wide beams and gradually narrow down the beam-width to find the best beam pairs for transmission [3, 4]. As it is shown in Fig. C.2b, at the first stages AP transmits omnidirectionally, and UT finds the best combiner. Subsequently, AP tries to find its best precoder. At each step of the hierarchical search, it needs feedback from UT to find out the right direction for further search. Thus, $\log_2 N_{\mathrm{AP}}$ feedbacks are needed to be transmitted in HBS [4]. Again, we assume sub-6 GHz feedback to be error-free.

4 Data-Driven Beam Selection

In this section, we discuss the data collection phase as an important step for data-driven based methods and how the labeling can be done for different purposes. Then, we propose the deep-learning based beam selection methods with three novel structures: single-task, multi-task, and extended multi-task. In addition, the motivations for proposing each structure are explained.

4.1 Dataset structure and construction

As mentioned in the previous section, the properties of the propagation environment can be extracted from measurements in the specific site. The measurements captured in the particular environment can be collected in a dataset consisting of a set of inputs and outputs. Here, the position and orientation of measurements are the inputs, and the labels indicating the preferred beams for each input are the outputs.

In the data collection phase, the UT takes an arbitrary location and orientation at each scene of the environment. At each UT position and orientation, the measurements are captured by sensing the environment with all the possible combinations of precoders $\mathcal{U}$ and combiners $\mathcal{V}$ at the transceivers. Thus, the entries of $\boldsymbol{R}$ in (C.11) are set using the RSS measured using all beam pairs in the codebook. The entries of $\boldsymbol{R}$ are used to set the labels used in the collected datasets. In our work, we consider two types of label encoding options: the one-hot encoding scheme, and the multi-labeling scheme. In the one-hot

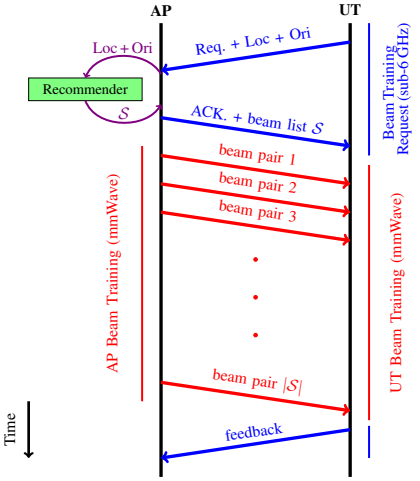

(a) Context-aware beam selection

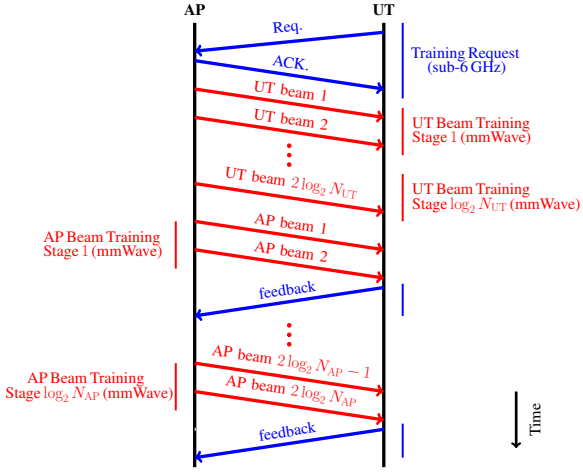

(b) Hierarchical beam search

Fig. C.2: The mmWave beam training procedure for the context-aware beam selection and hierarchical beam search approaches. In the former, the beam list is proposed based on the UT position and orientation.

encoding scheme, the beam pair with the highest RSS is marked in $\boldsymbol{L}$ as the label matrix, where

$$L_{i,j}^{(1)} = \begin{cases} 1, & \text{if } (i,j) = \arg\max\limits_{m,n} R_{m,n}, \\ 0, & \text{otherwise.} \end{cases} \tag{C.12}$$

In this case, in blockage-free situations the beam pair which covers the LOS path is marked[1]. When blockage occurs, we mark the beam pair covering the strongest NLOS path.

The one-hot encoding scheme labels only the strongest beam pair for each position and orientation, while all other beam pairs are treated equally. Since the purpose of the recommender in data-driven methods is to propose a list of several candidate beams, it may be useful to, instead, label multiple strong beam pairs as relevant, such that the recommender has information about the M-best beam pairs, rather than just the strongest one. As an example, in a LOS situation such labeling would allow marking both the beam pair capturing the LOS path and a few beam pairs aligned in the direction of strong NLOS paths. This would allow the recommender to, after training, provide a list of alternative candidate beams that can be used in the event that the LOS is blocked. Hence, in the M-hot encoding scheme ($M \in \{1, 2, \cdots, N_{\mathrm{AP}} N_{\mathrm{UT}}\}$), we mark the M best beam pairs with the M highest RSS in the label matrix $\boldsymbol{L}^{(M)}$ as

$$\boldsymbol{r} = \arg\operatorname*{sort}_{i,j} (R_{i,j}), \tag{C.13a}$$

$$\mathcal{T} = \{r_k | k = 1, \ldots, M\}, \tag{C.13b}$$

$$L_{i,j}^{(M)} = \begin{cases} 1, & \text{if } (i,j) \in \mathcal{T}, \\ 0, & \text{otherwise.} \end{cases} \tag{C.13c}$$

Therefore, each sample of the dataset contains the receivers coordinates ($\boldsymbol{p}_{\mathrm{UT}}$) and orientations ($\boldsymbol{\psi}_{\mathrm{UT}}$), the RSS matrix ($\boldsymbol{R}$), the type of encoding scheme (M), and the label matrix ($\boldsymbol{L}^{(M)}$). We represent the dataset as $\mathbb{D}^{\Xi} = \{(\boldsymbol{x}_m, \boldsymbol{L}_m^{(M)})\}, m = 1, \cdots, N^{\Xi}$, where $\boldsymbol{x} = [x_{\mathrm{UT}}, y_{\mathrm{UT}}, z_{\mathrm{UT}}, \alpha_{\mathrm{UT}}, \beta_{\mathrm{UT}}, \gamma_{\mathrm{UT}}]$ and N^{Ξ} shows the the dataset size. Indeed, $\boldsymbol{L}^{(M)}$ implicitly holds information about the propagation environment, as it is the post-processed form of $\boldsymbol{R}$. Thus, for given $\boldsymbol{x}$ the dataset contains information about the M strongest beam pairs for transmission, which can be exploited by probabilistic or machine learning based methods [24].

[1] The presence of measurement noise may impair labeling the LOS direction.

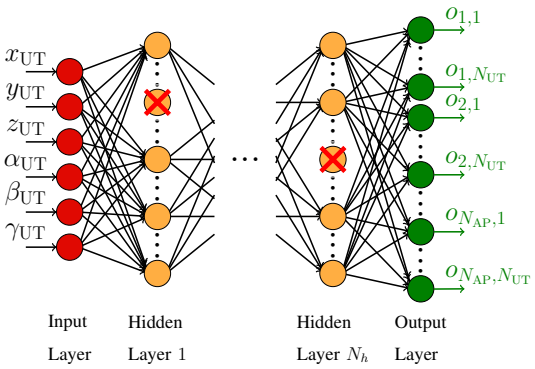

Fig. C.3: The proposed DNN architecture of the beam selection method using position and orientation information. We refer to this network with the term "single-task structure" as $N_{\mathrm{AP}}N_{\mathrm{UT}}$ neurons at its output layer correspond to all possible beam pairs.

4.2 Proposed Deep-Learning Based Methods

To extract the knowledge about the environment and beam patterns at the transceivers from the training data, probabilistic and machine learning based approaches are the two most popular strategies. In Section 4.3, we discuss a probabilistic beam selection method as a baseline to the proposed methods. Here, we discuss the motivations to use machine learning in beam selection and introduce our machine learning based beam selection methods.

As static and mobile scatterers in the site may change the propagation properties of the environment by blocking or reflecting paths with high power, beam selection leveraging both location and orientation information becomes a highly nonlinear classification problem. DNNs have shown remarkable achievements in learning complex nonlinear input-output relationships using training data in different applications [27]. Therefore, we choose DNNs as classifiers to predict the best beam pairs for transmission.

For training and evaluation of all the three proposed network structures, we use the labeling procedure described in (C.12) and (C.13). Categorical cross entropy is used as the loss function, $\mathcal{L}$, for training of all the three network structures, i.e.,

$$\mathcal{L}(\boldsymbol{o}, \boldsymbol{L}) = -\sum_{i=1}^{N_{\mathrm{AP}}} \sum_{j=1}^{N_{\mathrm{UT}}} L_{i,j} \log(o_{i,j}) \tag{C.14}$$

where $o_{i,j}$ and $L_{i,j}$ denote, respectively, the neural network's output and the label corresponding to the (i,j)th beam pair.

Single-Task Structure

As shown in Fig. C.3, the coordinates and orientations of the UT, $\boldsymbol{x} = [x_{\mathrm{UT}}, y_{\mathrm{UT}}, z_{\mathrm{UT}}, \alpha_{\mathrm{UT}}, \beta_{\mathrm{UT}}, \gamma_{\mathrm{UT}}]$, are fed as inputs to a feed-forward, fully connected, DNN. As the AP has fixed position and orientation, there is no need to explicitly feed this information to the NN. There are $N_{\mathrm{AP}} \times N_{\mathrm{UT}}$ neurons at the output layer, which correspond to all possible combinations of the N_{AP} and N_{UT} beams at the AP and UT, respectively. The network has N_h hidden layers with n_h neurons at each hidden layer. Neurons at the ith layer of the network, $\boldsymbol{y}^i$, are calculated as a non-linear function of all the neurons at the previous layer, $\boldsymbol{y}^{i-1}$, and the trainable parameters of the ith layer:

$$\boldsymbol{y}^i = \varpi(\boldsymbol{W}_i^c \boldsymbol{y}^{i-1} + \boldsymbol{w}_i^b), \qquad i \in \{1, \ldots, N_h + 1\} \tag{C.15}$$

where σ, $\boldsymbol{W}_i^c$ and $\boldsymbol{w}_i^b$ are the activation function, weights and biases of the ith layer, respectively. As it is illustrated in Fig. C.3, $\boldsymbol{y}^0$ and $\boldsymbol{y}^{N_h+1}$ are equal to the input and output vectors, $\boldsymbol{x}$ and $\boldsymbol{o}$, respectively. We define $\boldsymbol{W}_i = \{\boldsymbol{W}_i^c, \boldsymbol{w}_i^b\}$ which includes all the trainable parameters in the ith layer. We use $tanh$ function as the non-linear activation function of the hidden layers. By using $softmax$ function as the activation function at the output layer, each network's output represents the predicted probability of each beam pair being the best, meaning providing the largest RSS. The outputs of the network, $\boldsymbol{o}$, can be expressed as a non-linear function of the input and the weights of different layers:

$$\boldsymbol{o} = f_{\boldsymbol{W}_o}^{(o)}\left(f_{\boldsymbol{W}_{N_h}}^{(N_h)}\left(\ldots f_{\boldsymbol{W}_1}^{(1)}(\boldsymbol{x})\right)\right) \tag{C.16}$$

where $f_{\boldsymbol{W}_o}^{(o)}$ and $f_{\boldsymbol{W}_i}^{(i)}, i = 1, \cdots, N_h$ are the non-linear functions of the output layer and the ith hidden layer, respectively. With the datasets described in Section 4.1, the network can be trained using a stochastic gradient descent algorithm to learn the most favorable beam pairs for any position in the environment

To prevent overfitting, the dropout technique is used as a regularization mechanism at hidden layers [28]. In this technique, some neurons of the hidden layers are randomly dropped in each training data batch. Dropout helps the network to avoid memorizing training data by effectively using different network structures in the learning process. In Fig. C.3, we show the dropped out neurons in the hidden layers with red cross marks.

Once the model has been trained, it can be used to recommend a set of beam pairs by feeding the UT coordinates and orientation to the network as inputs. A list of recommended beams $\mathcal{S}$ is obtained from the output values $\boldsymbol{o}$, which represent the probability of each beam pair in the codebooks being the best for the input position and orientation. If the sensing phase of the environment is limited by N_b measurements, the N_b beam pairs with highest

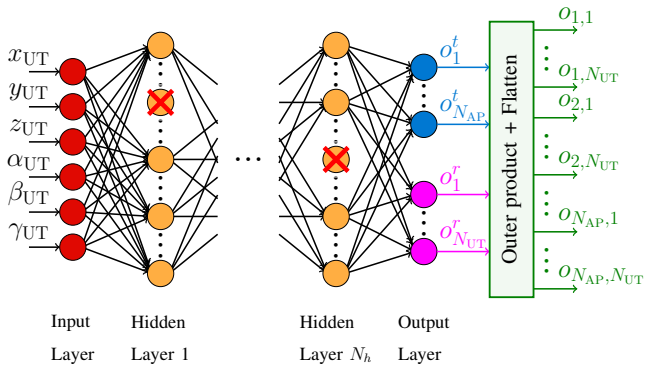

Fig. C.4: Structure of the proposed multi-task DNN. We coin this network a multi-task DNN since it includes two separate sets of neurons at the output layer: each set represents the selected AP and UT beams, respectively. This results in $N_{\mathrm{AP}} + N_{\mathrm{UT}}$ neurons at the output layer, leading to fewer trainable parameters than the single-task structure.

probabilities are chosen as candidates as follows:

$$\boldsymbol{g} = \underset{i,j}{\arg\,\mathrm{sort}}\,(o_{i,j}), \tag{C.17a}$$

$$\mathcal{S} = \{g_k | k = 1, \ldots, N_b\}, \tag{C.17b}$$

where $|\mathcal{S}| = N_b$.

Multi-Task Structure

Although the single-task structure of the NN can propose good beam candidates for a given UT position and orientation, it needs large training datasets to be trained well due to the large number of trainable weights it contains. By inspecting the number of trainable parameters at each layer, we see that there are $7n_h$, $(n_h + 1)n_h$, and $(n_h + 1)N_{\mathrm{AP}}N_{\mathrm{UT}}$ trainable weights, respectively, at the first hidden layer, other hidden layers, and the output layer. For large number of antenna elements, it is likely that $N_{\mathrm{AP}}N_{\mathrm{UT}} \gg n_h$. In this case, the output layer contains most of the trainable parameters. By changing the structure of the output layer, we can decrease the number of trainable weights significantly.

We propose a network structure that attempts to solve the AP and UT beamformer selection as separate problems or tasks. As shown in Fig. C.4, we consider two separate sets of neurons at the output layer, with different tasks for each branch: beam selection at the AP and beam selection at the UT. The two sets of neurons, $\boldsymbol{o}^t = [o_1^t, \ldots, o_{N_{\mathrm{AP}}}^t]^T$ and $\boldsymbol{o}^r = [o_1^r, \ldots, o_{N_{\mathrm{UT}}}^r]^T$, show the probability of each beam being the best at AP and UT for a given UT position and orientation. As the network aims to propose good beam pairs to

be sensed, we synthetically combine the probabilities of beams at the AP and the UT to construct probabilities of all possible beam pairs. Following this simplifying assumption, we use the outer product to calculate the probability of each beam pair being the best, $o_{i,j}$, i.e.

$$o_{i,j} = o_i^t o_j^r, \quad i \in \{1, \ldots, N_{\text{AP}}\}, \quad j \in \{1, \ldots, N_{\text{UT}}\}. \tag{C.18}$$

As the outer product of two vectors $\boldsymbol{o}^t$ and $\boldsymbol{o}^r$ is a matrix by size $N_{\text{AP}} \times N_{\text{UT}}$, we flatten the result of the outer product to obtain a vector with $N_{\text{AP}} N_{\text{UT}}$ entries, $\boldsymbol{o}$ [2]. As it is clear in (C.18), there is no trainable parameter in the construction of probabilities of beam pairs. As the output layer has $N_{\text{AP}} + N_{\text{UT}}$ neurons, the number of trainable weights at the output layer is $(n_h + 1)(N_{\text{AP}} + N_{\text{UT}})$. In practical scenarios where the training dataset is limited, the multi-task structured network can be trained better than the single-task structured one, as the former has far fewer trainable parameters. In the Appendix, we discuss the relation between the training of the multi-task network with outer-product and that of classical multi-task classifiers.

Extended Multi-Task Structure

To further decrease the number of trainable weights, we consider the assumption that the horizontal and vertical beamforming are independent at both AP and UT. Based on this simplifying assumption, we propose an extended version of the multi-task structured network, which is shown in Fig. C.5. There are 4 separate sets of neurons for horizontal and vertical beamforming at AP and UT. Similar to the previous structure, we use the outer product to obtain the probabilities of being the best for all possible beams at transceivers, i.e.,

$$o_i^t = o_m^{t^A} o_n^{t^E}, \; i \in \{1, \ldots, N_{\text{AP}}\}, \; m = \left\lfloor \frac{i}{N_{\text{AP}_\text{H}}} \right\rfloor, \; n = i \bmod N_{\text{AP}_\text{H}}, \tag{C.19}$$

$$o_j^r = o_p^{r^A} o_q^{r^E}, \; j \in \{1, \ldots, N_{\text{UT}}\}, \; p = \left\lfloor \frac{j}{N_{\text{UT}_\text{H}}} \right\rfloor, \; q = j \bmod N_{\text{UT}_\text{H}}, \tag{C.20}$$

where $o_m^{t^A}$, $o_n^{t^E}$, $o_p^{r^A}$, and $o_q^{r^E}$ denote the probability of mth, nth, pth, and qth beams being the best at horizontal and vertical beamforming at AP and UT, respectively. As an example, neuron $o_m^{t^A}$ denotes the output probability for the AP beams in the mth azimuth angle of the codebook, while $o_n^{t^E}$ represents the probability for the AP beams pointing at the nth elevation angle. As in the new structure the output layer includes $N_{\text{AP}_\text{H}} + N_{\text{AP}_\text{V}} + N_{\text{UT}_\text{H}} + N_{\text{UT}_\text{V}}$ neurons, the number of trainable parameters in the output layer decreases to $(n_h + 1)(N_{\text{AP}_\text{H}} + N_{\text{AP}_\text{V}} + N_{\text{UT}_\text{H}} + N_{\text{UT}_\text{V}})$. Such a reduction is advantageous when there amount of training data is limited.

[2] The operation "outer product + flatten" is equivalent to the Kronecker product, i.e. $\boldsymbol{o} = \boldsymbol{o}^t \otimes \boldsymbol{o}^r$.

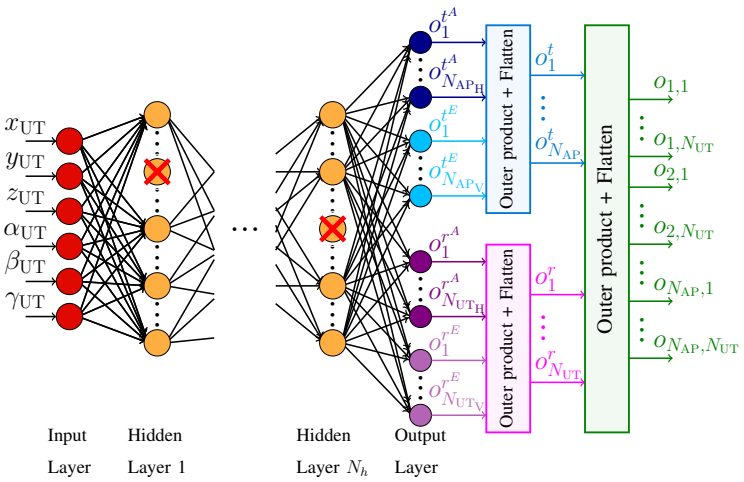

Fig. C.5: The extended multi-task structured DNN with $N_{\mathrm{AP_H}} + N_{\mathrm{AP_V}} + N_{\mathrm{UT_H}} + N_{\mathrm{UT_V}}$ neurons at its output layer.

4.3 Baselines

Generalized Inverse fingerprinting Method

The IFP is a data-driven method that uses training samples to make a lookup table of best beam pairs for different environment locations. However, the IFP method in [10] uses only the position information of the UT, not considering the arbitrary orientation of the UT. The bin definition of the IFP method is extended in a way that considers the rotation of the UT array about x,y, and z axes. This is a straightforward extension of the GIFP algorithm we proposed in [24]. By extending discretization to both the spatial and angular domains, position and orientation of the UT, $\boldsymbol{p}_{\mathrm{UT}}$ and $\boldsymbol{\psi}_{\mathrm{UT}}$ respectively, determine the corresponding bin for each observation. The kth bin may be defined as

$$\begin{aligned}\mathcal{B}_k = &[x_k, x_k + \Delta_s) \times [y_k, y_k + \Delta_s) \times [z_k, z_k + \Delta_s) \times \\ &[\alpha_k, \alpha_k + \Delta_a) \times [\beta_k, \beta_k + \Delta_a) \times [\gamma_k, \gamma_k + \Delta_a)\end{aligned} \tag{C.21}$$

where Δ_s and Δ_a, as hyper parameters of the generalized inverse fingerprinting (GIFP) method, are spatial bin size (SBS) and angular bin size (ABS), respectively. The values x_k, y_k, z_k, α_k, β_k, and γ_k are selected to obtain a set of bins that have no overlap and cover all the spatial and angular coordinates of interest. Note that the bin definition of the IFP method in [10] can be recovered by setting $\Delta_a = 2\pi$.

Following the IFP method approach in proposing a candidate list for the kth bin, $\mathcal{S}_k$, the beam pairs of this list are chosen to minimize the misalignment probability, i.e., the probability of not including the beam pair with the

highest RSS in the list. The misalignment probability may be expressed as

$$P_m(\mathcal{S}_k) = \mathbb{P}\left[\max_{(i,j)\in\mathcal{S}_k} R_{i,j} < \max_{(p,q)\in\mathcal{B}} R_{p,q}\right], \tag{C.22}$$

where $\mathcal{B}$ is a set including all possible beam pairs. Using the training samples assigned to the kth bin, the members of $\mathcal{S}_k$ are the top N_b ranked beam pairs which have the highest frequencies of being best [10]. In test mode, for a given new UT coordinate and orientation, the candidate list of the associated bin is used, and the beam selection follows the procedure in Fig. C.2a. Because of the discretization in the angular domain added to the spatial domain, there are significantly more bins in GIFP compared to classical IFP. Thus, the GIFP method becomes more data-demanding, and it needs a much larger training dataset to have the same density of training samples over bins as IFP.

Hierarchical Beam Search

As mentioned before, in hierarchical beam search, the space is covered and sensed in several stages with different beam width. For a UPA with $N = N_h * N_v$ antennas, there are $\log_2(N_h)+1$ and $\log_2(N_v)+1$ levels in horizontal and vertical directions. At the k_hth and k_vth horizontal and vertical level, there are $N_{k_h} \times N_{k_v}$ codewords, where $N_{k_h} = 2^{k_h}$ and $N_{k_v} = 2^{k_v}$. By extending the DEACT approach proposed in [4], the n_hth and n_vth codeword in the k_hth and k_vth horizontal and vertical level of the codebook can be written as

$$\begin{aligned}\boldsymbol{w}(k_h,k_v,n_h,n_v) &= [\boldsymbol{a}_{\mathrm{E}}^T(N_{k_v},\theta_v),\mathbf{0}^T_{(N_v-N_{k_v})\times 1}]^T \otimes [\boldsymbol{a}_{\mathrm{A}}^T(N_{k_h},\phi_h,\theta_v),\mathbf{0}^T_{(N_h-N_{k_h})\times 1}]^T,\\ \phi_h &= \arccos\frac{2n_h-1-N_{k_h}}{N_{k_h}},\ \theta_v = \arccos\frac{2n_v-1-N_{k_v}}{N_{k_v}},\end{aligned} \tag{C.23}$$

where $\boldsymbol{a}_{\mathrm{A}}$ and $\boldsymbol{a}_{\mathrm{E}}$ are defined in (C.5) and (C.6). Algorithm 1 illustrates the procedure of horizontal and vertical beamforming using a 3D codebook. The device first searches the vertical codewords while considering omnidirectional horizontal beamforming during this part. Then, the device tries to find the best horizontal codeword with the knowledge of the best vertical one. At each stage of the HBS, the beam decision region of a codeword is the subspace in the angular domain where the specified codeword has the highest gain among all the possible codewords. As an example, Fig. C.6 shows the beam decision regions for different levels of the DEACT method for a UPA with $N_h = 4$ and $N_v = 4$.

Algorithm 1: Vertical and Horizontal Analog beamforming Based on Codebook

Input: N_h, N_v, $\boldsymbol{w}$
Result: n_h, n_v
Initialize: Omnidirectional horizontal beamforming ($k_h = 0$), $n_h = 1$, $n_v = 1$
for $k_v = 1$ *to* $\log_2(N_v) + 1$ **do**
  1. $n_v^{(1)} = 2n_v - 1$, $n_v^{(2)} = 2n_v$
  2. Sensing the environment with the two selected codewords: $\boldsymbol{w}(k_h, k_v, n_h, n_v^{(1)})$ and $\boldsymbol{w}(k_h, k_v, n_h, n_v^{(2)})$
  if $\boldsymbol{w}(k_h, k_v, n_h, n_v^{(1)})$ *provides higher RSS* **then** $n_v = n_v^{(1)}$;
  else $n_v = n_v^{(2)}$;
end
for $k_h = 1$ *to* $\log_2(N_h) + 1$ **do**
  1. $n_h^{(1)} = 2n_h - 1$, $n_h^{(2)} = 2n_h$
  2. Sensing with the two selected codewords: $\boldsymbol{w}(k_h, k_v, n_h^{(1)}, n_v)$ and $\boldsymbol{w}(k_h, k_v, n_h^{(2)}, n_v)$
  if $\boldsymbol{w}(k_h, k_v, n_h^{(1)}, n_v)$ *provides higher RSS* **then** $n_h = n_h^{(1)}$;
  else $n_h = n_h^{(2)}$;
end

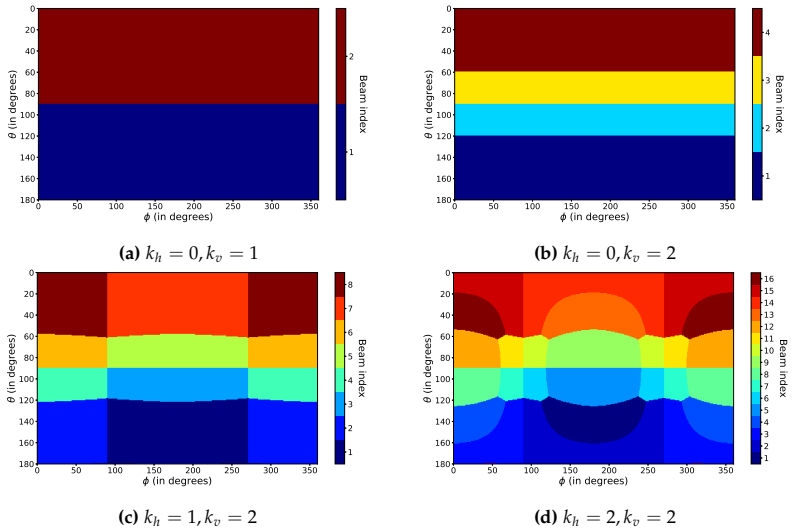

(a) $k_h = 0, k_v = 1$ **(b)** $k_h = 0, k_v = 2$

(c) $k_h = 1, k_v = 2$ **(d)** $k_h = 2, k_v = 2$

Fig. C.6: Beam decision regions in different levels of the DEACT method as a hierarchical beam search. The antenna array size is $\{N_h = 4, N_v = 4\}$. At each level of the search, different colors are representing different codewords in the codebook.

5 Performance and Complexity Evaluation

We start this section by introducing the ray-tracing setup. Following we compare the performance of the methods in terms of misalignment probability and effective spectral efficiency (ESE). In order to quantify the training data requirements of each of the analyzed data-driven methods, we investigate their performance when they are trained using datasets of different sizes. Finally, we evaluate the robustness of the deep learning based and GIFP methods with inaccurate position and orientation information.

5.1 Simulation Setup and Performance Measures

We consider the living room (LR) described and defined precisely in the IEEE 802.11ad task group [29]. Fig. C.7 illustrates the LR as the considered indoor environment. According to the standard, the LR dimensions are 7m $\times$7m $\times$3m (W$\times$ L$\times$ H). Two sofas, a table, and an armchair are placed in the LR, and a cabinet is placed between two windows of one of the outer walls. The AP is placed in the middle of one of the LR walls. The UT can take a position in a sector with the same height as the AP, where the sector has dimensions of 4m $\times$7m (W$\times$ L). In the ray tracing tool, we defined 70,000 UT positions in the user sector. In the standard, a cluster blockage model is considered where a NLOS path can be blocked with a probability that is defined in the standard.

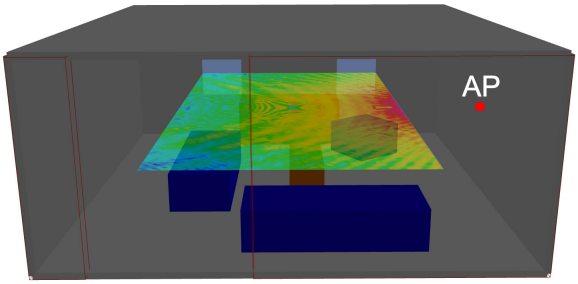

Fig. C.7: The ray-tracing simulation of the living room as the simulation scenario. The AP position is shown with the red circle. Also, the received LOS power is depicted in the user grid of the scenario.

Table C.1: Geometrical Information of the Living Room

	Dimension (m)	AP's pos. (m)	User grid (m)	# UT positions
LR	$7 \times 7 \times 3$	$(7, 3.5, 1.5)$	$[1.5-5.5] \times [0-7] \times [1.5]$	70,000

This probability depends on the order of reflection and the reflective surfaces. In addition, the probability of LOS blockage is considered a model parameter that can be set to 0 or 1. To construct datasets with arbitrary LOS blockage probability, we can combine the samples proportionally from datasets with 0 and 1 LOS blockage probability. Table C.1 gives a summary of the most important information about the LR.

To generate channel responses, we use Altair Feko-Winprop software [25] as a professional ray-tracing software, which considers empirical losses for transmission, reflection and diffraction in the simulations. Using the outputs of the ray-tracing tool including the AoD, AoA, and path gains of all the paths, the channel response can be constructed using (C.2). The 25 strongest multipath components are used at any UT position to generate the channel response.

For all samples of the dataset, we consider $P_{\text{AP}} = 0\,\text{dBm}$ and $\sigma_n^2 = -84\,\text{dBm}$ as the transmit power and noise variance, respectively. We consider $\{8, 8\}$ and $\{4, 4\}$ UPA at the AP and UT, respectively. After constructing the channel response for each UT location, we calculate the RSS for each beam pair using (C.11). According to the type of encoding scheme, M, the labels are calculated and stored in $\mathbb{D}^{\Xi}$. We consider 80% of each dataset for the training scheme and the remaining 20% as the test samples. To reduce the dependencies between the training samples and the performance of the data-driven methods, we use the $5-$fold technique. In this technique, the dataset is divided into 5 parts. Then, the training and testing experiments are repeated 5 times, each of them with a different part of the datset selected as test data, with the end result obtained by averaging over all 5 experiments.

There are 70,000 UT positions in the user grid of the LR, which are stored in $\mathbb{D}^{\Xi}$. To evaluate the performance of the data-driven methods with limited training datasets, we make two sub-datasets $\mathbb{D}^{\Xi}_{10\%}$ and $\mathbb{D}^{\Xi}_{1\%}$, respectively, consisting of 7,000 and 700 samples randomly selected from $\mathbb{D}^{\Xi}$. In the performance evaluations, we consider 5 beam alignment approaches:

1. **DNN-ST**: The DNN method with single-task structure described in Section 4.2,
2. **DNN-MT**: The DNN method with multi-task structure explained in Section 4.2,
3. **DNN-EMT**: The DNN method with extended multi-task structure described in Section 4.2,
4. **GIFP**: The generalized inverse fingerprinting method explained in Section 4.3,
5. **HBS**: The hierarchical beam search method with the deactivation technique represented in Section 4.3.

All the NNs structures have $N_h = 5$ hidden layers with $n_h = 128$ neurons at each hidden layer. Also, to prevent overfitting in the NNs, 10% dropout for all the hidden layers is used. We use Adam optimizer [30] in the training phase with 50 epochs, while the minibatch size is progressively increased from 32 to 8192 samples [24]. To reduce the effects of initial weights of NNs on the BA performance, we averaged over 3 results with 3 random weight initializations for each experiment. To reproduce the numerical results, the code and datasets are released at `https://github.com/SajadRezaie/3DOriLocBeamSelection`.

For a channel with a given coherence time, the channel resources used for the BA phase should be deducted from the achievable data rate of the system [31]. Fig. C.8 shows the frame structure of the initial BA procedures. T_{fr}, T_s, and N_b are the frame duration, beam scanning time of one beam pair, and the number of sensed beam pairs in the BA phase, respectively. We assume the frame duration is less than the coherence time of the channel, and the channel response is not varying during the whole frame. In contrast to the beam selection methods, in the HBS approach the number of sensed beam pairs is fixed and entirely determined by the antenna array configurations as $N_b = 2\log_2(N_{\text{UT}}) + 2\log_2(N_{\text{AP}})$. The transceivers use the selected beam pair in the initial BA phase to communicate the actual data.

In the beam selection methods, the transceivers sense the environment with all the beam pairs in the candidate list $\mathcal{S}$ ($|\mathcal{S}| = N_b|$) and select the one that provides the highest RSS, i.e.

$$i^*, j^* = \arg\max_{i,j} (R_{i,j}). \tag{C.24}$$

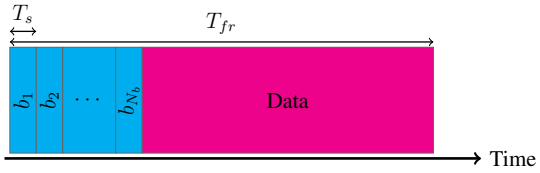

Fig. C.8: Frame structure of the BA procedures. In the beam selection method, the transceivers sense the environment with N_b beam pairs, and then use the rest of the frame to transmit the actual data.

As a performance measure, we define the misalignment probability by reformulating (C.22) as:

$$P_m(\mathcal{S}_k) = \mathbb{P}\left[R_{i^*,j^*} < \max_{(p,q)\in\mathcal{B}} R_{p,q}\right] \tag{C.25}$$

where $\mathcal{B}$ ($|\mathcal{B}| = N_{\text{AP}}N_{\text{UT}}$) includes all the possible beam pair combinations. For the HBS approach, i^*, j^* are found by sensing the environment with different beam width, and then we use (C.25) to calculate the misalignment probability. In addition, the ESE as another performance measure may be written as

$$\text{SE}_{\text{eff}} = \frac{T_{fr} - N_b T_s}{T_{fr}} \log_2(1 + \text{SNR}_{i^*,j^*}), \quad N_b T_s \leq T_{fr} \tag{C.26}$$

where $\text{SNR}_{i,j}$ is the SNR of (i,j)th beam pair, i.e.

$$\text{SNR}_{i,j} = \frac{\left\|\sqrt{P_{\text{AP}}}\boldsymbol{v}_j^H \boldsymbol{H}\boldsymbol{u}_i s\right\|^2}{\sigma_n^2}. \tag{C.27}$$

We use $T_{fr} = 20$ms and $T_s = 0.1$ms in the numerical evaluations [31]. In addition to the described baselines in Section 4.3, we use perfect alignment as a genie-aided method that always selects the beam pair with highest SNR out of all the possible beam combinations. The perfect alignment provides an upper bound for ESE.

5.2 Numerical Evaluation

In Fig. C.9, the performance of the different investigated beam selection methods is depicted. The plots show the misalignment probability and spectral efficiency of the methods as a function of the the number of beam pairs scanned. For data-driven methods, this corresponds to the size N_b of the candidate beam list $\mathcal{S}$. For HBS, on the other hand, the number of scanned

beams is fixed and determined by the size of the hierarchical codebooks defined at AP and UT; in the selected configurations, this corresponds to $2\log_2(16) + 2\log_2(64) = 20$ beam pairs. As it can be seen from Fig. C.9a, the data-driven beam selection methods have much lower misalignment probability and up to 60% higher ESE than the HBS method. In addition, in the data-driven beam selection methods, the candidate list may include a different number of beam pairs for scanning, N_b. For example, the DNN-ST structure with a candidate list size of $N_b = 3$ can reach more than 50% higher ESE and 85% less latency than the HBS method, which scans 20 beam pairs. Also, all the deep-learning based methods perform significantly better than GIFP methods with different spatial and angular bin sizes. For example, the GIFP with SBS = 1m and ABS = 22.5° has $4 \times 7 \times 1 \times 16 \times 4 \times 4 = 7168$ bins, which end up with around 8 samples on average at each bin. The excellent performance of DNN-ST is a consequence of training it with a large dataset of sufficient size. It clearly outperforms the DNN-MT and DNN-EMT methods, which suffer from the decoupling of the beam selection process at AP and UT for both cases, and between horizontal and vertical beam directions in the latter case. On the other hand, the DNN-MT and DNN-EMT networks have much less computational cost than the DNN-ST structure in the training and test. The computational complexity is proportional to the number of trainable parameters, and there are significantly fewer trainable weights in the DNN-MT and DNN-EMT.

As the dataset size is decreased, the performance advantages of DNN-ST progressively fade away. This is illustrated in Fig. C.9b where, with a dataset size of 7000 samples, the DNN-MT method with fewer trainable parameters has the best performance. In spite of the 90% reduction of the training dataset size, the deep learning-based methods work significantly better than the HBS method. The performance of GIFP is further deteriorated with the decrease in dataset-size, and the DNN-MT method reaches up to 30% higher spectral efficiency than the GIFP methods with different spatial and angular bin sizes. Also, Fig. C.9c shows the performance of different BA approaches with the minimal dataset, $\mathbb{D}^{\Xi}_{1\%}$, including only 700 samples. As it can be seen, the DNN-EMT method has the best performance in terms of misalignment probability and ESE, regardless of the size of the candidate list. Following our expectation, by limiting the dataset size significantly, the performance gap between data-driven BA methods and the HBS method is reduced. These results illustrates the trade off between accuracy and dataset size in DNN based methods: with large datasets, the DNN-ST model with a large number of trainable parameters leads to more accurate results than DNN-MT and DNN-EMT; when training data is scarce, however, the DNN-MT and DNN-EMT achieve better performance due to their much smaller number of trainable parameters.

Fig. C.10 shows the misalignment probability of the deep learning-based

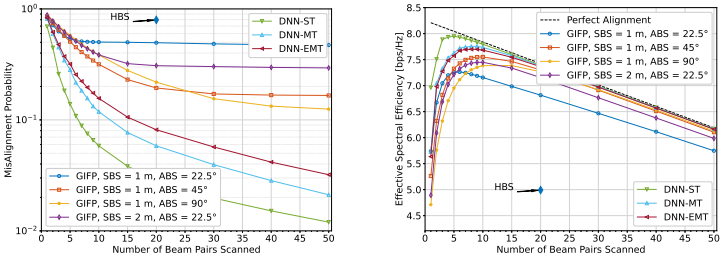

(a) $\mathbb{D}^{\Xi}$ with 70,000 samples

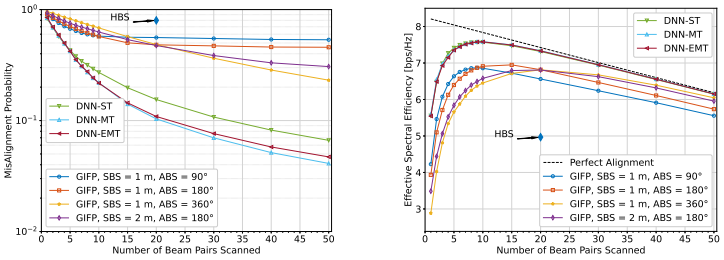

(b) $\mathbb{D}^{\Xi}_{10\%}$ with 7,000 samples

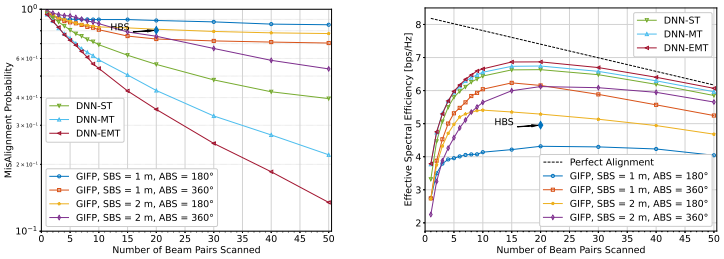

(c) $\mathbb{D}^{\Xi}_{1\%}$ with 700 samples

Fig. C.9: Misalignment probability and effective spectral efficiency for different dataset sizes.

beam selection methods using the labels with M-hot encoding scheme. We use both $\mathbb{D}^{\Xi}$ and $\mathbb{D}^{\Xi}_{1\%}$ datasets to see the effects of the multi-labeling technique on the performance of the methods with different structures. As there are many trainable parameters in the DNN-ST structure, multi-labeling works like data augmentation to fill the performance gap because of insufficient training samples. However, the DNN-MT and DNN-EMT structures have significantly fewer trainable parameters. Thus, training these methods using multi-labeling with the large dataset $\mathbb{D}^{\Xi}$ does not show any advantage over using a single label. When the training examples are limited in $\mathbb{D}^{\Xi}_{1\%}$, however, the multi-labeling technique is helpful to have a lower misalignment probability.

The robustness of the data-driven based BA methods against different

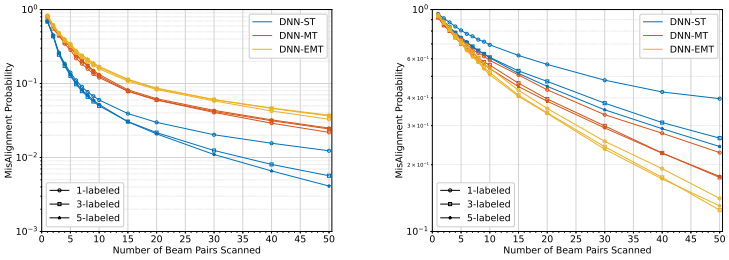

(a) $\mathbb{D}^{\Xi}$ with 70,000 samples **(b)** $\mathbb{D}^{\Xi}_{1\%}$ with 700 samples

Fig. C.10: Effects of the multi-labeling scheme on the performance of the proposed DNNs with large and small training datasets.

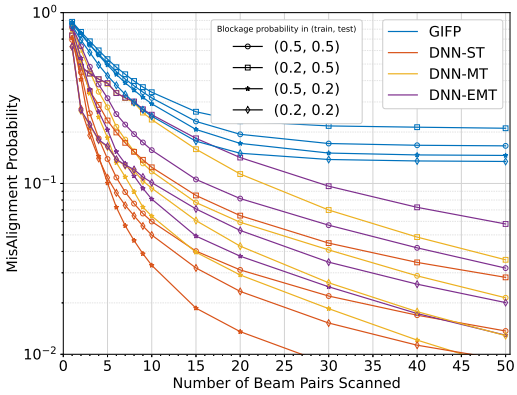

Fig. C.11: The misalignment probability of different data-driven BA methods with various LOS blockage probability in the training and test datasets.

propagation properties in the training and test samples is evaluated in an experiment. We consider to have two datasets with 70,000 samples, $\mathbb{D}^{\Xi}$ and $\mathbb{D}^{\Upsilon}$, with LOS blockage probability of 0.5 and 0.2, respectively. For the rest of simulations, we use SBS = 1m and ABS = 45° parameters for the GIFP method. Fig. C.11 shows the performance of the GIFP and deep learning-based methods when there is a match/mismatch of LOS blockage rate between the training and test samples. As it can be seen in Fig. C.11, in the case where the LOS blockage rate is lower in the training set than in the test set, the network learns better the LOS direction but has fewer opportunities to learn NLOS directions. Thus, in comparison to the matched case when there is high LOS blockage probability in the training and test sets, the performance is degraded. Contrary, by training a NN at a higher LOS blockage probability compared to the test samples, the network learns better the NLOS paths at the expense of a worse learning of the LOS one. Due to this, the network trained with matched LOS blockage probability performs better when

few beam pairs are scanned. On the other hand, when more beam pairs are scanned there is a good chance to scan candidates for both LOS and NLOS paths. Thus, the network trained in a higher LOS blockage rate has a better performance compared to the matched case with large N_b. To summarize, the NNs are robust to mismatch in the LOS blockage probability, and we see more robustness in the networks if trained in a high LOS blockage probability.

Although context information can reduce the overhead of initial BA, in practical scenarios the position and orientation of the UT are subject to estimation errors. To account for this in our numerical assessment, we use a simple model of such inaccuracies. Consider $\boldsymbol{p}_{\mathrm{UT}}$ and $\boldsymbol{\psi}_{\mathrm{UT}}$ as the true position and orientation vector of the UT. By adding random perturbation to these vectors, we can model the measured position and orientation, $\hat{\boldsymbol{p}}_{\mathrm{UT}}$ and $\hat{\boldsymbol{\psi}}_{\mathrm{UT}}$, as

$$\hat{\boldsymbol{p}}_{\mathrm{UT}} = \boldsymbol{p}_{\mathrm{UT}} + \boldsymbol{\epsilon}_p, \tag{C.28}$$

$$\hat{\boldsymbol{\psi}}_{\mathrm{UT}} = \boldsymbol{\psi}_{\mathrm{UT}} + \boldsymbol{\epsilon}_\psi, \tag{C.29}$$

where $\boldsymbol{\epsilon}_p$ and $\boldsymbol{\epsilon}_\psi$, respectively, denote the random perturbation of the position and orientation sensors on the UT. In line with the known statistics of the measuring error, the entries of the random perturbation vectors $\boldsymbol{\epsilon}_p$ and $\boldsymbol{\epsilon}_\psi$ are generated from independent Gaussian distributions with zero mean and variance σ_p^2 and σ_ψ^2, respectively.

In Fig. C.12, the performance of the GIFP, DNN-ST, and DNN-MT methods including inaccuracies in the position and/or orientation information of the UT device are shown. The dataset with $70,000$ samples are used, and the estimation error is included in both the train and test sets. When applying perturbation only on the position information, we see a slight degradation with $\sigma_p = 0.1m$. This level of accuracy can be obtained with, e.g., ultra wideband (UWB) positioning [32]. As shown in Fig. C.12a, by increasing σ_p to $0.5m$, both the GIFP and deep learning-based methods have performance loss, respectively, around 10% and 5% in the maximum of achievable ESE. The sensitivity of data-driven based BA methods to position inaccuracy depends on the dimensions of the environment. Thus, we expect to see less performance degradation due to inaccurate positions in big rooms or outdoor scenarios. Fig. C.12b shows the performance of different BA methods by feeding inaccurate orientation information. All the data-driven approaches offer good robustness to the different amounts of orientation perturbations. When we apply the perturbation model on both position and orientation information, as we expected, more degradation in their performance can be seen in Fig. C.12c. At all the considered σ_p and σ_o cases, the data-driven based methods show better performance than the HBS method. Thus, the data-driven methods still leverage inaccurate context information to reduce the latency of the BA procedure and reach higher spectral efficiency. By looking at the ESE

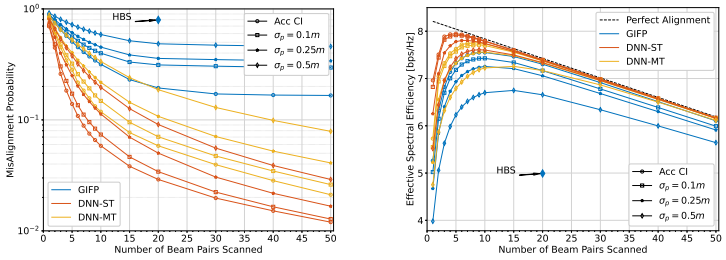

(a) Inaccurate position

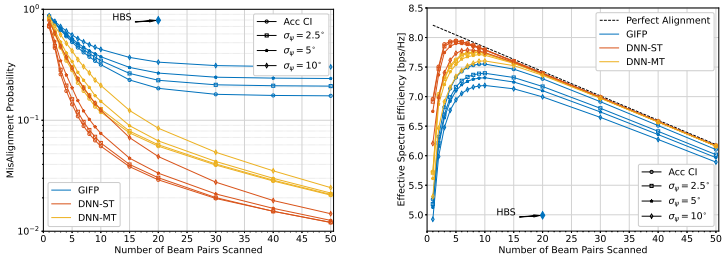

(b) Inaccurate orientation

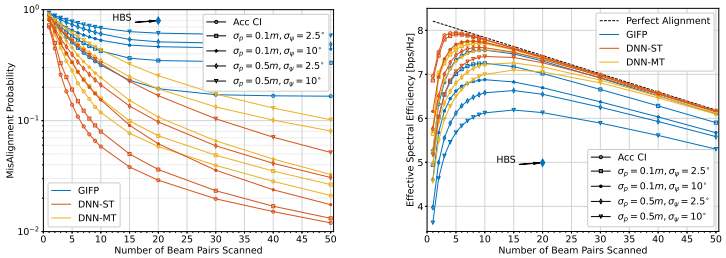

(c) Inaccurate position and orientation

Fig. C.12: Misalignment probability and effective spectral efficiency with inaccurate position and orientation information.

curves, it can be seen that the DNN-ST method has the least sensitivity to inaccurate location and orientation information. This shows that, during the training process, the DNN is able to learn how to deal with different degrees of CI uncertainty, leading to a robust performance against these inaccuracies.

5.3 Computational Complexity Analysis

The DNN-ST, DNN-MT, and DNN-EMT methods respectively need $6n_h + (N_h - 1)n_h^2 + n_h(N_{\text{AP}}N_{\text{UT}}) = 197376$, $6n_h + (N_h - 1)n_h^2 + n_h(N_{\text{AP}} + N_{\text{UT}}) + N_{\text{AP}}N_{\text{UT}} = 77568$, and $6n_h + (N_h - 1)n_h^2 + n_h(N_{\text{AP}_\text{H}} + N_{\text{AP}_\text{V}} + N_{\text{UT}_\text{H}} + N_{\text{UT}_\text{V}}) + N_{\text{AP}_\text{H}}N_{\text{AP}_\text{V}} + N_{\text{UT}_\text{H}}N_{\text{UT}_\text{V}} + N_{\text{AP}}N_{\text{UT}} = 70480$ real multiply-accumulate operations in the evaluation phase for each test sample [33]. Using the MT and

EMT structures reduces the computational complexity by more than 50% with respect to the ST structure. However, the GIFP has no significant computational load, as the best beam pairs for the corresponding cell of the UT location and orientation just need to be loaded from memory. Also, the computational complexity of the HBS method is negligible as the beamforming vectors at each level of the hierarchical search are predefined.

6 Conclusion

In this work, we have shown that position and orientation of UT as a kind of context information can play an important role in the initial beam alignment procedure of mmWave links in pedestrians applications. We have presented a deep-learning based approach for beam recommendation based solely on the position and orientation of the UT. Three neural network structures are designed for the task: a standard feed forward network coined DNN-ST, and two alternative and simplified designs. The simplified structures, coined DNN-MT and DNN-EMT, are inspired by multitask networks and separate the beamforming tasks at AP and UT, as well as the horizontal and vertical beam directions in the latter design. This results in a significant reduction of trainable parameters and size of the DNN model.

Our extensive performance assessment based on ray-traced channel responses reveals that the DNN-ST design shows excellent performance when enough training samples are in the dataset. However, the DNN-MT and DNN-EMT designs have less computational cost in the training and evaluation phase, and these networks perform better with small training datasets. The proposed beam selection methods outperform the GIFP method as a CI-based lookup table approach and the DEACT method as a CI-agnostic hierarchical beam search solution in terms of latency and spectral efficiency. Our proposed methods show low sensitivity to changes in the propagation properties in the evaluation compared to the data collection time as well as displaying high robustness against measurement inaccuracies in the position and orientation of the UT.

References

[1] M. Giordani, M. Polese, M. Mezzavilla, S. Rangan, and M. Zorzi, "Toward 6G Networks: Use Cases and Technologies," *IEEE Commun. Mag.*, vol. 58, no. 3, pp. 55–61, Mar. 2020.

[2] C. Liu, M. Li, S. V. Hanly, P. Whiting, and I. B. Collings, "Millimeter-Wave Small Cells: Base Station Discovery, Beam Alignment, and System

Design Challenges," *IEEE Wirel. Commun.*, vol. 25, no. 4, pp. 40–46, Aug. 2018.

[3] M. Giordani, M. Mezzavilla, and M. Zorzi, "Initial Access in 5G mmWave Cellular Networks," *IEEE Commun. Mag.*, vol. 54, no. 11, pp. 40–47, Nov. 2016.

[4] Z. Xiao, T. He, P. Xia, and X. Xia, "Hierarchical Codebook Design for Beamforming Training in Millimeter-Wave Communication," *IEEE Trans. Wireless Commun.*, vol. 15, no. 5, pp. 3380–3392, May 2016.

[5] C. N. Manchón, E. de Carvalho, and J. B. Andersen, "Ping-pong beam training with hybrid digital-analog antenna arrays," in *Proc. IEEE Int. Conf. Commun.*, May 2017, pp. 1–7.

[6] F. Sohrabi, Z. Chen, and W. Yu, "Deep Active Learning Approach to Adaptive Beamforming for mmWave Initial Alignment," *IEEE Journal on Selected Areas in Communications*, vol. 39, no. 8, pp. 2347–2360, Aug. 2021.

[7] C. Antón-Haro and X. Mestre, "Learning and Data-Driven Beam Selection for mmWave Communications: An Angle of Arrival-Based Approach," *IEEE Access*, vol. 7, pp. 20 404–20 415, 2019.

[8] M. Polese, F. Restuccia, and T. Melodia, "DeepBeam: Deep Waveform Learning for Coordination-Free Beam Management in mmWave Networks," in *Proc. ACM MobiHoc '21*, Jul. 2021, pp. 61–70.

[9] M. Kok, J. D. Hol, and T. B. Schön, "Using Inertial Sensors for Position and Orientation Estimation," *Found. Trends Signal Process.*, vol. 11, no. 1-2, pp. 1–153, 2017.

[10] V. Va, J. Choi, T. Shimizu, G. Bansal, and R. W. Heath, "Inverse Multipath Fingerprinting for Millimeter Wave V2I Beam Alignment," *IEEE Trans. Veh. Technol.*, vol. 67, no. 5, pp. 4042–4058, May 2018.

[11] M. S. Mollel, A. I. Abubakar, M. Ozturk, S. F. Kaijage, M. Kisangiri, S. Hussain, M. A. Imran, and Q. H. Abbasi, "A Survey of Machine Learning Applications to Handover Management in 5G and Beyond," *IEEE Access*, vol. 9, pp. 45 770–45 802, 2021, conference Name: IEEE Access.

[12] Y. Zhang, M. Alrabeiah, and A. Alkhateeb, "Reinforcement Learning of Beam Codebooks in Millimeter Wave and Terahertz MIMO Systems," *arXiv:2102.11392 [cs, eess, math]*, Feb. 2021. [Online]. Available: http://arxiv.org/abs/2102.11392

[13] W. Xu, F. Gao, S. Jin, and A. Alkhateeb, "3D Scene-Based Beam Selection for mmWave Communications," *IEEE Wireless Commun. Lett.*, vol. 9, no. 11, pp. 1850–1854, Nov. 2020.

[14] L.-H. Shen, T.-W. Chang, K.-T. Feng, and P.-T. Huang, "Design and Implementation for Deep Learning Based Adjustable Beamforming Training for Millimeter Wave Communication Systems," *IEEE Transactions on Vehicular Technology*, vol. 70, no. 3, pp. 2413–2427, Mar. 2021.

[15] Z. Zhu, K. Lin, and J. Zhou, "Transfer Learning in Deep Reinforcement Learning: A Survey," *arXiv:2009.07888 [cs, stat]*, Mar. 2021. [Online]. Available: http://arxiv.org/abs/2009.07888

[16] M. Alrabeiah and A. Alkhateeb, "Deep Learning for mmWave Beam and Blockage Prediction Using Sub-6 GHz Channels," *IEEE Trans. Commun.*, vol. 68, no. 9, pp. 5504–5518, Sep. 2020.

[17] F. Liu, W. Yuan, C. Masouros, and J. Yuan, "Radar-Assisted Predictive Beamforming for Vehicular Links: Communication Served by Sensing," *IEEE Trans. Wireless Commun.*, vol. 19, no. 11, pp. 7704–7719, Nov. 2020.

[18] M. Dias, A. Klautau, N. González-Prelcic, and R. W. Heath, "Position and LIDAR-Aided mmWave Beam Selection using Deep Learning," in *Proc. IEEE Int. Workshop Signal Process. Adv. Wireless Commun. (SPAWC)*, Jul. 2019, pp. 1–5.

[19] G. Charan, M. Alrabeiah, and A. Alkhateeb, "Vision-Aided Dynamic Blockage Prediction for 6G Wireless Communication Networks," in *Proc. IEEE Int. Conf. Commun.*, Jun. 2021, pp. 1–6.

[20] M. Alrabeiah, A. Hredzak, and A. Alkhateeb, "Millimeter Wave Base Stations with Cameras: Vision-Aided Beam and Blockage Prediction," in *Proc. IEEE Vehicular Technology Conference (VTC)*, May 2020, pp. 1–5.

[21] S. Rezaie, A. Amiri, E. de Carvalho, and C. N. Manchón, "Deep Transfer Learning for Location-Aware Millimeter Wave Beam Selection," *IEEE Commun. Lett.*, vol. 25, no. 9, pp. 2963–2967, Sep. 2021.

[22] Y. Heng, J. G. Andrews, J. Mo, V. Va, A. Ali, B. L. Ng, and J. C. Zhang, "Six Key Challenges for Beam Management in 5.5G and 6G Systems," *IEEE Commun. Mag.*, vol. 59, no. 7, pp. 74–79, Jul. 2021.

[23] A. Ali, J. Mo, B. L. Ng, V. Va, and J. C. Zhang, "Orientation-Assisted Beam Management for Beyond 5G Systems," *IEEE Access*, vol. 9, pp. 51 832–51 846, 2021.

[24] S. Rezaie, C. N. Manchón, and E. de Carvalho, "Location- and Orientation-Aided Millimeter Wave Beam Selection Using Deep Learning," in *Proc. IEEE Int. Conf. Commun.*, Jun. 2020, pp. 1–6.

[25] "Altair Feko WinProp," [online] Available: https://www.altair.com/feko.

[26] C. De Lima, D. Belot, R. Berkvens, A. Bourdoux, D. Dardari, M. Guillaud, M. Isomursu, E.-S. Lohan, Y. Miao, A. N. Barreto, M. R. K. Aziz, J. Saloranta, T. Sanguanpuak, H. Sarieddeen, G. Seco-Granados, J. Suutala, T. Svensson, M. Valkama, B. Van Liempd, and H. Wymeersch, "Convergent Communication, Sensing and Localization in 6G Systems: An Overview of Technologies, Opportunities and Challenges," *IEEE Access*, vol. 9, pp. 26 902–26 925, 2021.

[27] I. Goodfellow, Y. Bengio, and A. Courville, *Deep Learning*. Cambridge, MA, USA: MIT Press, Nov. 2016. [Online]. Available: https://www.deeplearningbook.org/

[28] N. Srivastava, G. Hinton, A. Krizhevsky, I. Sutskever, and R. Salakhutdinov, "Dropout: A Simple Way to Prevent Neural Networks from Overfitting," *J. Mach. Learn. Res.*, vol. 15, no. 56, pp. 1929–1958, 2014.

[29] A. Maltsev, "Channel models for 60GHz WLAN systems," *IEEE802. 11 09/0334r8*, 2010.

[30] D. P. Kingma and J. Ba, "Adam: A Method for Stochastic Optimization," in *Proc. Int. Conf. Learn. Representations*, 2015.

[31] M. Hussain and N. Michelusi, "Second-Best Beam-Alignment via Bayesian Multi-Armed Bandits," in *Proc. IEEE GLOBECOM*, Dec. 2019, pp. 1–6.

[32] C. Zhang, M. J. Kuhn, B. C. Merkl, A. E. Fathy, and M. R. Mahfouz, "Real-Time Noncoherent UWB Positioning Radar With Millimeter Range Accuracy: Theory and Experiment," *IEEE Trans. Microwave Theory Tech.*, vol. 58, no. 1, pp. 9–20, Jan. 2010.

[33] P. J. Freire, Y. Osadchuk, B. Spinnler, A. Napoli, W. Schairer, N. Costa, J. E. Prilepsky, and S. K. Turitsyn, "Performance Versus Complexity Study of Neural Network Equalizers in Coherent Optical Systems," *J. Lightw. Technol.*, vol. 39, no. 19, pp. 6085–6096, Oct. 2021.

Paper D

Location- and Orientation-aware Millimeter Wave Beam Selection for Multi-Panel Antenna Devices

Sajad Rezaie, João Morais, Elisabeth de Carvalho, Ahmed Alkhateeb, Carles Navarro Manchón

The paper has been published in the
IEEE Global Communications Conference (GLOBECOM), pp. 597–602, Jan. 2023.

The layout has been revised.

Abstract

While initial beam alignment (BA) in millimeter-wave networks has been thoroughly investigated, most research assumes a simplified terminal model based on uniform linear/planar arrays with isotropic antennas. Devices with non-isotropic antenna elements need multiple panels to provide good spherical coverage, and exhaustive search over all beams of all the panels leads to unacceptable overhead. This paper proposes a location- and orientation-aware solution that manages the initial BA for multi-panel devices. We present three different neural network structures that provide efficient BA with a wide range of training dataset sizes, complexity, and feedback message sizes. Our proposed methods outperform the generalized inverse fingerprinting and hierarchical panel-beam selection methods for two considered edge and edge-face antenna placement designs.

1 Introduction

Directional beamforming by employing antenna arrays with a large number of elements is the most common way to compensate for the higher propagation and penetration loss at the millimeter-wave (mmWave) and sub-terahertz bands. Codebook-based analog or hybrid analog-digital beamforming are popular solutions for arrays with a number of radio-frequency (RF) chains significantly smaller than the number of antenna elements [1]. In order to overcome the pathloss, access point (AP) and user terminal (UT) should then select beams from their respective codebooks which are aligned with the directions of departure/arrival of a strong multipath component of the channel. Finding the optimal beam pair at the AP and UT using an exhaustive search yields unacceptable latency due to the large beam space. On the other hand, hierarchical beam search (HBS) suffers from low signal-to-noise ratio (SNR) at the first search stages [2]. Data driven methods like inverse fingerprinting (IFP) and machine learning (ML) approaches use context information (CI) in addition to prior knowledge of the environment to reduce the search space by proposing a beam candidate list [3, 4]. Besides user location and orientation information, light detection and ranging (LIDAR) and visual images are helpful CI for beam selection and blockage prediction [5]. However, most of these methods have been proposed and assessed assuming isotropic antenna elements at the transceivers.

In practice, antenna arrays at mmWave transceivers are implemented using non-isotropic antenna elements, such as patch antennas, leading to directional coverage. To provide full spherical coverage, multi-panel antenna designs are often used in UT designs [6]. Such multi-panel designs should be taken into account in both the definition of codebooks and the design of beam alignment (BA) algorithms. As hand blockage can impact the coverage

of a UT, data-driven approaches are proposed in [7, 8] to generate a non-directional beamforming codebook considering the effects of hand blockage on the antenna radiation pattern. The grip-aware analog beam codebook adaptation presented in [9] provides better spherical coverage over the grip-agnostic scheme by finding a codebook for each hand-gripping mode. Authors in [10] proposed a beam switching approach to detect hand blockage by utilizing power detectors at all the panels, and in case of blockage, use beams on other panels. However, they focus on beam adjustment after successful initial access. UT panels can be connected to a single or multiple RF chains, possibly with constraints such as each RF chain only being connected to a panel in partially connected hybrid beamforming architectures [11]. Incorporating the limitations and features of multi-panel antenna design in the initial BA process allows for higher spectral efficiency and lower power consumption by efficiently turning off some RF chains [12].

This paper proposes location- and orientation-aware methods to reduce the overhead of initial BA for multi-panel devices by recommending a short beam/panel candidate list. We present two multi-network (MN) designs that are tailor-made for multi-panel devices. In addition, we generalize the single-network (SN) structure in [4]. MN designs containing fewer trainable parameters can outperform SN design, especially when trained with datasets of limited size. We consider two baselines for evaluations: generalized IFP (GIFP) as a benchmark using context information and hierarchical panel-beam selection (HP-BS) as a context-free approach. We use 3-dimensional (3D) ray tracing modeling of the channel responses using an IEEE standard indoor environment. This study considers static and mobile blockers like humans in the environment, while the impact of hand blockage on the initial BA process is left for future work. In our simulations, we use patch antenna elements with radiation pattern following a 3GPP model. The results demonstrate the performance improvement in latency and achievable rate using the proposed deep learning (DL)-based methods over the baselines.

2 System and Channel Model

A single-panel fixed AP and a multi-panel mobile UT are located in an indoor 3D scenario. The AP panel is made of a standard uniform planar array (UPA) with size of $\{N_{\mathrm{AP_x}}, N_{\mathrm{AP_y}}, N_{\mathrm{AP_z}}\}$ including $N_{\mathrm{AP}} = N_{\mathrm{AP_x}} N_{\mathrm{AP_y}} N_{\mathrm{AP_z}}$ elements [1]. The UT has N_P panels where each panel is made of a standard uniform linear array (ULA) or UPA in each module. The pth panel of the UT consists of a $\{N_{\mathrm{UT_x}}^{(p)}, N_{\mathrm{UT_y}}^{(p)}, N_{\mathrm{UT_z}}^{(p)}\}$ antenna array with $N_{\mathrm{UT}}^{(p)} = N_{\mathrm{UT_x}}^{(p)} N_{\mathrm{UT_y}}^{(p)} N_{\mathrm{UT_z}}^{(p)}$ elements.

[1] For the sake of notation generality, we formulate the considered arrays as 3D arrays on x,y,z. However, as specified below and in Section IV, we use only two-dimensional UPAs or 1-dimensional ULAs in the performance assessment.

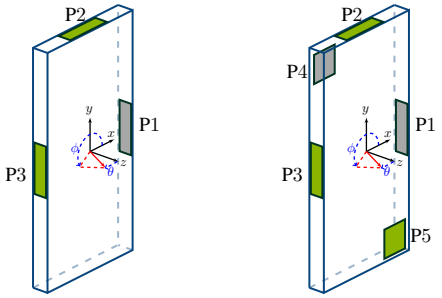

(a) Edge design **(b)** Edge-face design

Fig. D.1: Antenna placement designs inspired by [6] (a) Edge design with 3 ULAs on the device's edges (b) Edge-face design which has 2 extra UPAs on the device's face and back. Also, the UT LCS is depicted.

The total number of UT antenna elements is thus $N_{\mathrm{UT}} = \sum_{p=1}^{N_p} N_{\mathrm{UT}}^{(p)}$. Fig. D.1 shows the edge and edge-face designs of antenna placement at UT, inspired by [6]. The edge design contains 3 ULA panels, while the edge-face design includes 2 additional UPA modules on the device's face and back.

The position and orientation of the AP and UT are defined in a global coordinate system (GCS) [13]. Both the AP and UT have their own local coordinate systems (LCS) such that the AP's UPA and the UT's screen are oriented parallel to the yz and xy plane of their respective LCSs. The AP is placed at $\boldsymbol{p}_{\mathrm{AP}} = (x_{\mathrm{AP}}, y_{\mathrm{AP}}, z_{\mathrm{AP}}) \in \mathbb{R}^3$ with their LCSs rotated by angles $\boldsymbol{\psi}_{\mathrm{AP}} = (\alpha_{\mathrm{AP}}, \beta_{\mathrm{AP}}, \gamma_{\mathrm{AP}})$ around z, y, and x axes of the GCS. The UT takes a random position in the environment at position $\boldsymbol{p}_{\mathrm{UT}} = (x_{\mathrm{UT}}, y_{\mathrm{UT}}, z_{\mathrm{UT}}) \in \mathbb{R}^3$ with rotation vector $\boldsymbol{\psi}_{\mathrm{UT}} = (\alpha_{\mathrm{UT}}, \beta_{\mathrm{UT}}, \gamma_{\mathrm{UT}})$ defined analogously to $\boldsymbol{\psi}_{\mathrm{AP}}$ [14]. Two modes of device orientation are considered in this study: portrait and landscape. In portrait mode, $\beta_{\mathrm{UT}} = 0$ and α_{UT}, γ_{UT} are uniformly random in the ranges $\alpha_{\mathrm{UT}} \in [-\pi, \pi)$ and $\gamma_{\mathrm{UT}} \in [0, \pi/2]$. In the landscape mode, $\gamma_{\mathrm{UT}} = 0$ and α_{UT}, β_{UT} are drawn uniformly in the ranges $\alpha_{\mathrm{UT}} \in [-\pi, \pi)$ and $\beta_{\mathrm{UT}} \in [-\pi/2, 0]$.

2.1 Channel and Signal Model

We use Altair WinProp™ as ray-tracing software [15] to generate channel responses between AP and UT panels for each considered UT location and orientation. The channel to each UT panel is built using the outputs of the tool such as angle of departure (AoD), angle of arrival (AoA), and gains of all paths between the AP and the panel. The channel matrix $\boldsymbol{H}^{(p)} \in \mathbb{C}^{N_{\mathrm{UT}}^{(p)} \times N_{\mathrm{AP}}}$

between the AP and the pth UT panel is modeled as

$$\boldsymbol{H}^{(p)} = \sum_{l=0}^{L^{(p)}} \sqrt{\rho_l^{(p)}}\, e^{j\vartheta_l^{(p)}}\, \boldsymbol{a}_{\mathrm{UT}}^{(p)}(\phi_l^{(p)}, \theta_l^{(p)})\, \boldsymbol{a}_{\mathrm{AP}}^{H}(\psi_l^{(p)}, \omega_l^{(p)}) \tag{D.1}$$

where $L^{(p)}$, $\rho_l^{(p)}$, and $\vartheta_l^{(p)}$ denote the number of multipath components reaching the pth panel, the received power, and the phase of the lth path, respectively. $\boldsymbol{a}_{\mathrm{UT}}^{(p)}$ and $\boldsymbol{a}_{\mathrm{AP}}$ show the antenna array response of the pth UT panel and the AP. Also, $\phi_l^{(p)}$ and $\theta_l^{(p)}$ are the azimuth and elevation AoAs of the lth path in the UT LCS, respectively. Likewise, $\psi_l^{(p)}$ and $\omega_l^{(p)}$ denote the azimuth and elevation AoDs of the lth path in the AP LCS. The array response of a $\{N_{\mathrm{x}}, N_{\mathrm{y}}, N_{\mathrm{z}}\}$ antenna array with $N_{\mathrm{a}} = N_{\mathrm{x}} N_{\mathrm{y}} N_{\mathrm{z}}$ elements may be written as

$$\boldsymbol{a}(\phi, \theta) = \frac{1}{\sqrt{N_{\mathrm{a}}}} g_{\mathrm{a}}(\phi, \theta) \boldsymbol{a}_{\mathrm{z}}(\theta) \otimes \boldsymbol{a}_{\mathrm{y}}(\phi, \theta) \otimes \boldsymbol{a}_{\mathrm{x}}(\phi, \theta) \tag{D.2}$$

where $g_{\mathrm{a}}(\phi, \theta)$ is the antenna gain at azimuth and elevation angles ϕ and θ, and $\boldsymbol{a}_{\mathrm{x}} \in \mathbb{C}^{N_{\mathrm{x}} \times 1}$, $\boldsymbol{a}_{\mathrm{y}} \in \mathbb{C}^{N_{\mathrm{y}} \times 1}$, and $\boldsymbol{a}_{\mathrm{z}} \in \mathbb{C}^{N_{\mathrm{z}} \times 1}$ are given by

$$\boldsymbol{a}_{\mathrm{x}}(\phi, \theta) = [1, e^{j\pi sin(\theta)\, cos(\phi)}, \ldots, e^{j\pi (N_{\mathrm{x}}-1)\, sin(\theta)\, cos(\phi)}]^T, \tag{D.3}$$

$$\boldsymbol{a}_{\mathrm{y}}(\phi, \theta) = [1, e^{j\pi sin(\theta)\, sin(\phi)}, \ldots, e^{j\pi (N_{\mathrm{y}}-1)\, sin(\theta)\, sin(\phi)}]^T, \tag{D.4}$$

$$\boldsymbol{a}_{\mathrm{z}}(\theta) = [1, e^{j\pi cos(\theta)}, \ldots, e^{j\pi (N_{\mathrm{z}}-1)\, cos(\theta)}]^T. \tag{D.5}$$

The received signal at the pth UT panel reads

$$y^{(p)} = \sqrt{P_{\mathrm{AP}}} \boldsymbol{v}^{(p)^H} \boldsymbol{H}^{(p)} \boldsymbol{u} s + \boldsymbol{v}^{(p)^H} \boldsymbol{n}^{(p)} \tag{D.6}$$

where P_{AP}, s, and $\boldsymbol{u}$ respectively denote the transmission power, the unit-power transmitted symbol, and the beamforming vector used at the AP. $\boldsymbol{v}^{(p)}$, $\boldsymbol{n}^{(p)}$ are, respectively, the combiner and a zero-mean complex Gaussian noise vector with variance σ_n^2 at the pth panel of the UT.

2.2 Analog and Hybrid Beamforming

This study considers analog phased antenna arrays with one RF chain at the AP. The UT has N_{RF} RF chains, where $1 < N_{RF} < N_P$ and a panel is either turned off or connected to one RF chain. In case of $N_{RF} = 1$, only one panel at a time is sensing the environment. When $N_{RF} > 1$, simultaneous sensing with different panels can be performed. For simplicity, however, we do not consider multi-panel beamforming in this study. In addition, discrete Fourier transform (DFT)-based codebooks using analog phase shifters are used. For the codebook of each AP or UT panel, we consider the same number of

beams as the number of elements in the panel. We consider the set $\boldsymbol{\mathcal{U}} = \{\boldsymbol{u}_1, \ldots, \boldsymbol{u}_{N_{\mathrm{AP}}}\}$ including all the accessible beamforming vectors at the AP. For the pth UT panel, we define $\boldsymbol{\mathcal{V}}^p = \{\boldsymbol{v}_1^p, \ldots, \boldsymbol{v}_{N_{\mathrm{UT}}^{(p)}}^p\}$ as the panel codebook. The set $\boldsymbol{\mathcal{V}} = \{\boldsymbol{v}_1, \ldots, \boldsymbol{v}_{N_{\mathrm{UT}}}\}$ includes all combiners at the UT, as the union of all panel codebooks. The received signal strength (RSS) using the beamforming vector $\boldsymbol{u}_i$ and combiner $\boldsymbol{v}_j$ at the AP and UT can be written as

$$R_{i,j} = \left| \sqrt{P_{\mathrm{AP}}} \boldsymbol{v}_j^H \boldsymbol{H}^{(p_j)} \boldsymbol{u}_i s + \boldsymbol{v}_j^H \boldsymbol{n} \right|^2 \tag{D.7}$$

where p_j denotes the panel corresponding to combiner $\boldsymbol{v}_j$.

3 Deep Learning based Beam Selection

The UT location and orientation can be obtained using different sensors and positioning systems on the device at the expense of additional implementation cost and overhead to the system [16]. In beyond 5G systems, joint communication, sensing, and localization will further facilitate location- and orientation-aware BA [17]. As the environment geometry affects the potential LOS and strong NLOS paths from static objects, the UT location and orientation can be used to reduce the beam search space.

3.1 Beam Selection Procedure

Let the set $\mathcal{B}$ include the indices of all possible combinations of beamforming vectors and combiners in the AP and UT. Beam ranking, as a beam selection approach for a UT with a known position and orientation, is a way to reduce the search space by recommending a subset $\mathcal{S}$ from $\mathcal{B}$. We call the set $\mathcal{S}$ the beam-pair candidate list. This approach can be seen as an optimization problem in finding the subset $\mathcal{S}$ from $\mathcal{B}$ which minimizes the misalignment probability, i.e.,

$$\begin{aligned} \min_{\mathcal{S}} \quad & \mathbb{P}\left[\max_{(t,w)\in\mathcal{S}} R_{t,w} < \max_{(i,j)\in\mathcal{B}} R_{i,j} \right], \\ \text{s.t.} \quad & |\mathcal{S}| = C \end{aligned} \tag{D.8}$$

where C is a pre-defined constant specifying the number of beam pairs in the candidate list. The optimal AP/UT beam pair for transmission is

$$i^\star, j^\star = \arg\max_{(i,j)\in\mathcal{B}} R_{i,j}. \tag{D.9}$$

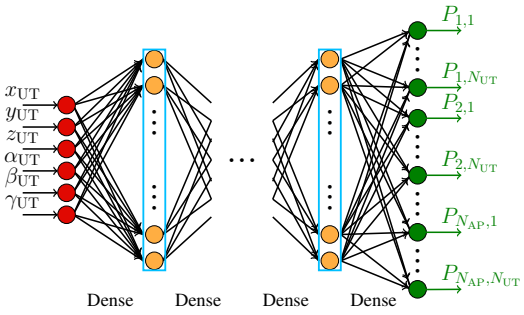

Fig. D.2: The single-network structure directly estimates the optimality probability of each beam pair.

In addition, we define $p^\star$ as the panel corresponding to the optimal UT beam $j^\star$. $P_{i,j} = \mathbb{P}\left[(i,j) = (i^\star, j^\star)\right]$[2] denotes the probability of beam pair (i,j) being optimal, i.e., being the beam pair in the codebook yielding the highest RSS. The AP and UT sense the environment with the beam pairs included in $\mathcal{S}$, and the UT reports the beam pair $(\hat{i},\hat{j})$ with highest RSS as a result of the beam selection procedure. For known UT location and orientation, the optimal $\mathcal{S}$ includes beam pairs with the highest probabilities of optimality [3].

We present next our proposed deep learning methods, which estimate optimality probabilities of all beam pairs. We consider three different approaches to propose a candidate list for a UT with known location and orientation. The first approach, which is an extension of the solution we proposed in [4], uses one network to predict, for all beam pairs, their probability of being optimal. In addition, we propose two novel designs, each using two networks to adapt beam selection for multi-panel devices. In this approach, the first network estimates probabilities of being optimal for all beams at AP. The corresponding list of panels or combiners at the UT for each AP beams are subsequently found by using the second network multiple times.

3.2 Single-Network Design

In this structure, the UT location and orientation are fed to a network with N_h hidden layers with n_h neurons each. There are $N_{\mathrm{UT}}N_{\mathrm{AP}}$ neurons at the output layer, each neuron yielding an estimate of $P_{i,j}$ for the (i,j)th beam pair. The network includes $7n_h + (N_h - 1)(n_h + 1)n_h + (n_h + 1)N_{\mathrm{UT}}N_{\mathrm{AP}}$ trainable parameters [14]. After sorting the network's outputs, a beam candidate list $\mathcal{S}$ including the first N_b indices of beam pairs is made. The AP communicates the combiners selected in $\mathcal{S}$, and then the transceivers sense the environment

[2] $P_{i,j}$ is a conditional probability given the UT location and orientation. To alleviate the notation, we drop this conditionality from the equations.

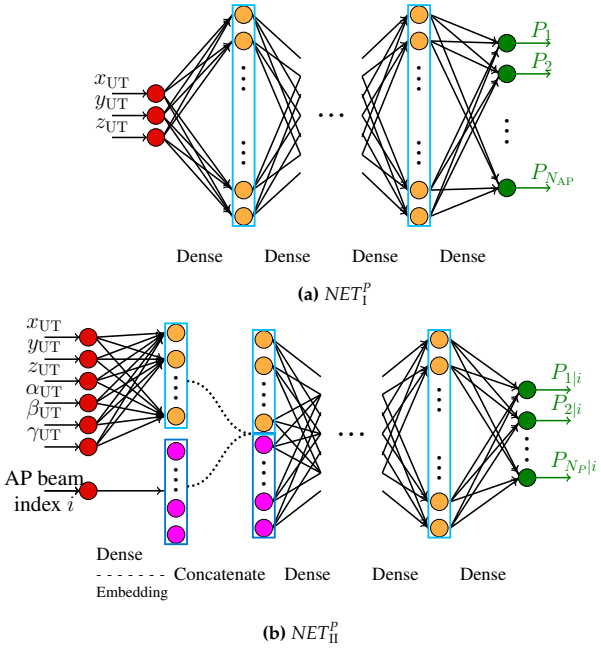

(a) NET_{I}^{P}

(b) NET_{II}^{P}

Fig. D.3: Multi-network structure of proposing candidate beam-panels by finding the proper AP beams and UT panels sequentially.

using N_b time slots during the BA phase [4]. Originally, this method was developed assuming a UT with a single array and RF chain. In this paper, we generalize this method to propose a beam candidate list accounting for hybrid beamforming at UT. The generalization is achieved by re-sorting the beam candidate list to allow for sensing multiple beam pairs with different panels in each time slot. A UT with N_{RF} RF chains can sense $N_{RF}N_b$ beam pairs in N_b time slots, thus set $\mathcal{S}$ has $N_{RF}N_b$ members. Here, $\mathcal{S}$ includes the beam pairs with the highest probabilities of optimality but considering two extra constraints. First, the beam pairs sensed in each time slot should have the same AP beam. Second, the UT beams sensed in each time slot should correspond to different panels.

3.3 Multi-Network Panel Selection Design

The multi-network panel selection (MN-PS) design uses two networks to propose pairs of AP beams and UT panels. Fig. D.3 shows the networks NET_{I}^{P} and NET_{II}^{P} of this method. The role of NET_{I}^{P} is to sort AP beams based on the UT location. As the rotation of the device does not change the AP beamforming, NET_{I}^{P} does not require orientation information of the UT. The outputs of NET_{I}^{P} are therefore estimates of $P_i = \mathbb{P}[i = i^{\star}]$. NET_{I}^{P} has

$4n_h + (N_h - 1)(n_h + 1)n_h + (n_h + 1)N_{\text{AP}}$ trainable parameters.

As antenna panels are placed on different sides of the device, rotations of the device may change the optimal reception panel. Thus, both the UT location and orientation information are fed to NET^P_{II}. NET^P_{II} also has N_h hidden layers, but the first hidden layer has $n_h/2$ neurons, where the first layer outputs are concatenated with $n_h/2$ neurons from the embedding layer. The embedding layer maps the AP beam index to a point in $\mathbb{R}^{n_h/2}$, and the mapping is also a part of the learning process in training. NET^P_{II} includes $(7 + N_{\text{AP}})n_h/2 + (N_h - 1)(n_h + 1)n_h + (n_h + 1)N_P$ trainable parameters. We run NET^P_{II} multiple times with different indices of AP beams to get estimates of the optimality probabilities of each panel for the chosen AP beam, $P_{p|i} = \mathbb{P}\left[p = p^\star | i = i^\star\right]$. The estimates of joint probabilities of AP beam i and UT panel p as the optimal choice can be obtained as

$$P_{i,p} = P_{p|i} P_i. \tag{D.10}$$

A beam-panel candidate list can be made by selecting the combinations providing the highest probabilities. In this method, all the beams at the selected panels should be sensed by the UT. In case of using multiple RF chains at UT, in a time slot with a fixed beamforming vector $i^\star$ at AP, we can sense the environment simultaneously with the $N_{RF} - 1$ other panels that provide higher $P_{i^\star,p}$. MN-PS is robust to inaccuracy in orientation information, as slight changes in orientation may change the optimal UT beam, but the optimal panel is less likely to change. If the UT has N_p RF chains (one RF chain per panel), then each AP beam can be sensed simultaneously with all the panels, and there is no need for panel selection. Thus, in this case, NET^P_{II} is not needed, and the BA can be done using only UT location.

3.4 Multi-Network Beam Selection Design

The multi-network beam selection (MN-BS) design follows a structure similar to the MN-PS one, with the second network providing optimality probabilities directly for the UT beams, instead of for the UT panels. The design of NET^B_{I} is exactly like NET^P_{I} in the UT panel selection method. The structure of NET^B_{II} is the same as NET^P_{II} except with N_{UT} neurons at the output instead of N_P. NET^B_{II} provides estimates of conditional probabilities of UT beam j as the optimal beam for a given AP beam, i.e.,

$$P_{j|i} = \mathbb{P}\left[j = j^\star | i = i^\star\right]. \tag{D.11}$$

The joint probabilities of transceivers beam pair (i, j) as the optimal beam pair can be written as:

$$P_{i,j} = P_{j|i} P_i. \tag{D.12}$$

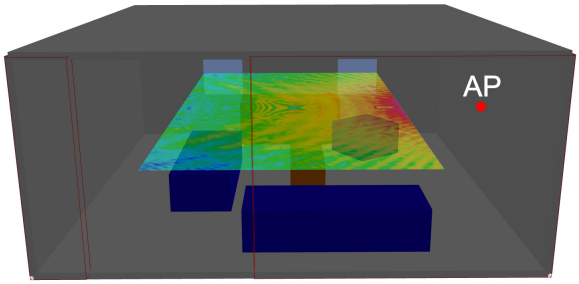

Fig. D.4: The living room, an IEEE standard indoor scenario, in the ray-tracing simulation. The received LOS power at the user region is illustrated.

The candidate beam list $\mathcal{S}$ is made of beam-pairs with the highest estimated probabilities $P_{i,j}$ of being optimal. In case of having multiple RF chain at UT, we use the approach described in Section 3.2 to sense with N_{FR} panels simultaneously.

4 Simulation Results

In this study, we consider the living room proposed in the IEEE 802.11ad task group as an indoor environment with $7 \times 7 \times 3$ meters dimension. The user grid is a rectangle of 4×7 meters at 1.5m height above the floor. The scenario and its propagation properties are described in detail in [18]. As shown in Fig. D.4, the AP is fixed and located in the center of one of the side walls. The AP is made of a UPA panel with $\{1, 8, 8\}$ antenna elements. In this evaluation, we consider both designs for antenna placement shown in Fig. D.1. Panels P1 to P3 have ULAs with 4 antenna elements and UPAs with the configuration of $\{2, 2, 1\}$ antenna elements are used for P4 and P5. We use the antenna radiation pattern described in [19] to simulate the antenna gain of a patch antenna. We use $tanh$ and $softmax$, respectively, as the activation function of the hidden layers and output layer for all the proposed NN structures. In addition, $P_t = 24$ dBm, and $\sigma_n^2 = -84$ dBm are used. For all the networks, we consider $N_h = 5$ and $n_h = 128$ and follow the training procedure explained in [4]. Thus, for the edge-face design, the SN, MN-PS, and MN-BS include $232K$, $146K$, and $148K$ trainable parameters, respectively. To replicate the numerical results, the datasets and code are publicly available at `https://github.com/SajadRezaie/MultiPanelBeamSelection`.

Fig. D.5 shows the spherical coverage with all the panels for the edge design with 12 beams and the edge-face design with 20 beams. The edge design provides lower antenna gain in the directions perpendicular to the device face and back, and suffers from the lack of panel at the bottom. To evaluate the performance of DL-based BA methods, we consider two base-

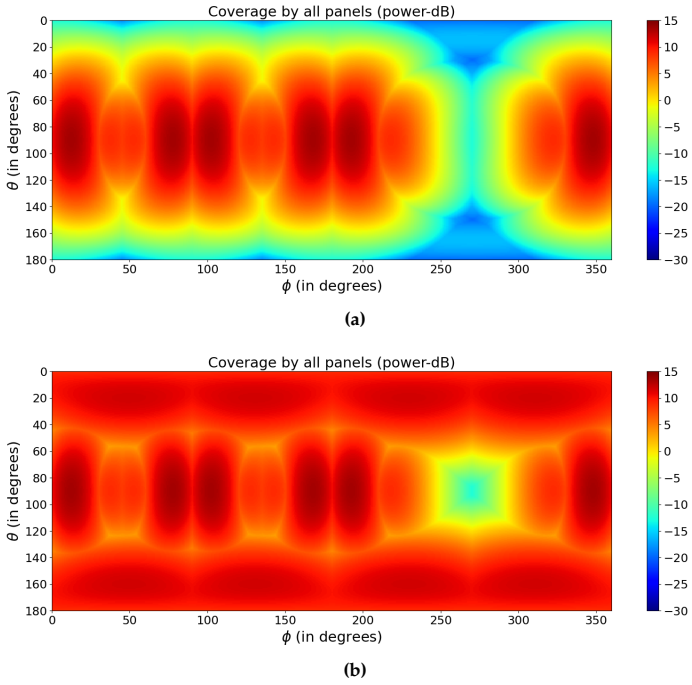

Fig. D.5: Antenna array factor for (a) Edge design (b) Edge-face design.

lines: GIFP and HP-BS methods. The GIFP is a look-up table method and is described in detail in [3, 14]. In the HP-BS, the UT senses the environment with a wide beam for each panel while the AP transmits with a wide beam. Then, all beams of the selected panel are used to find the UT beam that provides the highest RSS. Later, the AP finds the best AP beam using a HBS algorithm [14].

The UT position is uniformly drawn from the user grid, and the UT orientation is 50% in portrait mode and 50% in landscape mode, as defined in Section 2. The line-of-sight (LOS) path is available in half of the realizations, while the other half is generated in non-LOS conditions to emulate blockage situations. The training and test datasets for the proposed DL models are constructed as follows. The AP and UT sense the environment with all possible combinations of beamforming vectors and combiners. We collect the RSS measurements in a dataset, besides each sample's UT location and orientation. To evaluate the performance of CI-based methods with different training dataset sizes, training datasets $\mathbb{D}_1^{\Xi}$ and $\mathbb{D}_2^{\Xi}$ respectively include $56,000$ and 560 training samples. We use a test dataset with $14,000$ samples for evaluation. To account for the overhead introduced by the beam alignment procedure, we evaluate the achievable spectral efficiency of the different

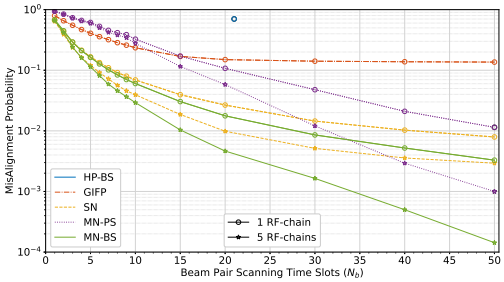

(a)

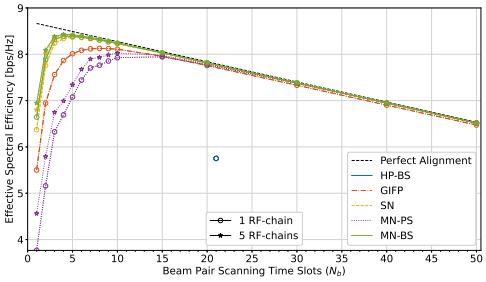

(b)

Fig. D.6: Misalignment probability and effective spectral efficiency for the edge-face design with 56,000 training samples in $\mathbb{D}_1^{\Xi}$.

methods. We assume that the beam pairs chosen during the beam selection procedure are used in a frame of duration T_{fr} smaller than the channel's coherence time. The effective spectral efficiency (ESE) of a BA procedure using N_b time slots is modeled as $\text{SE}_{\text{eff}} = \frac{T_{fr}-N_b T_s}{T_{fr}} \log_2(1+\text{SNR}_{\hat{i},\hat{j}})$, where $\hat{i}$ and $\hat{j}$ are the indices of the AP and UT beams chosen after the beam scanning procedure. Also, $\text{SNR}_{i,j}$ and T_s denote the SNR of (i,j)th beam pair and the beam scanning time slot duration, respectively. $T_{fr} = 20$ms and $T_s = 0.1$ms are used in this study [20].

4.1 Numerical Evaluation

The performance of the described BA methods using $\mathbb{D}_1^{\Xi}$ with 56,000 training samples is shown in Fig. D.6. The MN-BS method has the highest accuracy, which shows the power of the multi-network design using the embedding layer. Also, we see almost no performance degradation in DL-based methods using only 1 RF-chain instead of all 5 RF-chains at the device. As a result of a large training dataset, the MN-BS is trained to reach high accuracy. Thus, at each time slot with a selected AP beam, the MN-BS predicts the proper UT beam from the right panel, and there is nothing to gain by simultaneously

sensing with other panels. Thus, the UT can save power during the BA procedure by turning off all the panels except one of them. The MN-PS method senses all the beams at each panel, which leads to inefficiency compared to MN-BS. However, MN-PS with 5 RF chains can perform well using only the UT location as a unique solution.

The MN-BS method using 3 beam scanning time slots provides 5% more ESE and 50% less latency than the GIFP method, which using 6 beam sensing time slots. Although the HP-BS using 22 sensing time slots does not require any CI and has negligible computational complexity [21], it provides 30% less ESE and around 7 times more latency than the MS-BS method with sensing in 3 time slots. Also, note that the computations of the DL-based methods are done on the AP side. In conclusion, the CI-based BA methods using a large training dataset outperform the HP-BS method significantly.

Since the acquisition of training data is costly, it is also of interest to examine the performance of DL-based methods when trained with small datasets. Fig. D.7a shows the performance of the different BA methods using $\mathbb{D}_2^{\Xi}$ with 560 training samples. Having fewer trainable parameters, the MN designs offer a significant gain compared to the SN structure. In spite of the small dataset size, the MN-BS method significantly outperforms the GIFP as an alternative data-driven approach. Moreover, due to the fact that our proposed methods are DL-based, the transfer learning technique proposed in [22] can be used with the proposed DL-based method to reduce further the performance gap with large training datasets. The edge design has advantages over the edge-face design in hardware complexity and cost with only a slight performance degradation, as shown in Fig. D.7b.

5 Conclusion

This work shows the usefulness of UT location and orientation in the initial BA of multi-panel devices in mmWave communications. Our results show that the deep learning-based methods offer excellent performance in proposing proper beam/panels which leads to power saving by turning off panels for a given UT coordinate and orientation. The numerical evaluations show that the multi-network designs provide the best performance in limited training dataset sizes due to having fewer trainable parameters than the single-network structure. The edge design can offer comparable performance to the edge-face design while reducing the cost and power at UT. Future research will focus on DL based methods with low computational complexity.

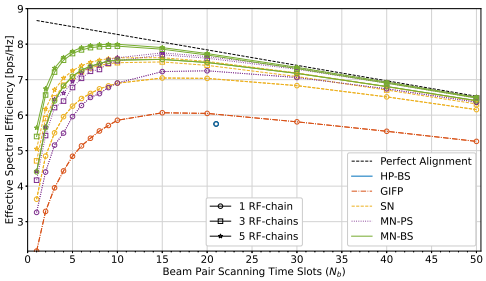

(a)

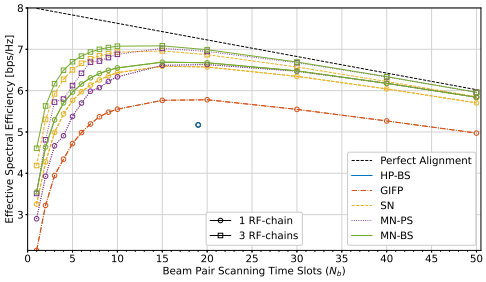

(b)

Fig. D.7: Performance of beam alignment methods with 560 training samples in $\mathbb{D}_2^{\Xi}$ (a) edge-face design (b) edge design.

References

[1] M. Giordani, M. Polese, M. Mezzavilla, S. Rangan, and M. Zorzi, "Toward 6G Networks: Use Cases and Technologies," *IEEE Commun. Mag.*, vol. 58, no. 3, pp. 55–61, Mar. 2020.

[2] M. Giordani, M. Mezzavilla, and M. Zorzi, "Initial Access in 5G mmWave Cellular Networks," *IEEE Commun. Mag.*, vol. 54, no. 11, pp. 40–47, Nov. 2016.

[3] V. Va, J. Choi, T. Shimizu, G. Bansal, and R. W. Heath, "Inverse Multipath Fingerprinting for Millimeter Wave V2I Beam Alignment," *IEEE Trans. Veh. Technol.*, vol. 67, no. 5, pp. 4042–4058, May 2018.

[4] S. Rezaie, C. N. Manchón, and E. de Carvalho, "Location- and Orientation-Aided Millimeter Wave Beam Selection Using Deep Learning," in *Proc. IEEE Int. Conf. Commun.*, Jun. 2020, pp. 1–6.

[5] W. Xu, F. Gao, S. Jin, and A. Alkhateeb, "3D Scene-Based Beam Selection for mmWave Communications," *IEEE Wireless Commun. Lett.*, vol. 9, no. 11, pp. 1850–1854, Nov. 2020.

[6] V. Raghavan, M.-L. Chi, M. A. Tassoudji, O. H. Koymen, and J. Li, "Antenna Placement and Performance Tradeoffs With Hand Blockage in Millimeter Wave Systems," *IEEE Trans. Commun.*, vol. 67, no. 4, pp. 3082–3096, Apr. 2019.

[7] V. Raghavan, R. A. Motos, M. A. Tassoudji, Y.-C. Ou, O. H. Koymen, and J. Li, "Mitigating Hand Blockage with Non-Directional Beamforming Codebooks," *arXiv:2104.06472 [cs, math]*, Apr. 2021. [Online]. Available: http://arxiv.org/abs/2104.06472

[8] J. Mo, B. L. Ng, S. Chang, P. Huang, M. N. Kulkarni, A. Alammouri, J. C. Zhang, J. Lee, and W.-J. Choi, "Beam Codebook Design for 5G mmWave Terminals," *IEEE Access*, vol. 7, pp. 98 387–98 404, 2019.

[9] A. Alammouri, J. Mo, B. L. Ng, J. C. Zhang, and J. G. Andrews, "Hand Grip Impact on 5G mmWave Mobile Devices," *IEEE Access*, vol. 7, pp. 60 532–60 544, 2019.

[10] W.-T. Shih, C.-K. Wen, S.-H. Tsai, and S. Jin, "Fast Antenna and Beam Switching Method for mmWave Handsets with Hand Blockage," *IEEE Trans. Wireless Commun.*, pp. 1–1, 2021.

[11] X. Song, T. Kuhne, and G. Caire, "Fully-/Partially-Connected Hybrid Beamforming Architectures for mmWave MU-MIMO," *IEEE Trans. Wireless Commun.*, vol. 19, no. 3, pp. 1754–1769, Mar. 2020.

[12] Y. Heng, J. G. Andrews, J. Mo, V. Va, A. Ali, B. L. Ng, and J. C. Zhang, "Six Key Challenges for Beam Management in 5.5G and 6G Systems," *IEEE Commun. Mag.*, vol. 59, no. 7, pp. 74–79, Jul. 2021.

[13] A. Ali, J. Mo, B. L. Ng, V. Va, and J. C. Zhang, "Orientation-Assisted Beam Management for Beyond 5G Systems," *IEEE Access*, vol. 9, pp. 51 832–51 846, 2021.

[14] S. Rezaie, E. de Carvalho, and C. N. Manchón, "A Deep Learning Approach to Location- and Orientation-aided 3D Beam Selection for mmWave Communications," *arXiv:2110.06859 [eess]*, Oct. 2021, arXiv: 2110.06859. [Online]. Available: http://arxiv.org/abs/2110.06859

[15] "Altair Feko WinProp," [online] Available: https://www.altair.com/feko.

[16] M. Kok, J. D. Hol, and T. B. Schön, "Using Inertial Sensors for Position and Orientation Estimation," *Found. Trends Signal Process.*, vol. 11, no. 1-2, pp. 1–153, 2017.

[17] C. De Lima, D. Belot, R. Berkvens, A. Bourdoux, D. Dardari, M. Guillaud, M. Isomursu, E.-S. Lohan, Y. Miao, A. N. Barreto, M. R. K. Aziz, J. Saloranta, T. Sanguanpuak, H. Sarieddeen, G. Seco-Granados, J. Suutala, T. Svensson, M. Valkama, B. Van Liempd, and H. Wymeersch, "Convergent Communication, Sensing and Localization in 6G Systems: An Overview of Technologies, Opportunities and Challenges," *IEEE Access*, vol. 9, pp. 26 902–26 925, 2021.

[18] A. Maltsev, "Channel models for 60GHz WLAN systems," *IEEE802. 11 09/0334r8*, 2010.

[19] 3GPP, *Study on channel model for frequencies from 0.5 to 100 GHz*. TR 38.901 V16.1.0, 2020. [Online]. Available: http://www.3gpp.org/DynaReport/38901.htm

[20] M. Hussain and N. Michelusi, "Second-Best Beam-Alignment via Bayesian Multi-Armed Bandits," in *Proc. IEEE GLOBECOM*, Dec. 2019, pp. 1–6.

[21] V. Raghavan, J. Cezanne, S. Subramanian, A. Sampath, and O. Koymen, "Beamforming Tradeoffs for Initial UE Discovery in Millimeter-Wave MIMO Systems," *IEEE J. Sel. Top. Signal Process.*, vol. 10, no. 3, pp. 543–559, Apr. 2016.

[22] S. Rezaie, A. Amiri, E. de Carvalho, and C. N. Manchón, "Deep Transfer Learning for Location-Aware Millimeter Wave Beam Selection," *IEEE Commun. Lett.*, vol. 25, no. 9, pp. 2963–2967, Sep. 2021.

Paper E

Device-Agnostic Millimeter Wave Beam Selection using Machine Learning

Sajad Rezaie, João Morais, Ahmed Alkhateeb, Carles Navarro Manchón

The paper has been submitted to the
IEEE Transactions on Wireless Communications, Nov. 2022.

The layout has been revised.

Abstract

Most research in the area of machine learning-based user beam selection considers a structure where the model proposes appropriate user beams. However, this design requires a specific model for each user-device beam codebook, where a model learned for a device with a particular codebook can not be reused for another device with a different codebook. Moreover, this design requires training and test samples for each antenna placement configuration/codebook. This paper proposes a device-agnostic beam selection framework that leverages context information to propose appropriate user beams using a generic model and a post processing unit. The generic neural network predicts the potential angles of arrival, and the post processing unit maps these directions to beams based on the specific device's codebook. The proposed beam selection framework works well for user devices with antenna configuration/codebook unseen in the training dataset. Also, the proposed generic network has the option to be trained with a dataset mixed of samples with different antenna configurations/codebooks, which significantly eases the burden of effective model training.

1 Introduction

Initial beam alignment (BA) in multiple-input multiple-output (MIMO) systems operating at millimeter wave (mmWave) band is critical for establishing a reliable communication link. Using predefined beams in codebook-based beamforming is a popular approach to simplify the BA process. An exhaustive search over all possible beam pairs at the transceivers finds the optimal beam configuration, but results in undesirable overhead and latency for the network. Although hierarchical beam search imposes a limited overhead to the network, it is prone to errors due to the low signal-to-noise ratio (SNR) at the first search stages with wide beams [1]. Machine learning (ML)-based methods are proposed to overcome these challenges by leveraging the knowledge available in data captured in a specific environment. In [2], an ML-based procedure is proposed to estimate the dominant path's angle of arrival (AoA) with an adaptive compressed sensing approach. Also, the authors of [3] use the ML capabilities in a beam selection framework to recommend the best beam for the base station (BS) in a multi-user SIMO scenario. However, these methods assume a single path channel for the mmWave link, therefore the proposed frameworks may not work well in multipath channels.

Another research track has focused on context information (CI)-based beam selection methods leveraging additional information like user position, camera images, and sub-6 GHz channel state information. The extra information provides the opportunity to reduce the beam search space, which subsequently leads to reducing the latency and increasing the accuracy of the BA process [4–6]. As it is not a straightforward task to use CI in the beam

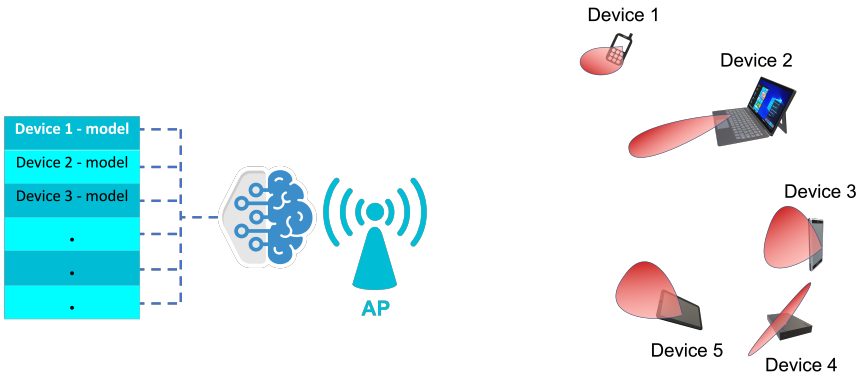

Fig. E.1: An access point communicates with different user terminals, such as smartphones, tablets, and laptops from different vendors. The user terminals have different beam codebooks because of different antenna configurations and hardware, which requires the network to maintain a specific ML model for each type of user device.

selection process, deep learning (DL) capabilities are often used to boost the performance of CI-based methods [7–9]. The acquisition of CI may apply additional latency or overhead to the system, which constitutes the main challenge for the CI-based approach in some applications.

However, in both context-free and context-aware ML-based beam selection methods, most research assumes a network structure specific to the user antenna configuration/beam-codebook to recommend the best user beam from the codebook. In this structure, the ML model estimates the optimality probability for each beam from the codebook. However, as shown in Fig. E.1, an access point may serve several user terminals (UTs) from different vendors, which may have different antenna configurations/codebooks. Thus, different ML networks are needed for different device codebook configurations, making the ML-based beam selection less attractive. Another challenge is collecting training datasets for different antenna placement designs/beam-codebook configurations [3, 8, 10]. Here, UT terminal indicates the type of device, its antenna configuration, and its beam codebook. Thus, using UT-specific ML models for each possible terminal implies the collection of UT-specific training datasets, along with the associated training computational and memory challenges of having to train, store, and manage a multiplicity of models.

Transfer learning (TL) provides the option to reuse the information learned by a network with a large training dataset and a given antenna configuration to reach an acceptable performance for a new antenna configuration with a smaller training dataset [11]. However, directly reusing the learned network without additional samples is not feasible with this technique. Moreover, the

TL method in [11] does not solve the issue of training a network with samples from different antenna configurations/codebooks.

One possible avenue to overcome the need for UT-specific beam selection NNs is to design models that rank beamforming directions rather than specific codebook beams. To discretize the angular direction space in such an approach, Fibonacci grids [12] can employed. A Fibonacci grid (FG) is a set of points in which the points are placed evenly on the sphere. FGs have already been applied to solve other problems in mmWave beam management. For instance, an orientation-assisted beam alignment method using particle filters is proposed in [13], where a FG is used for initialization of particles. To design codebooks that account for coupling and the impacts of the user hand grip, the authors in [14, 15] use the FG as a way to pick uniformly distributed sampling points on the unit sphere. Also, a similarity metric/measure using the FG is used to match beams in two different antenna configurations [16].

1.1 Contributions

As a solution to the above mentioned challenges with device-specific structure for ML-based beam alignment methods, this paper proposes a device-agnostic ML-based beam selection framework. The proposed framework includes two main parts: a generic neural network (NN) that recommends directions instead of UT beams, and a post processing unit that maps the proposed directions to the UT beams in the codebook. The main contributions of this paper are:

1. We use the FG to discretize the AoAs at the UT side. Using this technique, we replace the device-specific beam selection task with the discretized direction selection as a device-agnostic task. The generic NN provides the optimality probability for each point in the Fibonacci grid.

2. The generic NN is followed by a post processing unit implementing a deterministic mapping function. The proposed unit calculates the optimality probability of UT beams using the optimality probability of the FG points.

3. We consider a multi-labeling training procedure for the generic NN. By reversing the mapping process in 2), the optimal UT beam corresponds to a subset of the Fibonacci grid, and we mark those points as labels in the generic NN training procedure.

4. To illustrate the proposed device-agnostic framework in the ML-based beam selection methods, we implement the device-agnostic framework in the two CI-based beam alignment methods respectively proposed in [17] and [6]: (a) Beam pair selection for user handsets leveraging the

user location and orientation information, and (b) mmWave beam pair selection using the uplink sub-6 GHz channel information.

5. We use accurate 3-dimensional (3D) ray-tracing tools to generate the training and test samples for the two CI-based studies. The numerical evaluations show that the proposed device-agnostic framework works well even for devices with beam codebooks that were unseen in the training samples. In addition, the generic NN can be trained with a dataset measured with different devices.

6. We extended the work presented in [6] to support beamforming at the user side. The results show that the sub-6 GHz channel as CI can be used for mmWave UT beamforming in both line-of-sight (LOS) and non-line-of-sight (NLOS) conditions.

1.2 Organization and Notations

The rest of the paper is organized as follows. First, the overall view of the beam selection problem, the components of the proposed device-agnostic framework, and the labeling vector for the generic NN are described in Section 2. In Section 3, we explain the system model of the location and orientation-aware beam selection method and show how the network structure can be updated based on the proposed device-agnostic design. Also, the numerical results of this work are shown in this section. The system model of the beam selection method leveraging the sub-6 GHz channel is explained in Section 4. This section includes the results before and after integrating the device-agnostic framework in this study. Finally, we summarise the conclusions of the study in Section 5.

The notations used in this paper are as follows. $\mathbb{R}$ and $\mathbb{C}$ denote the fields of real and complex numbers, respectively. We denote by $\mathcal{A}$ a finite set and by $|\mathcal{A}|$ its cardinality. In addition, we use a, $\boldsymbol{a}$, and $\boldsymbol{A}$ to denote a scalar, a vector, and a matrix, respectively. a_i is the ith entry of the column vector $\boldsymbol{a}$, and $A_{i,j}$ represents the entry in the ith row and jth column of the matrix $\boldsymbol{A}$. Notations $(\cdot)^T$ and $(\cdot)^H$ denote, respectively, transposition and complex transposition of vectors and matrices. Also, $\otimes$ is the Kronecker product. $\arg\max_{i,j} A_{i,j}$ denotes the row and column index of the maximum entry of matrix $\boldsymbol{A}$ as a tuple. $\mathbf{0}_t$ and $\boldsymbol{I}_p$ denote a zero column vector of length t and the $p \times p$ identity matrix, respectively. $\mathbb{P}(A)$ denotes the probability of the event A.

2 Device-agnostic Beam Selection framework

A brief background on the codebook-based beam selection procedure from a general perspective is introduced in Section 2.1. Then, the widely used device-specific DL-based beam selection is explained in Section 2.2. Our proposed device-agnostic beam selection framework is introduced in Section 2.3, including the generic NN and post processing unit as the main blocks of the framework. Lastly, Section 2.4 describes the dataset collection and labeling procedure for the device-specific and device-agnostic frameworks.

2.1 Codebook-based Beam Selection

Consider $\boldsymbol{H}$ as the mmWave downlink channel between an access point (AP) and UT placed in an environment, and the AP and UT respectively use $\boldsymbol{u}$ and $\boldsymbol{v}$ beamforming vectors for communication. The received signal at the UT may be written as

$$y = \sqrt{P_{\text{AP}}}\boldsymbol{v}^H \boldsymbol{H}\boldsymbol{u}s + \boldsymbol{v}^H \boldsymbol{n} \tag{E.1}$$

where s and P_{AP} are the unit power symbol s and the AP transmission power, respectively. In addition, $\boldsymbol{n}$ is a zero-mean complex Gaussian noise with variance σ_n^2.

Consider the UT has a codebook with N_{UT} beams, and the set $\mathcal{B}_{\text{UT}}$ includes the indices of all beams in the UT codebook. In this section, for the sake of simplicity of explanation, we focus only on the selection of the UT beamforming vector $\boldsymbol{v}$. We assume that the AP beamforming vector $\boldsymbol{u}$ has already been chosen by other means. However, Sections 3 and 4 show that the proposed technique can be applied to joint beamforming applications where both the AP and UT are capable of beamforming. In the beam selection approach, we target predicting a beam candidate list, $\mathcal{S} \subset \mathcal{B}_{\text{UT}}$, for sensing the environment, which leads to a smaller beam search space. The optimal choice of $\mathcal{S}$ depends on the propagation properties of the environment and the UT properties like its location and orientation. As it is proven in [4], the optimal UT beam candidate list for a given UT condition includes the beam indices that have the highest probabilities of optimality. The probability of optimality for the ith beam may be expressed as $P_j^B = \mathbb{P}\left[j = j^\star\right]$, where $j^\star$ is the optimal UT beam for communication providing the highest received signal strength (RSS).

2.2 Device-Specific framework

In prior work, the CI-based beam selection was mainly performed using a common device-specific NN that takes some assistance information (such as LIDAR, camera images, user position, etc.) as input and provides the

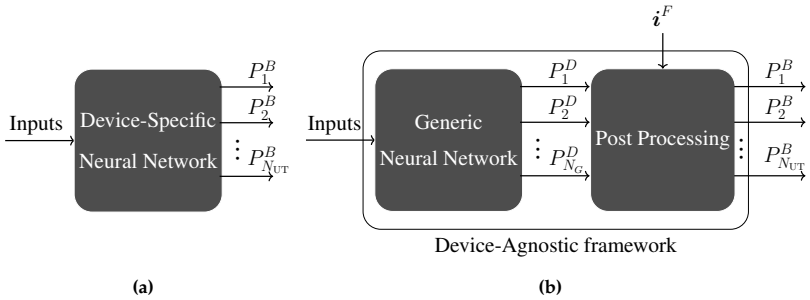

Fig. E.2: Neural network-based beam selection using (a) a device-specific and (b) the proposed device-agnostic structures. In both cases, the inputs to the networks may include data relevant for beam management, such as location information, orientation information, out-of-band channel state information, RGB camera images, RADAR, LIDAR, etc.

optimality probability for each beam in the codebook, $P_j^B, j = 1, 2, \cdots, N_{\text{UT}}$, as shown in Fig. E.2a. The device-specific NN structure includes a series of dense and/or convolutional layers followed by an output layer with N_{UT} neurons. The weights of the network are trained for a specific device with a specific codebook. Thus, several sets of trained weights need to be stored to serve different UTs, which causes challenges with memory and management of models.

2.3 Device-Agnostic framework

In this study, we propose a device-agnostic framework that can solve the above mentioned problem and provides performance as good as the device-specific design. As shown in Fig. E.2b, the proposed device-agnostic framework includes two main parts, the generic NN and a post processing unit.

Generic NN

As each beam of the UT codebook covers parts of the unit sphere, it is sufficient to know the AoA in a discretized set of directions. We use the spherical Fibonacci grid to obtain an equal-area grid of points on the sphere [12]. Set $\mathcal{A} = \{(\phi_k, \theta_k), k = 1, ..., n_{Fib}\}$ containing n_{Fib} elements, where each element is a tuple (azimuth, elevation) describing potential directions of transmission/reception. We consider that set $\mathcal{I} = \{1, 2, \cdots, n_{Fib}\}$ includes the indexes of elements in set $\mathcal{A}$. Fig. E.3 shows the Fibonacci grid with $n_{Fib} = 100$ points on the unit sphere.

The generic network predicts the optimality probabilities of the UT AoA

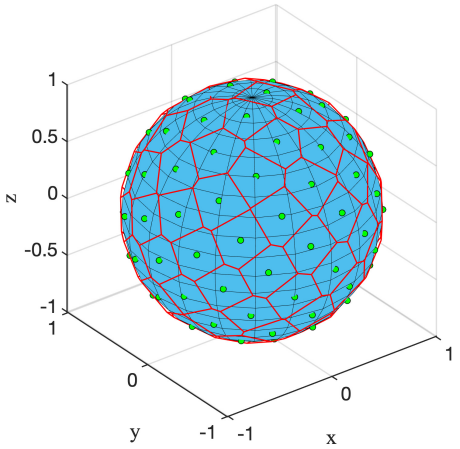

Fig. E.3: Fibonacci grid with 100 points. Cells corresponding to each Fibonacci point cover equal areas on the sphere surface.

in the UT local coordinate system (LCS), i.e.,

$$P_k^D = \mathbb{P}\left[k = k^\star\right] \tag{E.2}$$

where $k^\star$ denotes the index of element of $\mathcal{A}$ containing the optimal direction of transmission/reception in the UT LCS.

Post Processing

In the post processing unit, the probabilities of optimal direction, P_k^D, are combined to construct the optimality probabilities of UT beams, P_j. Thus, the generic probabilities as outcomes of the generic NN are combined based on the UT-specific codebook mapping information to generate the UT-specific beam probabilities. This operation needs information about the beam index providing the highest gain for each Fibonacci point, $\boldsymbol{i}^F \in \mathbb{N}^{n_{Fib}\times 1}$, which depends solely on the device codebook and antenna geometry. The kth entry of $\boldsymbol{i}^F$ indicates the index of the beam which has highest gain in the direction of the kth element of $\mathcal{A}$. The mapping is required to be shared only one time by the UT, and we assume the AP have knowledge of such mapping. We define set $\mathcal{I}^j, j = 1, \cdots, N_{\text{UT}}$, a partition of set $\mathcal{I}$, including the index of Fibonacci points that the UT beam i provides the highest gains in those directions, i.e., $\boldsymbol{i}_k^F = j \iff k \in \mathcal{I}^j$. $\mathcal{I}^j$ are non-overlapping sets whose union is equal to $\mathcal{I}$. Thus, the post processing unit uses the subsets $\mathcal{I}^j$ to map the FG optimality probabilities, P_k^D, onto UT beam optimality probabilities as

$$P_j^B = \sum_{k\in\mathcal{I}^j} P_k^D. \tag{E.3}$$

In the last step, the beam candidate list $\mathcal{S}$ is proposed by including the indices of beams that have the highest optimality likelihood, P_j^B.

2.4 Dataset Generation and Labeling

To construct the training and evaluation datasets, all the possible UT beam are sensed for each realization of the scenario. Considering beam $j^\star$ provides the highest RSS, the labeling vector of the device-specific network is

$$L_j^S = \begin{cases} 1, & \text{if } j = j^\star, \\ 0, & \text{otherwise.} \end{cases} \tag{E.4}$$

However, for training the generic NN, the Fibonacci points in the beam region of the optimal UT beam are marked, i.e.,

$$L_k^G = \begin{cases} 1, & \text{if } k \in \mathcal{I}^{j^\star}, \\ 0, & \text{otherwise.} \end{cases} \tag{E.5}$$

We use the mapping function between the Fibonacci points and the UT beams, $\mathcal{I}^{j^\star}$, to mark the right neurons at the output layer of the generic network. Thus, we mark all the directions where the UT beam $j^\star$ provides the highest gain in the labeling vector. Each dataset sample includes the inputs to the network, the RSS measurements for all the UT beams, and the corresponding labeling vector.

3 Location- and Orientation-aware Beam Selection

The study in this section extends the beam selection method proposed in [17] by integrating the described device-agnostic framework. This work shows how the device-specific structure can be replaced with the device-agnostic framework without (noticeable) losses in performance.

3.1 System and Channel Model

We consider a point to point communication between a fixed AP and a mobile UT in an indoor environment. The AP uses a uniform planar array (UPA) with array size of $\{N_{\mathrm{AP_x}}, N_{\mathrm{AP_y}}, N_{\mathrm{AP_z}}\}$. The UT is made of N_P panels, where the pth panel has an uniform linear array (ULA) or UPA of size $\{N_{\mathrm{UT_x}}^{(p)}, N_{\mathrm{UT_y}}^{(p)}, N_{\mathrm{UT_z}}^{(p)}\}$. Thus, the AP, the pth UT panel, and the UT include $N_{\mathrm{AP}} = N_{\mathrm{AP_x}} N_{\mathrm{AP_y}} N_{\mathrm{AP_z}}$, $N_{\mathrm{UT}}^{(p)} = N_{\mathrm{UT_x}}^{(p)} N_{\mathrm{UT_y}}^{(p)} N_{\mathrm{UT_z}}^{(p)}$, and $N_{\mathrm{UT}} = \sum_{p=1}^{N_P} N_{\mathrm{UT}}^{(p)}$ antenna elements, respectively. Inspired by [18], we consider the edge (E), face

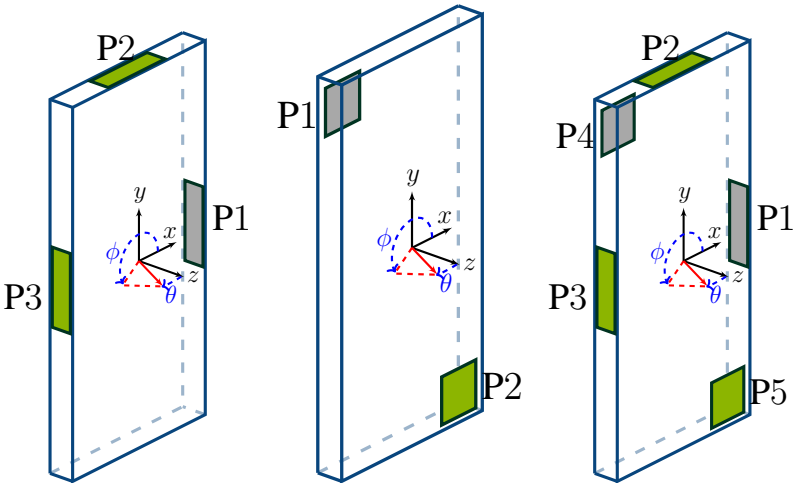

(a) Edge design **(b)** Face design **(c)** Edge-face design

Fig. E.4: Antenna placement designs inspired from [18] (a) edge design with 3 ULAs on the device's edges (b) face design with 2 UPAs on the device's face and back (c) edge-face design with 5 panels.

(F), and edge-face (EF) antenna placement designs, respectively, with 3, 2, and 5 panels at UTs, which are illustrated in Fig. E.4.

A global coordinate system (GCS) is considered for the environment and we define the position and orientation of the transceivers in the GCS [13]. In addition, we consider an LCS for each transceiver. The LCSs are defined in a way that the yz and xy plane of the AP and UT LCSs are alligned parallel to the AP's UPA and UT's screen, respectively. $\boldsymbol{p}_{\mathrm{AP}} = (x_{\mathrm{AP}}, y_{\mathrm{AP}}, z_{\mathrm{AP}}) \in \mathbb{R}^3$ and $\boldsymbol{p}_{\mathrm{UT}} = (x_{\mathrm{UT}}, y_{\mathrm{UT}}, z_{\mathrm{UT}}) \in \mathbb{R}^3$ denote the positions of the AP and UT in the GCS. The AP and UT LCSs are rotated about z, y, and x axes of the GCS by angles $\boldsymbol{\psi}_{\mathrm{AP}} = (\alpha_{\mathrm{AP}}, \beta_{\mathrm{AP}}, \gamma_{\mathrm{AP}})$ and $\boldsymbol{\psi}_{\mathrm{UT}} = (\alpha_{\mathrm{UT}}, \beta_{\mathrm{UT}}, \gamma_{\mathrm{UT}})$, respectively [19].

Channel Model

We consider a narrow band channel between the AP and the pth UT panel, $\boldsymbol{H}^{(p)} \in \mathbb{C}^{N_{\mathrm{UT}}^{(p)} \times N_{\mathrm{AP}}}$. The channel considering the contribution of $L^{(p)}$ paths may be modeled as

$$\boldsymbol{H}^{(p)} = \sum_{l=0}^{L^{(p)}} \sqrt{\rho_l^{(p)}}\, e^{j\vartheta_l^{(p)}}\, \boldsymbol{a}_{\mathrm{UT}}^{(p)}(\phi_l^{(p)}, \theta_l^{(p)})\, \boldsymbol{a}_{\mathrm{AP}}^{H}(\psi_l^{(p)}, \omega_l^{(p)}) \tag{E.6}$$

where $\rho_l^{(p)}$ and $\vartheta_l^{(p)}$ are, respectively, the power and phase of the lth path. The azimuth and elevation angle of departure (AoD) of the lth path in the

AP LCS are $\phi_l^{(p)}$ and $\theta_l^{(p)}$, respectively. $\psi_l^{(p)}$ and $\omega_l^{(p)}$ denote, analogously, the azimuth and elevation AoA for the lth path in the UT LCS. $\boldsymbol{a}_{\mathrm{UT}}^{(p)}$ and $\boldsymbol{a}_{\mathrm{AP}}$ respectively stands for the antenna array response of the pth UT panel and the AP. Considering an antenna array of size $\{N_{\mathrm{x}}, N_{\mathrm{y}}, N_{\mathrm{z}}\}$, the antenna array response can be defined as

$$\boldsymbol{a}(\phi,\theta) = \frac{1}{\sqrt{N_{\mathrm{a}}}} g_{\mathrm{a}}(\phi,\theta)\boldsymbol{a}_{\mathrm{z}}(\theta) \otimes \boldsymbol{a}_{\mathrm{y}}(\phi,\theta) \otimes \boldsymbol{a}_{\mathrm{x}}(\phi,\theta) \tag{E.7}$$

where $N_{\mathrm{a}} = N_{\mathrm{x}}N_{\mathrm{y}}N_{\mathrm{z}}$. At azimuth and elevation angles ϕ and θ, $g_{\mathrm{a}}(\phi,\theta)$ denotes the antenna gain of an antenna element[1]. Also, $\boldsymbol{a}_{\mathrm{x}} \in \mathbb{C}^{N_{\mathrm{x}}\times 1}$, $\boldsymbol{a}_{\mathrm{y}} \in \mathbb{C}^{N_{\mathrm{y}}\times 1}$, and $\boldsymbol{a}_{\mathrm{z}} \in \mathbb{C}^{N_{\mathrm{z}}\times 1}$ are defined as

$$\boldsymbol{a}_{\mathrm{x}}(\phi,\theta) = [1, e^{j\pi sin(\theta)\, cos(\phi)}, \ldots, e^{j\pi(N_{\mathrm{x}}-1)\, sin(\theta)\, cos(\phi)}]^T, \tag{E.8}$$

$$\boldsymbol{a}_{\mathrm{y}}(\phi,\theta) = [1, e^{j\pi sin(\theta)\, sin(\phi)}, \ldots, e^{j\pi(N_{\mathrm{y}}-1)\, sin(\theta)\, sin(\phi)}]^T, \tag{E.9}$$

$$\boldsymbol{a}_{\mathrm{z}}(\theta) = [1, e^{j\pi cos(\theta)}, \ldots, e^{j\pi(N_{\mathrm{z}}-1)\, cos(\theta)}]^T. \tag{E.10}$$

Considering the AP transmits the unit power symbol s with transmission power P_{AP}, the received signal at the pth UT panel is

$$y^{(p)} = \sqrt{P_{\mathrm{AP}}}\boldsymbol{v}^{(p)^H}\boldsymbol{H}^{(p)}\boldsymbol{u}s + \boldsymbol{v}^{(p)^H}\boldsymbol{n}^{(p)} \tag{E.11}$$

where $\boldsymbol{u}$ and $\boldsymbol{v}^{(p)}$ respectively denote the beamforming vector at the AP and pth UT panel. Also, $\boldsymbol{n}^{(p)} \in \mathbb{C}^{N_{\mathrm{UT}}^{(p)}}$ denotes a complex Gaussian noise vector with zero mean and variance σ_n^2.

Codebook Definition

We consider an analog phased array design for beamforming at the AP and each UT panel. Both the AP and UT have one RF chain, and the UT RF chain is connected to one of the panels. For simplicity, multi-panel beamforming is not considered in this paper. We use discrete Fourier transform (DFT)-based analog codebook for each panel [20]. All the available beamforming vectors at the AP are included in the set $\boldsymbol{\mathcal{U}} = \{\boldsymbol{u}_1, \ldots, \boldsymbol{u}_{N_{\mathrm{AP}}}\}$. $\boldsymbol{\mathcal{V}}^p = \{\boldsymbol{v}_1^p, \ldots, \boldsymbol{v}_{N_{\mathrm{UT}}^{(p)}}^p\}$ includes all the beams for the pth UT panel. The beam codebook of the UT, $\boldsymbol{\mathcal{V}} = \{\boldsymbol{v}_1, \ldots, \boldsymbol{v}_{N_{\mathrm{UT}}}\}$, can be expressed as union of all the panel codebooks. Using the beamforming vectors $\boldsymbol{u}_i$ and $\boldsymbol{v}_j$ at the AP and UT, the RSS at the UT is

$$R_{i,j} = \left|\sqrt{P_{\mathrm{AP}}}\boldsymbol{v}_j^H\boldsymbol{H}^{(p_j)}\boldsymbol{u}_i s + \boldsymbol{v}_j^H\boldsymbol{n}\right|^2 \tag{E.12}$$

where p_j is the corresponding panel of combiner $\boldsymbol{v}_j$. We define set $\mathcal{B}$, including the indices of all beam pairs in the AP and UT codebooks.

[1]We assume all antennas have the same radiation pattern.

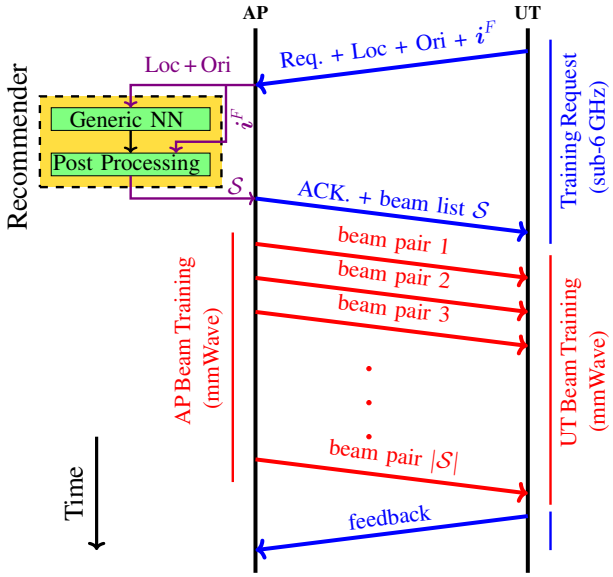

Fig. E.5: The device agnostic DL-based mmWave beam training procedure using location and orientation information.

3.2 Deep Learning based Beam Selection

The beam candidate list, $\mathcal{S}$, is the key component of the beam selection approach, which reduces the search space over all the possible combinations of AP and UT beams. As mentioned in Section 2 [4], the optimal candidate list for a known UT position and orientation includes the beam pair indices that provides the highest likelihood of optimality. The optimality probability for the (i,j)th beam pair is $P^B_{i,j} = \mathbb{P}\left[(i,j) = (i^\star, j^\star)\right]$, where $(i^\star, j^\star)$ is the optimal AP/UT beam pair for communication, i.e.,

$$(i^\star, j^\star) = \underset{(i,j)\in\mathcal{B}}{\arg\max}\, R_{i,j}. \tag{E.13}$$

Taking advantage of the device-agnostic framework, we propose a generic context-aware beam selection procedure that uses the location and orientation of the UT to recommend a beam candidate list. Fig. E.5 shows the proposed device/codebook-agnostic beam selection procedure where the connection request and feedback are communicated in sub-6 GHz links. A generic model processes the location and orientation information to predict the optimal AP beam - UT direction for establishing a mmWave link. A post processing framework is needed to map the directions in the UT LCS to the UT beams.

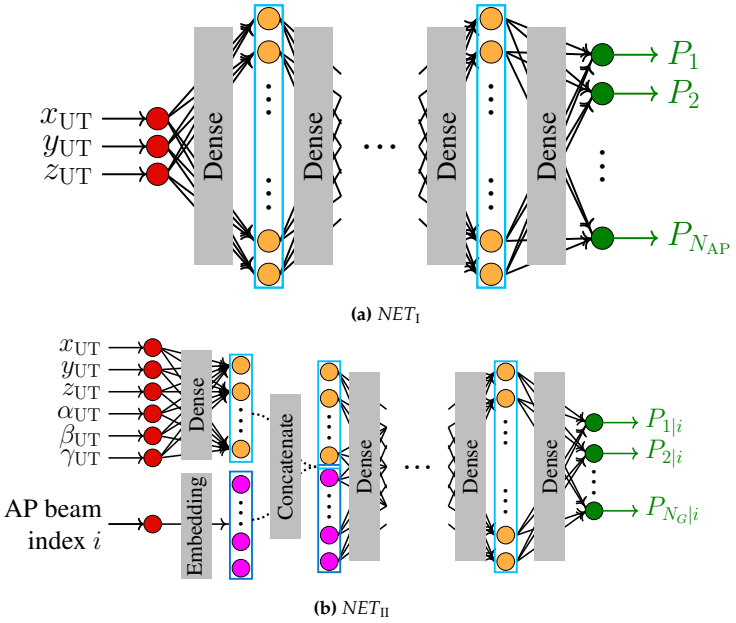

(a) NET_{I}

(b) NET_{II}

Fig. E.6: Multi-network structure of the proposed generic neural network predicting the optimality probability for AP beam-UT directions, including (a) NET_{I} used to select AP beam based on UE location, (b) NET_{II} used to select UE beamforming direction based on AP beam and UE location and orientation.

Inspired by our previous work in [17], we propose a multi-network structure that can predict proper directions of transmission covering the LOS or strong NLOS paths. Fig. E.6 shows our proposed design for the generic NN, which is able to point directions instead of the UT beams. The first network, NET_{I}, predicts the optimality probabilities of the AP beams, i.e.,

$$P_i = \mathbb{P}\left[i = i^\star\right] \tag{E.14}$$

Subsequently, NET_{II} predicts the conditional probabilities of optimality given the AP beam index for the directions given by the FG in the UT LCS as

$$P^D_{k|i} = \mathbb{P}\left[k = k^\star | i = i^\star\right] \tag{E.15}$$

where $k^\star$ denotes the optimal direction of transmission in the UT LCS. Thus, NET_{II} needs to be executed N_{AP} times, once for each AP beam. Both the NET_{I} and NET_{II} have N_h hidden layers where each hidden layer is made of n_h neurons. NET_{II} includes an embedding layer that maps the AP beam index as an integer to a point in hyperspace $\mathbb{R}^{n_h/2}$. The weights of the embedding layer are trained as part of the learning process [17]. Thus, the conditional

probabilities of UT beam optimality given the AP beam i can be written as

$$P^B_{j|i} = \sum_{k \in \mathcal{I}^j} P^D_{k|i}. \tag{E.16}$$

The joint optimality probability of beam pair (i, j) reads

$$P_{i,j} = P^B_{j|i} P_i. \tag{E.17}$$

The beam pair candidate list $\mathcal{S}$ includes the index of beam pairs with the highest joint probabilities.

3.3 Dataset Generation and Labeling

To construct the training and evaluation datasets, the AP is kept fixed in the environment, and the UT is placed randomly in different positions with different orientations. All the possible transceivers beam pairs are sensed for each UT location and orientation. Considering beam pair $(i^\star, j^\star)$ provides the highest RSS, the labeling vector of NET_{I} is

$$L^{\mathrm{I}}_i = \begin{cases} 1, & \text{if } i = i^\star, \\ 0, & \text{otherwise.} \end{cases} \tag{E.18}$$

For training NET_{II}, the AP beam index used as input to the network is set to $i^\star$, and we mark all the directions where the UT beam $j^\star$ provides the highest gain in the labeling vector, i.e.,

$$L^{\mathrm{II}}_k = \begin{cases} 1, & \text{if } k \in \mathcal{I}^{j^\star}, \\ 0, & \text{otherwise.} \end{cases} \tag{E.19}$$

Thus, each dataset sample is made of UT location and orientation, the RSS measurements, and the labeling vectors.

3.4 Simulation Results

In the simulation setup, we consider the living room presented in the IEEE 802.11ad task group as a standard indoor environment, shown in Fig. C.7. The room has $7 \times 7 \times 3$ (m) dimensions, and the propagation properties of the environment are defined precisely in [21]. A UPA panel with $\{1, 8, 8\}$ antenna elements is used for the AP. For all the antenna placement shown in Fig. E.4, we consider ULAs with 4 antenna elements at the edge panels. Also, UPAs with $\{2, 2, 1\}$ antenna elements are used for the face and back panels. To model the antenna radiation pattern of a patch antenna, the model proposed in [22] is used. Also, we set $P_t = 24$ dBm and $\sigma_n^2 = -84$ dBm in

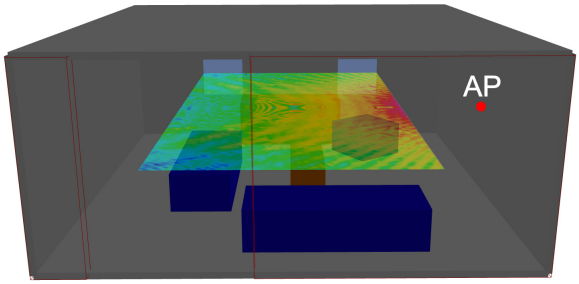

Fig. E.7: The IEEE standard indoor scenario. In this environment, a rectangle of 4×7 meters at 1.5m height above the floor is considered as the user grid. The LOS power is shown for the user grid.

the simulations. we consider $N_h = 5$ hidden layers with $n_h = 128$ neurons for the proposed generic NN, and we stick to the training policy described in [20].

The AP is placed close to the center of one of the side walls, and the LOS power is shown in Fig. E.7 for the considered user grid. The UT is placed uniformly in the user grid, and the UT orientation is uniformly chosen between portrait and landscape modes. In the portrait and landscape mode, an orientation is uniformly drawn form the angle ranges $\{\alpha_{\text{UT}} \in [-\pi, \pi), \beta_{\text{UT}} = 0, \gamma_{\text{UT}} \in [0, \pi/2]\}$ and $\{\alpha_{\text{UT}} \in [-\pi, \pi), \beta_{\text{UT}} \in [-\pi/2, 0], \gamma_{\text{UT}} = 0\}$, respectively. In addition, 50% of realizations are generated in the LOS condition and the other 50% in NLOS condition. In this study, we use training and evaluation datasets, respectively, with $56,000$ and $14,000$ samples. In obtaining the results, three random initialization of NNs were trained and averaged to de-emphasize the effects of initial weights on the model performance. $\mathbb{D}^E$, $\mathbb{D}^F$, and $\mathbb{D}^{EF}$ denote the datasets with the E, F, and EF antenna placement designs, respectively.

Fig. E.8 shows the beam decision region in azimuth-elevation space for all the three edge, face, and edge-face antenna placements. In addition, the Fibonacci points for a grid of 100 points are marked to illustrate the distribution of the points for each antenna placement/codebook. The mapping $\boldsymbol{i}^F$ for each antenna placement can be constructed by using the beam indices of the beam regions in which the Fibonacci points are located. The considered baseline to evaluate the performance of the proposed generic NN is the multi-network beam selection (MN-BS) device-specific method presented in [17].

We use the misalignment probability as a performance measure of missing the beam pair with the highest RSS, i.e.,

$$P_m(\mathcal{S}) = \mathbb{P}\left[R_{\hat{i},\hat{j}} < \max_{(p,q)\in\mathcal{B}} R_{p,q}\right] \tag{E.20}$$

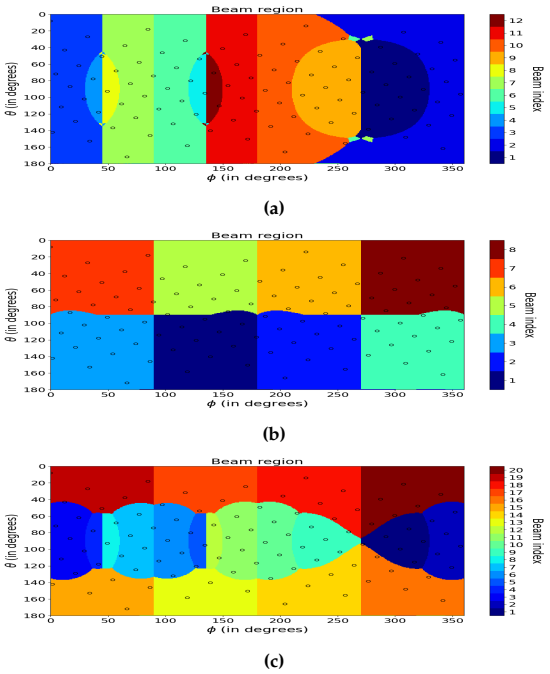

Fig. E.8: Beam decision regions (a) edge design (b) face design (c) edge-face design.

where $(\hat{i}, \hat{j})$ denote the selected beam pair after sensing the environment with all the beam pairs in the beam list $\mathcal{S}$. Also, the effective spectral efficiency (ESE) of the beam selection procedure is:

$$\mathrm{SE}_{\mathrm{eff}} = \frac{T_{fr} - N_b T_s}{T_{fr}} \log_2(1 + \mathrm{SNR}_{\hat{i},\hat{j}}), \quad N_b T_s \leq T_{fr} \tag{E.21}$$

where $N_b = |\mathcal{S}|$ is the number of required time slots for sensing the environment in the beam alignment phase. Also, $\mathrm{SNR}_{i,j}$ denotes the SNR of ith and jth beamforming vectors at the transceivers, i.e.

$$\mathrm{SNR}_{i,j} = \frac{\left\| \sqrt{P_{\mathrm{AP}}} \boldsymbol{v}_j^H \boldsymbol{H}^{(p_j)} \boldsymbol{u}_i s \right\|^2}{\sigma_n^2}, \tag{E.22}$$

where p_j is the corresponding panel of combiner $\boldsymbol{v}_j$. In this work, we use a frame duration of $T_{fr} = 20$ms and beam-sensing time of $T_s = 0.1$ms [23]. The perfect alignment method, as a genie-aided beam alignment approach, selects the beam pair with highest SNR out of all the possible beam pairs in $\mathcal{B}$. As a result, the perfect alignment is an upper bound for ESE of the device-specific and device-agnostic beam selection methods.

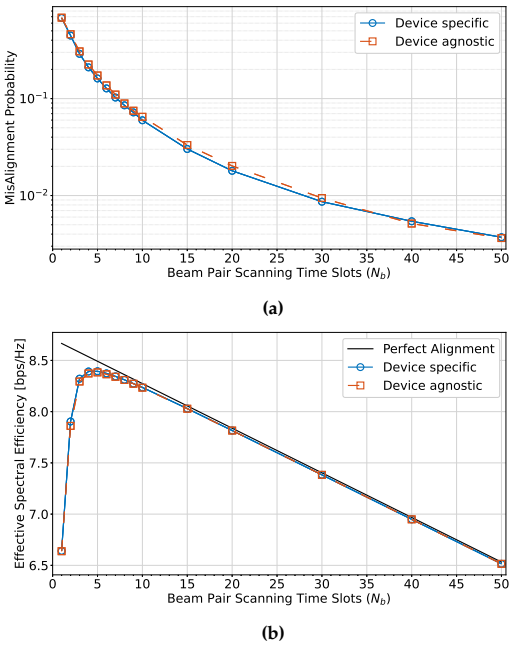

Fig. E.9: Performance of the device-specific and device-agnostic BA methods for the edge-face design.

Numerical Evaluation

Fig. E.9 shows the performance in terms of misalignment probability and spectral efficiency as a function of the candidate beam list size N_b of different BA methods for the EF antenna placement. The performance of the generic NN is as good as the MN-BS method, which shows that the degradation by pointing the directions instead of UT beams is negligible.

Since the number of Fibonacci points, n_{Fib}, is a hyperparameter of the proposed generic NN, the performance of this method for different n_{Fib} is shown in Fig. E.10. In this experiment, we consider that the beam candidate list, $\mathcal{S}$, includes 5 beam pairs, and evaluate the effective spectral efficiency as a function of the training dataset sizec. The generic NN performance is almost as good as the MN-BS method as an upper bound for $n_{Fib} > 50$. Although the NN is quite robust to this hyperparameter, a tiny number of Fibonacci points like $n_{Fib} = 10$ causes performance degradation because some of the beams may not include any Fibonacci points in their beam regions. It is worth pointing out that the proposed device-agnostic framework is quite robust to the FG size.

Fig. E.11 shows the performance of the proposed generic NN with a mismatch in the antenna placement/codebook in the training and test samples.

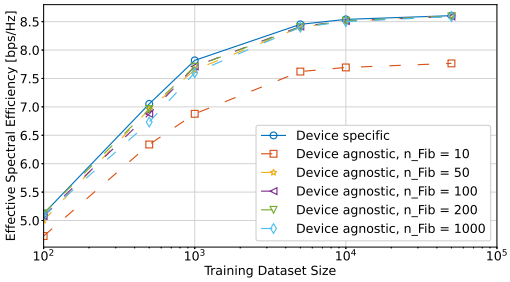

Fig. E.10: Performance of the generic NN method with different Fibonacci grid size for the edge-face design with a beam list including 5 beam pairs ($N_b = 5$).

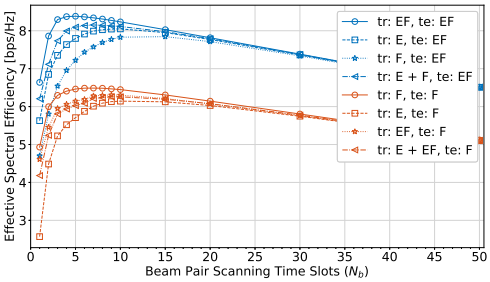

Fig. E.11: Generalization of the proposed device/codebook-agnostic method for unseen configuration in the training datasets. In the legend, 'tr' and 'te' terms, respectively, are used to determine the datasets used for training and testing of the proposed method.

To see the degradation because of mismatched datasets, the performance of the matched cases is also shown. As the EF antenna placement design has more beams, resulting in smaller beam regions, it is likely that a beam region in the EF design can be entirely covered by only one beam in the F design. Thus, the degradation of training with the $\mathbb{D}^{EF}$ and test on the $\mathbb{D}^{F}$ is not significant. We see more degradation by training with $\mathbb{D}^{E}$ and testing on $\mathbb{D}^{F}$, as the beam regions of these two antenna configurations are quite different. Note that even in this case, the generic NN can provide an acceptable performance with limited degradation by sensing larger beam lists like $N_b = 10$.

On the other hand, we see a degradation when the generic NN is trained with $\mathbb{D}^{F}$ and is tested with $\mathbb{D}^{EF}$. The same conclusions can be drawn from training with $\mathbb{D}^{E}$ while evaluating with $\mathbb{D}^{EF}$. The performance degradation is due to the fact that the beam regions in the F or E design are larger than in the EF design, so the generic NN cannot pinpoint the directions precisely enough. Using $\mathbb{D}^{E+F}$, including samples mixed of both E and F antenna designs, helps to reduce the performance degradation over test samples $\mathbb{D}^{EF}$, even though the antenna configuration of test samples is not observed in the training samples. Overall, the results show the ability of the proposed

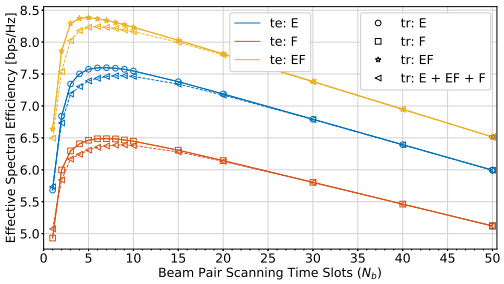

Fig. E.12: Performance of the proposed generic NN using a dataset mixed of all antenna configurations compared to the matched training datasets. For example, for evaluating the EF dataset (yellow curves), the curve with tr:EF shows the performance of the matched condition since the same dataset is used in the training and evaluation processes. However, when the mixed dataset is used for training the device-agnostic framework (tr: E + EF + F), the curve shows the performance in a mismatched condition.

generic NN in generalization for unseen antenna placement/codebook configurations without the need for any additional training samples.

Fig. E.12 illustrates the performance of the generic NN with a training dataset mixed of all the antenna configurations, $\mathbb{D}^{E+F+EF}$. It is promising that the trained network with the mixed dataset can achieve almost the same performance as the matched training datasets for all three antenna configurations.

4 Beam Selection using sub-6 GHz channel

As another example of integrating the proposed device-agnostic framework in beam selection methods proposed in literature, in this section expand the method using sub-6 GHz channel state information (CSI) proposed in [6].

4.1 System Model

Consider a point-to-point OFDM system where the base station (BS) and mobile user are equipped with sub-6 GHz and mmWave antenna elements. The BS has two ULAs made of $M_{\text{sub-6}}$ and M_{mmW} antenna elements at the sub-6 GHz and mmWave bands, respectively. The user employs a single antenna at the sub-6 GHz band. However, different from the assumption in [6], we assume a ULA of size M^{U}_{mmW} is used by the mobile user. The sub-6 GHz and mmWave bands are used for the uplink signaling and the downlink data transmission, respectively. The uplink received signal at the kth subcarrier, $\boldsymbol{y}_{\text{sub-6}}[k]$, may be written as:

$$\boldsymbol{y}_{\text{sub-6}}[k] = \boldsymbol{h}_{\text{sub-6}}[k]s_{\text{p}}[k] + \boldsymbol{n}_{\text{sub-6}}[k], k = 1, \ldots, K \tag{E.23}$$

where $\boldsymbol{h}_{\text{sub-6}}[k] \in \mathbb{C}^{M_{\text{sub-6}} \times 1}$, $s_{\text{p}}[k]$, and $\boldsymbol{n}_{\text{sub-6}}[k] \in \mathbb{C}^{M_{\text{sub-6}} \times 1}$ respectively are the uplink channel vector, uplink pilot signal and received noise at the BS sub-6 GHz array at the kth subcarrier. $\mathbb{E}[s_{\text{p}}[k]] = P_{\text{sub-6}}/K$, where $P_{\text{sub-6}}$ is the transmit power at the mobile user and K is the number of sub-6GHz subcarriers. Also, $\boldsymbol{n}_{\text{sub-6}}[k] \in \mathbb{C}^{M_{\text{sub-6}} \times 1}$ is a zero-mean complex Gaussian vector with variance $\sigma^2_{\text{sub-6}}$. The uplink channel estimation at the baseband processor is assumed to be available using digital beamforming at the BS sub-6 GHz array.

For the mmWave downlink transmission, we consider analog beamforming at the BS and user. Using $\boldsymbol{f} \in \mathbb{C}^{M_{\text{mmW}} \times 1}$ and $\boldsymbol{w} \in \mathbb{C}^{M^U_{\text{mmW}} \times 1}$ respectively for beamforming at the BS and user, the received signal by the user at the $\bar{k}$th subcarrier, $\boldsymbol{y}_{\text{sub-6}}[\bar{k}]$, is

$$\boldsymbol{y}_{\text{mmW}}[\bar{k}] = \boldsymbol{w}^T \boldsymbol{H}^T_{\text{mmW}}[\bar{k}] \boldsymbol{f} s_{\text{d}}[\bar{k}] + \boldsymbol{n}_{\text{mmW}}[\bar{k}], \bar{k} = 1, \ldots, \bar{K} \tag{E.24}$$

where $\boldsymbol{H}_{\text{mmW}}[\bar{k}] \in \mathbb{C}^{M_{\text{mmW}} \times M^U_{\text{mmW}}}$ denotes the MIMO downlink channel at the $\bar{k}$th subcarrier. $s_{\text{d}}[\bar{k}]$ is the known downlink signal with $\mathbb{E}[s_{\text{d}}[\bar{k}]] = P_{\text{mmW}}/\bar{K}$, where P_{mmW} and $\bar{K}$ are the transmission power at the BS and the number of mmWave subcarriers. Also, $\boldsymbol{n}_{\text{mmW}}[\bar{k}] \sim \mathcal{CN}(\boldsymbol{0}_{M_{\text{mmW}}}, \sigma^2_{\text{mmW}} \boldsymbol{I}_{M_{\text{mmW}}})$ is a complex Gaussian vector. $\mathcal{F}$ and $\mathcal{W}$ respectively are the beamforming codebooks at the BS and user with cardinality $|\mathcal{F}| = N^{\text{BS}}_{\text{CB}}$ and $|\mathcal{W}| = N^{\text{U}}_{\text{CB}}$. A geometric channel model is considered for the sub-6 GHz and mmWave channels. The uplink sub-6 GHz channel may be written as

$$\boldsymbol{h}_{\text{sub-6}}[k] = \sum_{d=0}^{D_c-1} \sum_{l=1}^{L} \alpha_l \, e^{-j\frac{2\pi k}{K} d} \, p(d\,T_s - \tau_l) \boldsymbol{a}_{\text{BS-sub-6}}(\phi_l, \theta_l). \tag{E.25}$$

Also, the downlink mmWave channel can be written as

$$\boldsymbol{H}_{\text{mmW}}[\bar{k}] = \sum_{d=0}^{D_c-1} \sum_{l=1}^{L} \alpha_l \, e^{-j\frac{2\pi \bar{k} d}{\bar{K}}} \, p(d\,T_s - \tau_l) \boldsymbol{a}_{\text{U-mmW}}(\phi_l, \theta_l) \boldsymbol{a}_{\text{BS-mmW}}(\psi_l, \omega_l). \tag{E.26}$$

L, D_c, and T_s denote number of channel components, the cyclic prefix length, and the the sampling time, respectively. α_l and τ_l are the complex path gain and delay of the lth path, and $p(\cdot)$ denotes the pulse shaping filter. In addition, ϕ_l, θ_l, ψ_l, and ω_l are the azimuth AoA, elevation AoA, azimuth AoD, elevation AoD, respectively. $\boldsymbol{a}_{\text{BS-sub-6}}$ and $\boldsymbol{a}_{\text{BS-mmW}}$ are the sub-6 GHz and mmWave antenna array responses at the BS. Also, $\boldsymbol{a}_{\text{U-mmW}}$ is the mmWave antenna array response at the mobile user. Note that L, D_c, and T_s may be different for the sub-6 GHz and mmWave channels.

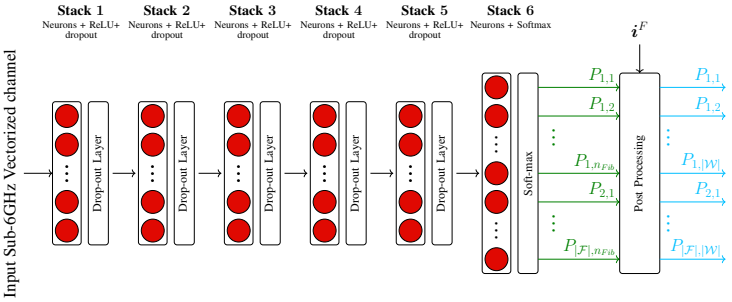

Fig. E.13: The device agnostic design for predicting the optimal mmWave beam pair using the sub-6 GHz channel. This design is a modified version of the device specific network proposed in [6]. The output layer includes $|\mathcal{F}| \times n_{Fib}$ neurons. The post processing unit provides the prediction probability of optimality for all the beam pairs with $|\mathcal{F}| \times |\mathcal{W}|$ outputs.

4.2 Beam prediction using sub-6 GHz channel

The optimal pair of mmWave beamforming vectors at the transceivers provides the highest spectral efficiency, i.e.,

$$(\boldsymbol{f}^\star, \boldsymbol{w}^\star) = \underset{\boldsymbol{f}\in\mathcal{F}, \boldsymbol{w}\in\mathcal{W}}{\arg\max}\ R(\boldsymbol{H}_{\text{mmW}}, \boldsymbol{f}, \boldsymbol{w}) \tag{E.27}$$

where the achievable spectral efficiency can be expressed as

$$R(\boldsymbol{H}_{\text{mmW}}, \boldsymbol{f}, \boldsymbol{w}) = \sum_{\bar{k}=1}^{\bar{K}} \log_2(1 + \text{SNR}|\boldsymbol{w}\boldsymbol{H}_{\text{mmW}}^T[\bar{k}]\boldsymbol{f}|^2). \tag{E.28}$$

However, exhaustive search over all the beam pairs leads to large training overhead and latency. In this study, the sub-6 GHz channel $\boldsymbol{h}_{\text{sub-6}}$ is used to reduce the overhead in mmWave link. The objective of this work is to maximize the success probability in predicting the optimal beam pair $(\boldsymbol{f}^\star, \boldsymbol{w}^\star)$, i.e.,

$$\kappa_1 = \mathbb{P}\left((\hat{\boldsymbol{f}}, \hat{\boldsymbol{w}}) = (\boldsymbol{f}^\star, \boldsymbol{w}^\star)|\boldsymbol{h}_{\text{sub-6}}\right) \tag{E.29}$$

where $\hat{\boldsymbol{f}} \in \mathcal{F}$ and $\boldsymbol{w} \hat{\in} \mathcal{W}$ are, respectively, the predicted beamforming vectors at the BS and user using the sub-6 GHz channel. The mapping function from the sub-6 GHz channel to the mmWave channel can be interpreted as a fingerprinting approach that uses the propagation properties to propose the probable proper beam pairs. Because of the high non-linearity of the mapping, deep learning is an appropriate choice for this application.

Fig. E.13 shows the beam selection network in the device-agnostic framework. This network uses several hidden layers to extract the information in the sub-6 GHz channel and map it to the beams at the BS and AoAs at the user. Thus, the generic network has $|\mathcal{F}| \times n_{Fib}$ neurons for the optimality

probability of all the possible BS beams and user AoAs at the transceivers. The post processing unit uses the mapping information between the user terminal beams and AoAs, $\boldsymbol{i}^F$, to provide the optimality probability of the beam pairs at the transceivers based on the generic network's outputs.

4.3 DL Training and Deployment Phases

DL Training Phase: The DL training phase needs dual-band communication in sub-6 GHz and mmWave bands. In a coherence time, all the beam pairs of the mmWave codebooks at the transceivers, $\mathcal{F}$ and $\mathcal{W}$, are exhaustively sensed, and the achievable spectral efficiency by each beam pair is stored in R. We store index of the optimal beam pair $(\boldsymbol{f}^\star, \boldsymbol{w}^\star)$ in $(i^\star, j^\star)$. Also, the mapping from the beam indices to the Fibonacci points, $\boldsymbol{i}^F$, is needed for each dataset sample. Furthermore, the sub-6 GHz channel is sounded and stored in $\boldsymbol{h}_{\text{sub-6}}$. Thus, each training sample is made of $\{\boldsymbol{h}_{\text{sub-6}}, \boldsymbol{i}^F, i^\star, j^\star\}$. We train the generic NN using the training samples and corresponding labels as ground truth. We use categorical cross entropy as the loss function of the generic NN, i.e.,

$$\mathcal{L} = -\sum_{i=1}^{|\mathcal{F}|}\sum_{j=1}^{n_{Fib}} L_{i,j}\log(P_{i,j}) \tag{E.30}$$

where $L_{i,j}$ and $P_{i,j}$ are the labels and outputs of the generic NN for the ith and jth beamforming vectors at the BS and user, respectively. In a similar way that is explained in (E.5), the label can be defined as

$$L_{i,j} = \begin{cases} 1, & \text{if } i = i^\star \text{ and } k \in \mathcal{I}^{j^\star}, \\ 0, & \text{otherwise} \end{cases} \tag{E.31}$$

where $\mathcal{I}^{j^\star}$ includes indices of the FG with $\boldsymbol{i}_k^F = j^\star$.

DL Deployment Phase: Dual-band communication is operated in the deployment phase. The trained NN has learned the mapping from the sub-6 GHz channel to the optimal beam pair. The user only sends an uplink pilot at sub-6 GHz for estimation of $\boldsymbol{h}_{\text{sub-6}}$ at the BS. The device-agnostic framework uses the estimated channel $\boldsymbol{h}_{\text{sub-6}}$ for predicting the optimal mmWave beam pairs.

4.4 Simulation Results

We consider two outdoor scenarios to evaluate performance of the proposed device-agnostic framework from the DeepMIMO dataset [24]. As shown in Fig. E.14, the 'O1' scenario considers LOS condition for all the points in the user region. In the 'O1 Blockage' scenario, a blocker and two reflectors are

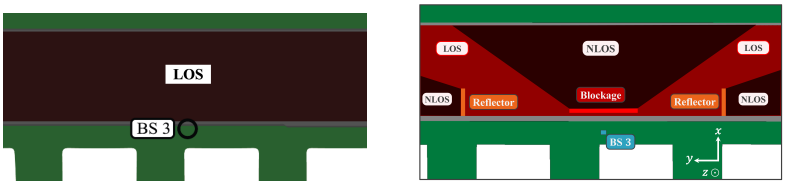

(a) 'O1' scenario **(b)** 'O1 Blockage' scenario

Fig. E.14: Top view of the considered 'O1' and 'O1 Blockage' outdoor scenarios [24].

Table E.1: DeepMIMO dataset [24] parameters for the 'O1' and 'O1 Blockage' scenarios

Parameters	'O1'		'O1' Blockage'	
	mmW	sub-6	mmW	sub-6
scenario name	O1_28	O1_3p5	O1_28B	O1_3p5B
Active BS	3	3	3	3
Active users	$700-1300$	$700-1300$	$700-1300$	$700-1300$
Number of BS antennas	64	4	64	4
Number of user antennas	4 or 8	1	4 or 8	1
Antenna spacing (wave-length)	0.5	0.5	0.5	0.5
Bandwidth (GHz)	0.5	0.02	0.5	0.02
Number of OFDM subcarriers	512	32	512	32
Number of paths	5	15	5	15

placed in the environment. The LOS and NLOS user regions are illustrated in Fig. E.14. In the 'O1' and 'O1 Blockage' scenarios, dual-band communication with 3.5 GHz and 28 GHz links are considered. We consider co-located ULAs with $M_{\text{sub-6}} = 4$ and $M_{\text{mmW}} = 64$ antenna elements at the BS3 that enables dual-band communication. The user is equipped with a single antenna at the sub-6 GHz and a ULA including 4 or 8 mmWave antenna elements. An ideal pulse shaping filter is assumed in the generation of channel responses. Table E.1 provides parameters used in the dataset generation of the 'O1' and 'O1 Blockage' scenarios. For each scenario and configuration, a dataset with 27391 samples is collected and split randomly $70\% - 30\%$ into training and test data, respectively. Thus, the training dataset includes 19173 samples while the test data is made of 8218 samples. For training the device-specific and device-agnostic ML models, we consider 40 epochs with a batch size of 64 samples. Each network is trained and averaged out with three random weight initialization, which leads to playing down the initialization effects.

We consider Top-n accuracy metric, denoted $A_{\text{Top-}n}$, to evaluate the performance of beam prediction methods as classifiers. Top-n accuracy can be defined as

$$A_{\text{Top-}n} = \frac{1}{N_{\text{test}}} \sum_{k=1}^{N_{test}} \mathbb{1}_{(f_k^\star, \boldsymbol{w}_k^\star) \in \mathcal{S}_k^n} \tag{E.32}$$

where $\mathcal{S}_k^n$ is a candidate list of beam pairs that provide the n highest opti-

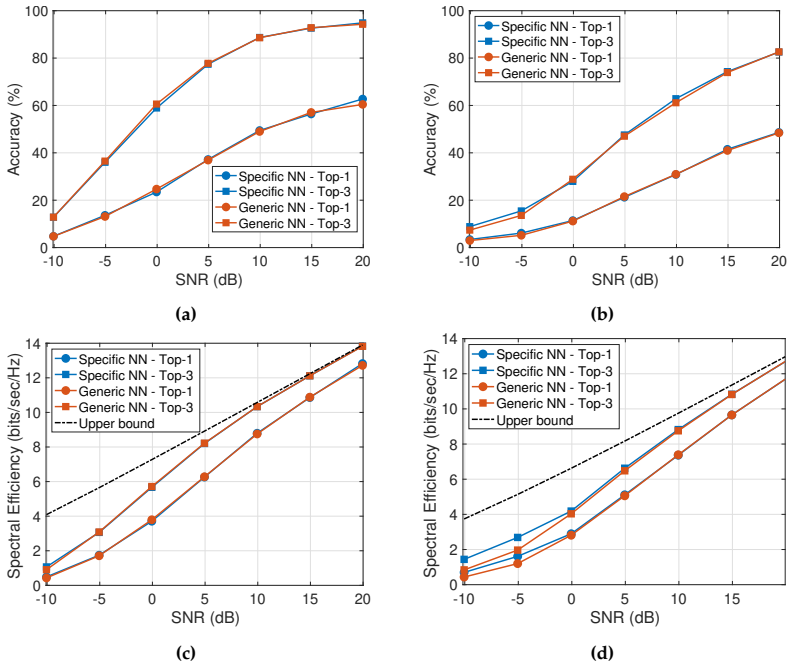

Fig. E.15: Performance of the device-specific [6] compared to the proposed device-agnostic framework with $M^{U}_{\text{mmW}} = 8$ and $n_{Fib} = 100$ in the 'O1' (a, c) and 'O1 Blockage' (b, d) scenarios.

mality likelihood, P, for the kth test sample. $\mathbb{1}_{(f_k^\star, \boldsymbol{w}_k^\star) \in \mathcal{S}_k^n}$ results in 1 when the n-long beam list includes the optimal beam pair, otherwise 0. Moreover, we use the Top-n spectral efficiency as the average spectral efficiency provided by the best beam pair in the n-long beam pair candidate list, $\mathcal{S}^n$. For each sample in the test dataset, spectral efficiency of the best beam pair in the candidate list is calculated using (E.28).

Fig. E.15 shows the Top-1 and Top-3 accuracy and Top-1 and Top-3 spectral efficiency of the device-specific and device-agnostic methods for the 'O1' and 'O1 Blockage' scenarios. A ULA array made of 8 antenna elements is considered for the mmWave communication at the user. We consider a FG with $n_{Fib} = 100$ points for the device-agnostic framework. There is almost no performance degradation by using the proposed device-agnostic framework compared to the device-specific one. The results show that the performance of the generic network providing the optimality probability for the FG is as good as the device-specific network pointing the beam pairs.

The effects of considering a Fibonacci Grid with 25 points are shown in Fig. E.16. In the case $M^{U}_{\text{mmW}} = 8$, the device-agnostic framework cannot achieve the same performance as the device-specific method. Moreover, a

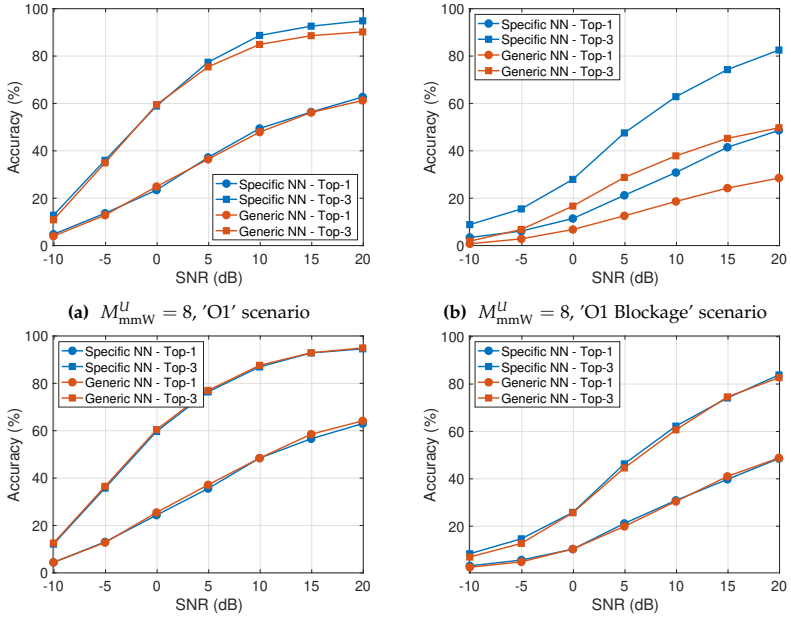

(a) $M^{U}_{\text{mmW}} = 8$, 'O1' scenario

(b) $M^{U}_{\text{mmW}} = 8$, 'O1 Blockage' scenario

(c) $M^{U}_{\text{mmW}} = 4$, 'O1' scenario

(d) $M^{U}_{\text{mmW}} = 4$, 'O1 Blockage' scenario

Fig. E.16: Accuracy of the device-agnostic framework where the Fibonacci grid is made of 25 points ($n_{Fib} = 25$).

FG with $n_{Fib} = 25$ incurs more severe performance degradation in the 'O1 Blockage'. However, for the 'O1' and 'O1 Blockage' scenarios, there is no performance loss when $M^{U}_{\text{mmW}} = 4$. These results show that selecting the number of points in the FG may depend on the number of antenna elements codebook size at the user side. Figs. E.17a, c depict the beam regions for devices with 8 and 4 antenna elements. We plot the Fibonacci points for two cases with 25 and 100 points. As it is illustrated in Fig. E.17a, for the FG with $n_{Fib} = 25$, no points are placed in the beam region for beam 1. This explains the performance loss in the case of $M^{U}_{\text{mmW}} = 8$ and a FG with $n_{Fib} = 25$. Figs. E.17b, d show the normalized frequency of best user beam for devices with $M^{U}_{\text{mmW}} = 8$ and $M^{U}_{\text{mmW}} = 4$. The frequency of beam 1 in the 'O1 Blockage' scenario is several times more than its frequency in the 'O1' scenario, which justifies the more severe performance degradation in the 'O1 Blockage' scenario.

Fig. E.18 shows the Top-3 accuracy and achievable spectral efficiency for different training dataset sizes with 25, 100, and 1000 points in the FG. Considering insufficient points in the FG may not cover some beams in the user codebook. For example, a significant performance degradation for the device-agnostic framework with $n_{Fib} = 25$ can be seen in different training

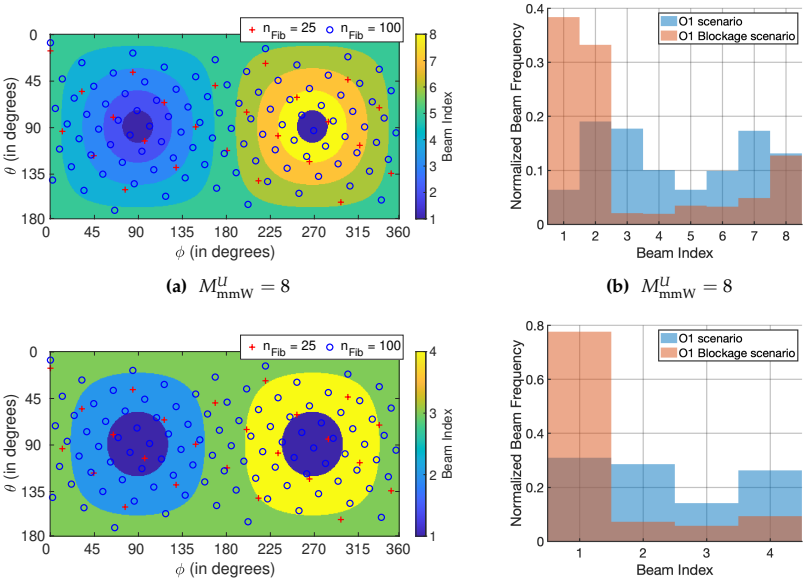

(a) $M^{U}_{\text{mmW}} = 8$ **(b)** $M^{U}_{\text{mmW}} = 8$

(c) $M^{U}_{\text{mmW}} = 4$ **(d)** $M^{U}_{\text{mmW}} = 4$

Fig. E.17: Beam region and normalized histogram of the user beam index with 4 or 8 antenna elements. In the case $M^{U}_{\text{mmW}} = 8$, a FG with 25 points has no point inside the beam region of first beam.

dataset sizes. On the other hand, a FG with too many points results in a huge number of training parameters at the output layer. In the case with $n_{Fib} = 1000$, the accuracy of the device-agnostic framework with limited training samples is dropped. However, with a large training dataset, the device-agnostic framework with a FG with a moderate or large number of points provides the same performance as the device-specific method.

The proposed device-agnostic framework can be trained with a specific device and be used for other devices with different antenna configurations in the deployment phase. Fig. E.19 shows the Top-3 accuracy of the device-agnostic framework in the 'O1 Blockage' scenario when there is a mismatch in the antenna configuration of the devices in the training and deployment phases. The performance degradation is more noticeable when the training samples are collected with devices with 4 antenna elements, but the framework is evaluated for devices with 8 antenna elements. However, in the opposite case, when the device is trained with an antenna of 8 elements and generalized to operate with an antenna of 4 elements, there is less loss in performance. Although there is a performance loss due to the mismatch effects, the results are promising as the device-agnostic framework achieves acceptable accuracy without additional training samples.

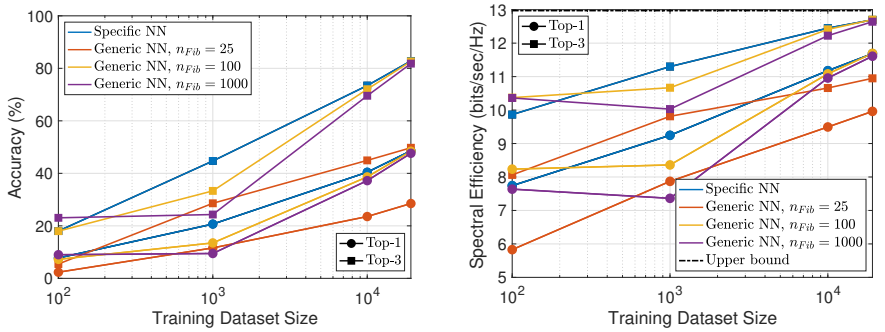

Fig. E.18: Effect of training dataset size on the performance of the device-agnostic framework.

5 Conclusions

In this paper, we have shown that a generic neural network followed by a post processing unit can be used to recommend an accurate beam candidate list for the initial beam selection process of devices having diverse beam codebook and hardware configurations. We use the Fibonacci grid to point the directions in the unit sphere so that each point covers an equal area from the sphere. The generic network leverages the information from inputs (e.g., location, orientation, sub-6 GHz CSI) to pinpoint appropriate beamforming directions in the Fibonacci grid. The proposed framework works well with unseen antenna and hardware configurations in the training dataset. Also, it can be trained with data collected with different device antenna configurations/codebooks.

In this study, two ML-based beam alignment methods are considered that receive position and orientation information and out-of-band channel response as the models' inputs. These two beam alignment problems are intended as mere illustrations of the applicability of our proposed approach, which is much more general. The proposed framework can be used not only with other types of context information (CI) but also in non-CI-based beam management and other codebook-specific applications. As an example, future research can investigate the feasibility of the proposed technique in beam refinement and tracking problems.

References

[1] M. Giordani, M. Polese, M. Mezzavilla, S. Rangan, and M. Zorzi, "Toward 6G Networks: Use Cases and Technologies," *IEEE Commun. Mag.*, vol. 58, no. 3, pp. 55–61, Mar. 2020.

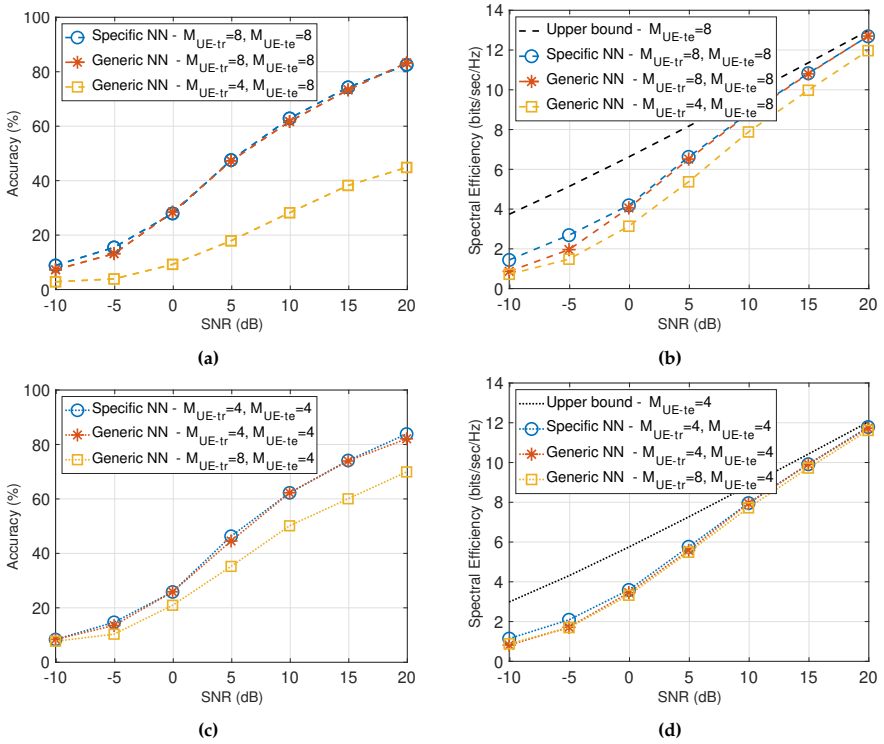

Fig. E.19: The Top-3 accuracy and spectral efficiency of the proposed device-agnostic framework when there is a mismatch in the training and test datasets. The 'O1 Blockage' scenario and a FG with $n_{Fib} = 100$ are considered.

[2] F. Sohrabi, Z. Chen, and W. Yu, "Deep Active Learning Approach to Adaptive Beamforming for mmWave Initial Alignment," *IEEE Journal on Selected Areas in Communications*, vol. 39, no. 8, pp. 2347–2360, Aug. 2021.

[3] C. Antón-Haro and X. Mestre, "Learning and Data-Driven Beam Selection for mmWave Communications: An Angle of Arrival-Based Approach," *IEEE Access*, vol. 7, pp. 20 404–20 415, 2019.

[4] V. Va, J. Choi, T. Shimizu, G. Bansal, and R. W. Heath, "Inverse Multipath Fingerprinting for Millimeter Wave V2I Beam Alignment," *IEEE Trans. Veh. Technol.*, vol. 67, no. 5, pp. 4042–4058, May 2018.

[5] M. Alrabeiah, A. Hredzak, and A. Alkhateeb, "Millimeter Wave Base Stations with Cameras: Vision-Aided Beam and Blockage Prediction," in *Proc. IEEE Vehicular Technology Conference (VTC)*, May 2020, pp. 1–5.

[6] M. Alrabeiah and A. Alkhateeb, "Deep Learning for mmWave Beam and Blockage Prediction Using Sub-6 GHz Channels," *IEEE Trans. Commun.*, vol. 68, no. 9, pp. 5504–5518, Sep. 2020.

[7] W. Xu, F. Gao, S. Jin, and A. Alkhateeb, "3D Scene-Based Beam Selection for mmWave Communications," *IEEE Wireless Commun. Lett.*, vol. 9, no. 11, pp. 1850–1854, Nov. 2020.

[8] M. Dias, A. Klautau, N. González-Prelcic, and R. W. Heath, "Position and LIDAR-Aided mmWave Beam Selection using Deep Learning," in *Proc. IEEE Int. Workshop Signal Process. Adv. Wireless Commun. (SPAWC)*, Jul. 2019, pp. 1–5.

[9] F. Gao, B. Lin, C. Bian, T. Zhou, J. Qian, and H. Wang, "FusionNet: Enhanced Beam Prediction for mmWave Communications Using Sub-6 GHz Channel and a Few Pilots," *IEEE Transactions on Communications*, vol. 69, no. 12, pp. 8488–8500, Dec. 2021, conference Name: IEEE Transactions on Communications.

[10] V. Va, T. Shimizu, G. Bansal, and R. W. Heath, "Position-aided millimeter wave V2I beam alignment: A learning-to-rank approach," in *2017 IEEE 28th Annual International Symposium on Personal, Indoor, and Mobile Radio Communications (PIMRC)*, Oct. 2017, pp. 1–5.

[11] S. Rezaie, A. Amiri, E. de Carvalho, and C. N. Manchón, "Deep Transfer Learning for Location-Aware Millimeter Wave Beam Selection," *IEEE Commun. Lett.*, vol. 25, no. 9, pp. 2963–2967, Sep. 2021.

[12] R. Swinbank and R. James Purser, "Fibonacci grids: A novel approach to global modelling," *Quarterly Journal of the Royal Meteorological Society*, vol. 132, no. 619, pp. 1769–1793, 2006.

[13] A. Ali, J. Mo, B. L. Ng, V. Va, and J. C. Zhang, "Orientation-Assisted Beam Management for Beyond 5G Systems," *IEEE Access*, vol. 9, pp. 51 832–51 846, 2021.

[14] J. Mo, B. L. Ng, S. Chang, P. Huang, M. N. Kulkarni, A. Alammouri, J. C. Zhang, J. Lee, and W.-J. Choi, "Beam Codebook Design for 5G mmWave Terminals," *IEEE Access*, vol. 7, pp. 98 387–98 404, 2019.

[15] A. Alammouri, J. Mo, B. L. Ng, J. C. Zhang, and J. G. Andrews, "Hand Grip Impact on 5G mmWave Mobile Devices," *IEEE Access*, vol. 7, pp. 60 532–60 544, 2019.

[16] J. Mo, D. Park, B. Loong Ng, V. Va, A. Ali, C. Seo, and J. Charlie Zhang, "Sub-Chain Beam for mmWave Devices: A Trade-off between Power Saving and Beam Correspondence," in *2021 55th Asilomar Conference on Signals, Systems, and Computers*, Oct. 2021, pp. 1–6, iSSN: 2576-2303.

[17] S. Rezaie, J. Morais, E. de Carvalho, A. Alkhateeb, and C. N. Manchón, "Location- and Orientation-aware Millimeter Wave Beam Selection for Multi-Panel Antenna Devices," in *arXiv:2203.11714 [eess]*, Mar. 2022, arXiv: 2203.11714. [Online]. Available: http://arxiv.org/abs/2203.11714

[18] V. Raghavan, M.-L. Chi, M. A. Tassoudji, O. H. Koymen, and J. Li, "Antenna Placement and Performance Tradeoffs With Hand Blockage in Millimeter Wave Systems," *IEEE Trans. Commun.*, vol. 67, no. 4, pp. 3082–3096, Apr. 2019.

[19] S. Rezaie, E. De Carvalho, and C. N. Manchón, "A Deep Learning Approach to Location- and Orientation-aided 3D Beam Selection for mmWave Communications," *IEEE Trans. Wireless Commun.*, vol. 21, no. 12, pp. 11 110–11 124, 2022.

[20] S. Rezaie, C. N. Manchón, and E. de Carvalho, "Location- and Orientation-Aided Millimeter Wave Beam Selection Using Deep Learning," in *Proc. IEEE Int. Conf. Commun.*, Jun. 2020, pp. 1–6.

[21] A. Maltsev, "Channel models for 60GHz WLAN systems," *IEEE802. 11 09/0334r8*, 2010.

[22] 3GPP, *Study on channel model for frequencies from 0.5 to 100 GHz*. TR 38.901 V16.1.0, 2020. [Online]. Available: http://www.3gpp.org/DynaReport/38901.htm

[23] M. Hussain and N. Michelusi, "Second-Best Beam-Alignment via Bayesian Multi-Armed Bandits," in *Proc. IEEE GLOBECOM*, Dec. 2019, pp. 1–6.

[24] A. Alkhateeb, "DeepMIMO: A Generic Deep Learning Dataset for Millimeter Wave and Massive MIMO Applications," *arXiv:1902.06435 [cs, eess, math]*, Feb. 2019, arXiv: 1902.06435. [Online]. Available: http://arxiv.org/abs/1902.06435

Paper F

Machine Learning-based Millimeter Wave Beam Management for Dynamic Terminal Orientation

Filipa Fernandes, Sajad Rezaie, Christian Rom, Johannes Harrebek, Carles Navarro Manchón

The paper has been submitted to the
97th IEEE Vehicular Technology Conference, VTC2023-Spring, Dec. 2022.

The layout has been revised.

Abstract

Time-varying terminal orientation is an often overlooked challenge of beam alignment in millimeter wave communications with multi-panel handset terminals. The use of narrow beams, allied with fast and hard to predict device orientation changes, cause the current measurement-based beam management procedure to rely on potentially outdated beam information, degrading its accuracy. This paper explores the capabilities of deep neural networks to improve user equipment (UE) beam selection under dynamic terminal orientation conditions. Contrary to other works, the proposed solution relies solely on reference signal received power beam measurements, without the aid of other context information. Results show that this simple solution can successfully improve beam selection accuracy for fast rotating UEs, especially in line-of-sight scenarios. No-line-of-sight environments however reduce the proposed solution's effectiveness due to low power-levels and increased channel angular spread.

1 Introduction

Current 5th generation (5G) millimeter wave (mmWave) communications are enabled by large antenna arrays with high beamforming gains [1]. Although achieving unprecedented data rates, the narrow nature of the transmitter and receiver beams causes a link to become more directional and, consequently, vulnerable to disruptions. This prompted 3rd generation partnership project (3GPP) to define a set of layer 1 (L1) and layer 2 (L2) operations, namely beam management, to acquire and maintain beam alignment between the next generation node base station (gNodeB) and the user equipment (UE) beams [2]. Since the current beam management procedure is based on a simplistic approach of beam sweeping, measurement and reporting, extensive research has been conducted in works such as [3–6] to strengthen its robustness against dynamic channel conditions. Concurrently, 3GPP is currently investigating beam management enhancements for Release 18 based on machine learning (ML) [7].

Most of these studies consider the UE to be modeled as a single panel with an isotropic or directional antenna array. In reality, devices must be equipped with multiple directional antenna array panels to be able to offer adequate spherical coverage. The performance benefits of multi-panel UE design are highlighted in [8] where a panel switching mechanism is introduced based on reference signal received power (RSRP). This work, along with [9], further elaborate on practical aspects such as the impact of sequential and simultaneous panel activation on beam management performance for distinct mobility scenarios. Furthermore, [10] proposes to use context information, specifically location and orientation data, for a ML beam selection method.

This approach recommends a subset of candidate beams/panels to be tested, reducing the beam acquisition overhead and improving the device's power efficiency by deactivating unused panels.

However, these works assume a time-static orientation for the UE thus concealing an additional challenge for beam alignment: device orientation tracking. Under the current beam management framework, beam selection relies on measurements collected over a span of time. A device whose orientation is shifting, while simultaneously moving through the cell, may cause measurements to become outdated, leading to erroneous beam selection and, ultimately, link performance degradation. This is particularly challenging for handset terminal use cases, where fast and hard to predict orientation changes are common. Therefore, time-varying rotation should be modelled along with other straining factors like user mobility or blockage to truly capture the challenges of beam alignment in multi-panel devices [11]. A few works in the literature have tackled this issue through the use of orientation data obtained from the device's sensors. By employing a particle filter in [12] and a recurrent neural network in [13], the authors show that leveraging this information, along with RSRP measurements, outperforms the current procedure, particularly in scenarios where fast and abrupt device rotation is experienced. However it is worth mentioning that both these approaches require a significant number of samples to be implemented. The particle filter method can not be trained in advance and requires a high number of samples to accomplish its prediction tasks, which can result in a high computation load for the UE. Moreover, while the type of ML model pursued can be trained offline, obtaining a large enough dataset size to train it can be difficult.

Contrary to [12] and [13], this paper explores the feasibility of handling time-varying terminal rotation without resorting to context information sources. A ML solution is proposed based solely on information available to the UE through the current beam management procedure: RSRP measurements. Results show that this information, even if outdated, can be used by a simple neural network (NN) to infer the UE's orientation pattern and therefore predict the best beam in dynamic orientation scenarios. The proposed solution's performance is compared to a 3GPP-based beam management procedure and its suitability is tested for different usage scenarios based on propagation environment, user speed and time-dynamic device rotation.

The remainder of this paper is organized as follows: Section 2 details the study's system model and Section 3 describes both the 3GPP-based and the ML-based solutions for UE beam selection. Section 4 presents the comparative performance results and Section 5 concludes the paper.

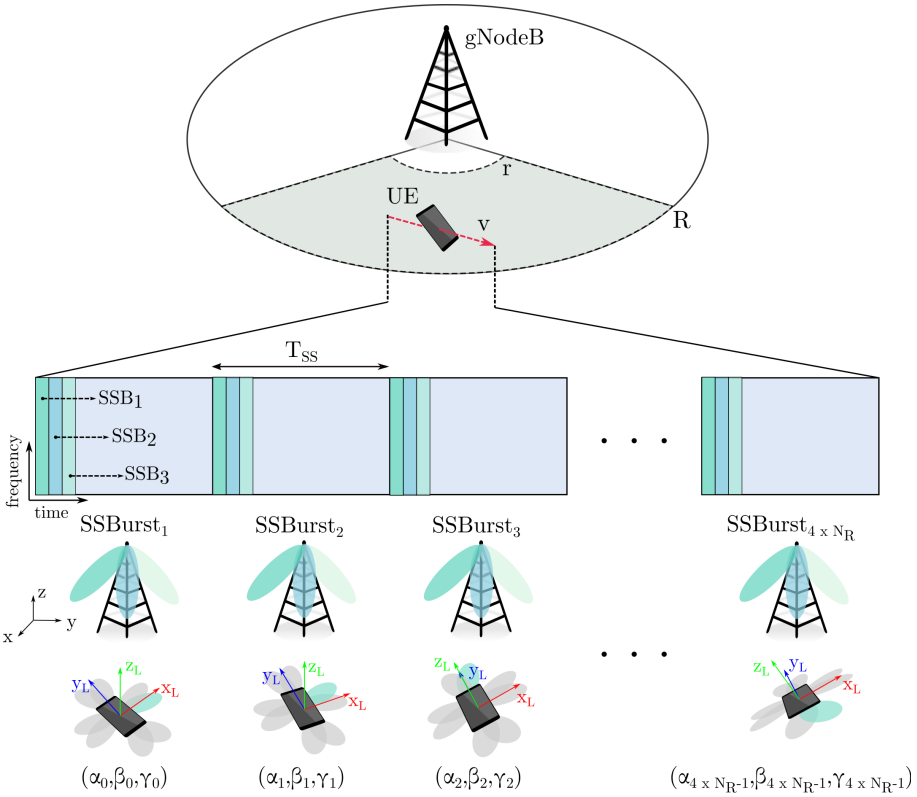

Fig. F.1: Network layout and beam sweeping procedure for $N_T = 3$ and $N_R = 2$. During its trajectory (dashed red), the UE activates one panel beam (highlighted in green) and progressively changes its orientation $(\alpha_t, \beta_t, \gamma_t)$ every T_{SS} ms, as indicated by its LCS (x_L,y_L,z_L). The gNodeB remains aligned with GCS (x,y,z).

2 System model

Fig. F.1 illustrates a downlink (DL) single cell mmWave system, where beam alignment takes place between the gNodeB and a single user. This user moves in a straight line at constant speed through the cell while changing the terminal's orientation along its trajectory. The gNodeB is modelled as a uniform planar array (UPA) of N_t patch antennas and the UE as a multi-panel device. Each of the $I = 4$ panels at the UE is equipped with a uniform linear array (ULA) module of N_r patch antennas and placed on each side of the form factor according to an edge design [14], as seen in Fig. F.2.

2.1 Channel model

The mmWave DL channel response for the ith UE panel is modelled for a frequency-time resource element (s, k) as

$$\boldsymbol{H}^i(s,k) = \sum_{l=1}^{L(k)} g_l(k)\boldsymbol{a}_r^i(\boldsymbol{\varphi}_{r,l}^i(k))\boldsymbol{a}_t^H(\boldsymbol{\varphi}_{t,l}(k))e^{-j2\pi\tau_l(k)f(s)}, \tag{F.1}$$

where $L(k)$, $g_l(k)$, $\tau_l(k)$ are the time-varying total multipath components of the channel, the path l's complex gain and its delay values at time k, respectively. These are obtained with QUAsi Deterministic RadIo channel GenerAtor (QuaDRiGa), a 3D geometry-based stochastic channel model generator which enables continuous time evolution of a channel, spatially correlated large and small-scale-fading and a plethora of different 3GPP-compliant propagation scenarios [15]. Additionally, $f(s)$ denotes the sth subcarrier frequency. The transmitter and ith receiver panel array responses are expressed in $\boldsymbol{a}_t$ and $\boldsymbol{a}_r^i$ for a path l's time-varying angles of arrival, $\boldsymbol{\varphi}_r^i$, and departure, $\boldsymbol{\varphi}_t$. These angles, expressed in elevation and azimuth (θ, ϕ), are given by

$$\boldsymbol{\varphi}_{r,l}^i(k) = (\theta_{r,l}^i(k), \phi_{r,l}^i(k)), \tag{F.2}$$

$$\boldsymbol{\varphi}_{t,l}(k) = (\theta_{t,l}(k), \phi_{t,l}(k)). \tag{F.3}$$

The array response for a gNodeB or UE array panel of size $N = N_x N_y N_z$ is written as

$$\boldsymbol{a}(\theta,\phi) = \frac{1}{\sqrt{N}} g_{ae}(\theta,\phi)\boldsymbol{a}_z(\theta) \otimes \boldsymbol{a}_y(\theta,\phi) \otimes \boldsymbol{a}_x(\theta,\phi) \tag{F.4}$$

where $g_{ae}(\theta, \phi)$ pertains to the antenna element's gain and $\otimes$ expresses the Kronecker product, with $\boldsymbol{a_x} \in \mathbb{C}^{N_x}$, $\boldsymbol{a_y} \in \mathbb{C}^{N_y}$ and $\boldsymbol{a_z} \in \mathbb{C}^{N_z}$ given by

$$\boldsymbol{a_x}(\theta,\phi) = [1, e^{j\pi \sin\theta\cos\phi}, ..., e^{j\pi(N_x-1)\sin\theta\cos\phi}]^T \tag{F.5}$$

$$\boldsymbol{a_y}(\theta,\phi) = [1, e^{j\pi \sin\theta\sin\phi}, ..., e^{j\pi(N_y-1)\sin\theta\sin\phi}]^T \tag{F.6}$$

$$\boldsymbol{a_z}(\theta) = [1, e^{j\pi \cos\theta}, ..., e^{j\pi(N_z-1)\cos\theta}]^T. \tag{F.7}$$

2.2 Signal model

The received signal at any UE panel i in a single frequency-time resource element is given by

$$y^i(s,k) = \boldsymbol{w}^H(k)\boldsymbol{H}^i(s,k)\boldsymbol{f}(k)x(s,k) + \boldsymbol{w}^H(k)\boldsymbol{n}^i(s,k), \tag{F.8}$$

where $\boldsymbol{H}^i(s,k) \in \mathbb{C}^{N_r \times N_t}$ expresses the channel matrix between the gNodeB and the ith UE panel, as denoted in (F.1). The gNodeB beamforming vector $\boldsymbol{f}(k) \in \mathbb{C}^{N_t}$ contains a beam's analog phase shifts with a constant modulus of $\frac{1}{\sqrt{N_t}}$. This beam is employed to spatially filter the transmitted signal $x(s,k)$, received at the UE with a beam defined by the analog phase shifts in the beamforming vector $\boldsymbol{w}(k) \in \mathbb{C}^{N_r}$ and a constant modulus of $\frac{1}{\sqrt{N_r}}$. The receiver noise is modelled as a complex additive white Gaussian noise (AWGN) vector with variance σ_n^2 and given by $\boldsymbol{n}^i(s,k) \in \mathbb{C}^{N_r} \backsim \mathcal{CN}(\boldsymbol{0}, \sigma_n^2 \boldsymbol{I})$.

2.3 Beamforming codebooks

gNodeB codebook

For beam sweeping at the gNodeB, a directional beamforming codebook is adopted, dividing the cell's sector coverage into angular regions. These beams belong to a finite pre-defined set of N_T vectors $\mathcal{C}_t = \{\boldsymbol{f}_{\psi_t} | \psi_t = 1, \ldots, N_T\}$ which is referred to henceforth as the gNodeB codebook. The array steering vector for a transmit beam ψ_t pointing towards $(\theta_{\psi_t}, \phi_{\psi_t})$ is defined in the ψ_t^{th} vector of the codebook as

$$\boldsymbol{f}_{\psi_t} = \boldsymbol{a}_t(\theta_{\psi_t}, \phi_{\psi_t}). \tag{F.9}$$

The azimuth steering angles, ϕ_{ψ_t}, are linearly spaced within the angular range of the sector such that

$$\phi_{\psi_t} = -\frac{\pi}{3} + (\psi_t - 1) \times \frac{2\pi}{3 \times (N_T - 1)}, \psi_t = 1, ..., N_T. \tag{F.10}$$

Moreover, all the beams share the same elevation steering angle, θ_{ψ_t}.

UE panel codebook

Each UE panel produces a finite set of N_R vectors $\mathcal{C}_r^i = \{\boldsymbol{w}_{\psi_r} | \psi_r = 1, \ldots, N_R\}$, constituting the UE panel codebook. In any of the panels the array steering vector for a receive beam ψ_r directed towards $(\frac{\pi}{2}, \phi_{\psi_r})$ is expressed as

$$\boldsymbol{w}_{\psi_r} = \boldsymbol{a}_r\left(\frac{\pi}{2}, \phi_{\psi_r}\right). \tag{F.11}$$

Each ULA panel in the UE covers a $\frac{\pi}{2}$ sector of the angular space in the azimuth domain, with linearly spaced steering angles ϕ_r such that

$$\phi_{\psi_r} = -\frac{\pi}{4} + (\psi_r - 1) \times \frac{\pi}{2 \times (N_R - 1)}, \psi_r = 1, ..., N_R. \tag{F.12}$$

2.4 Beam management model

The gNodeB periodically sweeps N_T beams, where each beam ψ_t is associated to a distinct synchronization signal block (SSB). SSBs are sets of resources spanning 4 orthogonal frequency-division multiplexing (OFDM) symbols in time and 240 subcarriers in frequency employed for power-based measurements that determine the best serving beam pair [16]. An SSBurst is composed of one or multiple SSBs and is transmitted according to a numerology-dependent transmission pattern [17]. The SSBurst generation is performed through MATLAB®'s 5G Toolbox™ [18]. The UE receives each SSB with one of its N_R beams in panel i, ψ_r^i. The received signal is measured for synchronization signal (SS)-RSRP, defined in [19] as the linear average over the power contributions of the resource elements carrying SS signals. Thus, considering $\mathcal{V}_{ss}$ as a resource data set containing the SS sequence of an SSB, the RSRP measurement for the beam pair (ψ_t,ψ_r^i) is computed as

$$RSRP(\psi_t, \psi_r^i) = \frac{1}{|\mathcal{V}_{ss}|} \sum_{(s,k)\in\mathcal{V}_{ss}} |\boldsymbol{w}_{\psi_r^i}^H \boldsymbol{H}^i(s,k)\boldsymbol{f}_{\psi_t} + \boldsymbol{w}_{\psi_r^i}^H \boldsymbol{n}^i(s,k)|^2. \tag{F.13}$$

This work assumes a sequential panel activation at the UE. In other words, as stated by 3GPP's multi-panel "Assumption-1", the UE can only activate one panel at a time for measurement purposes [20]. Moreover, analog beamforming is considered on the panels to reduce power consumption. As a result, the SS-RSRP measurements for all beam pair combinations must be collected at the UE in a round robin fashion: to measure all the beam pair combinations across all panels, $4 \times N_R$ SSBursts must be transmitted during the UE's trajectory, one per UE beam[1]. $\boldsymbol{P}_{meas} \in \mathbb{R}^{4N_R \times N_T}$ stores all measured RSRP values to be used afterwards for beam pair selection.

2.5 Device mobility and rotation model

This work models both time-varying device mobility and device rotation as two independent processes in time. The user moves linearly in the cell sector with constant speed v. The UE's initial position and trajectory direction follow a uniform distribution in the xy plane, with the user's height fixed in the z-axis. Mobility bounds r and R are enforced (see Fig. F.1) where the user is considered to always remain within appropriate coverage range. The UE position is defined according to the global coordinate system (GCS) represented in black in Fig. F.1. The gNodeB has a fixed orientation coinciding

[1] Although the new radio (NR) standard supports hierarchical beam sweeping practices, this works opts for a UE with simplistic capabilities in order to highlight a particularly detrimental rotation scenario.

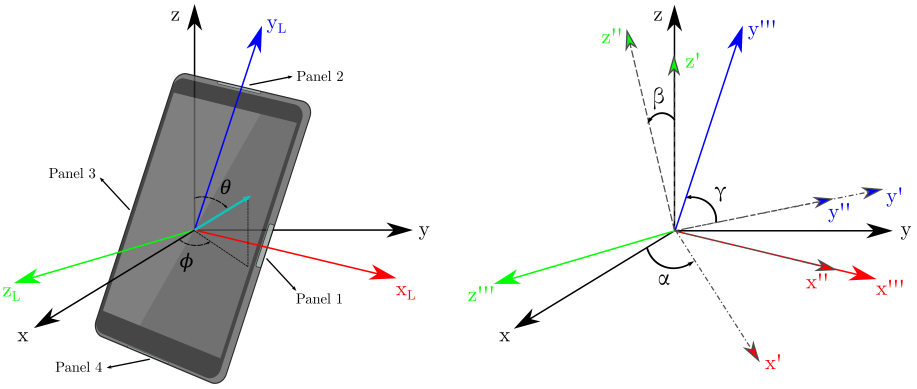

Fig. F.2: Spherical coordinates and LCS transformation (x''', y''', z''') with respect to the GCS (x, y, z) by a sequence of 3 rotations: α, β, γ [21].

with the GCS (x,y,z) while the UE is considered to experience time-varying rotation over its trajectory. The UE's orientation is dictated by a local coordinate system (LCS) (x_L,y_L,z_L), resulting from any 3D rotation with respect to the GCS over three distinct angles: the bearing angle α, the downtilt angle β and the slant angle γ, as shown in Fig. F.2. This set of angles represents three elemental rotations about the z, y and x axes, respectively [21]. The UE's initial orientation, described as (α_0, β_0, γ_0), is drawn from an uniform random distribution, taking values between 0° and 360°. The time-varying device rotation is characterized through a filtered random walk model as in [12] and [13]. The process to obtain the UE's orientation for a time sample t is exemplified for α as

$$\bar{\alpha}_t = \bar{\alpha}_{t-1} + \mathcal{N}(0, \sigma^2), \tag{F.14}$$

with σ representing the random walk's standard deviation and $\bar{\alpha}_0 \backsim \mathcal{U}[0^o, 360^o]$. Filtering of the random walk $\bar{\alpha}_t$ is given by

$$\alpha_t = \frac{1}{M} \sum_{m=0}^{M-1} \bar{\alpha}_{t-m}, \tag{F.15}$$

where M is described as the filter's length. The same procedure is applied to obtain β_t and γ_t, with all angles wrapped within $[0^o, 360^o]$. These values are used to update the $\boldsymbol{\varphi}^i_{r,l}$ values in (F.1) over time. This study considers t to match an SSBursts's periodicity T_{SS}. In other words, the device's orientation is assumed to remain constant over each periodic SSBurst transmission and progressively change between consecutive SSBursts as defined in (F.14) and (F.15).

3 UE Beam selection

This work focuses on improving UE beam selection in dynamic device rotation scenarios. Overlooking the procedure to select the best gNodeB beam $\psi_t^\star$ for a moment, two types of UE beam selection are considered: max-measurement based selection and ML-measurement based selection. Both methods rely solely on $\boldsymbol{P}_{meas}^{\psi_t^\star} \in \mathbb{R}^{4N_R \times 1}$, i.e. the RSRP measurements obtained with the UE beams across all panels when the gNodeB uses $\psi_t^\star$, collected as described in Section 2.4.

3.1 Max-measurement based beam selection

This method is based on the current beam sweeping and measurement procedure instated by 3GPP. The best UE panel and beam are selected based on a highest instantaneous power metric such that

$$\psi_r^{i\star} = \arg\max_{\psi_r^i} (\boldsymbol{P}_{meas}^{\psi_t^\star}(\psi_r^i)). \tag{F.16}$$

Such a solution is prone to errors in a dynamic environment since the beam selection may be based on outdated beam measurements.

3.2 ML-measurement based beam selection

This method uses the same potentially outdated RSRP measurements in an ML context to choose the best UE panel and beam based on its orientation, even if said orientation is never explicitly known. A supervised learning approach is chosen in the form of a feed-forward neural network solving a classification task. The network consists of several dense layers used to process the RSRP measurements for different UE beams. The hidden layers' purpose is to process the RSRP measurements and infer the orientation changes experienced by the UE during the measurement process, thus enabling the network to predict the optimal UE beam at the time of beam selection. During training, each hidden layer is followed by a dropout layer to make the neural network more robust to overfitting. The output layer is made of $4 \times N_R$ neurons, which approximate the optimality probabilities of each of the beams in the UE codebook. Fig. F.3 shows the considered NN structure for UE beam selection, where *tanh* and $softmax$ functions are used as non-linear activation functions for the hidden layers and the output layer, respectively.

Each training sample contains $4 \times N_R$ RSRPs, measured along a UE's trajectory in $4 \times N_R$ SSBursts, and the index of the best UE beam for communication at the $4 \times N_R + 1$ SSBurst, which is used as label for training. The categorical cross entropy is used as the loss function of the neural network,

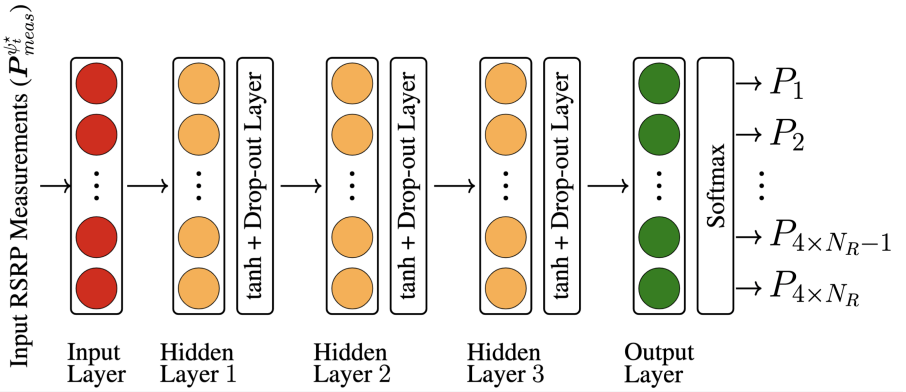

Fig. F.3: The proposed fully connected neural network structure of the ML-measurement based beam selection using RSRPs measured with dynamic terminal orientation.

i.e.,

$$\mathcal{L} = -\sum_{i=1}^{4\times N_R} L_i \log(P_i), \tag{F.17}$$

where L_i and P_i denote the label and output of the neural network for the ith UE beam. L is a one-hot vector with 1 at the entry corresponding to the best UE beam at the $4 \times N_R + 1$ SSBurst and 0 in all other entries. This training is UE-specific and done offline, using a 5000-sample dataset size.

4 Results and Discussion

This section assesses the performance of the solutions presented in Section 3 under three distinct factors: user mobility, dynamic device rotation and increasingly challenging propagation conditions. Table F.1 summarizes the simulation parameters used. This study evaluates 2 UE speeds, 2 UE rotation speeds and 3 different propagation environments, resulting in 12 distinct training datasets of 5000 samples for the ML-measurement based solution. Each sample includes the RSRP measurements for all the beam pair combinations in the $4 \times N_R = 12$ SSBursts that constitute the measurement period and the RSS measurements for all those beam pairs at the evaluation period, in the 13th SSBurst window. A neural network architecture is considered, which consists of 5 layers including an input layer with 12 neurons, 3 hidden layers with respectively 120, 120, and 60 neurons, followed by an output layer with 12 neurons. A drop-out rate of 0.3 is used for all the hidden layers. In the training process, an Adam optimizer is used [22] with the learning rate 0.001 and 15 epochs of training with progressively growing minibatch sizes

Table F.1: Simulation parameters.

Parameter	Notation	Value
Carrier frequency	f_c	28 GHz
Carrier bandwidth	B	104 MHz
Subcarrier spacing	Δf	120 kHz
RX noise figure	NF	9 dB
Thermal noise density	N_0	$-174\,\mathrm{dBm\,Hz^{-1}}$
Beam sweeping configuration		
SSBurst size	N_T	12
SSBurst periodicity	T_{ss}	20 ms
UE beams per panel	N_R	3
Layout configuration		
Inner mobility bound	r	15 m
Outer mobility bound	R	100 m
Channel model	-	Freespace, UMi LOS, UMi NLOS
gNodeB position	(x, y)	$(0, 0)$
gNodeB height	h_t	10 m
gNodeB codebook elevation	θ_{ψ_t}	103°
gNodeB array size	N_t	8×8
UE initial position	(x, y)	uniformly distributed
UE height	h_r	1.5 m
UE panels	I	4
UE panel size	N_r	1×4
UE speed	v	$3\,\mathrm{km\,h^{-1}}$, $60\,\mathrm{km\,h^{-1}}$
Number of UE trajectories	-	5000 per dataset
Random walk orientation configuration		
Standard deviation	σ	1°, 10°
Filter length	M	21

from 4 to 32 samples [23]. The training and test data split is set as 80 % and 20 %, respectively. The aforementioned parameters have been experimentally tuned according to the dataset sizes and the NN's structure.

4.1 Performance criteria

This work characterizes the beam selection process as consisting of two stages: the measurement period and the evaluation period. The measurement period refers to the SSBurst transmission and measurement stage, while the evaluation period pertains to a small time frame following the measurement period where all RSRP values have been collected and beam determination occurs. During the evaluation period, RSS measurements are computed over a set of

frequency-time resources, $\mathcal{V}_{eval}$, for every beam pair combination, (ψ_t, ψ_r^i), as

$$R(\psi_t, \psi_r^i) = \frac{1}{|\mathcal{V}_{eval}|} \sum_{(s,k)\in\mathcal{V}_{eval}} |\boldsymbol{w}_{\psi_r}^i \boldsymbol{H}^i(s,k)^\top \boldsymbol{f}_{\psi_t}|^2, \tag{F.18}$$

where $|\mathcal{V}_{eval}|$ denotes the cardinality of $\mathcal{V}_{eval}$. The RSS value of the selected beam pair is then given by

$$R_{meas} = R(\psi_t^\star, \psi_r^{i\star}), \tag{F.19}$$

where $\psi_t^\star$ and $\psi_r^{i\star}$ are determined either through max-measurement beam selection or ML-measurement based selection. To measure beam selection accuracy, a genie-aided solution is considered where optimal beam alignment is always guaranteed. In this case the maximum achievable RSS over all beam pair combinations is described as

$$R_{genie} = \max_{\psi_t, \psi_r^i} R(\psi_t, \psi_r^i). \tag{F.20}$$

The beam selection process occurs successfully when the beam pair selected matches the genie solution. Otherwise, a misdetection takes place. Depending on the degree of misalignment between the selected beam pair and the ideal beam pair, link power loss can be experienced. In such cases, R_{loss} expresses the beam misdetection loss given by

$$R_{loss} = \frac{R_{genie}}{R_{meas}}. \tag{F.21}$$

Therefore, two main performance criteria are considered:

- **Beam selection accuracy (BS_{acc}):** percentage of occasions where the beam pair selection matches the genie-aided selection.
- **Average misdetection loss ($\bar{R}_{loss}$):** average value of R_{loss} across all samples in dB.

4.2 Beam selection schemes

To properly assess the impact of the proposed solution, distinct gNodeB and UE beam selection schemes are established with an increasing level of realism, summarized in Table F.2:

- **Genie aided beam pair (G-gNB/G-UE):** The best beam pair is chosen based on the highest RSS measured at the evaluation period. This is an ideal, misalignment-free scenario that establishes the upper bound for beam management performance.

Table F.2: Beam selection schemes.

Schemes	gNodeB beam	UE beam
G-gNB/G-UE	max RSS	
G-gNB/B-UE	max RSS	max RSRP
G-gNB/ML-UE	max RSS	ML-RSRP
B-gNB/B-UE	max RSRP	
B-gNB/ML-UE	max RSRP	ML-RSRP

- **Genie-aided gnodeB beam and baseline UE beam (G-gNB/B-UE):** This scenario maintains an ideal gNodeB beam selection while the UE beam selection is achieved through the baseline method detailed in 3.1.
- **Genie-aided gNodeB beam and ML-based UE beam (G-gNB/ML-UE):** Similarly, this scenario considers ideal gNodeB beam selection but employs the UE beam selection method from Section 3.2 instead.
- **Baseline beam pair (B-gNB/B-UE):** A more realistic approach is taken based on the current 3GPP procedure where the best beam pair is chosen through the highest RSRP value. This method is taken as the baseline that the proposed solution should outperform.
- **Baseline gnodeB beam and ML-based UE beam (B-gNB/ML-UE):** This scenario describes the proposed beam management solution presented in this work. The gNodeB beam is selected through the highest RSRP measurement and the UE beam selection follows the ML procedure from Section 3.2.

4.3 Beam management performance - Freespace

Beam management performance is first assessed in Freespace, a simplified propagation scenario portraying free space loss with only one LOS path and no shadow fading. This allows for the evaluation of the proposed solution's potential in a favourable propagation environment, unencumbered by additional effects introduced by complex channel models with several multipath components. The beam selection schemes detailed in Section 4.2 are evaluated for both a low speed, $3\,\mathrm{km\,h^{-1}}$, and a moderate user speed, $60\,\mathrm{km\,h^{-1}}$. Additionally two σ values are taken to characterize the rotation of the device, $\sigma = 1^o$ and $\sigma = 10^o$, which translate into a rotation speed per axis of $6.0422\,^\circ\,\mathrm{s^{-1}}$ in Table F.3 and $60.4218\,^\circ\,\mathrm{s^{-1}}$ in Table F.4, respectively.

BS_{acc} results in Table F.3 show that misalignments can occur fairly frequently for both the proposed solution, B-gNB/ML-UE, and the baseline, B-gNB/B-UE, but lead to almost negligible losses in this slow UE rotation

Table F.3: Beam management performance for Freespace, $\sigma = 1^o$.

	BS_{acc} (%)		$\bar{R}_{loss}$ (dB)	
Schemes	$3\,\mathrm{km\,h^{-1}}$	$60\,\mathrm{km\,h^{-1}}$	$3\,\mathrm{km\,h^{-1}}$	$60\,\mathrm{km\,h^{-1}}$
G-gNB/G-UE	100	100	0	0
G-gNB/B-UE	94.5	93.0	0.07	0.09
G-gNB/ML-UE	89.3	90.3	0.11	0.12
B-gNB/B-UE	93.6	79.2	0.07	0.28
B-gNB/ML-UE	88.4	76.3	0.12	0.31

scenario. Furthermore, it is evident that the B-gNB/ML-UE scheme performs marginally worse than the B-gNB/B-UE scheme by less than 0.1 dB, indicating that the proposed solution has no impact on this scenario's beam management performance. For a low UE speed and slow UE rotation, the B-gNB/B-UE scheme performs quite well since the time it takes to collect all the RSRP measurements is short enough to keep up with the UE's mobility and rotation rates. However the beam selection accuracy of the B-gNB/B-UE scheme drops 14.4 % when UE speed increases. This performance drop at high speeds is due to misselections of the gNodeB beam: while the G-gNB/B-UE scheme causes a 7 % accuracy degradation when compared to the ideal scheme G-gNB/G-UE, the transition to the B-gNB/B-UE scheme results in an additional, more significant, accuracy reduction of 13.8 %. Considering the source of misalignment in this scenario takes place at the gNodeB side, where $\psi_t^\star$ selection is based on a max-RSRP method vulnerable to errors in mobility scenarios, it is unsurprising that the B-gNB/ML-UE scheme fails to offer any benefits, since it employs RSRP measurements from a misselected sub-optimal gNodeB beam.

In Table F.4, where UE rotation is more accentuated ($\sigma = 10°$), it is noticeable that the loss levels experienced are much larger. At $v = 3\,\mathrm{km\,h^{-1}}$, this additional dynamic factor in the environment warrants an accuracy drop of 37.2 % and a loss of 3.75 dB when comparing G-gNB/G-UE to G-gNB/B-UE. This means that significant UE rotation is occurring before it can finish collecting all RSRP measurements, which leads the G-gNB/B-UE scheme to base its beam selection on outdated beam information, resulting in beam misalignment and link performance degradation. The baseline B-gNB/B-UE scheme displays its worst performance at $v = 60\,\mathrm{km\,h^{-1}}$, since this scenario harbours both the effects of mobility and rotation of the device. This showcases perfectly the impact that lack of device orientation tracking can have on beam management performance.

The B-gNB/ML-UE scheme is shown to successfully improve accuracy and reduce misalignment losses by up to 2.5 dB in this particular scenario. This suggests that, for dynamic terminal orientation scenarios, the NN is able

Table F.4: Beam management performance for Freespace, $\sigma = 10^o$.

	BS_{acc} (%)		$\bar{R}_{loss}$ (dB)	
Scheme	$3\,\mathrm{km\,h^{-1}}$	$60\,\mathrm{km\,h^{-1}}$	$3\,\mathrm{km\,h^{-1}}$	$60\,\mathrm{km\,h^{-1}}$
G-gNB/G-UE	100	100	0	0
G-gNB/B-UE	62.8	61.9	3.75	3.76
G-gNB/ML-UE	75.2	76.0	1.24	1.26
B-gNB/B-UE	62.4	53.4	3.75	3.99
B-gNB/ML-UE	74.9	65.5	1.24	1.41

to analyze how the RSRP levels progress over time and infer the UE's orientation changes, allowing it to select the beam that maximizes link performance. This is something the B-gNB/B-UE scheme cannot achieve, since it chooses the beam with the highest power at the time of measurement, which for UEs with rapidly changing orientation may no longer be the optimal beam at the beam selection stage.

4.4 Beam management performance - realistic propagation scenarios

The Freespace study shows that the B-gNB/ML-UE scheme can improve the current procedure through RSRP measurements alone. However, it remains to be investigated if this approach is still feasible under realistic multipath rich environments. This section focuses on high mobility and high device rotation, since this has been established as the most challenging scenario for the baseline method. The beam management performance of the B-gNB/B-UE and B-gNB/ML-UE schemes are compared in Fig. F.4 under two additional 3GPP-compliant channel enviroments: UMi LOS and UMi NLOS. These are typically used to portray densely populated urban micro-cell areas with gNodeB deployment below rooftop level [21].

It is clear that the trends observed in Freespace are preserved in the UMi LOS scenario, where the gains of the proposed ML-based method over the baseline are only ever-so-slightly reduced. Results further suggest that the proposed solution's performance is significantly reduced in NLOS, despite still performing marginally better than the current baseline solution. As the environment transitions to a predominantly NLOS environment, propagation conditions progressively worsen: the received signal strength drops considerably and RSRP measurements start to blend together, due to the channel power being more spread in the angular domain. This makes it more challenging for the NN to infer the UE's orientation at the evaluation period, since all measurements have similar low power levels.

In summary, the B-gNB/ML-UE scheme can be leveraged to handle dy-

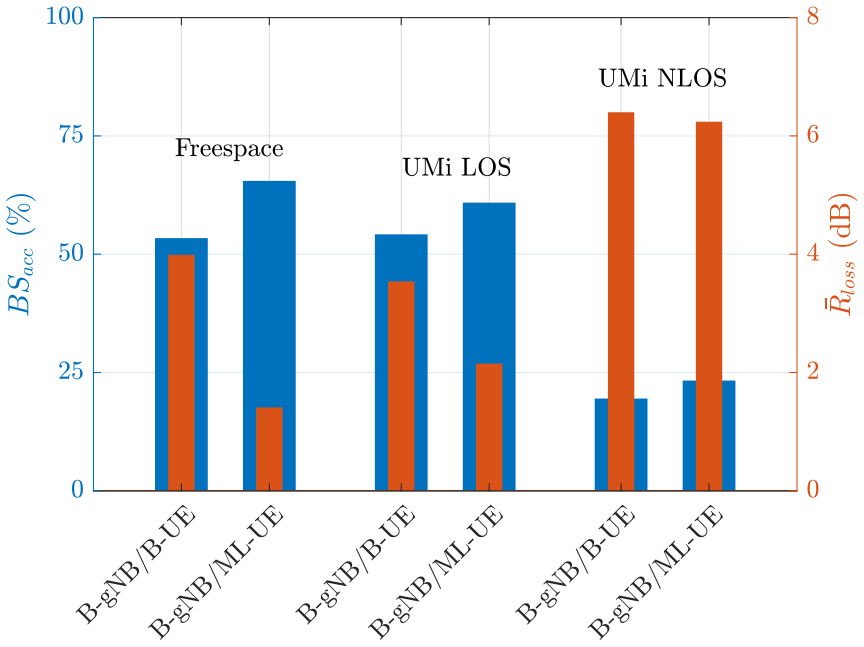

Fig. F.4: Beam management performance comparison of B-gNB/B-UE vs. B-gNB/ML-UE for Freespace, UMi LOS and UMi NLOS at $v = 60\,\mathrm{km\,h^{-1}}$ and $\sigma = 10^{o}$.

namic mobility and rotation scenarios, ultimately improving the robustness of the current beam management procedure, but only in environments with a dominant LOS component.

5 Conclusions

This work focuses on improving multi-panel UE beam selection robustness to mobility and time-varying terminal orientation without relying on context information. The feasibility of an ML solution based solely on RSRP measurements is investigated as an attempt to introduce a simpler alternative to UE beam selection with more manageable training dataset sizes than other context information aided methods in the literature.

Results indicate that the proposed ML-based scheme does not improve beam management performance for high-speed, slow rotating UEs. Instead, fast UE rotation scenarios respond positively to the proposed solution, showing that, in dominant LOS, outdated RSRP measurements can in fact be explored to successfully infer the UE's rotation pattern to predict its best beam and significantly reduce misdetection losses.

However, this approach's effectiveness suffers in predominantly NLOS environments. The drastically lowered received signal strength levels in these environments, along with the increased angular spread of the channel, cause all RSRP measurements to deteriorate to a point where the ML model struggles to extract the UE's rotation pattern, reducing its accuracy margin over the baseline 3GPP-based solution. This seems to indicate that in realistic scenarios with mixed LOS and NLOS conditions, the ML-solution could only be beneficial if LOS probability is high, potentially requiring more sophisticated solutions to mitigate the misdetections that would occur when transitioning to NLOS. An interesting iteration on this study, left for further investigation, is to determine whether a single model trained in mixed LOS/NLOS conditions could also offer robust beam management, maintaining good performance in LOS channels while not performing worse than the baseline method in NLOS conditions.

References

[1] M. Enescu, Ed., *5G New Radio: A Beam-based Air Interface*, 1st ed. John Wiley & Sons, 2020.

[2] 3GPP, “"Study on New Radio Access Technology Physical Layer Aspects",” Tech. Rep. 38.802, V14.2.0 2017.

[3] U. B. Elmali, A. Awada, U. Karabulut, and I. Viering, “"Analysis and Performance of Beam Management in 5G Networks",” *2019 IEEE 30th Annual International Symposium on Personal, Indoor and Mobile Radio Communications (PIMRC)*, pp. 1 – 7, 2019.

[4] I. Aykin and M. Krunz, “"Efficient Beam Sweeping Algorithms and Initial Access Protocols for Millimeter-Wave Networks",” *IEEE Transactions on Wireless Communications*, vol. 19, no. 4, pp. 2504 – 2514, 2020.

[5] S. Tomasin, C. Mazzuco, D. D. Donno, and F. Capellaro, “"Beam-Sweeping Design Based on Nearest Users Position and Beam in 5G mmWave Networks",” *IEEE Access*, vol. 8, pp. 124 402 – 124 413, 2020.

[6] H. Soleimani, R. Parada, S. Tomasin, and M. Zorzi, “"Fast Initial Access for mmWave 5G Systems with Hybrid Beamforming Using Online Statistics Learning",” *IEEE Communications Magazine*, vol. 57, no. 9, pp. 132 – 137, 2019.

[7] “"Study on Artificial Intelligence (AI)/Machine Learning (ML) for NR Air Interface",” 3GPP TSG RAN Meeting #94e, - RP-213599, May 2022.

[8] F. Abinader, C. Rom, K. Pedersen, S. Hailu, and N. Kolehmainen, “"System-Level Analysis of mmWave 5G Systems with Different Multi-Panel Antenna Device",” *2021 IEEE 93rd Vehicular Technology Conference (VTC2021-Spring)*, pp. 1 – 6, 2021.

[9] S. B. Iqbal, A. Awada, U. Karabulut, I. Viering, P. Schulz, and G. P. Fettweis, “"Analysis and Performance Evaluation of Mobility for Multi-Panel User Equipment in 5G Networks",” *2022 IEEE 95th Vehicular Technology Conference: (VTC2022-Spring)*, pp. 1–7, 2022.

[10] S. Rezaie, J. Morais, E. de Carvalho, A. Alkhateeb, and C. N. Manchón, “"Location- and Orientation-aware Millimeter Wave Beam Selection for Multi-Panel Antenna Devices",” *arXiv:2203.11714v1*, pp. 1–5, 2022.

[11] Y. Heng, J. G. Andrews, J. Mo, V. Va, A. Ali, B. L. N. nd, and J. C. Zhang, “"Six Key Challenges for Beam Management in 5.5G and 6G Systems",” *IEEE Communications Magazine*, vol. 59, no. 7, pp. 74 – 79, 2021.

[12] K. N. Nguyen, A. Ali, J. Mo, B. L. Ng, V. Va, and J. C. Zhang, “"Beam Management with Orientation and RSRP using Deep Learning for Beyond 5G Systems",” *2022 IEEE International Conference on Communications Workshops (ICC Workshops)*, pp. 133 – 138, 2022.

[13] A. Ali, J. Mo, B. L. Ng, V. Va, and J. C. Zhang, “"Orientation-Assisted Beam Management for Beyond 5G Systems",” *IEEE Access*, vol. 9, pp. 51 832 – 51 846, 2021.

[14] V. Raghavan, M.-L. Chi, M. A. Tassoudji, O. H. Koymen, and J. Li, “"Antenna Placement and Performance Tradeoffs With Hand Blockage in Millimeter Wave Systems",” *IEEE Transactions on Communications*, vol. 67, no. 4, pp. 3082 – 3096, 2019.

[15] S. Jaeckel, L. Raschkowski, K. Börner, and L. Thiele, “"QuaDRiGa: A 3-D Multicell Channel Model with Time Evolution for Enabling Virtual Field Trials",” *IEEE Transactions on Antennas Propagation*, vol. 62, no. 6, pp. 3242 – 3256, 2014.

[16] 3GPP, “"NR; Physical channels and modulation",” Tech. Spec. 38.211, V17.3.0 2022.

[17] ——, “"NR; Physical layer procedures for control",” Tech. Spec. 38.213, V17.3.0 2022.

[18] MathWorks, *5G Toolbox*, 2020.

[19] 3GPP, “"NR; Physical layer measurements",” Tech. Spec. 38.215, V17.1.0 2022.

[20] “"Feature lead summary #3 of Enhancements on Multi-beam Operations",” 3GPP TSG RAN WG1 Meeting #97, - R1-1907860, May 2019.

[21] 3GPP, “"Study on channel model for frequencies from 0.5 to 100 GHz",” Tech. Rep. 38.901, V17.0.0 2022.

[22] D. P. Kingma and J. Ba, “Adam: A Method for Stochastic Optimization,” in *Proc. Int. Conf. Learn. Representations*, 2015.

[23] S. Rezaie, C. N. Manchón, and E. de Carvalho, “Location- and Orientation-Aided Millimeter Wave Beam Selection Using Deep Learning,” in *Proc. IEEE Int. Conf. Commun.*, Jun. 2020, pp. 1–6.

Paper G

Context-aware Machine Learning-based Beam Selection with Multi-Panel Devices in the Presence of Self-Blockage

Sajad Rezaie, João Morais, Ahmed Alkhateeb, Carles Navarro Manchón

The paper has been submitted to the
IEEE Transactions on Machine Learning in Communications and Networking,
Feb. 2023.

The layout has been revised.

Abstract

Context-aware beam management in millimeter wave (mmWave) wireless communication systems has received increasing attention over the past several years. Machine learning (ML) has played a key role in leveraging different types of context information from device position and orientation to more ambitious scenarios using RADAR, LIDAR, or camera images. However, most of the work in this area considers simplified configurations for the user terminals without considering the self-blockage effects due to the user's hand and body. This paper is a step towards more realistic configurations and scenarios, where methods for location- and orientation-aware beam alignment are evaluated for multi-panel hand-held devices under mild and severe self-blockage conditions. We propose deterministic and probabilistic hand grip schemes that determine the blockage status of device panels. The probabilistic schemes are introduced to account for the inherent randomness of self-blockage due to variations of the user's hand grip. Contrary to the blockage models that introduce attenuation in multipath components depending on their angles-of-arrival, we propose two blockage models that introduce blockage losses over all the received paths - this emulates panels blocked by "hard" hand gripping more realistically. Our numerical simulations show that the multi-panel ML-based beam alignment method is able to leverage the terminal's location and orientation information even in severe self-blockage conditions, performing closely to optimal alignment with only a handful of beam-pair measurements.

1 Introduction

High definition mixed reality applications are gaining increasing popularity and will be commonplace in beyond 5G systems. They require large data rates and low latencies, a combination that can benefit from the abundant electromagnetic spectrum available at mmWave frequency bands [1]. MmWave frequencies, however, suffer from adverse propagation conditions, such as high path loss, high penetration loss, and low diffraction; these conditions difficult the establishment of reliable mmWave links [2]. As a solution, the wireless community widely acknowledges the potential of multiple-input multiple-output (MIMO) systems in the establishment of directional links that compensate propagation. But the establishment of such links constitutes a challenging task since it requires precise beam alignment without incurring in excessive channel acquisition overhead [3].

Codebook-based Beamforming Facilitates Beam Alignment Codebook-based beamforming appeals as a solution to reduce the complexity of beam alignment, while also facilitating the RF implementation of beamformers. Codebook-based beamforming consists in using pre-configured codewords or beam-

forming vectors [4]. In the space of all possible combinations of beams for AP and UT, searching all possible combinations leads to prohibitively high overhead and latency. As such, solutions like HBS emerged to reduce the beam search space by sensing the environment progressively using narrower beams and leveraging receiver feedback to make adjustments [4, 5]. As promising as HBS methods may sound, they are error-prone in their first iterations due to the low gain and directivity of wide beams, which often leads to subsequent wrongful hierarchical choices and longer convergence times.

ML for More Efficient Beam Alignment ML has been proposed to obtain solutions that converge faster and more reliably. They are envisioned to use pre-trained models that are further tuned with deployment-specific measurement data. There has been plenty of research contributions in the field. While some works focus on providing auxiliary information, like distributions of the AOA of the dominant path, e.g., via adaptive compressed sensing [6], other works intend to leverage such estimates and feed them into data-driven models, like support vector classifiers and neural networks, to perform beam selection in mmWave communication systems [7]. On the other hand, full-fledged frameworks that both estimate and directly use information such as the AOA of the main path to perform beam alignment and management have also been proposed [8].

CI Can Further Enhance Beam Alignment More recently, approaches that exploit CI about the users and/or environment have shown promising performances. These approaches leverage data acquired by different types of sensors besides antennas, and can be placed in the AP, UT or distributed across the environment [9, 10]. For example, the IFP method proposed in [11] suggests the use of a candidate beam list based on the user locations and the history of optimal beam pairs. Understandably, ML-based methods have been widely used to leverage context information effectively due to their inherent capability to deal with non-linearities. In the vast field of AI and ML, RL and DNNs have been the two techniques most frequently employed in mmWave beam alignment (BA) [12–14]. In [15], for instance, the authors present a method based in RL that uses past beam management data to reduce the overhead of beam training. RL-based methods, however, generally require many iterations for approaching an optimal policy, which is particularly undesirable in wireless settings [16]. A method using a DNN is proposed in [17] – the network uses sub-6 GHz channel measurements and the inherent spatial correlation of sub-6 GHz and mmWave propagation to extrapolate the optimal transmission beam in the mmWave band. Other examples of methods that leverage CI include the use of RADAR signals from joint sensing and communication functionalities at road side units [18].

Also directed towards V2X application, the authors of [19] propose a learning framework that crosses LIDAR data and the position of vehicles to gain knowledge of obstacles in the environment and optimize beam choices by avoiding blockages. Another way of predicting future link blockage is via camera images processed using computer vision paired with deep learning techniques [14, 20, 21].

Extending Beam Alignment to Multi-Panel devices Most studies in literature consider single-panel or even single-antenna devices. Typically, however, mmWave transceivers employ non-isotropic antenna elements, such as patch antennas, for directional coverage, and to provide full spatial coverage UT manufacturers resort to multi-panel designs [22, 23]. Therefore, multi-panel designs should be considered when designing codebooks and algorithms. In [23] we proposed an architecture for ML-based BA that considers a multi-panel antenna placement and evaluates the performance of CI-aware BA methods with different ML architectures. In this work, we propose to extend that study to hand blockages.

Considering Hand Grip in Beam Alignment with Multi-Panel devices The consideration of human blockages is key to accurate algorithm design. In particular, hand blockages are one of the most common type of human blockages. Several works attempted to circumvent the hand blockage problem by proposing wide-beam codebook design approaches [24, 25]. Other authors propose beam switching when the current panel received power suggests a blockage [26]. Overall, grip-aware codebooks provide better spherical coverage when compared with grip-agnostic codebooks [27]. But it is important to consider that RF constraints that come from the UT panels being connected to single or multiple RF chains, in partial or fully connected architectures [28].

Self-Blockage Effects can be Simulated with the Calibrated Self-Blockage Models Although grip-aware codebook adaptation can make the beam alignment robust to the self-blockage effects, it needs measurements in different directions to find a codebook with good coverage over different azimuth and elevation angles. As the self-blockage effects depend on the body and hand position, this approach suffers from the need for continual measurements in different directions. In addition, due to the adaptive properties of grip-aware codebook adaptation, the high computational complexity of this approach is another bottleneck. Thus, studies on the robustness to self-blockage of beam alignment procedures with a fixed codebook have strong motivation. Since the self-blockage effects highly depend on the position of the hands and body, it is not possible to acquire measurements or accurate electromagnetic simulations for every hand and body position. As

alternatives to measurements and accurate simulations for considering the self-blockage effects, self-blockage models are proposed to include the blockage effects in the beam alignment evaluation. In [29] 3GPP has proposed the 3GPP-Region (3GPP-R) self-blockage model that introduces a 30 dB loss to the paths arriving in a pre-determined area of azimuth and elevation angles. A beam alignment evaluation in [30] shows that the results using the 3GPP-R blockage model are similar to the case with an accurate electromagnetic simulation of hand blockage. Because a flat 30 dB loss may be too pessimistic for modeling blockage situations, the authors in [31] propose a statistical blockage model that considers a Gaussian-distributed variable for self-blockage loss. Similar to the 3GPP-R blockage model, the Statistical-Region (STAT-R) model introduces blockage to the paths with AOAs in a predefined range of azimuth and elevation. In addition, measurement results in [32] show that a loose or hard hand grip changes the blockage region and loss. These measurements suggest that a given antenna panel may be fully blocked by a hard hand grip and the user's body.

1.1 Contributions

In this paper, we evaluate the performance of CI-aware beam alignment methods under different self-blockage models and conditions. As established by the studies referenced above, hand-grip mode provides relevant information about the user-induced blockage characteristics of the terminal. In addition, terminal orientation and hand-grip mode are, obviously, statistically related. Thus, our hypothesis is that terminal orientation provides useful information to, to an extent, predict the effects that self-blockage will impose on the different beam measurements. Therefore, terminal orientation can be used to mitigate the impact of blockage in the beam alignment task. This paper investigates this hypothesis and has the following contributions:

1. In this study, the behavior of CI-aware BA methods to different self-blockage models is investigated. In addition to the 3GPP-R and STAT-R blockage models, we consider extending the blockage area to the entire unit sphere in the 3GPP-Sphere (3GPP-S) and Statistical-Sphere (STAT-S) self-blockage models. These models simulate situations where a panel is completely blocked due to the user's hard hand grip and body.

2. We consider probabilistic panel blockage schemes to incorporate the effects of different hand and body positions on multi-panel devices. Although the 3GPP-R and statistical blockage models are calibrated using measurements, these models do not account for different hand-gripping modes which are not considered in the measurement dataset. In these

schemes, each panel is blocked with some probability, which simulates randomness in the self-blockage impacts.

3. The method proposed in [33] for location- and orientation-aware beam selection using ML is evaluated for multi-panel devices in the presence of self-blockage.

4. To compare the performance of the ML-based approach in the presence of self-blockage, we consider several baselines. The GIFP method as a lookup table approach besides the exhaustive and hierarchical beam search methods.

5. Numerical results reveal that a data-driven approach is able to extract the correlation between the device orientation and blockage status. Therefore, the ML model considers this relation in the proposal of candidate beam pairs that account for the predicted blockage situations.

2 System and Channel Model

To study the effects of hand blockage, we consider a single-panel AP connected to a multi-panel UT in an indoor 3D scenario. The AP is equipped with a UPA with N_{AP} antenna elements while the UT is made of P panels. The UT uses UPAs and ULAs with N_{UT} total antenna elements, $N_{\mathrm{UT}}^{(p)}$ on the pth panel. For generality, we define $N_{\mathrm{AP}} = N_{\mathrm{AP_x}} N_{\mathrm{AP_y}} N_{\mathrm{AP_z}}$ and $N_{\mathrm{UT}}^{(p)} = N_{\mathrm{UT_x}}^{(p)} N_{\mathrm{UT_y}}^{(p)} N_{\mathrm{UT_z}}^{(p)}$, where each term of the product is the number of elements along the respective coordinate axis. Note, however, that some panels have only a single element across some dimensions, depending on UPA or ULA panels. Shown in Fig. G.1 is the edge-face (EF) UT antenna placement design in the portrait and landscape modes. The design is inspired by [22], where it contains 3 ULA panels at the edges and 2 UPA panels on the front and back of the device.

Position and orientation coordinates are defined in a GCS. The AP and UT have their own LCS, with positions coordinates $\boldsymbol{p}_{\mathrm{AP}} = (x_{\mathrm{AP}}, y_{\mathrm{AP}}, z_{\mathrm{AP}})$ and $\boldsymbol{p}_{\mathrm{UT}} = (x_{\mathrm{UT}}, y_{\mathrm{UT}}, z_{\mathrm{UT}}) \in \mathbb{R}^3$ rotated by $\boldsymbol{\psi}_{\mathrm{AP}} = (\alpha_{\mathrm{AP}}, \beta_{\mathrm{AP}}, \gamma_{\mathrm{AP}})$ and $\boldsymbol{\psi}_{\mathrm{UT}} = (\alpha_{\mathrm{UT}}, \beta_{\mathrm{UT}}, \gamma_{\mathrm{UT}})$ around the z, y and x axes of the GCS [33]. The rotation angles are such that the UPA on the AP is parallel to the yz plane (therefore $N_{\mathrm{AP_x}} = 1$) and the UT screen is parallel to the xy plane. Two modes of device orientation are considered in this study: portrait and landscape. In portrait mode, $\beta_{\mathrm{UT}} = 0$ and α_{UT}, γ_{UT} are uniformly random in the ranges $\alpha_{\mathrm{UT}} \in [-\pi, \pi)$ and $\gamma_{\mathrm{UT}} \in [0, \pi/2]$. In the landscape mode, $\gamma_{\mathrm{UT}} = 0$ and α_{UT}, β_{UT} are drawn uniformly in the ranges $\alpha_{\mathrm{UT}} \in [-\pi, \pi)$ and $\beta_{\mathrm{UT}} \in [-\pi/2, 0]$.

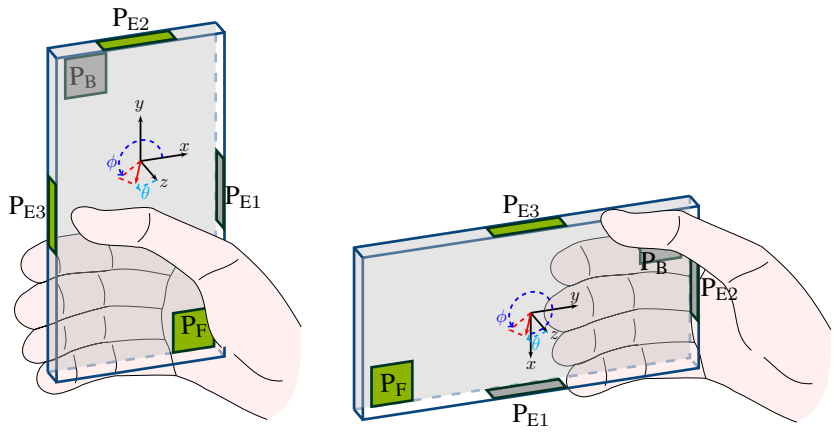

(a) Portrait mode **(b)** Landscape mode

Fig. G.1: The edge-face (EF) multi-panel device in different orientation modes (a) Portrait (b) Landscape. The antenna placement design is inspired by [22].

2.1 Channel and Signal Model

The model of the wireless channel between the AP and the pth UT panel is given by the matrix $\boldsymbol{H}^{(p)} \in \mathbb{C}^{N_{\mathrm{UT}}^{(p)} \times N_{\mathrm{AP}}}$ represented in (G.1), where we consider $L^{(p)}$ paths, each path carrying $\rho_l^{(p)}$ power with $\vartheta_l^{(p)}$ phase difference to the LOS, $\phi_l^{(p)}$ azimuth and $\theta_l^{(p)}$ elevation AOAs, $\psi_l^{(p)}$ and $\omega_l^{(p)}$ the AOD, and $\boldsymbol{a}_{\mathrm{UT}}^{(p)}$ and $\boldsymbol{a}_{\mathrm{AP}}$ as the antenna response vectors:

$$\boldsymbol{H}^{(p)} = \sum_{l=1}^{L^{(p)}} \sqrt{\rho_l^{(p)}}\, e^{j\vartheta_l^{(p)}}\, \boldsymbol{a}_{\mathrm{UT}}^{(p)}(\phi_l^{(p)}, \theta_l^{(p)})\, \boldsymbol{a}_{\mathrm{AP}}^{H}(\psi_l^{(p)}, \omega_l^{(p)}). \tag{G.1}$$

Note that the AODs and AOAs are measured with respect to the LCSs of the AP and UT, respectively.

The array response of a $\{N_{\mathrm{x}}, N_{\mathrm{y}}, N_{\mathrm{z}}\}$ antenna array with $\lambda/2$ antenna spacing may be written as

$$\boldsymbol{a}(\phi,\theta) = \frac{1}{\sqrt{N_{\mathrm{a}}}} g_{\mathrm{eff}}(\phi,\theta)\boldsymbol{a}_{\mathrm{z}}(\theta) \otimes \boldsymbol{a}_{\mathrm{y}}(\phi,\theta) \otimes \boldsymbol{a}_{\mathrm{x}}(\phi,\theta) \tag{G.2}$$

$$\boldsymbol{a}_{\mathrm{x}}(\phi,\theta) = [1, e^{j\pi sin(\theta)\, cos(\phi)}, \ldots, e^{j\pi(N_{\mathrm{x}}-1)\, sin(\theta)\, cos(\phi)}]^T, \tag{G.3}$$

$$\boldsymbol{a}_{\mathrm{y}}(\phi,\theta) = [1, e^{j\pi sin(\theta)\, sin(\phi)}, \ldots, e^{j\pi(N_{\mathrm{y}}-1)\, sin(\theta)\, sin(\phi)}]^T, \tag{G.4}$$

$$\boldsymbol{a}_{\mathrm{z}}(\theta) = [1, e^{j\pi cos(\theta)}, \ldots, e^{j\pi(N_{\mathrm{z}}-1)\, cos(\theta)}]^T. \tag{G.5}$$

where $g_{\text{eff}}(\phi, \theta)$ is the effective antenna gain, and $\boldsymbol{a}_{\text{x}} \in \mathbb{C}^{N_{\text{x}} \times 1}$, $\boldsymbol{a}_{\text{y}} \in \mathbb{C}^{N_{\text{y}} \times 1}$, and $\boldsymbol{a}_{\text{z}} \in \mathbb{C}^{N_{\text{z}} \times 1}$ are the linear responses along each axis. Here, g_{eff} includes both the effects of the radiation patterns of the antenna elements and of the self-blockage events. Also, it is assumed that g_{eff} is identical for all antenna elements in a given panel.

Considering an AP transmission power P_{AP}, the beamforming vector $\boldsymbol{u}$, and a symbol s, the received signal at the pth UT panel can be represented as

$$y^{(p)} = \sqrt{P_{\text{AP}}} \boldsymbol{v}^{(p)^H} \boldsymbol{H}^{(p)} \boldsymbol{u} s + \boldsymbol{v}^{(p)^H} \boldsymbol{n}^{(p)} \tag{G.6}$$

where $\boldsymbol{v}^{(p)}$ and $\boldsymbol{n}^{(p)}$ are, respectively, the combiner and a white complex Gaussian noise vector with component variance σ_n^2 at the pth panel of the UT. We generate channel matrices for each considered UT location and orientation using the Altair WinProp™ ray-tracing software [34].

2.2 Codebook-based Beamforming

The antenna arrays in this work are assumed to be analog, i.e., they use a single RF chain. The AP has a single panel, and, hence, a single RF chain. At the UT, a single RF chain is considered, which is switched over the different antenna panels. Hence, only a single panel in the UT is active at a time, and multi-panel beamforming is left out the scope of this study. For beamforming, the AP and UT use analog phase shifters paired with discrete Fourier transform (DFT) codebooks with size equal to the number of elements in the panel. The set of all available beamforming vectors for the AP and UT pth panel is respectively given by $\boldsymbol{\mathcal{U}} = \{\boldsymbol{u}_1, \ldots, \boldsymbol{u}_{N_{\text{AP}}}\}$ and $\boldsymbol{\mathcal{V}}^p = \{\boldsymbol{v}_1^p, \ldots, \boldsymbol{v}_{N_{\text{UT}}^{(p)}}^p\}$. We further define the set of all combiners at the UT $\boldsymbol{\mathcal{V}} = \{\boldsymbol{v}_1, \ldots, \boldsymbol{v}_{N_{\text{UT}}}\}$ as the union of all UT panel codebooks. The resultant RSS from using the AP beamforming vector $\boldsymbol{u}_i$ and UT combiner $\boldsymbol{v}_j$ can be written as

$$R_{i,j} = \left| \sqrt{P_{\text{AP}}} \boldsymbol{v}_j^H \boldsymbol{H}^{(p_j)} \boldsymbol{u}_i s + \boldsymbol{v}_j^H \boldsymbol{n} \right|^2 \tag{G.7}$$

where p_j is the index of the panel corresponding to combiner $\boldsymbol{v}_j$.

3 Modeling and Simulating Self-Blockages

This section presents the procedure we consider for modeling and simulating hand and body blockages. We propose a procedure consisting of two steps: (a) a hand grip scheme, and (b) a self-blockage model. We propose three deterministic and probabilistic hand grip schemes to define the blockage status of each panel. In case a panel is blocked according to the considered hand grip scheme, we use a self-blockage model to attenuate the received signal strength of the affected multipath components.

Table G.1: The considered hand grip schemes in this study with the corresponding panel blockage probabilities.

Hand grip scheme	Orientation mode	Panel blockage probability				
		P_{E1}	P_{E2}	P_{E3}	P_F	P_B
Fixed (FX)	Portrait	1	0	1	1	0
	Landscape	0	1	0	0	1
Non-uniform (NU)	Portrait	0.75	0.25	0.75	0.75	0.25
	Landscape	0.25	0.75	0.25	0.25	0.75
Uniform (U)	Portrait	0.5	0.5	0.5	0.5	0.5
	Landscape	0.5	0.5	0.5	0.5	0.5

3.1 Hand Grip Schemes

Whether a panel is blocked by the user's hand depends on the hand position and panel placement on the device. User hand position is linked to the usage of the device (e.g., game, call, typing, etc.), which are also linked to the terminal orientation mode [27]. In Table G.1, we define fixed (FX), non-uniform (NU), and uniform (U) hand grip schemes, which determine the blockage probabilities for all the panels on the device. The proposed hand grip schemes have the following properties:

- FX: depending on the orientation mode, a subset of the panels are always blocked, while others are always unblocked.
- NU: depending on the orientation mode, some panels have a high probability (0.75) of being blocked, while the rest of the panels have a low blockage probability (0.25).
- U: All panels in the device are blocked with probability 0.5.

In the NU and U hand grip schemes, the blockage statuses are drawn independently across the panels. It is worth pointing out that there is a small probability that all the panels are blocked in the NU and U schemes.

3.2 Hand and body blockage models

In (G.2), the effective antenna gain at azimuth and elevation angles ϕ and θ can be written as

$$g_{\text{eff}}(\phi,\theta) = g_{\text{a}}(\phi,\theta) g_{\text{b}}(\phi,\theta) \tag{G.8}$$

where $g_{\text{a}}(\phi,\theta)$ and $g_{\text{b}}(\phi,\theta)$ denote the antenna element gain and self-blockage coefficient, respectively. The self-blockage coefficient can be written as $g_{\text{b}}(\phi,\theta) = 10^{-l_{\text{b}}(\phi,\theta)/20}$, where $l_{\text{b}}(\phi,\theta)$ is the AOA-dependent self-blockage power loss in dB. In case of no self-blockage ($l_{\text{b}} = 0$ dB), $g_{\text{b}}(\phi,\theta) = 1$ which results to $g_{\text{eff}}(\phi,\theta) = g_{\text{a}}(\phi,\theta)$.

Table G.2: The self-blockage models proposed in [29, 35].

Orientation mode	ϕ_1	x_1	θ_1	y_1	Blockage loss (in dB)
Portrait	260	120	100	80	3GPP-R: 30
Landscape	40	160	110	75	STAT-R: $\mathcal{N}(\mu = 15.3 \text{ dB}, \sigma = 3.8 \text{ dB})$

Self-Blockage Models Over a Region

Several studies have been conducted to model hand and body blockage effects on the received signal by a UT. A hand blockage model is proposed by 3GPP, which we refer to as 3GPP-R. The 3GPP-R model introduces 30 dB power loss for paths with AOA in a pre-defined angular range [29]. As an alternative, several statistical models calibrated using measurement data and accurate electromagnetic simulations are proposed in [35]. In this work, we use the calibrated Gaussian model, which introduces a Gaussian density power loss on a predefined angular range of the UT LCS. In our study, this model is referred to as STAT-R. The blockage regions of the 3GPP-R and STAT-R are defined similarly, being centered on (ϕ_1, θ_1) with a size of (x_1, y_1) in azimuth and elevation angles, respectively. Thus, the blocking range includes part of the unit sphere with azimuth $\phi \in [\phi_1 - (x_1/2), \phi_1 + (x_1/2)]$ and elevation $\theta \in [\theta_1 - y_1/2, \theta_1 + y_1/2]$. It is important to note that the blockage region is a function of the UT orientation mode. The details of the 3GPP-R and STAT-R models are presented in Table G.2. Although the 3GPP-R and the STAT-R models make it possible to analyze and simulate self-blockage effects on UT devices, these models do not consider several important factors, e.g., the position of the hand and body, single- or dual-hand grips, and antenna placement design [27], which is reflected in the fixed (predefined) blockage region.

Self-Blockage Models Over the Sphere

To model the cases in which a "hard" hand grip results in some panels being fully blocked, we propose two additional blockage models where the blockage region is not limited to a part of the sphere. The proposed 3GPP-S and STAT-S self-blockage models introduce, respectively, $l_{\text{b}}(\phi, \theta) = 30$ dB and $l_{\text{b}}(\phi, \theta) \sim \mathcal{N}(\mu = 15.3 \text{ dB}, \sigma = 3.8 \text{ dB})$ self-blockage loss over all the received paths. It is worth mentioning that the self-blockage coefficient caused by 3GPP-S and STAT-S models can be formulated as $g_{\text{b}}(\phi, \theta) = 10^{-l_{\text{b}}(\phi,\theta)/20}$.

4 mmWave Beam Selection

Far-field mmWave wireless propagation is inherently geometric in nature which results in a strong correlation between the wireless channel and UT

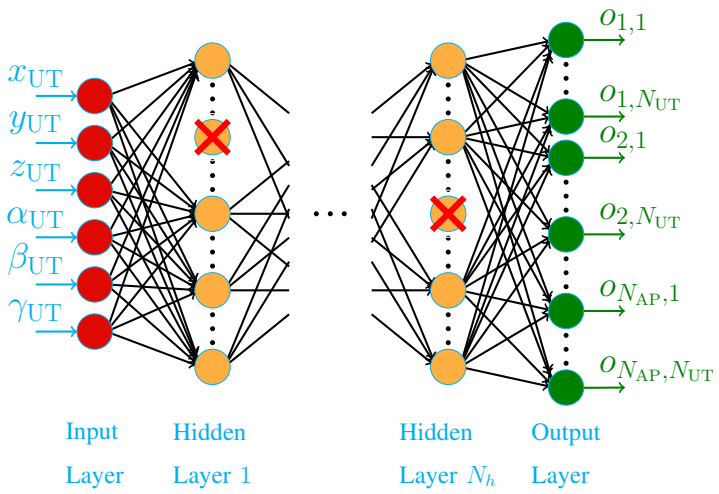

Fig. G.2: The proposed DNN architecture in [33] with $N_{\mathrm{AP}}N_{\mathrm{UT}}$ neurons at its output layer for estimation of optimality probabilities of the AP-UT beam pairs based on the UT location and orientation.

location and orientation [36, 37]. Besides the localization systems and inertial sensors on the device that can acquire the device location and orientation [38], beyond 5G systems are envisioned to leverage joint communication, sensing and localization to perform BA, particularly via UT location and orientation-aware approaches [39]. The following section describes precisely how this work proposes leveraging UT location and orientation for reducing the beam search space in BA.

4.1 Beam Selection Procedure

Let set $\mathcal{B}$ include all possible combinations of beamforming vectors and combiners between the AP and UT. Then, let $\mathcal{S}$ be a subset of $\mathcal{B}$ constructed via analysis of UT location and orientation to form a reduced beam-pair candidate list. For a given location and orientation of the UT, the optimal candidate beam-pair list $\mathcal{S}$ of size C can be built by minimizing the beam misalignment probability as in

$$\begin{aligned} \min_{\mathcal{S}} \quad & \mathbb{P}\left[\max_{(t,w)\in\mathcal{S}} R_{t,w} < \max_{(i,j)\in\mathcal{B}} R_{i,j}\right], \\ \text{s.t.} \quad & |\mathcal{S}| = C \end{aligned} \tag{G.9}$$

where C is a pre-defined constant specifying the number of beam pairs in the candidate list. Then, the optimal beam pair indices ($i^\star$ for AP transmission,

$j^\star$ for UT reception) is given by

$$i^\star, j^\star = \underset{(i,j)\in\mathcal{B}}{\arg\max}\, R_{i,j}. \tag{G.10}$$

We further define $p^\star$ as the panel that corresponds to the optimal UT beam $j^\star$. $P_{i,j} = \mathbb{P}\left[(i,j) = (i^\star, j^\star)\right]$ denotes the probability of beam pair (i,j) being optimal, i.e., being the beam pair in the codebook yielding the highest RSS [1]. The optimal $\mathcal{S}$ includes beam pairs with the highest probabilities of optimality [11]. In the beam selection procedure, the AP and UT sense the environment using the beam pairs in $\mathcal{S}$, and the UT reports the beam pair $(\hat{i}, \hat{j})$ with highest RSS.

To estimate the probabilities of each beam pair to be the optimal pair, which are used to construct the candidate list $\mathcal{S}$ for a given UT location and orientation, we consider two data-driven approaches (a) an ML-based approach, (b) a lookup table approach. In the ML approach, the proposed fully connected neural network (FCNN) in [33] is considered. Fig. G.2 shows the architecture of the DNN, which includes an input layer with 6 neurons, N_h hidden layers with n_h neurons per hidden layer, and an output layer with $N_{\text{AP}}N_{\text{UT}}$ neurons. The DNN gets 6 inputs, corresponding to 3D terminal location and 3D terminal orientation. Also, the DNN delivers $N_{\text{AP}}N_{\text{UT}}$ outputs, each providing estimates of the optimality probability for each of the $N_{\text{AP}}N_{\text{UT}}$ possible beam pairs. As an alternative lookup table approach, the GIFP method is considered to use historical data to propose the optimality probabilities. The details of the GIFP method are explained in [11, 33].

5 Simulation Results

5.1 Simulation Setup and Performance Measures

To assess the aforementioned deep learning methods, we conduct simulations in an indoor scenario proposed in the IEEE 802.11ad task group. The scenario consists of a $7 \times 7 \times 3$ meters living room, onto which we place a grid of possible UT positions: a rectangle of 4×7 meters at 1.5m height above the floor. For propagation statistics and other properties, refer to [40]. The setup is illustrated in Fig. G.3. There, we see the AP fixed in the center of one of the side walls. It uses a panel with $\{N_{\text{AP}_\text{x}}, N_{\text{AP}_\text{y}}, N_{\text{AP}_\text{z}}\} = \{1, 8, 8\}$ antenna elements. On the UT side, we consider the edge panels P1 to P3 to have 4-element ULAs, and the face panels having a UPAs configuration of $\{2, 2, 1\}$. The antenna radiation patterns are described by 3GPP [29], and we further consider $P_t = 24$ dBm and $\sigma_n^2 = -84$ dBm.

[1] $P_{i,j}$ is a conditional probability given the UT location and orientation but we drop this conditionality to alleviate notation.

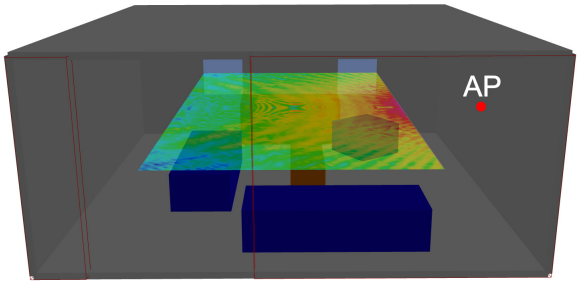

Fig. G.3: The considered $7 \times 7 \times 3$ meters living room (LR) as the indoor environment in our simulations. The user grid covers an area of 4×7 meters. The AP is placed in the center of a side wall, and the LOS power is illustrated for the user area. The properties of the environment are provided by IEEE 802.11ad task group [40].

Regarding learning parameters, the hidden layers and output layer of our NN models are respectively activated by $tanh$ and $softmax$. We also use $N_h = 5$ and $n_h = 128$. To make the DNN robust to overfitting, we use the dropout technique with a dropout rate of 10% for all the hidden layers in the network. The DNN is trained as a classifier, using categorical cross entropy as the loss function with Adam as the optimizer [41]. We consider 50 epochs of training, where the minibatch size is gradually enlarged from a small minibatch with 32 samples to a large minibatch with 8192 samples [33].

To evaluate the performance of DL-based BA methods, we consider two baselines: GIFP and hierarchical panel-beam search (HP-BS) methods. In the HP-BS method, the UT considers a wide beam to sense the environment in each panel while the AP transmits using a wide beam as well. Then the UT measures all the beams in the selected panel to find the beam with the highest RSS. In the next stage, UT beam is fixed, while AP finds the best beamforming vector using the HBS explained in [33].

The training and test datasets are composed as follows. A dataset consists of multiple samples with each sample including a specific UT location, UT orientation, and list of RSS measurements obtained with all beam pairs in $\mathcal{B}$. To evaluate the performance of CI-based methods, we consider a training dataset with $25,000$ samples and a test set with $2,000$ samples for evaluation. Furthermore, we assume that the candidate beam pairs $\mathcal{S}$ obtained during the beam selection are measured in a frame of duration T_{fr}, smaller than the channel coherence time. The first part of the frame is used to measure the N_b beam pairs in the candidate beam pair list $\mathcal{S}$, with each beam measurement having a duration of T_s. Then, the index of the beam pair in $\mathcal{S}$ providing the highest RSS is ideally reported back to the AP without delay or error. The remaining part of the frame, of duration $T_{fr} - N_b T_s$, is used to communicate data over the selected beam pair. Therefore, we account for the overhead of BA in the method of estimation of effective spectral effi-

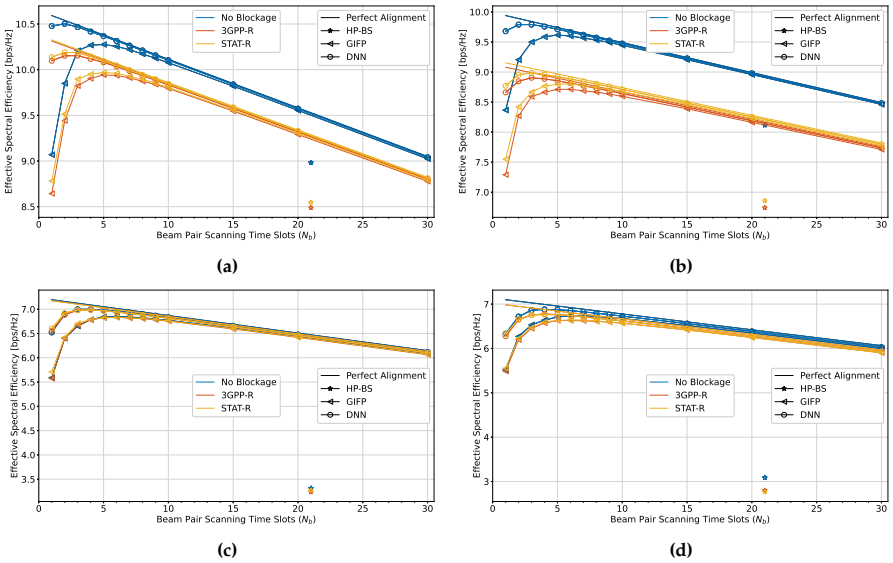

Fig. G.4: Performance of different BA methods with the FX hand grip scheme under the 3GPP-R and STAT-R self-blockage models. (a) LOS condition and portrait mode, (b) LOS condition and landscape mode, (c) NLOS condition and portrait mode, (d) NLOS condition and landscape mode.

ciency (ESE). The ESE of a BA procedure using N_b time slots can be written as $\text{SE}_{\text{eff}} = \frac{T_{fr}-N_b T_s}{T_{fr}} \log_2(1+\text{SNR}_{\hat{i},\hat{j}})$, where $\hat{i}$ and $\hat{j}$ are the indices of the selected beams of the AP and UT, $\text{SNR}_{i,j}$ is the SNR achieved by using the (i,j)th beam pair, and T_s is the beam-scanning time slot duration. We use $T_{fr} = 20$ms and $T_s = 0.1$ms as in [42].

5.2 Numerical Evaluation

The ML-based beam alignment is robust to mild self-blockage conditions with the FX hand grip scheme followed by the 3GPP-R or STAT-R blockage models

Considering the 3GPP-R and STAT-R blockage models with the FX hand grip scheme, Fig. G.4 shows the performance degradation of the beam selection methods due to self-blockage for devices with the edge-face antenna placement design illustrated in Fig. G.1. In LOS conditions, a significant degradation can be seen with a small beam candidate list size, N_b. However, the performance degradation in NLOS conditions is negligible. We conclude from these results that several NLOS paths with similar power are available in the environment. Thus, blockage of the strongest NLOS path does not lead to a

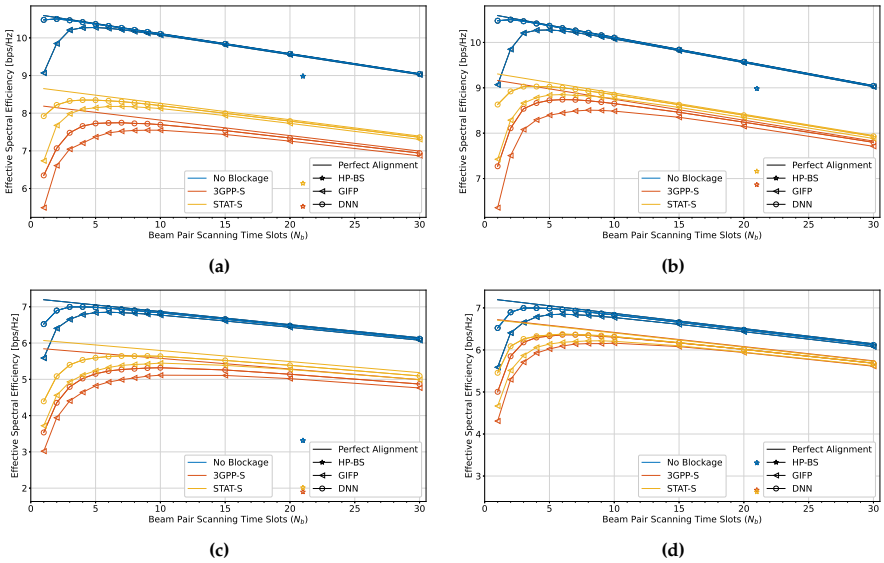

Fig. G.5: Performance of different BA methods under severe self-blockage settings in portrait orientation mode. Probabilistic NU and U hand grip schemes under the 3GPP-S and STAT-S self-blockage models are used in this experiment. (a) NU hand gripping in LOS condition, (b) U hand gripping in LOS condition, (c) NU hand gripping in NLOS condition, (d) U hand gripping in NLOS condition.

notable decrease in the achieved ESE. In addition, the orientation mode of the terminal –portrait or landscape– does not significantly impact the results.

The ML-enabled beam alignment method leverages the CI even in severe self-blockage conditions with the NU or U hand grip schemes followed by the 3GPP-S or STAT-S blockage models

In order to inspect the BA performance in severe hand blockage conditions, we consider experiments with 3GPP-S and STAT-S blockage models, while the probabilistic hand grip schemes NU and U are considered for panel blockage. Fig. G.5 shows the ESE with portrait orientation mode. Different from the results with 3GPP-R and STAT-R in Fig. G.4, the performance degradation induced by hand blockage is now significant in both LOS and NLOS conditions. Also, the NU hand grip scheme results in more performance degradation than the U hand grip scheme. An explanation of this observation can be that the probability of simultaneous blockage of adjacent panels –i.e., panels covering adjacent and partly overlapping regions of the sphere– in the NU hand grip scheme is higher, which results in an increased chance of missing the LOS or strong NLOS paths due to self-blockage.

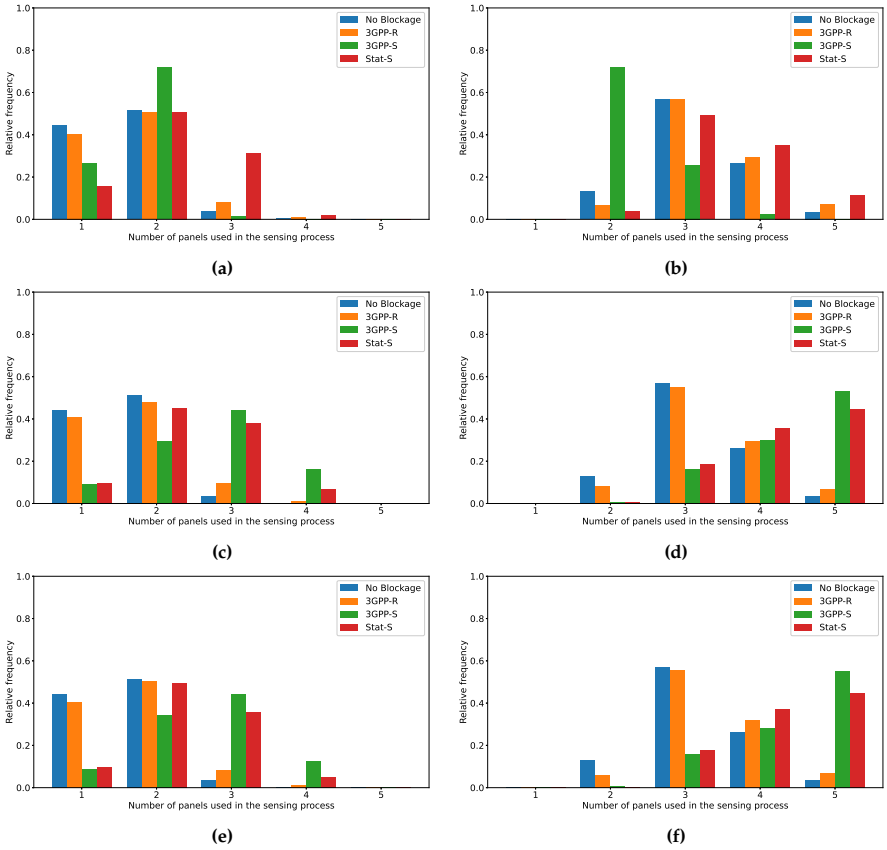

Fig. G.6: Relative frequency histogram of the number of different panels used in the beam measurement phase. In this experiment, we consider UTs in portrait mode and LOS condition. (a) and (b) FX hand grip scheme, (c) and (d) NU hand grip scheme, (e) and (f) U hand grip scheme. (a), (c), and (e): candidate list with 5 beams ($Nb = 5$), (b), (d), and (f): candidate list with 20 beams ($N_b = 20$)

The ML model adapts the beam pair recommendation to the self-blockage condition

Although self-blockage, especially blockage over the entire sphere in the 3GPP-S and STAT-S models, may cause severe performance degradation, the ML-based beam selection method finds a way to deal with the blockage situation. To gain a better understanding of the ML-beam selection outcome, Fig. G.6 shows the relative frequency histogram of the number of panels involved in sensing the beam pairs proposed in the beam candidate list. With a small beam candidate list including 5 beam pairs (left column subplots), mainly the UT beams belonging to one or two panels are included in the candidate

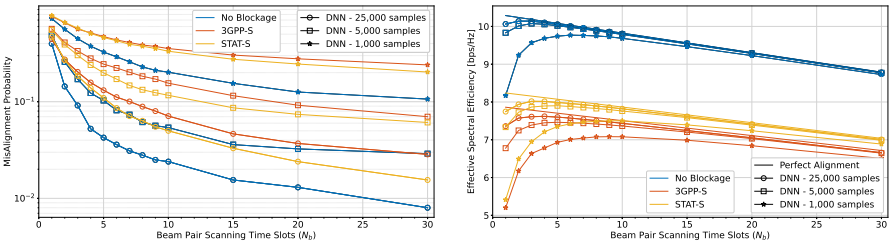

Fig. G.7: The effects of training dataset size on the performance of the DNN-based BA method under different blockage situations. UTs are equally distributed between the portrait and landscape orientation modes, while UTs are in LOS condition.

list in the case of no blockage. However, self-blockage results in the fact that the recommended UT beams are distributed over different panels, especially with the severe blockage loss and the broad blockage region in the 3GPP-S model. Also, increasing the panel blockage uncertainty in the NU and U hand grip schemes compared to the FX scheme leads to more diverse panel sensing. Similar conclusions can be drawn for a longer beam candidate list with 20 beam pairs (right column subplots). It is worth highlighting that using the 3GPP-S blockage model with the FX hand grip scheme, the ML model has learnt not to point the beams from the 3 blocked panels. However, in the cases with NU and U hand grip schemes, the ML model proposes beams from all the panels even with the 3GPP-S blockage model. A conclusion from these results is that the proposed ML model can, through training data fitting the hand-blockage conditions of a given user, adapt its beam recommendation to those by proposing a more diverse list of beams in uncertain blockage conditions, while proposing a more concentrated list for blockage conditions that are less random.

Larger training dataset allows the ML model recognize better the blockage patterns

ML models rely on training data for pattern recognition, thus the performance offered by ML is highly dependent on the distribution and amount of training data. Fig. G.7 shows the performance of the DL-based beam alignment methods with different training dataset sizes under various blockage models. In this experiment, the FX hand grip scheme is considered, where the training and test samples are generated in LOS condition. Also, 50% samples are in portrait orientation mode, whereas the rest are in landscape. This experiment considers small (S), medium (M), and large (L) training datasets, respectively, with $1,000$, $5,000$, and $25,000$ samples. Compared to the performance obtained when training with the L dataset, the ML performance

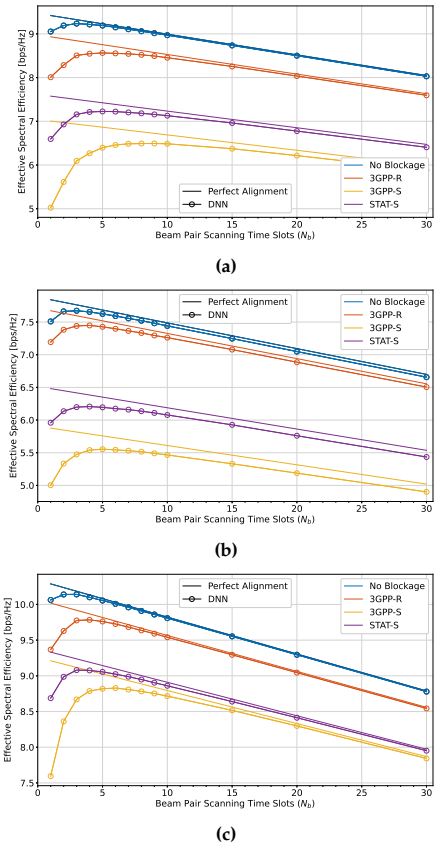

Fig. G.8: Hand-blockage effects on devices with the edge (E), face (F), and EF antenna placement designs. We consider the U hand grip scheme, where UTs are also uniformly in the portrait and landscape orientation modes. (a) E design, (b) F design, (c) EF design.

is not significantly affected when the M training dataset is used. However, severe performance degradation can be seen in the case of training with the S dataset. In addition, we see more performance loss in the case of self-blockage compared to the no-blockage scenario, which shows a higher need for training data to recognize the self-blockage patterns. The transfer learning technique proposed in [43] can be considered as a solution to reduce performance degradation with small training datasets. Therefore, we can conclude that the ML model can learn blockage patterns in order to mitigate the blockage effects, at the expense of a larger amount of training data.

Diversity in antenna placement makes the BA more robust to self-blockage, even though the beam selection task with a larger codebook is more challenging

Although ML-based mmWave beam selection can deal with the self-blockage effects on the EF device with 5 panels, it is interesting to see the performance for devices with fewer panels. We consider in this experiment two additional terminal designs, which we coin the E and F designs. Both are simpler versions of the EF design of Fig G.1, but keeping only a subset of its antenna panels. In the E design, only the three ULA panels on the edges of the terminal are present. Conversely, the F design is equipped with just the two UPA panels placed at the front and back of the terminal [23]. In this experiment, we consider the U hand grip scheme where each panel can be blocked with a probability of 0.5. The training and test datasets contain an equal amount of samples in the portrait and landscape orientation modes. Fig. G.8 shows the self-blockage effects on devices with the E, F, and EF designs in LOS condition. Due to the lower antenna array gain obtained with the E and F devices than the EF design, lower ESE is achieved in the E and F designs. However, the ML-based beam selection can deal with severe self-blockage effects, even with severe and probabilistic blockage conditions with the U hand grip scheme followed by the 3GPP-S blockage model. It is important to note that all the panels in the E, F, and EF designs are blocked, respectively, with probability $0.5^3 = 0.125$, $0.5^2 = 0.25$, and $0.5^5 = 0.03125$, which explains the severe performance degradation with fewer panels in this experiment.

6 Conclusions

In this paper, context-aware ML-based beam selection methods have been evaluated over a novel framework for simulating self-blockage effects due to the user hand grip on hand-held multi-panel devices. Inspired by the blockage models proposed by 3GPP and other previous works, we proposed a set of models that emulate mild and severe self-blockage conditions over different types of hand grips. Our results showed that the ML model is able to learn the blockage patterns from the training data, and thus adapt its beam pair recommendation to the predicted blockage conditions.

From this study, we conclude that the availability of information about terminal orientation can greatly benefit the beam alignment process when hand grip-induced blockage is present. Due to the connection between the terminal's orientation and the user's hand-grip mode, the orientation provides significant amount of information about potentially blocked panels. The evaluated ML-based beam alignment solution can use this information in order to produce a list of recommended beam pairs that is less sensitive

to the possibility of blockages. We observed that, generally, the ML model learns to recommend a list of beam pairs that is more diversified over the different panels under blockage conditions than when no blockage is present. This yields the observed robustness against blockage, resulting in only a minor performance degradation in the beam alignment process.

Although we have seen limited beam alignment performance degradation due to self-blockage, especially in mild self-blockage conditions, the conclusion may change in the case of multi-panel beamforming in the user terminal. Future studies may study the self-blockage impact over context-aware beam alignment performance for devices with multi-panel beamforming capability. Furthermore, calibration of the parameters of the proposed blockage models using data from real users, while out of the scope of this study, would be desirable to further increase the models' degree of realism.

References

[1] M. Giordani, M. Polese, M. Mezzavilla, S. Rangan, and M. Zorzi, "Toward 6G Networks: Use Cases and Technologies," *IEEE Commun. Mag.*, vol. 58, no. 3, pp. 55–61, Mar. 2020.

[2] C. Liu, M. Li, S. V. Hanly, P. Whiting, and I. B. Collings, "Millimeter-Wave Small Cells: Base Station Discovery, Beam Alignment, and System Design Challenges," *IEEE Wirel. Commun.*, vol. 25, no. 4, pp. 40–46, Aug. 2018.

[3] M. Giordani, M. Mezzavilla, and M. Zorzi, "Initial Access in 5G mmWave Cellular Networks," *IEEE Commun. Mag.*, vol. 54, no. 11, pp. 40–47, Nov. 2016.

[4] Z. Xiao, T. He, P. Xia, and X. Xia, "Hierarchical Codebook Design for Beamforming Training in Millimeter-Wave Communication," *IEEE Trans. Wireless Commun.*, vol. 15, no. 5, pp. 3380–3392, May 2016.

[5] C. N. Manchón, E. de Carvalho, and J. B. Andersen, "Ping-pong beam training with hybrid digital-analog antenna arrays," in *Proc. IEEE Int. Conf. Commun.*, May 2017, pp. 1–7.

[6] F. Sohrabi, Z. Chen, and W. Yu, "Deep Active Learning Approach to Adaptive Beamforming for mmWave Initial Alignment," *IEEE Journal on Selected Areas in Communications*, vol. 39, no. 8, pp. 2347–2360, Aug. 2021.

[7] C. Antón-Haro and X. Mestre, "Learning and Data-Driven Beam Selection for mmWave Communications: An Angle of Arrival-Based Approach," *IEEE Access*, vol. 7, pp. 20 404–20 415, 2019.

[8] M. Polese, F. Restuccia, and T. Melodia, "DeepBeam: Deep Waveform Learning for Coordination-Free Beam Management in mmWave Networks," in *Proc. ACM MobiHoc '21*, Jul. 2021, pp. 61–70.

[9] S. Jiang and A. Alkhateeb, "Digital Twin Based Beam Prediction: Can we Train in the Digital World and Deploy in Reality?" Jan. 2023, arXiv:2301.07682 [cs, eess, math]. [Online]. Available: http://arxiv.org/abs/2301.07682

[10] J. Morais, A. Behboodi, H. Pezeshki, and A. Alkhateeb, "Position Aided Beam Prediction in the Real World: How Useful GPS Locations Actually Are?" Sep. 2022, arXiv:2205.09054 [cs, eess, math]. [Online]. Available: http://arxiv.org/abs/2205.09054

[11] V. Va, J. Choi, T. Shimizu, G. Bansal, and R. W. Heath, "Inverse Multipath Fingerprinting for Millimeter Wave V2I Beam Alignment," *IEEE Trans. Veh. Technol.*, vol. 67, no. 5, pp. 4042–4058, May 2018.

[12] M. S. Mollel, A. I. Abubakar, M. Ozturk, S. F. Kaijage, M. Kisangiri, S. Hussain, M. A. Imran, and Q. H. Abbasi, "A Survey of Machine Learning Applications to Handover Management in 5G and Beyond," *IEEE Access*, vol. 9, pp. 45 770–45 802, 2021, conference Name: IEEE Access.

[13] Y. Zhang, M. Alrabeiah, and A. Alkhateeb, "Reinforcement Learning of Beam Codebooks in Millimeter Wave and Terahertz MIMO Systems," *arXiv:2102.11392 [cs, eess, math]*, Feb. 2021. [Online]. Available: http://arxiv.org/abs/2102.11392

[14] W. Xu, F. Gao, S. Jin, and A. Alkhateeb, "3D Scene-Based Beam Selection for mmWave Communications," *IEEE Wireless Commun. Lett.*, vol. 9, no. 11, pp. 1850–1854, Nov. 2020.

[15] L.-H. Shen, T.-W. Chang, K.-T. Feng, and P.-T. Huang, "Design and Implementation for Deep Learning Based Adjustable Beamforming Training for Millimeter Wave Communication Systems," *IEEE Transactions on Vehicular Technology*, vol. 70, no. 3, pp. 2413–2427, Mar. 2021.

[16] Z. Zhu, K. Lin, and J. Zhou, "Transfer Learning in Deep Reinforcement Learning: A Survey," *arXiv:2009.07888 [cs, stat]*, Mar. 2021. [Online]. Available: http://arxiv.org/abs/2009.07888

[17] M. Alrabeiah and A. Alkhateeb, "Deep Learning for mmWave Beam and Blockage Prediction Using Sub-6 GHz Channels," *IEEE Trans. Commun.*, vol. 68, no. 9, pp. 5504–5518, Sep. 2020.

[18] F. Liu, W. Yuan, C. Masouros, and J. Yuan, "Radar-Assisted Predictive Beamforming for Vehicular Links: Communication Served by Sensing," *IEEE Trans. Wireless Commun.*, vol. 19, no. 11, pp. 7704–7719, Nov. 2020.

[19] M. Dias, A. Klautau, N. González-Prelcic, and R. W. Heath, "Position and LIDAR-Aided mmWave Beam Selection using Deep Learning," in *Proc. IEEE Int. Workshop Signal Process. Adv. Wireless Commun. (SPAWC)*, Jul. 2019, pp. 1–5.

[20] G. Charan, M. Alrabeiah, and A. Alkhateeb, "Vision-Aided Dynamic Blockage Prediction for 6G Wireless Communication Networks," in *Proc. IEEE Int. Conf. Commun.*, Jun. 2021, pp. 1–6.

[21] M. Alrabeiah, A. Hredzak, and A. Alkhateeb, "Millimeter Wave Base Stations with Cameras: Vision-Aided Beam and Blockage Prediction," in *Proc. IEEE Vehicular Technology Conference (VTC)*, May 2020, pp. 1–5.

[22] V. Raghavan, M.-L. Chi, M. A. Tassoudji, O. H. Koymen, and J. Li, "Antenna Placement and Performance Tradeoffs With Hand Blockage in Millimeter Wave Systems," *IEEE Trans. Commun.*, vol. 67, no. 4, pp. 3082–3096, Apr. 2019.

[23] S. Rezaie, J. Morais, E. de Carvalho, A. Alkhateeb, and C. N. Manchón, "Location- and Orientation-aware Millimeter Wave Beam Selection for Multi -Panel Antenna Devices," in *GLOBECOM 2022 - 2022 IEEE Global Communications Conference*, Dec. 2022, pp. 597–602.

[24] V. Raghavan, R. A. Motos, M. A. Tassoudji, Y.-C. Ou, O. H. Koymen, and J. Li, "Mitigating Hand Blockage with Non-Directional Beamforming Codebooks," *arXiv:2104.06472 [cs, math]*, Apr. 2021. [Online]. Available: http://arxiv.org/abs/2104.06472

[25] J. Mo, B. L. Ng, S. Chang, P. Huang, M. N. Kulkarni, A. Alammouri, J. C. Zhang, J. Lee, and W.-J. Choi, "Beam Codebook Design for 5G mmWave Terminals," *IEEE Access*, vol. 7, pp. 98 387–98 404, 2019.

[26] W.-T. Shih, C.-K. Wen, S.-H. Tsai, and S. Jin, "Fast Antenna and Beam Switching Method for mmWave Handsets with Hand Blockage," *IEEE Trans. Wireless Commun.*, pp. 1–1, 2021.

[27] A. Alammouri, J. Mo, B. L. Ng, J. C. Zhang, and J. G. Andrews, "Hand Grip Impact on 5G mmWave Mobile Devices," *IEEE Access*, vol. 7, pp. 60 532–60 544, 2019.

[28] X. Song, T. Kuhne, and G. Caire, "Fully-/Partially-Connected Hybrid Beamforming Architectures for mmWave MU-MIMO," *IEEE Trans. Wireless Commun.*, vol. 19, no. 3, pp. 1754–1769, Mar. 2020.

[29] 3GPP, *Study on channel model for frequencies from 0.5 to 100 GHz*. TR 38.901 V16.1.0, 2020. [Online]. Available: http://www.3gpp.org/DynaReport/38901.htm

[30] F. Fernandes, C. Rom, J. Harrebek, S. Svendsen, and C. N. Manchón, "Hand Blockage Impact on 5G mmWave Beam Management Performance," *IEEE Access*, vol. 10, pp. 106 033–106 049, 2022, conference Name: IEEE Access.

[31] V. Raghavan, L. Akhoondzadeh-Asl, V. Podshivalov, J. Hulten, M. A. Tassoudji, O. H. Koymen, A. Sampath, and J. Li, "Statistical Blockage Modeling and Robustness of Beamforming in Millimeter-Wave Systems," *IEEE Transactions on Microwave Theory and Techniques*, vol. 67, no. 7, pp. 3010–3024, Jul. 2019.

[32] V. Raghavan, S. Noimanivone, S. K. Rho, B. Farin, P. Connor, R. A. Motos, Y.-C. Ou, K. Ravid, M. A. Tassoudji, O. H. Koymen, and J. Li, "Hand and Body Blockage Measurements with Form-Factor User Equipment at 28 GHz," *IEEE Trans. Antennas Propag.*, vol. 70, no. 1, pp. 607–620, 2021.

[33] S. Rezaie, E. De Carvalho, and C. N. Manchón, "A Deep Learning Approach to Location- and Orientation-aided 3D Beam Selection for mmWave Communications," *IEEE Trans. Wireless Commun.*, vol. 21, no. 12, pp. 11 110–11 124, 2022.

[34] "Altair Feko WinProp," [online] Available: https://www.altair.com/feko.

[35] V. Raghavan, L. Akhoondzadeh-Asl, V. Podshivalov, J. Hulten, M. A. Tassoudji, O. H. Koymen, A. Sampath, and J. Li, "Statistical Blockage Modeling and Robustness of Beamforming in Millimeter-Wave Systems," *IEEE Transactions on Microwave Theory and Techniques*, pp. 1–15, 2019.

[36] Y. Ma, L. Yang, and X. Zheng, "A geometry-based non-stationary MIMO channel model for vehicular communications," *China Communications*, vol. 15, no. 7, pp. 30–38, Jul. 2018, conference Name: China Communications.

[37] C. J. Park, H. W. Moon, W. Kim, and Y. J. Yoon, "WINNER channel model with geometric optics and probability for indoor environment," in *2014 International Symposium on Antennas and Propagation Conference Proceedings*, Dec. 2014, pp. 253–254.

[38] M. Kok, J. D. Hol, and T. B. Schön, "Using Inertial Sensors for Position and Orientation Estimation," *Found. Trends Signal Process.*, vol. 11, no. 1-2, pp. 1–153, 2017.

[39] C. De Lima, D. Belot, R. Berkvens, A. Bourdoux, D. Dardari, M. Guillaud, M. Isomursu, E.-S. Lohan, Y. Miao, A. N. Barreto, M. R. K. Aziz, J. Saloranta, T. Sanguanpuak, H. Sarieddeen, G. Seco-Granados, J. Suutala, T. Svensson, M. Valkama, B. Van Liempd, and H. Wymeersch, "Convergent Communication, Sensing and Localization in 6G Systems: An Overview of Technologies, Opportunities and Challenges," *IEEE Access*, vol. 9, pp. 26 902–26 925, 2021.

[40] A. Maltsev, "Channel models for 60GHz WLAN systems," *IEEE802. 11 09/0334r8*, 2010.

[41] D. P. Kingma and J. Ba, "Adam: A Method for Stochastic Optimization," in *Proc. Int. Conf. Learn. Representations*, 2015.

[42] M. Hussain and N. Michelusi, "Second-Best Beam-Alignment via Bayesian Multi-Armed Bandits," in *Proc. IEEE GLOBECOM*, Dec. 2019, pp. 1–6.

[43] S. Rezaie, A. Amiri, E. de Carvalho, and C. N. Manchón, "Deep Transfer Learning for Location-Aware Millimeter Wave Beam Selection," *IEEE Commun. Lett.*, vol. 25, no. 9, pp. 2963–2967, Sep. 2021.

ISSN (online): 2446-1628
ISBN (online): 978-87-7573-737-6

AALBORG UNIVERSITY PRESS